

MATERIALS PHYSICS AND MECHANICS

Vol. 52, No. 3, 2024

125[®]

MATERIALS PHYSICS AND MECHANICS

Principal Editors:

Alexander Belyaev

Andrei Rudskoi

Institute for Problems in Mechanical Engineering of the Russian Academy of Science (RAS), Russia

Peter the Great St. Petersburg Polytechnic University, Russia

Founder and Honorary Editor: Ilya Ovid'ko (1961-2017)

Institute for Problems in Mechanical Engineering of the Russian Academy of Sciences (RAS), Russia

Associate Editor:

Anna Kolesnikova

Artem Semenov

Institute for Problems in Mechanical Engineering of the Russian Academy of Sciences (RAS), Russia

Peter the Great St. Petersburg Polytechnic University, Russia

Editorial Board:

E.C. Aifantis

Aristotle University of Thessaloniki, Greece

K.E. Aifantis

University of Florida, USA

U. Balachandran

Argonne National Laboratory, USA

A. Bellosi

Research Institute for Ceramics Technology, Italy

S.V. Bobylev

Institute for Problems in Mechanical Engineering (RAS), Russia

A.I. Borovkov

Peter the Great St.Petersburg Polytechnic University, Russia

G.-M. Chow

National University of Singapore, Singapore

Yu. Estrin

Monash University, Australia

A.B. Freidin

Institute for Problems in Mechanical Engineering (RAS), Russia

Y. Gogotsi

Drexel University, USA

I.G. Goryacheva

Institute of Problems of Mechanics (RAS), Russia

D. Hui

University of New Orleans, USA

G. Kiriakidis

IESL/FORTH, Greece

D.M. Klimov

Institute of Problems of Mechanics (RAS), Russia

G.E. Kodzhaspirov

Peter the Great St. Petersburg Polytechnic University, Russia

S.A. Kukushkin

Institute for Problems in Mechanical Engineering (RAS), Russia

T.G. Langdon

University of Southampton, U.K.

V.P. Matveenko

Institute of Continuous Media Mechanics (RAS), Russia

A.I. Melker

Peter the Great St. Petersburg Polytechnic University, Russia

Yu.l. Meshcheryakov

Institute for Problems in Mechanical Engineering (RAS), Russia

N.F. Morozov

St. Petersburg State University, Russia

R.R. Mulyukov

Institute for Metals Superplasticity Problems (RAS), Russia

Yu.V. Petrov

St. Petersburg State University, Russia

N.M. Pugno

Politecnico di Torino, Italy

B.B. Rath

Naval Research Laboratory, USA

A.E. Romanov

Ioffe Institute (RAS), Russia

A.M. Sastry

University of Michigan, Ann Arbor, USA

B.A. Schrefler

University of Padua, Italy

N.V. Skiba

Institute for Problems in Mechanical Engineering (RAS), Russia

A.G. Sheinerman

Institute for Problems in Mechanical Engineering (RAS), Russia

R.Z. Valiev

Ufa State Aviation Technical University, Russia

K. Zhou

Nanyang Technological University, Singapore

"Materials Physics and Mechanics" Editorial Office:

Phone: +7(812)552 77 78, ext. 224 E-mail: mpmjournal@spbstu.ru Web-site: http://www.mpm.spbstu.ru

International scientific journal "Materials Physics and Mechanics" is published by Peter the Great St. Petersburg Polytechnic University in collaboration with Institute for Problems for Mechanical Engineering in the Russian Academy of Sciences in both hard copy and electronic versions. The journal provides an international medium for the publication of reviews and original research papers written in English and focused on the following topics:

- Mechanics of composite and nanostructured materials.
- Physics of strength and plasticity of composite and nanostructured materials.
- Mechanics of deformation and fracture processes in conventional materials (solids).
- Physics of strength and plasticity of conventional materials (solids).
- Physics and mechanics of defects in composite, nanostructured, and conventional materials.
- Mechanics and physics of materials in coupled fields.

Owner organizations: Peter the Great St. Petersburg Polytechnic University; Institute of Problems of Mechanical Engineering RAS.

Materials Physics and Mechanics is indexed in Chemical Abstracts, Cambridge Scientific Abstracts,
Web of Science Emerging Sources Citation Index (ESCI) and Elsevier Bibliographic Databases (in particular, SCOPUS).

© 2024, Peter the Great St. Petersburg Polytechnic University © 2024, Institute for Problems in Mechanical Engineering RAS



МЕХАНИКА И ФИЗИКА МАТЕРИАЛОВ

Materials Physics and Mechanics

Том 52, номер 3, 2024 год

Учредители:

Редакционная коллегия журнала Главные редакторы:

д.ф.-м.н., чл.-корр. РАН А.К. Беляев Институт проблем машиноведения Российской академии наук (РАН)

д.т.н., академик РАН А.И. Рудской Санкт-Петербургский политехнический университет Петра Великого

Основатель и почетный редактор: д.ф.-м.н. И.А. Овидько (1961-2017)

Институт проблем машиноведения Российской академии наук (РАН)

Ответственные редакторы

д.ф.-м.н. А.Л. Колесникова

Институт проблем машиноведения Российской академии наук (РАН)

д.ф.-м.н. А.С. Семенов Санкт-Петербургский политехнический университет Петра Великого

Международная редакционная коллегия:

д.ф.-м.н. С.В. Бобылев

Институт проблем машиноведения РАН, Россия

к.т.н., проф. А.И. Боровков

Санкт-Петербургский политехнический ун-т Петра Великого, Россия

д.ф.-м.н., проф. Р.З. Валиев

Уфимский государственный технический университет, Россия

д.ф.-м.н., академик РАН И.Г. Горячева

Институт проблем механики РАН, Россия

д.ф.-м.н., академик РАН Д.М. Климов

Институт проблем механики РАН, Россия

д.т.н., проф. Г.Е. Коджаспиров

Санкт-Петербургский политехнический ун-т Петра Великого, Россия

д.ф.-м.н., проф. С.А. Кукушкин

Институт проблем машиноведения РАН, Россия

д.ф.-м.н., академик РАН В.П. Матвеенко

Институт механики сплошных сред РАН, Россия

д.ф.-м.н., проф. А.И. Мелькер

Санкт-Петербургский политехнический ун-т Петра Великого, Россия

д.ф.-м.н., проф. Ю.И. Мещеряков

Институт проблем машиноведения РАН, Россия

д.ф.-м.н., академик РАН Н.Ф. Морозов

Санкт-Петербургский государственный университет, Россия

д.ф.-м.н., чл.-корр. РАН Р.Р. Мулюков

Институт проблем сверхпластичности металлов РАН, Россия

д.ф.-м.н., чл.-корр. РАН Ю.В. Петров Санкт-Петербургский государственный университет, Россия

д.ф.-м.н., проф. А.Е. Романов

Физико-технический институт им. А.Ф. Иоффе РАН, Россия д.ф.-м.н. **Н.В. Скиба**

Институт проблем машиноведения РАН, Россия

д.ф.-м.н., проф. А.Б. Фрейдин

Институт проблем машиноведения РАН, Россия

д.ф.-м.н. А.Г. Шейнерман

Институт проблем машиноведения РАН, Россия

Prof., Dr. E.C. Aifantis

Aristotle University of Thessaloniki, Greece

Dr. K.E. Aifantis

University of Florida, USA

Dr. U. Balachandran

Argonne National Laboratory, USA

Dr. A. Bellosi

Research Institute for Ceramics Technology, Italy

Prof., Dr. G.-M. Chow

National University of Singapore, Singapore

Prof., Dr. Yu. Estrin Monash University, Australia

Prof., Dr. Y. Gogotsi

Drexel University, USA

Prof., Dr. **D. Hui**

University of New Orleans, USA

Prof., Dr. G. Kiriakidis

IESL/FORTH. Greece

Prof., Dr. T.G. Langdon

University of Southampton, UK

Prof., Dr. N.M. Pugno

Politecnico di Torino, Italy

Dr. B.B. Rath

Naval Research Laboratory, USA

Prof., Dr. A.M. Sastry

University of Michigan, Ann Arbor, USA

Prof., Dr. B.A. Schrefler

University of Padua, Italy

Prof., Dr. K. Zhou Nanyang Technological University, Singapore

Тел.: +7(812)552 77 78, доб. 224 E-mail: mpmjournal@spbstu.ru Web-site: http://www.mpm.spbstu.ru

Тематика журнала

Международный научный журнал "Materials Physics and Mechanics" издается Санкт-Петербургским политехническим университетом Петра Великого в сотрудничестве с Институтом проблем машиноведения Российской академии наук в печатном виде и электронной форме. Журнал публикует обзорные и оригинальные научные статьи на английском языке по следующим тематикам:

- Механика композиционных и наноструктурированных материалов.
- Физика прочности и пластичности композиционных и наноструктурированных материалов.
- Механика процессов деформации и разрушения в традиционных материалах (твердых телах).
- Физика прочности и пластичности традиционных материалов (твердых тел).
- Физика и механика дефектов в композиционных, наноструктурированных и традиционных материалах.
- Механика и физика материалов в связанных полях.

Редколлегия принимает статьи, которые нигде ранее не опубликованы и не направлены для опубликования в другие научные издания. Все представляемые в редакцию журнала "Механика и физика материалов" статьи рецензируются. Статьи могут отправляться авторам на доработку. Не принятые к опубликованию статьи авторам не возвращаются.

Журнал "Механика и физика материалов" ("Materials Physics and Mechanics") включен в систему цитирования Web of Science Emerging Sources Citation Index (ESCI), SCOPUS и РИНЦ.

Contents

Experimental determination of physical, chemical and surface properties of biocompatible thermoplastic D.A. Erofeev, P.B. Pirozhnikov, I.A. Keresten, A.G. Titov	1-12
Influence of adhesive interaction on the sound speed in layered composites RR.V. Razakova, R.A. Turusov	13-21
Topology optimization algorithm for heterogeneous anisotropic materials and structure <i>A.D. Novokshenov, D.V. Vershinin, I.I. Abdulin</i>	es 22-32
Variants of physical equations in a curvilinear coordinate system and their comparison based on mixed FEM R.Z. Kiseleva, N.A. Kirsanova, A.P. Nikolaev, Yu.V. Klochkov, V.N. Yushkin	33-43
Synthesis and tensile behavior of Al7475-nano B ₄ C particles reinforced composites at elevated temperatures G.L. Chandrasekhar, Y. Vijayakumar, M. Nagaral, A. Rajesh, K. Manjunath, R. Vara Prasad Kaviti,	44–57 <i>V. Auradi</i>
Unique properties of the Al-0.5Fe-0.3Cu alloy, obtained by casting into an electromagnetic crystallizer, after equal-channel angular pressing and cold of A.E. Medvedev, O.O. Zhukova, V.U. Kazykhanov, A. F. Shaikhulova, M.M. Motkov, V.N. Timofeev, N.A. Enikeev, M.Yu. Murashkin	58–72 drawing
Outstanding ductility of high-strength ultrafine-grained aluminium at cryogenic temperatures T.S. Orlova, D.I. Sadykov	73-79
The effect of high-temperature annealing on the properties of bulk β -Ga ₂ O ₃ obtained in different growth atmospheres <i>V.A. Spiridonov, D.I. Panov, A.Yu. Ivanov, D.A. Bauman, A.E. Romanov</i>	80-85
Influence of aluminum shell on the process of devitrification of amorphous titanium nanoparticles: molecular dynamics simulation G.M. Poletaev, Y.Y. Gafner, S.L. Gafner, I.V. Zorya, Y.V. Bebikhov, A.S. Semenov	86-95
Interaction of two circular holes in an infinite plate by body force method S. M. Badiger, D.S. Ramakrishna	96-107
The role of the hydrostatic pressure under dynamic fracture of rocks N.S. Selyutina, L.A. Igusheva, Y.V. Petrov	108-120

Laboratory study on use of lime and waste materials in improving geotechnical properties of clay G. Juneja, A. Bhardwaj, A. Sharma, R.K. Sharma	121-144
Research of hydrogen diffusion in a material with various types of traps V.A. Polyanskiy, E.A. Varshavchik, A.A. Chevrychkina	145-153
Chromium plating of steel parts using the thermoemission field N.A. Shaburova	154-160

Submitted: March 14, 2024 Revised: May 29, 2024 Accepted: July 16, 2024

Experimental determination of physical, chemical and surface properties of biocompatible thermoplastic

D.A. Erofeev ¹, ⁽ⁱ⁾ P.B. Pirozhnikov ¹, ⁽ⁱ⁾ I.A. Keresten ^{2 M}, ⁽ⁱ⁾ A.G. Titov ³, ⁽ⁱ⁾

ABSTRACT

The main purpose of this research is determination of physical, chemical and surface properties of thermoplastics, which were certificated for medical employment, for implant or prosthesis manufacturing. The physical and chemical structure of thermoplastics (polyacrylonitrile-co-butadiene-co-styrene, polycarbonate, polyetherimide) were investigated with the Fourier-transform infrared spectroscopy (FTIR), differential thermal and thermogravimetric analysis (DTA/TG), differential scanning calorimetry (DSC), wide-angle X-ray diffraction (XRD) and scanning electron microscopy (SEM). The surface of all investigated thermoplastics had a transition or a hydrophobic state. The contact angle hysteresis by distilled water was in range 95.6–103.0° that indicates "sticky" wetting behavior of surfaces. The contact angle by blood plasma was in the range 84.7–92.1°, depending on the chemical structure of the thermoplastic polymer. Despite the lower contact angle value of the blood plasma, the amount of its adsorption was greater than in case of distilled water, and it should be considered in development of medical polymer devices.

KEYWORDS

thermoplastics • polyacrylonitrile-co-butadiene-co-styrene • polycarbonate • polyetherimide • endoprosthetics physical and chemical properties • surface wetting

Citation: Erofeev DA, Pirozhnikov PB, Keresten IA, Titov AG. Experimental determination of physical, chemical and surface properties of biocompatible thermoplastic. *Materials Physics and Mechanics*. 2024;52(3): 1–12. http://dx.doi.org/10.18149/MPM.5232024 1

Introduction

Endoprosthetics is the widespread surgical procedure for normal function recovery of original joints after different defects or diseases [1]. The Increase of the joint's replacement surgery is conditioned by both a growth of average life expectancy and an implant service time (more than 12–15 years) due to the appearance of new materials [2]. Usually for implant production the titanium alloy Ti₆Al₄V is used as base material, because it contains a whole set of required properties for medical devices (a biocompatibility, an ultimate strength, etc.). Unfortunately, the usage of Ti₆Al₄V in the musculoskeletal system may lead to bone tissue destruction near the contact surface of bone-implant pairs for two reasons. Firstly, due to the difference in mechanical properties between the cortical bone and Ti₆Al₄V [3,4]. Secondly, the contact surface of the bone-implant pair includes screw holes for its connection, which represent a stress concentrator and lead to increase the stress and probability of bone failure [5–7]. In addition, it is necessary to identify the shape of the implant for greater compatibility of bone-implant contact pair, which leads to increasing the implant lifetime and shortening

¹ St. Petersburg Institute of Technology (Technical University), St. Petersburg, Russia

² Peter the Great St. Petersburg Polytechnic University, St. Petersburg, Russia

³ Institute of Medical Education of Almazov National Medical Research Centre, St. Petersburg, Russia

[™] keresten@compmechlab.com

the period of patient rehabilitation after the surgery. Today it is possible to manufacture personalized implants which consider individual patient's characteristics which are obtained using computerized tomography. However, standard-size implants are still used because personalized implants have a longer production cycle. Unfortunately, standard-size implants consider individual characteristics of the patient only partially, which lead to shortening the implant lifetime due to imperfect contact interaction [1].

A more complicated situation occurred with the revision of endoprosthetics. Standard-size metallic implants often have a polygonal shape that can lead to several problems. Firstly, it will require excessive bone removing for a precise augment placing. Secondly, the unrounded shape corners will be zones with increased mechanical stress, which lead to the bone tissue destruction. Therefore, it is crucial to simplify and shorten the production cycle of implants with complicated shapes (for example, it would be quite convenient to manufacture implants "near operating table") to increase the implant lifetime and to shorten the period of patient rehabilitation after the surgery. For such purpose, thermosetting polymers are more preferred for manufacturing implants with complicated shapes.

Polymeric materials can be very useful as polymer matrix composite for different kinds of medical devices (implants, prostheses, syringes, blood bags and other) [8]. Medical devices, which are made of polymeric materials, should satisfy special requirements caused by orthopedic surgery: biocompatibility, strength, durability, adhesion, osseointegration [9,10]. Polymeric materials should be durable to an aggressive environment during a sterilization process as well as have no toxic components in the compound during the usage of implant [3,4,8]. The modern thermoplastics could be easily manufactured, that allow creating implants with complicated shapes, and it is very suitable for personalized endoprosthetics. Most thermoplastic polymers don't cause an immune response, which is one of the criteria of biocompatibility [11]. However, during the usage of implant, several polymeric materials may release toxic monomers [8]. Surfaces of the most thermoplastic polymers are usually bioinert [12], that create difficulties for recovering of around laid tissues [13]. The bioinert property of thermoplastics lead to adhesion failure of the implant or the prosthesis with around laid tissues. As a result, additional surgery may be required [2]. Finally, thermoplastic implants and prosthesis have a long-lasting manufacturing cycle.

Today, the possibilities of thermosetting polymers usage in endoprosthetics have not been studied yet and represent scientific novelty [14–16]. That is due to special features of such thermosetting polymers, particularly the liquid-solid state transition during its curing, which leads to almost impossible full monomer conversation. This will lead to the presence of a small amount of residual unreacted toxic monomer around laid tissues. Another unpleasant feature concerns the necessity to precisely control the linking density of the thermosetting polymers, since a highly linked polymer matrix has the brittle failure behavior [17]. However, such limitations of the thermosetting polymers could be overcome by different methods of modification of their chemical composition, for example: an introduction of chain extensions to increase the plastic deformation of the polymer matrix; a selection of monomers and catalysts that increase conversion. It is safety to say that high speed between monomers shortens the time of manufacturing for

medical devices. The great advantage of thermosetting polymer matrix consists in high adhesion to various surfaces due to generation of chemical and physical bonding.

The main purpose of this research consists in investigation of the physical, chemical and surface properties of available biocompatible thermoplastics in order to determine requirements to chemical composition of thermosetting polymer matrix for satisfying special requirements caused by orthopedic surgery. Well known experimental methods (FTIR, DTA/TG, DSC, XRD and SEM) were used to determine the physical, chemical and surface properties of investigated thermoplastics [18–21].

Materials and Methods

In this article as the object of research several biocompatible (by the standard ISO 10993 USP Class VI according to the data provided by the manufacturer on the official website [22]) thermoplastic polymers are considered: polyacrylonitrile-co-butadiene-co-styrene (ABS-M30i, Stratasys Ltd.), polycarbonate (PC-ISO, Stratasys Ltd.) and polyetherimide (Ultem 1010 Resin, Stratasys Ltd.).

Samples manufacturing

The standard samples were manufactured with the industrial grade 3D-printer Stratasys Fortus 450mc (Stratasys Ltd.) by fused deposition modeling. 3D-printing is realized by a print head with 2 nozzle tips. The angle of thread laying was close to 90° during 3D-printing. The 3D-printing surface is presented by a plastic build sheet, which is held to the aluminum platen with a machined pattern using a vacuum source. The thickness of the one layer for ABS-M30i and PC-ISO was 178 μ m, whereas the thickness of the one layer of Ultem 1010 Resin was 254 μ m due to technological limitations of the 3D-printer. The thickness of each sample was 3 mm. 3D-printing was performed in a heated build chamber. The temperature of the chamber was around 88–105 °C, while the speed of 3D-printing was about 6–7.5 mm/sec.

Fourier-transform infrared spectroscopy

Fourier-transform infrared (FTIR) spectra were obtained by the spectrometer IRTracer-100 (Shimadzu Europa GmbH) using the attenuated total reflectance (ATR) console Quest (Specac Ltd.). Diamond was used as the crystal material. The incidence angle of the IR-beam on the crystal surface was 45°. The penetration depth was 2 µm. The FTIR spectroscopy was conducted in order to identify chemical structure, confirm data declared by the manufacturer and check the absence of additional chemical modification.

Contact angle measurement

Static and dynamic contact angles were measured with the goniometer KRUSS DS225 (KRUSS GmbH) using Advance software. Static contact angles were measured by the sessile drop method with drop volume about $2-4~\mu l$. The contact angle values were averaged between 5-10 measurements at different points of the surface. Dynamic contact angles were measured by a method of increasing and decreasing drop volume that is being in contact with the surface. Firstly, $4~\mu l$ were placed at the surface of the

polymers, wherein the syringe tip stayed in the drop. Advancing contact angle was obtained during simultaneously adding the following 6 μ l with measuring of contact line increasing. The receding contact angle was obtained by the contact line decreasing during removal of the liquid.

Differential thermal and thermogravimetric analysis

For the differential thermal and thermogravimetric analysis, the derivatograph DTG-60 (Shimadzu Europa GmbH) was used. Samples with 11 ± 1 mg mass were placed in an alumina crucible and heated from 20 to 600 °C with 10 °C/min speed in the air environment. The empty alumina crucible was used as a comparison sample.

Differential scanning calorimetry

The glass temperature (Tg) of polymers were obtained by differential scanning calorimeter (DSC) Netzsch DSC 214 Polyma (Netzsch GmbH). Samples with 10.5 ± 2.5 mg mass were placed in an alumina crucible with pierced lid and heated from 50 to 250 °C with 10°C/min speed in the N_2 environment in accordance with ISO 11357-1:2016. The DSC curve of empty alumina crucible, heated at the same conditions, was subtracted from all obtained DSC curves.

Distilled water and blood plasma absorption

The distilled water and blood plasma adsorption was measured in accordance with ISO 62:2008. In case of distilled water, the investigation was conducted at 23 °C with a 10-day duration of the exposition. In case of blood plasma, the investigation was conducted also at 23 °C but with an 8-day duration of the exposition.

X-ray diffraction

Wide-angle X-ray diffraction (XRD) data were obtained by Rigaku Corporation SmartLab 3 (Rigaku Americas Corp.) diffractometer using CuK_{α} radiation equipped with a nickel foil filter. K_{β} was not considered due to using nickel filter. The length of the emitted wave by the copper tube of the apparatus equals 1.54 Å. Samples were pre-cleaned and placed in a non-crushed state in a measuring cuvette. Data were obtained by counting for 2 s at each 0.01° step in 20. The blank curve was subtracted from all obtained data. Determination of interplanar distance with separation of peaks was performed using the Origin 2019 software. Obtained curves were pre-smoothed by 80 points using the Fourier transform.

Scanning electron microscopy

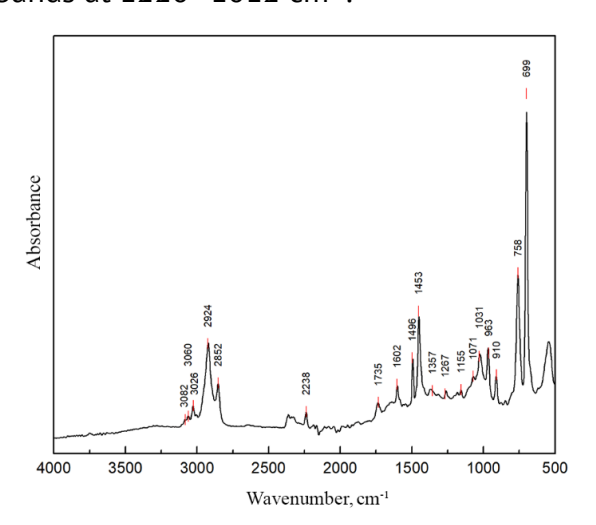
The cross-section of polymers was obtained using scanning electron microscopy (SEM) by TESCAN VEGA 3 SBH (TESCAN Ltd.) microscope. Accelerated voltage was about 5-20 kV, focus distance was 15 mm and probe current was 17 pA. Samples were frozen in liquid N₂, cracked, and fixed on a double-sided tape. The carbon layer with 5-20 nm thickness was sprayed on the sample surface using the Q150RE (Quorum Technologies Ltd.). For an image registration, the secondary electron detector was used.

Results and Discussion

The FTIR spectroscopy

The IR-spectra of ABS-M30i (Fig. 1) contains absorption bands of -C-H- groups at 2924–2852, 1453 and 1267 cm⁻¹. Absorption bands at 1735 and 1267–1031 cm⁻¹ indicate the presence of ester and ether groups. The presence of a styrene fragment is indicated by absorption bands 3060–3026, 1735, 1602, 1496, and 758–693 cm⁻¹. Absorption bands at 963–910 cm⁻¹ indicate the presence of polybutadiene fragments. The presence of -CN fragments of an acrylonitrile is indicated by the absorption band at 2238 cm⁻¹. Absorption band at 3082 cm⁻¹ indicates the presence of the aryl or of -C=C- groups. The absence of absorption bands near 3300, 1637 and 1552 cm⁻¹, which are typical for -NH- groups of amides, indicates on absence of antistatic agents, which are usually added in a commercial polyacrylonitrile-co-butadiene-co-styrene [23].

The IR-spectra of PC-ISO (Fig. 2) contains absorption bands of $-CH_3$ and $-CH_2$ -groups at 2967–2849 and 1413–1363 cm⁻¹. Absorption bands at 3050, 1602, 1500, 1465, and 760 cm⁻¹ indicate the presence of aryl and *p*-substituted aryl rings. The presence of aryl-aryl, aryl-alkyl and alkyl-alkyl -C-O-C- ether groups is indicated by absorption bands at 1220–1012 cm⁻¹.



4000 3500 3000 2500 2000 1500 1000 5000

Wavenumber, cm-1

Fig. 1. The IR-spectra of ABS-M30i

Fig. 2. The IR-spectra of PC-ISO

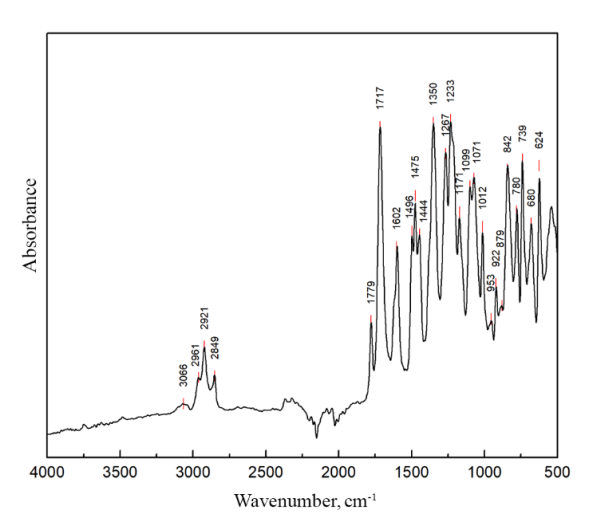


Fig. 3. The IR-spectra of Ultem 1010 Resin

More complicated the IR-spectra of Ultem 1010 Resin (Fig. 3) contains absorption bands of aryl ring at 3066 and 1602-1496 cm⁻¹, carbonyl groups of imide at 1717 cm⁻¹ and -C(0)-N-C(0) – ring of imide at 1350, 1171, 1071, 842, and 739 cm⁻¹. The presence of ester groups is indicated by the absorption band at 1779 cm⁻¹. Absorption bands at 1267–1233, 1091 and 1012 indicate the presence of aryl-aryl and alkyl-aryl groups. The presence of $-CH_3$ and $-CH_2$ – groups is indicated by absorption bands at 2961–2849 and 953–922 cm⁻¹ [24–26].

The investigation of wetting parameters

Surfaces of all investigated thermoplastics have transition or hydrophobic properties (Table 1), which leads to increasing persistence to an infection occurring [27]. At the same time the protein adhesion that leads to recovery of around laid tissues, could be shortened because of the hydrophobic property of the thermoplastics [3,28]. Ultem 1010 Resin has the largest contact angle hysteresis, which indicates high water adhesion to its surface. PC-ISO has the least contact angle hysteresis and ABS-M30i has the value between other thermoplastic polymers. However, all investigated thermoplastics have relatively high contact angle hysteresis, which may provide an increase of both proteins and bacterial adhesion [29,30]. Also, the blood plasma has high wettability of PC-ISO and Ultem 1010 Resin surfaces.

Table 1. The values of contact angles and hysteresis of all investigated thermoplastics

Thermoplastic	θ _W , °	θ _{Adv} , °	$ heta_{ ext{Rec}}$, °	Hysteresis θ, °	θ _P , °
ABS-M30i	89.6 ± 2.3	95.6 ± 0.6	24.4 ± 3.3	71.2 ± 3.9	92.1 ± 2.3
PC-ISO	89.5 ± 2.8	85 ± 1	22.6 ± 3.2	62.4 ± 4.1	84.7 ± 1.6
Ultem 1010 Resin	96.4 ± 3.1	103 ± 1.4	8.8 ± 1.2	94.2 ± 2.5	86.1 ± 2.9

DTA/TG and DSC investigations

All investigated thermoplastics have the same mass losing character (Fig. 4). The destruction temperature of ABS-M30i and PC-ISO (Fig. 4(a,b)) is about 375 °C. Ultem 1010 Resin is the most stable to oxidative destruction thermoplastic polymer, which starts to destruct at almost 500 °C (Fig. 4(c)). Ultem 1010 Resin loses about 2.5 wt. % of its mass up to 250 °C due to evaporation of volatile components. Weight loss may be caused by evaporation of the sorbed water from the sample, which is retained by hydrogen bonding between water molecules and amide groups of Ultem 1010 Resin. The same phenomena do not occur for ABS-M30i and PC-ISO.

All presented DSC curves include a single glass transition, which indicates the absence of crystal structure of all investigated thermoplastics (Fig. 5). Based on this study, it can be assumed that the investigated thermoplastics are amorphous. The glass transitions of ABS-M30i, PC-ISO and Ultem 1010 Resin equal 101.4, 135.8 and 207.2 °C.

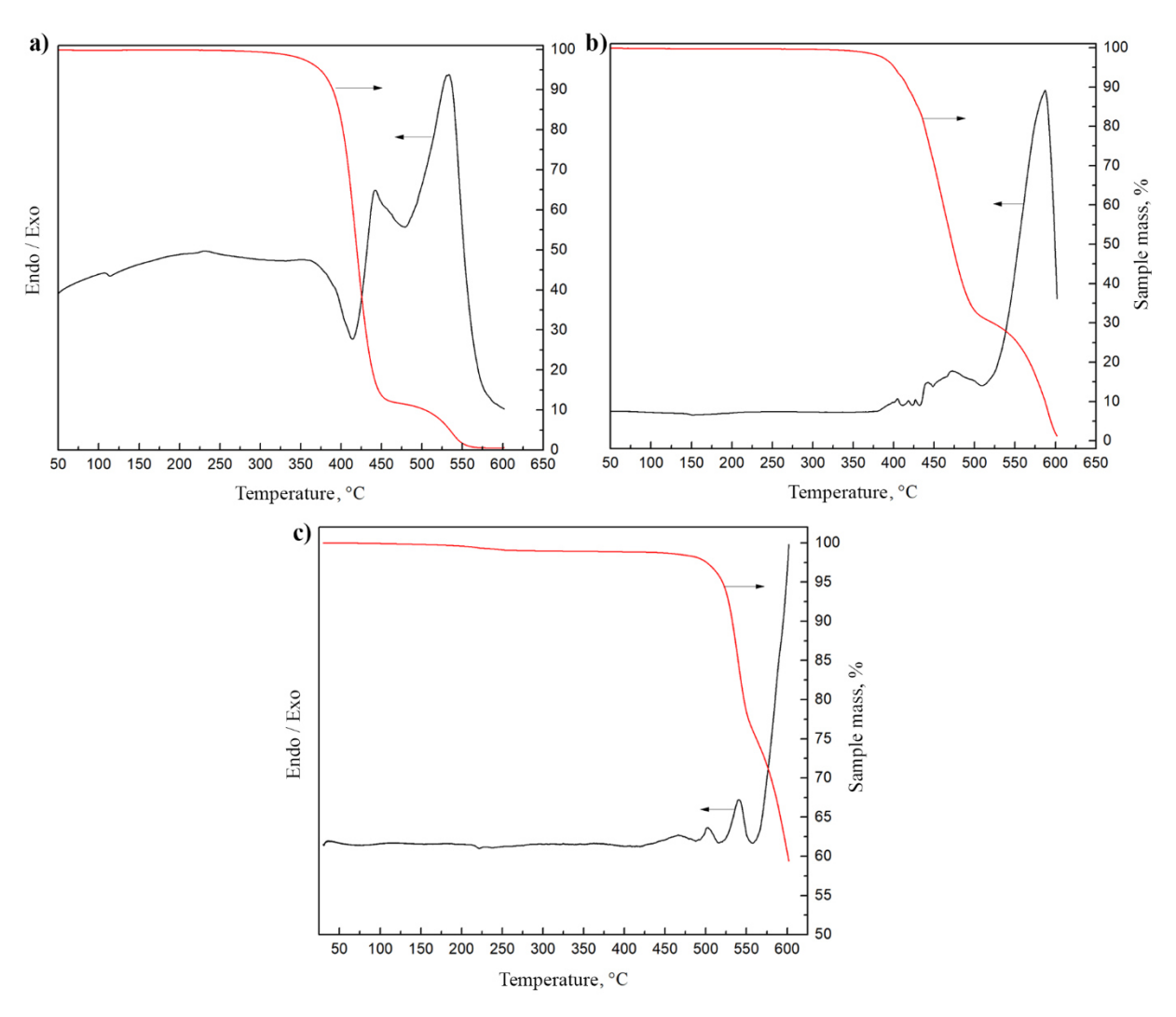


Fig. 4. DTA/TG curves: (a) ABS-M30i; (b) PC-ISO; (c) Ultem 1010 Resin

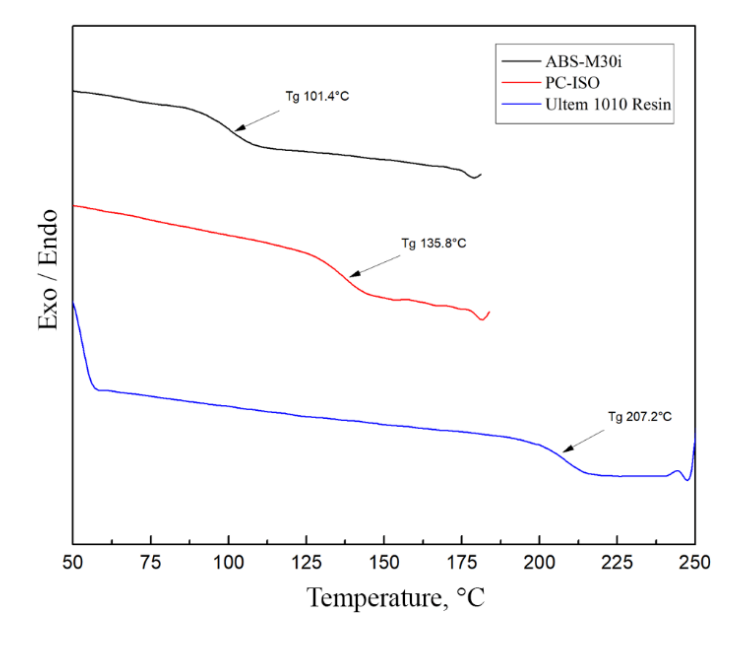


Fig. 5. DSC cooling curves of all investigated thermoplastics

Absorption investigation

It is well known that polymers tend to absorb surrounding substances. The amount of absorbed substance indicates the presence of open micropores or channels inside the polymer body or structure defects. It also may indicate the absence of water-soluble monomers. The absence of monomers in the final polymer is extremely important, since the toxicity of monomers significantly exceeds the toxicity of polymers. Moreover, the absorption of such substances can lead to undesirable both size changing and releasing components due to swelling. Since implants and prosthesis are not surrounded by the water, it would be useful to investigate behavior of thermoplastic polymers in bioliquids, for example blood plasma.

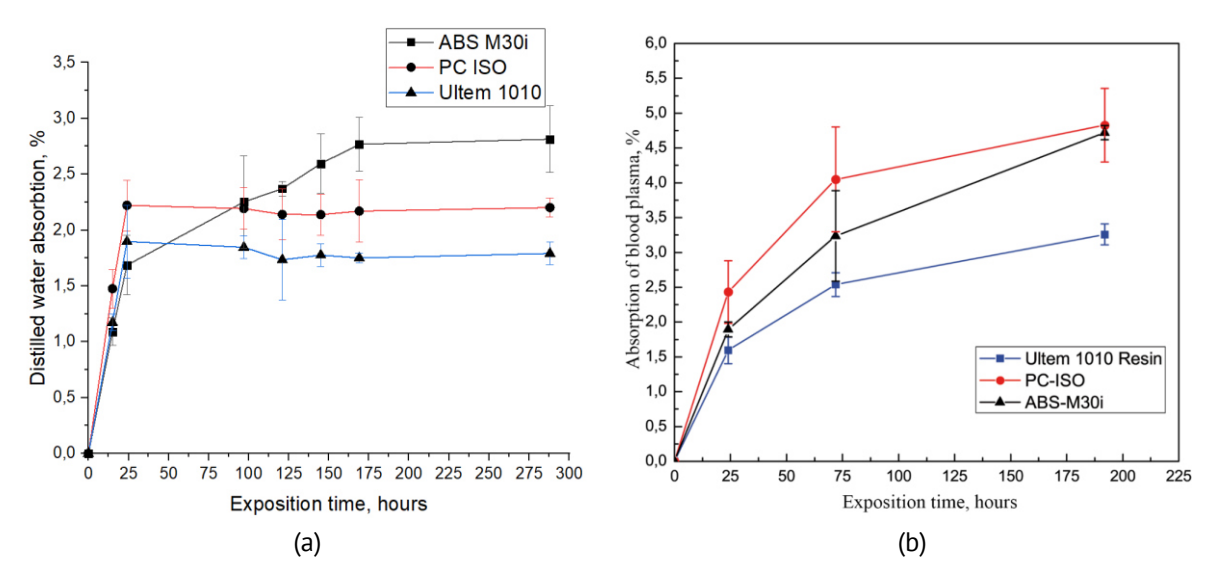


Fig. 6. The dependence of the distilled water (a) and blood plasma (b) absorption versus exposition time

It was expected that the hydrophobic property of thermoplastic polymers in relation to the distilled water and blood plasma will lead to decreasing of their adsorption. However, all investigated thermoplastic samples tend to adsorb water (Fig. 6(a)), and the value of water uptake depends precisely on chemical structure and doesn't depend on wetting parameters. Thus, ABS-M30i demonstrates the highest distilled water adsorption, which equals 2.8 % after 190 hours of exposition. At the same time, Ultem 1010 Resin has the lowest distilled water absorption, which equals only 1.7 % after 190 hours of exposition. In addition, despite the relatively high value of the θ_P of ABS-M30i (Table 2), the value of blood plasma absorption after 190 hours is more than 4.5 wt. % (Fig. 6(b)). PC-ISO has the less value of the θ_P compared to ABS-M30i. However, the value of the absorbed blood plasma of PC-ISO is close to ABS-M30i. Ultem 1010 Resin has the least value of the blood plasma absorption (lower than 3 wt. %). Thus, the distilled water and blood plasma adsorption tightly correlate with the glass transition. Increasing glass temperature leads to decreasing liquid absorption. It is also well known that glass temperature tightly correlates with the number of chemical or physical bonds. Therefore, using a polymer matrix with relatively high cross-linking density (high glass temperature) leads to reduction of bioliquids adsorption.

Thormonlastic	Distilled water adsorption	Blood plasma adsorption
Thermoplastic	after 190 hours, %	after 190 hours, %
ABS-M30i	3.12	4.83
PC-ISO	2.17	4.72

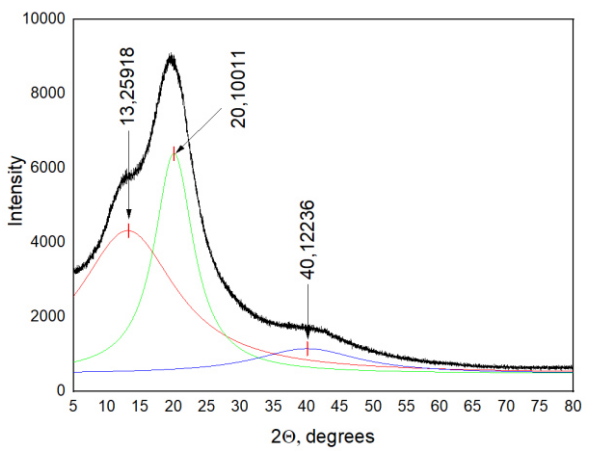
Table 2. The values of distilled water and blood plasma adsorption of all investigated thermoplastics

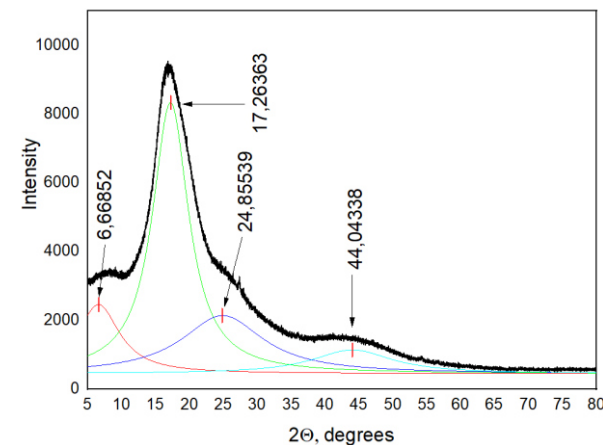
1.66

Wide-angle XRD investigations

Ultem 1010 Resin

XRD has been successfully used to study various aspects of polymer structures, which include thermoplastics, thermosetting polymers and liquid crystalline polymers [31]. The supposition of amorphous structure of all investigated thermoplastic polymers also was confirmed by the XRD results (Figs. 8-10), since narrow peaks are absent in all diffraction patterns. It should be mentioned that mineral fillers are not detected in all investigated thermoplastic samples. It is possible to detect wide peaks (17-22 °C) layered on the broad polymer halo signal using the Levenberg-Marquardt algorithm, which is widely used for curve fitting. Corresponding 2Θ values are presented in Table 3. In addition, according to Bragg's law, Table 3 shows calculated values of d-space – the distances between polymer chains, which tend to form a low ordered structure, due to intermolecular orientational interactions [32].





3.26

Fig. 8. Wide-angle XRD curve of ABS-M30i

Fig. 9. Wide-angle XRD curve of PC-ISO

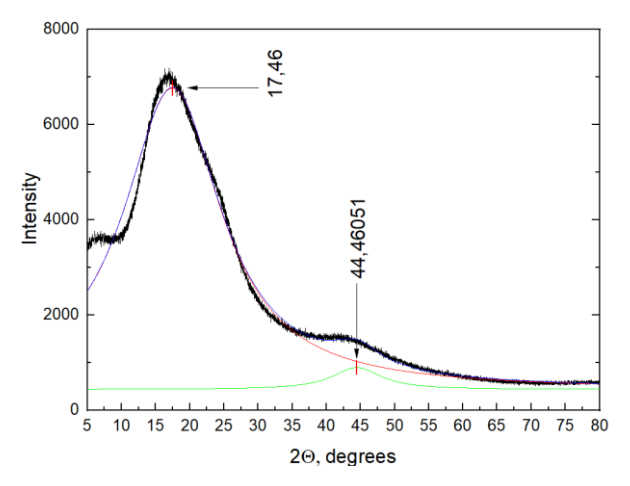


Fig. 10. Wide-angle XRD curve of Ultem 1010 Resin

Thermoplastic	20, °	d-space, Å
	13.26	4.38
ABS-M30i	20.1	2.2
	40.12	3.53
PC-ISO	6.66	13.25
	17.26	5.11
	24.86	3.55
	44.04	2
Ultem 1010 Resin	17.46	5.05
Ottem 1010 Kesin	44.46	1.98

Table 3. Interplane distance of all investigated thermoplastics

SEM investigation of the cross-section

The cross-sections of ABS-M30i (Fig. 11(a)) and PC-ISO (Fig. 11(b)) contain trays of plastic deformation, whereas the cross-section of Ultem 1010 Resin is smooth and typical for a brittle failure (Fig. 11(c)). Pores lower than 10 μ m are absent, whereas pores larger than 50 μ m are presented at all images. Such structure is the result of the sample manufacturing with 3D-printing by fused deposition modeling and can facilitate the osseointegration [28].

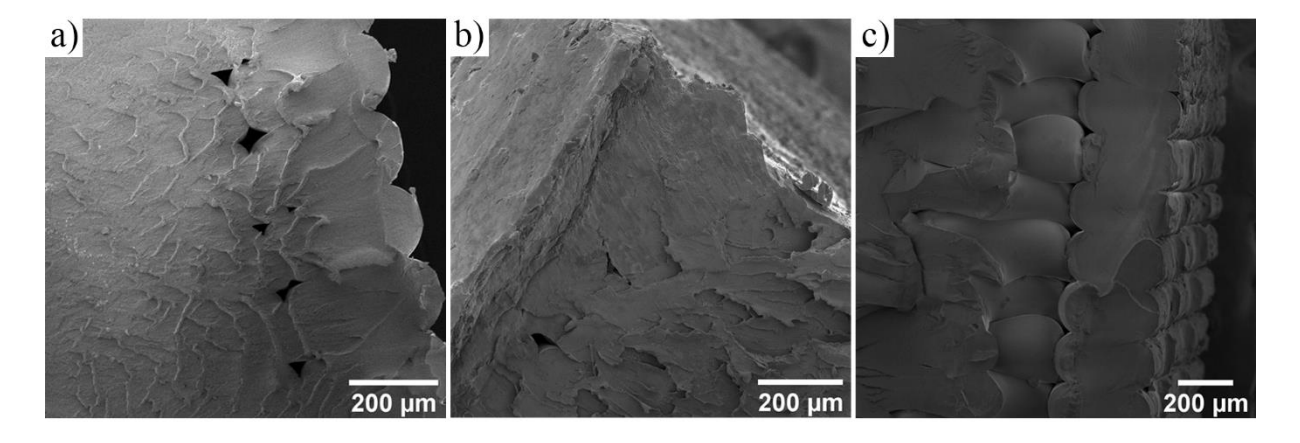


Fig. 11. The cross-section of thermoplastic samples after several cycles of loading: (a) ABS-M30i; (b) PC-ISO; (c) Ultem 1010 Resin

Conclusion

This paper focuses on experimental determination of physical, chemical and surface properties of several biocompatible thermoplastics: ABS-M30i (polyacrylonitrile-co-butadiene-co-styrene), PC-ISO (polycarbonate) and Ultem 1010 Resin (polyetherimide). Investigated samples were manufactured with the industrial grade 3D-printer by fused deposition modeling. In particular, the following physical, chemical and surface properties were obtained: IR-spectra, static and dynamic contact angles, DTA/TG curves, DSC curves, dependence of the distilled water and blood plasma absorption versus exposition time, wide-angle XRD curves, cross-section of samples after several cycles of loading.

For further research it is important to outline suggestions to chemical composition of thermosetting polymer matrix for satisfying orthopedic surgery requirements. Physical

and mechanical properties of thermosetting polymers may be varied by controlling the proportion of "hard" and "soft" blocks, which can be presented by block-copolymers. For example, aromatic ethers, alicyclic ethers and polyimides can be used as «hard» segments of thermosetting polymer matrix. While the demanding "soft" behavior of the whole thermosetting polymer matrix can be achieved by integration of long-chain polyurethanes or oligoether epoxy resins or derivatives of polyethylene terephthalate or derivatives of polycarbonate. It is quite desirable to include polar groups in thermosetting polymer, which will facilitate wettability of surfaces and increase adhesion. A special attention should be paid to the inclusion of mineral fillers in such polymers, since it may affect physical, chemical and surface properties.

References

- 1. Mamalis AG, Ramsden JJ, Grabchenko AI, Lytvynov LA, Filipenko VA, Lavrynenko SN. A novel concept for the manufacture of individual sapphire-metallic hip joint endoprostheses. *Journal of Biological Physics and Chemistry*. 2002;6(3): 113–118.
- 2. Grace EP, Webster TJ. A review of nanotechnology for the development of better orthopedic implants. *Journal of Biomedical Nanotechnology*. 2005;1(1): 18–29.
- 3. Mishra S, Chowdhary R. Peek materials as an alternative to titanium in dental implants: A systematic review. *Clinical Implant Dentistry and Related Research*. 2019;21(1): 208–222.
- 4. Venkata PM, Lecka-Czernik B, Ebraheim NA, Jayasuriya AC. An overview of recent advances in designing orthopedic and craniofacial implants. *Journal of Biomedical Materials Research Part A*. 2013;101(11): 3349–3364.
- 5. Borovkov AI, Maslov LB, Zhmaylo MA, Zelinskiy IA, Voinov IB, Keresten IA, Mamchits DV, Tikhilov RM, Kovalenko AN, Bilyk SS, Denisov AO. Finite element stress analysis of a total hip replacement in two-legged standing. *Russian Journal of Biomechanics*. 2018;22(4): 382–400. (In Russian)
- 6. Keresten IA, Borovkov AI, Zhmaylo MA, Kovalenko AN, Bilyk SS. Finite element modeling and stress analysis of hip components in two-legged standing. In: *Science week SPbPU: proceedings of the international scientific conference. Institute of applied mathematics and mechanics*. St. Petersburg: Polytechnic University Publishing; 2016. p.74–76. (In Russian)
- 7. Keresten IA, Sudneva AI. Finite element analysis of the effective properties of the lattice structure of the implant. In: *Science week SPbPU: proceedings of the international scientific conference. Institute of applied mathematics and mechanics.* St. Petersburg: POLITEKh-PRESS Publishing; 2018. p.329–332. (In Russian).
- 8. Eschbach LY. Nonresorbable polymers in bone surgery. *Injury*. 2000;31: D22–D27.
- 9. Shastri VP. Non-degradable biocompatible polymers in medicine: past, present and future. *Current Pharmaceutical Biotechnology*. 2003;4(5): 331–337.
- 10. Kumar N, Bharti A, Kumar A, Kushwaha RK, Patel KK. Nanomaterials coating for bio-implant applications: a re-analysis. *Materials Physics and Mechanics*. 2023;51(6): 92–106.
- 11. Asghari F, Samiei M, Adibkia K, Akbarzadeh A, Davaran S. Biodegradable and biocompatible polymers for tissue engineering application: a review. *Artificial Cells, Nanomedicine, and Biotechnology.* 2017;45(2): 185–192.
- 12. Oladapo BI, Zahedi SA, Ismail SO, Omigbodun FT, Bowoto OK, Olawumi MA, Muhammad MA. 3D printing of PEEK-cHAp scaffold for medical bone implant. *Bio-Design and Manufacturing*. 2021;4(1): 44–59.
- 13. Teo AJT, Mishra A, Park I, Kim Y-J, Park W-T, Yoon Y-J. Polymeric biomaterials for medical implants and devices. *ACS Biomaterials Science & Engineering*. 2016;2(4): 454–472.
- 14. Raquez JM, Deléglise M, Lacrampe MF, Krawczak P. Thermosetting bio(materials) derived from renewable resources: A critical review. *Progress in Polymer Science*. 2010;35(4): 487–509.
- 15. Zaokari Y, Persaud A, Ibrahim A. Biomaterials for adhesion in orthopedic applications: A review. *Engineered Regeneration*. 2020;1: 51–63.
- 16. Bashandeh K, Amiri A, Rafieerad A, Rahman S, Yan W, Dhingra S, Polycarpou AA. MXene-aromatic thermosetting copolyester nanocomposite as an extremely wear-resistant biocompatible implant material for osteoarthritis applications. *Applied Surface Science*. 2022;600: 154124.
- 17. Song HB, Baranek A, Worrell BT, Cook WD, Bowman CN. Photopolymerized triazole-based glassy polymer networks with superior tensile toughness. *Advanced Functional Materials*. 2018;28(22): 1801095.

- 18. Kobykhno IA, Kuznetcov DA, Didenko AL, Smirnova VE, Vaganov GV, Ivanov AG, Popova EN, Litvinova LS, Svetlichnyi VM, Vasilyeva ES, Tolochko OV, Yudin VE, Kudryavtsev VV. Multiblock copoly(urethane-amide-imide)s with the properties of thermoplastic elastomers. *Materials Physics and Mechanics*. 2018;40(2): 221–230.
- 19. Mohd Idrus MAM, Hamdan S, Rahman MdR, Islam MdS. Liquefied tropical wood/ polypropylene composites: preparation and physico-mechanical properties. *Materials Physics and Mechanics*. 2011;11(2): 126–136.
- 20. Hassan MF, Noruddin N. The effect of lithium perchlorate on poly (sodium 4-styrenesulfonate): studies based on morphology, structural and electrical conductivity. *Materials Physics and Mechanics*. 2018;36(1): 8–17.
- 21. Pearson A. *Are FDM materials biocompatible?* Available from: https://www.stratasys.com/en/resources/blog/fdm-materials-biocompatability/ [Accessed 11th July 2024].
- 22. Slonov AL, Zhansitov AA, Rzhevskaya EV, Khakulova DM, Khashirova SYu. On the plasticization on highly-filled polyphenylene sulfone. *Materials Physics and Mechanics*. 2019;42(5): 535–543.
- 23. Desrousseaux C, Cueff R, Aumeran C, Garrait G, Mailhot-Jensen B, Traoré O, Sautou V. Fabrication of acrylonitrile-butadiene- styrene nanostructures with anodic alumina oxide templates, characterization and biofilm development test for staphylococcus epidermidis. *PloS one*. 2015;10(8): e0135632.
- 24. Yang CP, Su YY, Chen YC. Colorless poly (ether-imide) s deriving from 2, 2-bis [4-(3, 4-dicarboxyphenoxy) phenyl] propane dianhydride (bpada) and aromatic bis (ether amine) s bearing pendent trifluoromethyl groups. *European Polymer Journal*. 2006;42(4): 721–732.
- 25. Liu Y, Xing Y, Zhang Y, Guan S, Zhang H, Wang Y, Wang Y, Jiang Z. Novel soluble fluorinated poly (ether imide) s with different pendant groups: synthesis, thermal, dielectric, and optical properties. *Journal of Polymer Science Part A: Polymer Chemistry.* 2010;48(15): 3281–3289.
- 26. Kiefer J, Fries J, Leipertz A. Experimental vibrational study of imidazolium-based ionic liquids: Raman and infrared spectra of 1-ethyl-3- methylimidazolium bis (trifluoromethylsulfonyl) imide and 1-ethyl-3-methylimidazolium ethylsulfate. *Applied Spectroscopy*. 2007;61(12): 1306–1311.
- 27. Zhukovskii VA, Filipenko TS, Sukovatykh BS, Valuiskaya NM. Polymeric endoprostheses for reconstructive–restorative surgery. *Fibre Chemistry*. 2018;50(3): 219–225.
- 28. Menzies KL, Jones L. The impact of contact angle on the biocompatibility of biomaterials. *Optometry and Vision Science*. 2010;87(6): 387–399.
- 29. Górecka Z, Teichmann J, Nitschke M, Chlanda A, Choińska E, Werner C, Święszkowski W. Biodegradable fiducial markers for x-ray imaging soft tissue integration and biocompatibility. *Journal of Materials Chemistry B.* 2016;4(34): 5700–5712.
- 30. Doll K, Fadeeva E, Schaeske J, Ehmke T, Winkel A, Heisterkamp A, Chichkov BN, Stiesch M, Stumpp NS. Development of laser-structured liquid-infused titanium with strong biofilm-repellent properties. *ACS Applied Materials & Interfaces*. 2017;9(11): 9359–9368.
- 31. Murthy NS, Minor H. General procedure for evaluating amorphous scattering and crystallinity from X-ray diffraction scans of semicrystalline polymers. *Polymer*. 1990;31(6): 996–1002.
- 32. Guo WF, Chung TS. Study and characterization of the hysteresis behavior of polyimide membranes in the thermal cycle process of pervaporation separation. *Journal of Membrane Science*. 2005;235(1–2): 13–22.

About Authors

Daniil A. Erofeev 10 Sc

PhD Student (St. Petersburg Institute of Technology (Technical University), St. Petersburg, Russia)

Pavel B. Pirozhnikov D Sc

Candidate of Chemical Sciences

Senior Lecturer (St. Petersburg Institute of Technology (Technical University), St. Petersburg, Russia)

Ilya A. Keresten 🗓 Sc

Candidate of Technical Sciences

Associate Professor (Peter the Great St. Petersburg Polytechnic University, St. Petersburg, Russia)

Alexey G. Titov D Sc

Candidate of Medical Sciences

Head of the Department (Institute of Medical Education of Almazov National Medical Research Centre, St. Petersburg, Russia)

Submitted: July 15, 2023 Revised: November 28, 2023 Accepted: May 23, 2024

Influence of adhesive interaction on the sound speed in layered composites

R.-R.V. Razakova ^{1 ™}, ¹ R.A. Turusov ^{1,2}, ¹

- ¹ Moscow State University of Civil Engineering, Moscow, Russia
- ² N.N. Semenov Federal Research Center for Chemical Physics, Russian Academy of Sciences, Moscow, Russia
- [™] chernova riorita@mail.ru

ABSTRACT

There are the adhesive interaction parameters influence between soft polymer and steel layers to the velocity of the longitudinal sound wave in this paper. Authors have presented numerical and experimental tests of the sound speed in two composite and one polymer samples. There are the mixture formula and a mathematical model whose were used to determine the elastic parameters in numerical calculations with contact layer. The model, which included the contact layer, allows calculating the layered composites elastic modulus with certain geometric and mechanical parameters of adhesive interaction. Authors have compared the results of numerical calculations and physical experiment. It was found that the adhesive interaction parameters in the calculation of layered structures is necessary to consider because the adhesive connecting polymer layers with the steel layers have experience comprehensive stretching which affects to the elastic and acoustic parameters of the samples.

KEYWORDS

layered materials • contact layer • Young's modulus • Poisson ratio • adhesion contact • tunable materials material properties • polymer

Citation: R.-R.V. Razakova, R.A. Turusov. Influence of adhesive interaction on the sound speed in layered composites. *Materials Physics and Mechanics*. 2024;52(3): 13–21.

http://dx.doi.org/10.18149/MPM.5232024_2

Introduction

One of the most important tasks of the national economy branches is improving structures quality and reliability. This task is especially important in the military, construction, energy and other industries, where structural destruction can lead to human casualties, as well as global financial losses. Therefore, it is necessary to develop methods for analyzing building materials. In aviation and other leading industries in the 1950s, designers began to use multilayer structures, which are rigidly interconnected metal and polymer layers. Since then, the development of materials science has progressed greatly and now scientists and engineers focused their efforts on creating tunable materials that can be layered, cellular ant etc. Most scientific researches in composite materials field are focused on possible technical applications, but at the same time, there are a shortage of scientific researches dedicated to the analysis of the material parameters influence, topologies, deformations and stiffness effects on the elastic wave's propagation in various artificial composite materials. A large number of numerical and physical experiments which significance to science were carried out by Mary C. Boyce. Some of them were presented in [1,2]. It was paid attention to the development of tunable materials, analyze the influence of geometry, pattern and topology of structures in 14 R.-R.V. Razakova, R.A. Turusov

heterogeneous materials on the physical and mechanical characteristics in these scientific publications. Engineering applications require high sound-insulating properties, safe, lightweight, as well as strong and durable from layered materials. The layered composites interlayer strength was studied in [3,4]. However, the authors do not describe the influence of the adhesive interaction parameters, which is one of the fundamental values for ensuring the required strength. In [5], the authors presented studies for optimizing laminated materials with a viscoelastic damping layer by the finite element method. It was done by changing the position of the damping layer. The authors did not indicate how adhesion modeling was performed in the ABAQUS system, although this is very important for optimizing the strength of such structural materials, as evidenced by the works of [6-8]. In these articles, the authors used the finite element method to model the layered structure. This method has been worked out with a fairly high accuracy, but solution of the layered structure stress-strain state problem leads to singular stresses at the corner points of the gluing surface [9]. There are some ways to bypass singularities [10,11], but these methods are often not verified by physical experiments. The contact layer method theory avoids such problems as infinite shear stresses that occur at the boundaries between layers and at the corner points of gluing. It has been verified by numerous experiments, which are presented in [12].

The contact layer method has been tested in numerical experiments, which aimed at determining the sound speed in layered material in the present investigation. The influence analysis on the sound speed of some physico-mechanical and geometric characteristics of the composite materials components was done with the framework of the theory method possibilities. This work was supposed to compare the results of a physical experiment with the numerical experiments data.

Materials and Methods

In [13], it was proposed a mathematical model (2) for calculating the effective Young's modulus of the layered sample, which include the contact layer and its parameters. We proposed the method for calculating the sound wave speed in a layered composite in this paper, which included the main mechanical parameters and sample cross-sectional dimensions. It is important to note that in the contact layer method, the interaction between the layers of the adhesive and the substrate was carried out with the contact layer (Fig. 1), which is a system of oriented normally to the contact surface short thin elastic rods-bonds. In this layer, there is not any direct contact of the rods with each other and, therefore, there are not any normal stresses σ_x and σ_z . Short rods perceive shear stresses σ_{yx} , σ_{zy} , σ_{xz} and normal stress σ_{y} . The most important physical feature in the layered structure model (steel + polymer) is that more than 95 % of the polymer adhesive layer is fully stretched (or compressed). Therefore, it follows that instead of the usual polymer elastic modulus, there is the modulus of all-round volumetric tension works. The proportion of fully stretched adhesive depends on the concentration zone with of the edge effect: if it is the smaller, the proportion of fully stretched adhesive is greater. The bulk modulus K is related to Young's modulus E and Poisson's ratio μ by the relation:

$$K = \frac{E}{3(1-2\mu)}. (1)$$

This specialty included in Eq. (2), which makes mathematical model more accurate than the mixture formula use. This rule is especially critical for layered structures where the polymer is relatively soft. This theory has been successfully tested in research for calculating the adhesive interaction of materials by Vladimir. I. Andreev, Robert A. Turusov and other [14,15].

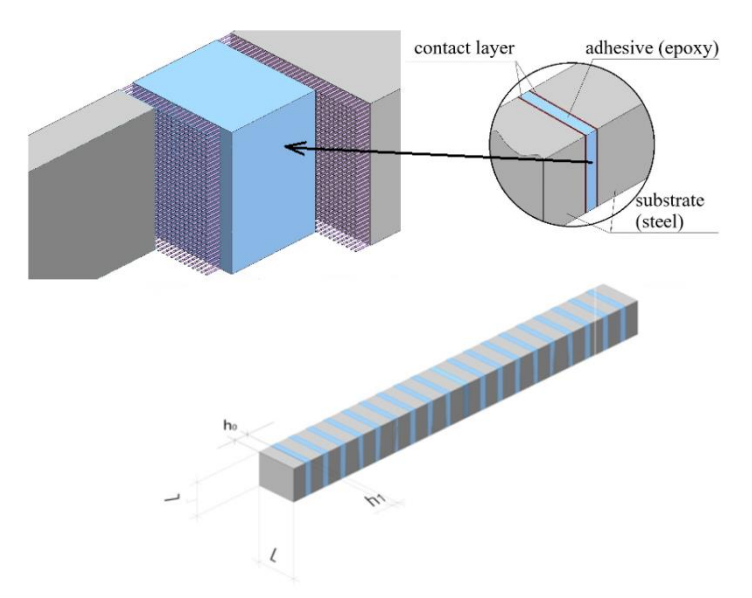


Fig. 1. Schematic diagram which is showing the model of the contact layer

The equation for calculating the effective Young's modulus $E_{eff.l.b.}$ according to contact layer theory can be represented in the following form (2):

$$E_{eff.l.b.} = \left[\left(\frac{V_0}{E_0} + \frac{V_1}{E_1} \right) - \frac{2 \cdot \left(\frac{\mu_0}{E_0} - \frac{\mu_1}{E_1} \right)^2}{\frac{(1 - \mu_1)}{E_1 \cdot V_1} + \frac{(1 - \mu_0)}{E_0 \cdot V_0}} \cdot \left(1 - \frac{tanh(v)}{v} \right) \right]^{-1}, \tag{2}$$

where E_0 and E_1 are Young's modules of the substrate and adhesive, respectively; μ_0 , μ_1 are Poisson's ratios of the substrate and adhesive, respectively; V_0 , V_1 are the relative volume fractions content of the substrate and adhesive, respectively.

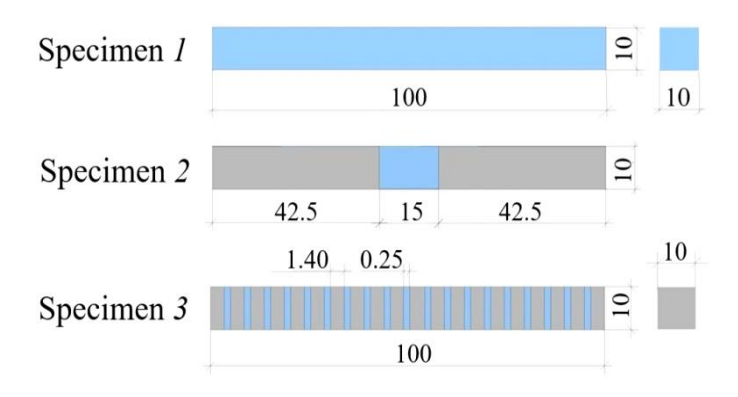


Fig. 2. The investigated composite specimens: 1- epoxy, 2- three-section, 3- layered

The parameter v in Eq. (2) characterizes the contact layer and determined as follows: $v = \frac{\omega \cdot L}{2}$; $\omega = \sqrt{G_h \left[\frac{1 - \mu_0}{E_0 h_0} + \frac{2(1 - \mu_1)}{E_1 h_1} \right]}$; L is the length of the section side; G_h is a stiffness of

16 R.-R.V. Razakova, R.A. Turusov

the contact layer; E_0 , E_1 are Young's modules of the substrate and adhesive; μ_0 , μ_1 are Poisson's ratios of the substrate and adhesive; h_0 , h_1 are thickness of the substrate and adhesive; The experimental study has been done on three rods, which are presented in Fig. 2. Initial data in the experimental study: E_0 = 210,000 MPa; μ_0 = 0.3; L = 10 mm; μ_1 = 0.5; G_h , E_1 are changes during polymer hardening. The geometric dimensions of the rods are shown in the Fig. 2. In composite rods, the relative proportions of polymer and steel were 15 and 85 %, respectively.

Layered rod elastic modulus calculating according to Eq. (2) and a composite rod according to Reuss model which based on rule of mixtures. This rule has been presented in Eq. (3):

$$E_{mix} = \frac{E_0 \cdot E_1}{V_0 \cdot E_1 + V_1 \cdot E_0}. (3)$$

The data from theoretical calculations obtained using Eqs. (2) and (3) were compared with the data from physical experiments. The experimental data which was used in this work has been published by the Semenov Institute of Chemical Physics Russian Academy of Sciences employees in [16]. The experiment included the acoustic resonance method, which is quite famous method to the non-destructive testing [17–20]. It is important to be noted that in acoustic methods it has been used elastic waves (longitudinal, shear, surface, normal, bending) of a wide frequency ultrasonic range, which have emitted in a continuous or pulsed mode. Elastic waves propagate different speeds in the sample material. Elastic waves are attenuated according to the parameters of the material. When a sound wave propagates in a transversally isotropic material at the boundaries of interfacial surfaces (in the area of adhesive interaction between layers), processes such as refraction, reflection, and scattering can occur. It affects the amplitude, phase, and other parameters.

There is a lot of scientific evidence that the section geometric dimensions, which are much less than rod length, are very important for ultrasonic control of the rod parameters. However, all this evidence is for rods with a homogeneous structure. Equation (2) could be used for makes it possible to include the length of the rod section L, the contact layer and the Poisson's ratio. Therefore, it becomes possible to see the effect of the section size on the speed of transmitted sound and check the effect of the elastic modulus and Poisson's ratio of a viscoelastic polymer (epoxy). The relationship between Young's modulus and the speed of sound is expressed by the following Eq. (4):

$$c = \sqrt{\frac{E}{\rho}},\tag{4}$$

where E is Young's modulus; ρ is a density (it is constant in this work).

Results

It has been shown the sound speed in composite samples, which were shown in Fig. 2, versus the sound speed in the polymer in Fig. 3. Also, it can be found that with an increase of Young's modulus of polymers, the layered and three-section rods samples sound speed increases too. As a result of the experiment, a significant discrepancy between Young's modulus of the layered and three-section (composite) rod was obtained. It has been shown in Fig. 3. The sound speed in a sample with thin polymer layers begins to increase sharply, exceeding the speed in a three-section rod many times over. As can be found

from the graph and numerical information (Table 1), the difference between the characteristics of the layered and three-section sample is significant. The result indicates that the interlayer effect is greater in a layered rod than in a three-section. It is worth recalling that in two composites, rods have the same volume fractions of polymer and steel (15 % polymer, 85 % steel). The obtained result could be explained by a physical and mechanical feature behavior of thin polymer layers, which enclosed between steel layers. Based on the relation for the bulk modulus (1), which is part of Eq. (2), it follows that the bulk modulus K can be much larger than Young's modulus. Also, it could be found that the closer Poisson's ratio is to the limit value of 0.5, the greater K and more the resistance of the layered structures stretching or compressing. The equation for determining the effective Young's modulus of a layered rod (2) includes the indicated physical dependence. The considered layered rod was created because a layer of polymer is glued to a solid steel layer. The transverse dimensions of the layers are the same and shown in Fig. 2. As a result, a tensile force can be applied to the rod across the layers along the rod, i.e. across the layers. In this case, the tensile stresses in all layers are the same. Since the tensile stresses are the same, the material with the lower young's modulus (i.e. polymer adhesive) is deformed first. When any rod is stretched, its transverse dimensions are reduced. These phenomena are reflected by Poisson's ratio. For isotropic material, its value is usually greater than zero, but less than 0.5. If it is equal to 0.5, then it is a comprehensively in extensible or comprehensively incompressible material. Also, it means that its volume does not change during deformation. But with other Poisson's ratios, the material changes its volume when there is a deformation. The interconnection between volumetric relative strain $\Delta V/V$ and confining pressure (tension) reflects the volumetric tension (compression) modulus $K = \Delta P/(\Delta V/V)$. It is related to Young's modulus by Poisson's ratio in elasticity (1). There is the following statement: when Poisson's ratio μ is close to 0.5, the value of bulk modulus tends to infinity. Obviously, as a result of applying a tensile force to the rod, the softer material responds to tension. In that situation, it is a polymer adhesive, but when there is a stretched process, it must reduce its transverse dimensions. However, because of the adhesion process to a rigid and practically non-deformable substrate (i.e. steel), the polymer cannot reduce its transverse size. As the result, the polymer adhesive became fully stretched. It happens during compression, too. Those, instead of Young's modulus, the modulus of all-round tension (compression) K operates, which can significantly exceed Young's modulus. Especially with Poisson's ratio close to 0.5. Solving the problem of the stress-strain state of a thin layer of adhesive using the contact layer method [12,13] makes it possible to determine the size and magnitude of stress concentration near the edge. The rest of the inside part of the adhesive is completely stretched. The result of these phenomena presented in Fig. 3 for a sound speed.

Equation (2) reflects not only volume fractions effect, Young's modulus, and Poisson's ratios of the polymer and steel, but also the stiffness of the contact layer G_h . The parameter G_h is the shear modulus ratio of the contact layer to its thickness. The data presented in Table 1 shows that if contact layer stiffness increase, the effective Young's modulus and the sound speed increases too. The contact layer stiffness changes its parameters at the beginning of gluing quite rapidly, but over time this process slows down. The stiffness of the contact layer G_h was calculated by

18 R.-R.V. Razakova, R.A. Turusov

using the function which was obtained from the approximation of experimental data: $G_h = -145.6 \cdot E_1^2 + 6438 \cdot E_1 - 33250$.

Table 1. Experimental and theoretical data of testing the sound in rods speed	Table 1. Experi	imental and theor	retical data of t	testing the sound	in rods speed
--	-----------------	-------------------	-------------------	-------------------	---------------

			The speed	l of sound, m/s	
	Experin	Theoretical meth	ods data		
E₁, MPa	Contact layer stiffness <i>G</i> _h , MPa/mm	Layered composite	Three-segment composite	Model taking into account the contact layer	Reuss model
6	136.4	129.962	87.655	98.518	76.396
7	4681.6	223.996	92.591	235.773	82.516
8	8935.6	278.537	101.082	286.401	88.212
9	12898.4	325.586	108.914	323.182	93.562
10	16570.0	368.029	112.625	353.127	98.621
11	19950.4	385.623	119.704	378.701	103.434
12	23039.6	401.020	123.090	401.091	108.031
13	25837.6	409.839	126.386	420.974	112.441
14	27968.4	418.472	129.598	438.773	116.684

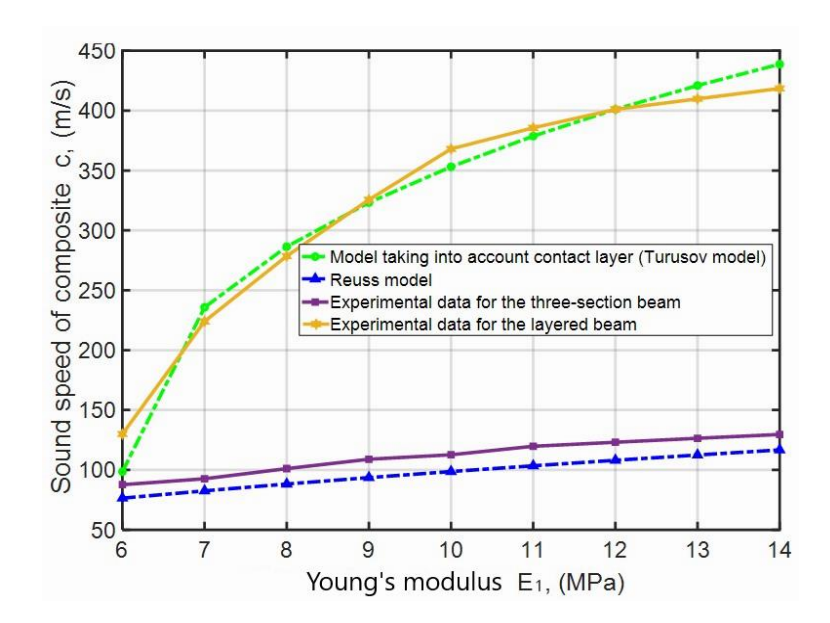


Fig. 3. Experimental and analytical study comparison of the three-section and layered rods sound speed and epoxy adhesive Young's modulus

There are the graphs and initial data for each case of the investigated composite rods by acoustic resonance method in this part of article. The processing of the measurement results and the necessary numerical experiments were performed by using a computer program which was written in the Matlab R2020b.

In the Fig. 4 it has been shown that the sound speed increased significantly when the size of the section was changed. This process occurs in connection with an increase of the composite Young's modulus. It was calculated by Eq. (2). The length is also taken into account the coefficient v in Eq. (2). It characterizes the contact layer of the considered object.

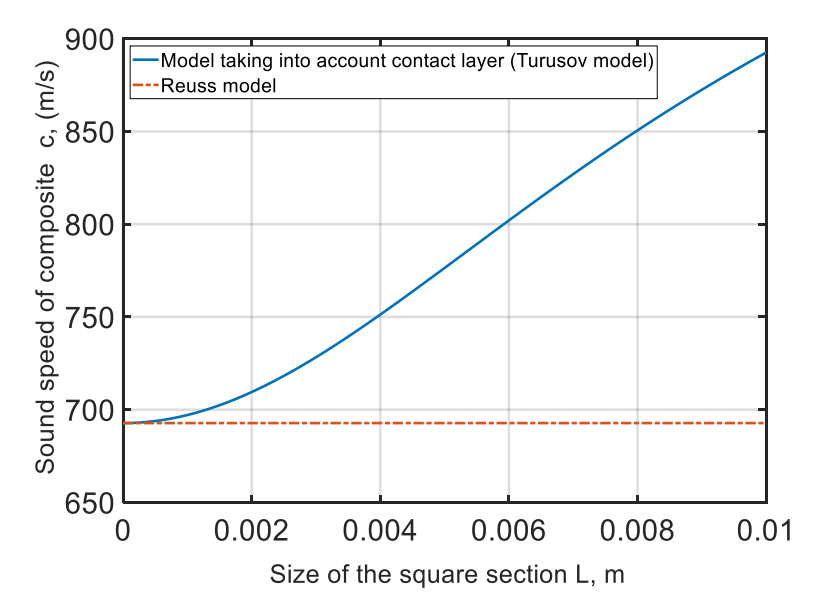


Fig. 4. Dependence of the sound speed and the size of the square section L. Initial data of the calculation case: L varies from 10^{-9} m to 0.01 m; $E_0 = 210,000$ MPa; $E_1 = 500$ MPa; $\mu_0 = 0.3$; $\mu_1 = 0.44$; $\rho_0 = 7800$ kg/m³; $G_h = 25000$ MPa/m; $\rho_1 = 1200$ kg/m³

The sound speed upraises with an increase of Young's modulus of the polymer, since the interatomic interaction becomes much stronger. Soft viscoelastic polymer layers of epoxy resin have relatively high damping properties, and in the process of hardening one can observe their decrease. It has accompanied by an increase in Young's modulus and the speed of sound. The speed of sound in crystalline solids has characterized by anisotropy, i.e. the dependence on the propagation direction. In anisotropic bodies, there are different distances between atoms in different directions, different values of the interaction force, and, consequently, different properties. All these characteristics affect the speed of propagating sound. Polymeric materials have a viscoelastic nature, which affects too.

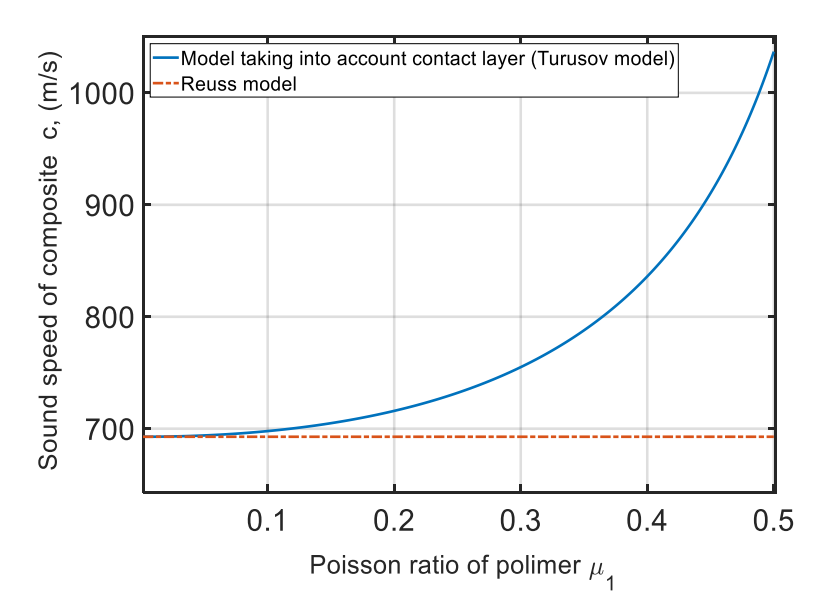


Fig. 5. Dependence of the sound speed passing through the composite and Poisson's ratio of polymer. Initial data: L = 0.01 m; $E_0 = 210,000$ MPa; $E_1 = 500$ MPa; $E_1 = 500$ MPa; $E_2 = 0.3$; $E_3 = 0.3$; $E_4 = 0.3$; $E_5 = 0.3$; $E_6 = 0.3$; $E_7 = 0.3$;

20 R.-R.V. Razakova, R.A. Turusov

It has been shown in Fig. 5 that with an increase in Poisson's ratio of the polymer to the limiting value of 0.5, the sound speed increases since the layered structure, acquires a greater ability to resist compression. Poisson's ratio which included in Eq. (2) must be used for accuracy of the calculations. The size of the square section L and Poisson's ratio do not affect the value of Young's modulus, which was calculated by Reuss model, and therefore the speed of sound remains unchanged. It was shown in Figs. 3 and 4.

Conclusion

We can conclude that the sound speed in a rod with a layered structure depends on many parameters, which must be included. It is important to note that the analytical formula for determining the effective Young's modulus with the contact layer model has a fairly good agreement with the results of a physical experiment and can be considered accurate. The formula of the effective Young's modulus, which included the contact layer for determining the sound speed, gives possible to carry out the numerical experiments by changing the size of the rectangular section and the mechanical properties values of the two materials constituent layered composite. It has been believed that as smaller the rectangular section size of the rod in relation to the length as the results of non-destructive testing are better, but it was found from the presented results, this rule does not match in the case of a layered composite rod. With a significant change in the modulus of elasticity depending on the section size, a significant synergistic effect can be found but with small cross-sectional dimensions, it can be lost.

References

- 1. Galich PI, Fang NX, Boyce MC, Rudykh S. Elastic wave propagation in finitely deformed layered materials. *Journal of the Mechanics and Physics of Solids*. 2017;98: 390-410.
- 2. Li Y, Kaynia N, Rudykh S, Boyce M. Wrinkling of Interfacial Layers in Stratified Composites. *Advanced Engineering Materials*. 2013;15(10): 921-926.
- 3. Coogan TJ, Kazmer DO, Prediction of interlayer strength in material extrusion additive manufacturing. *Additive Manufacturing*. 2020;35: 101368.
- 4. Nsengiyumva W, Zhong S, Lin J, Zhang Q, Zhong J, Huang Y. Advances, limitations and prospects of nondestructive testing and evaluation of thick composites and sandwich structures: A state-of-the-art review. *Composite Structures*. 2021;256: 112951.
- 5. Zhang G, Zheng H, Zhu X. Optimization of composite plates with viscoelastic damping layer for high sound transmission loss under stiffness and strength constraints. *Composite Structures*. 2023;306: 116563.
- 6. Gong M, Zhang H, Wu J. CZM analysis and evaluation of influencing factors on interlayer adhesion of asphalt mixture with double-layer continuous pave. *Construction and Building Materials*. 2021;302: 124211.
- 7. Mukherjee B, Batra RC, Dillard DA. Effect of confinement and interfacial adhesion on peeling of a flexible plate from an elastomeric layer. *International Journal of Solids and Structures*. 2017;110-111: 385-403.
- 8. Mohanty S, Das RR. Laminated FRP composite patch design for arresting joint fractures (Adhesion/cohesion) in resin-infilled centrally inclined V-notched Al-6061-T6 plate. *Theoretical and Applied Fracture Mechanics*. 2022;121: 103491.
- 9. Dionísio JMM, Ramalho LDC, Sánchez-Arce IJ, Campilho RDSG, Belinha J. Fracture mechanics approach to stress singularities in composite adhesive joints. *Composite Structures*. 2021;276: 114507.
- 10. Fu Z, Xi Q, Gu Y, Li J, Qu W, Sun L, Wei X, Wang F, Lin J, Weiwei Li, Xu W, Zhang C. Singular boundary method: A review and computer implementation aspects. *Engineering Analysis with Boundary Elements*. 2023;147: 231-266.
- 11. Bhowmick S, Liu GR. On singular ES-FEM for fracture analysis of solids with singular stress fields of arbitrary order. *Engineering Analysis with Boundary Elements*. 2018;86: 64-81.

- 12. Turusov RA. *Adhesive Mechanics*. Moscow: Moscow State University of Civil Engineering Publication; 2016. (In Russian)
- 13. Andreev V, Tsybin N, Turusov R. Layered composite and contact layer. Effective modulus of elasticity. *E3S Web of Conferences*. 2019;97: 04071.
- 14. Turusov RA, Kuperman AM. Mechanical behavior of an adhesive in the state of thin interlayers between rigid substrates. *Doklady Physical Chemistry*. 2011;437: 38-40.
- 15. Tsybin N. Merged contact layer in adhesion mechanics. E3S Web of Conferences. 2021; 281.
- 16. Turusov RA, Berlin AA. Adhesion and Adhesive Mechanics. *News of Materials Science. Science and Technology.* 2016;2: 17-23. (In Russian)
- 17. Ivanova Y, Partalin T, Georgiev I. Comparison of NDT techniques for elastic modulus determination of laminated composites. *Studies in Computational Intelligence*. 2018;728: 79-89.
- 18. Ivanova Y, Partalin T, Mihovski M. Experimental study of the ultrasonic wave propagation in materials with mechanical stresses. *Journal of Theoretical and Applied Mechanics*. 2010;40(2): 71-76.
- 19. Zhang Z, Guo S, Li Q, Cui F, Malcolm AA, Zhongqing Su, Liu M. Ultrasonic detection and characterization of delamination and rich resin in thick composites with waviness. *Composites Science and Technology*. 2020;189: 108016.
- 20. Chaki S, Krawczak P. Non-Destructive Health Monitoring of Structural Polymer Composites: Trends and Perspectives in the Digital Era. *Materials*. 2022;15: 7838.

About Authors

Rio-Rita V. Razakova D Sc

PhD Student (Moscow State University of Civil Engineering, Moscow, Russia)

Robert A. Turusov D Sc

Doctor of Physical and Mathematical Sciences

Chief Researcher (N.N. Semenov Federal Research Center for Chemical Physics, Russian Academy of Sciences, Moscow, Russia)

Submitted: April 5, 2024 Revised: April 27, 2024 Accepted: May 20, 2024

Topology optimization algorithm for heterogeneous anisotropic materials and structures

A.D. Novokshenov [™], ¹ D.V. Vershinin, I.I. Abdulin

Peter the Great St. Petersburg Polytechnic University, St. Petersburg, Russia

[™] novoksh ad@spbstu.ru

ABSTRACT

In this paper, a two-phase topology optimization method is proposed, determines not only the ratio of the phases of high and low stiffness at each point of the body, but also the angle of rotation of the axes of anisotropy. The proposed method makes it possible to significantly improve the functionality of the products being developed. The topology optimization of the two-phase material is implemented using the method of moving asymptotes, and the angle of rotation of the anisotropy axes is aligned along the main axes of the stress tensor. As an example, a rectangular elastic plate is considered, with joint constraints in the two lower corners and the force in the middle of the upper face. The problem of simultaneous optimization of phases and axes of anisotropy is solved for this plate. The obtained results are analyzed, after which the correctness of the developed algorithm is concluded.

KEYWORDS

topology optimization • method of moving asymptotes • solid isotropic material with penalization orthotropic materials • multi-material

Acknowledgements. This work has been supported by the Russian Science Foundation grant No. 22-71-00108. https://rscf.ru/project/22-71-00108/

Citation: Novokshenov AD, Vershinin DV, Abdulin II. Topology optimization algorithm for heterogeneous anisotropic materials and structures. *Materials Physics and Mechanics*. 2024;52(3): 22–32. http://dx.doi.org/10.18149/MPM.5232024_3

Introduction

With the fast grow of additive manufacturing technologies possibilities, it becomes possible to create complex shaped products based on topology optimization: bridges [1,2], porous structures [3], minimum-weight, symmetrically loaded wheel structures [4], and materials with required effective mechanical properties [5,6]. Until recently, most additive manufacturing technologies were limited to using a single-phase material, which limited the functionality of the products being developed. 3D printing for multiphase material is only an emerging technology, but it will certainly lead to more functional products. For example, the article [7] demonstrates the manufacture of a product obtained using two-phase topology optimization using PolyJet additive manufacturing technology, which allows printing bulk materials with a wide range of elastic modulus [8].

In the classical formulation, topology optimization is the task of finding the optimal distribution of material in a given area under certain loads and boundary conditions. The review of the articles allows us to identify 3 classes of existing topology optimization algorithms – algorithms based on optimality criteria, algorithms based on sensitivity analysis (mathematical programming methods), and so-called genetic algorithms of topology optimization [9]. The most stable method used by the authors in optimizing

structures made of anisotropic materials is the method of moving asymptotes (MMA) [10], therefore in this work it was chosen as the base optimization algorithm.

As a result of the analysis of existing sources for optimizing the phase ratio, it was observed that the most of the of works on topology optimization based on density, taking into account several material phases, are based on expanding the interpolation scheme of a solid isotropic material (SIMP), which uses a power law to determine intermediate densities, taking into account various regions of a solid and voids [11,12]. To optimize the topology of two materials (without voids) [13], a single design variable is used to interpolate between two phases of the material [14]. The approach has also been used, for example, to multiphysics actuators design, [15] and functionally graded structures with optimal eigenfrequencies design [16]. A three-phase expansion of SIMP has also been proposed [14], characterized by a topology design variable that controls the material/void distribution and a second design variable that interpolates between two solid material phases. This "three-phase mixing" scheme is expandable to an arbitrary number of materials [17,18], however, it is noted that with a further increase in the number of design variables, the optimization problem, as a rule, gets stuck in a local extremum. In fact, most of the results in the papers on optimizing topology from multiple materials using this "m-phase mixing" scheme were limited to two solid phases and a void [7,19]. The multi-material topology optimization by considering the volumes of multiple materials have also been applied to other problems, including simultaneous structural and thermal analyses [20], lattice structures [21], thermal buckling criteria [22], and cable-suspended membrane structures [23].

Development of composite 3D printers [24] make actual to use topology optimization with conjunction of material anisotropy axes optimization. As a result of the analysis of existing articles on the optimization of anisotropy axes directions, several approaches have been identified to solve this problem. In particular, there are approaches that do not introduce additional design variables for the orientation of the material. Instead, it is assumed that the main direction of the material coincides with the main direction of stress tensor or deformation tensor, which is reasonable for "shear-weak" materials [25,26]. Also, there are approaches that introduce additional design variables to optimize the orientation of the material [27,28]. However, due to the difficulty of avoiding local optima [29,30], the optimization of the orientation of the material based on the stress tensor and strain tensor is used in this work.

Methods

The classic state of topology optimization problem is to determine the optimal material distribution in terms of stiffness under given boundary conditions and resource constraints. Maximizing the stiffness of a body is equivalent to minimizing the elastic energy of deformation (i.e. compliance), which has the following form (1):

$$c = \frac{1}{2} \int_{\Omega} ({}^{4}\mathbf{C} \cdot \mathbf{\varepsilon}) \cdot \mathbf{\varepsilon} d\Omega, \tag{1}$$

where ${}^4{\bf C}$ is an elasticity tensor; ${m \epsilon}$ is a strain tensor; ${m \Omega}$ is a material volume (design domain).

Parameterization of the optimization space is performed through finite element discretization and the application of the approach SIMP (solid isotropic material with

penalization). The properties of the material in each element depend on the magnitude of the fictitious density ρ^e , the values of which vary from 0 to 1. It is assumed that (2):

$${}^{4}\boldsymbol{\mathcal{C}}^{e} = \rho^{e\,p\,4}\boldsymbol{\mathcal{C}}_{0}^{e},\tag{2}$$

where ${}^4{m C}_0^e$ is an initial elasticity tensor in a given finite element, p is a penalization factor.

The maximum allowed volume fracture is expressed by the following inequality (3): (r)d0 < V

$$\int_{\Omega} \rho(\mathbf{r}) d\Omega < V, \tag{3}$$

where Ω is a design domain, $\rho(r)$ is a fictitious density (design variable, which vary from 0 to 1).

Thus, the problem of finding the distribution of material in the considered area in the finite element formulation will have the form (4) subject to (5) [11]:

$$min(\mathbf{f}^T\mathbf{u}),$$
 (4)

$$\begin{cases}
\mathbf{K}\mathbf{u} = \sum_{e=1}^{N} \mathbf{K}^{e}(\rho^{e}) \mathbf{u}^{e} = \mathbf{f} \\
\mathbf{K}^{e}(\rho^{e}) = \rho^{ep} \mathbf{K}_{0}^{e} \\
\frac{V}{V_{0}} = \frac{\sum_{e=1}^{N} V^{e}}{V_{0}} = \alpha
\end{cases}$$

$$0 < \alpha < 1$$
(5)

where f^T is a force vector, u is a displacement vector, u^e is a displacement vector of the element nodes, K is a global stiffness matrix, $K^e(\rho^e)$ is a local stiffness matrix of the element, K_0^e is an initial local stiffness matrix of the element, V^e is a volume of the element, V_0 is an initial volume of the body.

To solve this problem, mathematical programming methods are further applied. In this work, the method of moving asymptotes (MMA) was used.

Topology optimization using two phases

Control of several phases in the optimization process is carried out using an extension of the SIMP method. In this work, a three-phase SIMP method (as shown in 1) was used, which is characterized by two design variables ρ_0^e and ρ_1^e (6) [15]:

$$\mathbf{K}^{e}(\rho_{0}^{e}, \rho_{1}^{e}) = \rho_{0}^{e p_{0}} \left(\rho_{1}^{e p_{1}} \mathbf{K}_{1}^{e} + (1 - \rho_{1}^{e})^{p_{1}} \mathbf{K}_{2}^{e} \right), \tag{6}$$

where ρ_0^e is a density of the total material in element, ρ_1^e is a ratio of the volume of phase 1 with respect to the volume of the total material in element, p_0 and p_1 are penalization factors, K_1^e is an initial local stiffness matrix of the element of phase 1, K_2^e is an initial local stiffness matrix of the element of phase 2.

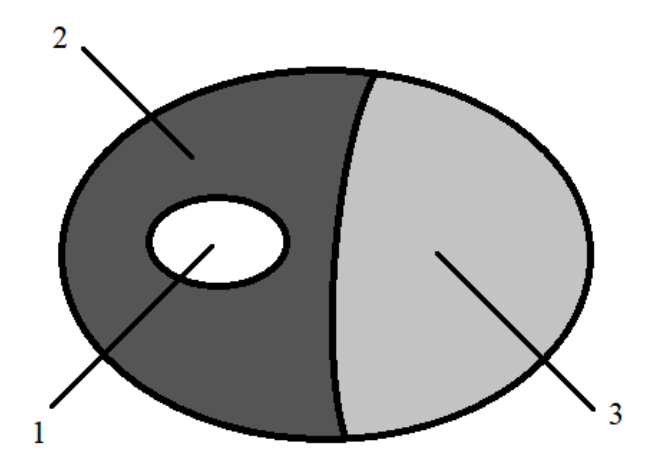


Fig. 1. 1 – void phase, 2 – phase 1, 3 – phase 2

The volume constraint for design domains of two materials can be written as (7) [31]:

$$\begin{cases}
\frac{v^e}{v_0} \sum_{e=1}^{N} (1 - \rho_0^e) = (1 - \alpha_0) \\
\frac{v^e}{v_0} \sum_{e=1}^{N} \rho_0^e \rho_1^e = \alpha_0 \alpha_1 \\
\frac{v^e}{v_0} \sum_{e=1}^{N} \rho_0^e (1 - \rho_1^e) = \alpha_0 (1 - \alpha_1)
\end{cases}$$
(7)

where α_0 is a volume fraction of the total material with respect to the volume of the design domain, α_1 is a ratio of the volume of the first phase to the volume of the total material.

The formulation of the topology optimization problem can be expressed as (8) subject to (9) [15]:

$$min(\mathbf{f}^{T}\mathbf{u}),$$

$$\mathbf{K}\mathbf{u} = \sum_{e=1}^{N} \mathbf{K}^{e}(\rho_{0}^{e}, \rho_{1}^{e}) \mathbf{u}^{e} = \mathbf{f}$$

$$\mathbf{K}^{e}(\rho_{0}^{e}, \rho_{1}^{e}) = \rho_{0}^{e p_{0}} \left(\rho_{1}^{e p_{1}} \mathbf{K}_{1}^{e} + (1 - \rho_{1}^{e})^{p_{1}} \mathbf{K}_{2}^{e} \right)$$

$$\frac{v^{e}}{v_{0}} \sum_{e=1}^{N} (1 - \rho_{0}^{e}) = (1 - \alpha_{0})$$

$$\frac{v^{e}}{v_{0}} \sum_{e=1}^{N} \rho_{0}^{e} \rho_{1}^{e} = \alpha_{0} \alpha_{1}$$

$$\frac{v^{e}}{v_{0}} \sum_{e=1}^{N} \rho_{0}^{e} (1 - \rho_{1}^{e}) = \alpha_{0} (1 - \alpha_{1})$$

$$0 < \alpha_{0}, \alpha_{1} < 1$$

$$(8)$$

$$\frac{v^{e}}{v_{0}} \sum_{e=1}^{N} \mathbf{K}^{e}(\rho_{0}^{e}, \rho_{1}^{e}) \mathbf{u}^{e} = \mathbf{f}$$

$$\frac{v^{e}}{v_{0}} \sum_{e=1}^{N} \rho_{0}^{e} (1 - \rho_{1}^{e}) = \alpha_{0} (1 - \alpha_{1})$$

$$0 < \alpha_{0}, \alpha_{1} < 1$$

Predicting the optimal orientation

An orthotropic material was considered. The stiffness of the structure was maximized by varying the orientation of the orthotropy axes in each finite element.

Optimization of the orthotropy axes was carried out in conjunction with topology optimization. The classical SIMP method with one design variable (10) was used, where the stiffness matrix can be expressed using a rotation tensor [32]:

$$\begin{cases}
\mathbf{K}^{e}(\varphi, \rho^{e}) = \rho^{e^{p}} \mathbf{K}_{0}^{e}(\varphi) \\
\mathbf{K}_{0}^{e}(\varphi) = \mathbf{B}^{T} \mathbf{T}^{T}(\varphi) \mathbf{D} \mathbf{T}(\varphi) \mathbf{B} \det(\mathbf{J})'
\end{cases}$$
(10)

where φ is a variable orientation of the orthotropy axes, $K_0^e(\varphi)$ is a local stiffness matrix of the element rotated by an angle φ , D is an elasticity matrix of an orthotropic material, B is a matrix of the derivatives of shape functions, $T(\varphi)$ is a rotation matrix, J is the Jacobi matrix.

The algorithm for optimizing the distribution of the material and the angle of rotation is constructed in such a way that the design variable is only a fictitious density ρ^e . The angle φ is aligned along the main stress or strain axes before each step of the topology optimization algorithm.

The scheme of algorithm is shown in Fig. 2. The constructed algorithm consists of the following steps:

- 1. Changing all design variables ρ^e to satisfy the volume fraction constraint.
- 2. Finite element calculation of the stress-strain state of the body.
- 3. Calculation of the sensitivities of the strain energy by design variables (11):

$$\frac{\partial c}{\partial \rho^e}$$
, (11)

where $c = \mathbf{u}^T \mathbf{K} \mathbf{u}$.

4. Finding the main direction of the stress/strain tensor.

- 5. Construction of a convex approximation of the function, finding the minimum through the dual function (internal MMA cycle) [10].
- 6. The found solution is the next step of the approximation point. Updating the vector of design variables.
- 7. Updating direction of anisotropy axes according to main stress/strain tensor directions.
- 8. Checking for convergence. If there is no convergence, return to step 2.

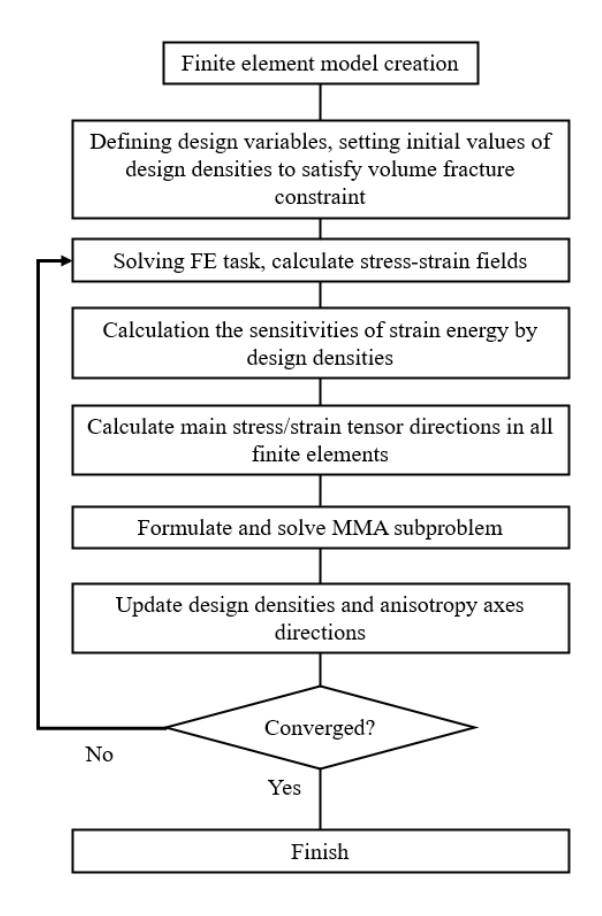


Fig. 2. Developed algorithm scheme

The formulation of the topology optimization problem can be expressed as (12) subject to (13):

$$\min(\mathbf{f}^{T}\mathbf{u}),$$

$$\{\mathbf{K}\mathbf{u} = \sum_{e=1}^{N} \mathbf{K}^{e}(\varphi, \rho^{e}) \mathbf{u}^{e} = \mathbf{f}$$

$$\mathbf{K}^{e}(\varphi, \rho^{e}) = \rho^{ep} \mathbf{K}_{0}^{e}(\varphi)$$

$$\frac{v}{v_{0}} = \frac{\sum_{e=1}^{N} v^{e}}{v_{0}} = \alpha$$

$$0 < \alpha < 1$$
(12)

Development of a topology optimization algorithm using two phases, taking into account the direction of the anisotropy axes

The optimization of heterogeneous orthotropic material was carried out using a combination of two approaches (14):

$$\begin{cases}
\mathbf{K}^{e}(\varphi, \rho_{0}^{e}, \rho_{1}^{e}) = \rho_{0}^{e^{p_{0}}} \left(\rho_{1}^{e^{p_{1}}} \mathbf{K}_{1}^{e}(\varphi) + (1 - \rho_{1}^{e})^{p_{1}} \mathbf{K}_{2}^{e}(\varphi) \right), \\
\mathbf{K}_{i}^{e}(\varphi) = \mathbf{B}^{T} \mathbf{T}^{T}(\varphi) \mathbf{D}_{i} \mathbf{T}(\varphi) \mathbf{B} det(\mathbf{J})
\end{cases} (14)$$

where $K_i^e(\varphi)$ is a local stiffness matrix of the element of the i-th phase, D_i is an elasticity matrix of the orthotropic i-th phase.

The algorithm for optimizing the distribution of phases and the angle of rotation is the same as in the previous subsection but uses only two design variables – ρ_0^e and ρ_1^e .

The formulation of the topology optimization problem can be expressed as (15) subject to (16):

$$\min(\mathbf{f}^{T}\mathbf{u}),$$

$$\mathbf{K}\mathbf{u} = \sum_{e=1}^{N} \mathbf{K}^{e}(\varphi, \rho_{0}^{e}, \rho_{1}^{e}) \mathbf{u}^{e} = \mathbf{f}$$

$$\mathbf{K}^{e}(\varphi, \rho_{0}^{e}, \rho_{1}^{e}) = \rho_{0}^{e p_{0}} \left(\rho_{1}^{e p_{1}} \mathbf{K}_{1}^{e}(\varphi) + (1 - \rho_{1}^{e})^{p_{1}} \mathbf{K}_{2}^{e}(\varphi) \right)$$

$$\frac{v^{e}}{v_{0}} \sum_{e=1}^{N} (1 - \rho_{0}^{e}) = (1 - \alpha_{0})$$

$$\frac{v^{e}}{v_{0}} \sum_{e=1}^{N} \rho_{0}^{e} \rho_{1}^{e} = \alpha_{0} \alpha_{1}$$

$$\frac{v^{e}}{v_{0}} \sum_{e=1}^{N} \rho_{0}^{e} (1 - \rho_{1}^{e}) = \alpha_{0} (1 - \alpha_{1})$$

$$0 < \alpha_{0}, \alpha_{1} < 1$$

$$(15)$$

Implementation of the developed topological optimization algorithms

To implement the optimization algorithm, the Python language was chosen as the most convenient and fastest from the point of view of development, as well as containing the NumPy and SciPy libraries with a large number of functions for working with matrices, including highly sparse large-dimensional matrices that arise when using the finite element method.

A proprietary 2D finite element solver has been developed, which includes not only well-known standard procedures, but also supplemented with the parameters necessary to solve the optimization problem. The finite element solver was tested on simple 2D problems of elasticity theory, the results coincided with ANSYS with high accuracy.

The MMA method did not need to be fully implemented, since an implementation of this algorithm in Python was found in open sources. However, it was necessary to adapt this program code to solve the problem of topological optimization, both in terms of algorithm settings and in terms of the connection of the algorithm with a finite element solver. In particular, a feature has been added that allows you to change the design variables in the finite element model after each completed internal MMA cycle.

To display the optimization results, a separate module was developed using the Python - matplotlib library.

Results and Discussion

Optimization of the material distribution, phases and orthotropy direction angle was tested on a two-dimensional plate with boundary conditions and loads shown in Fig. 3. Design domain with boundary conditions and load: L = 40 mm, finite element discretization 160×40 , F = 100 N.

The following parameters were used for each of the optimization tasks:

- number of iterations: 100;
- penalization powers: $p = p_0 = p_1 = 4$;
- volume constraints: $\frac{V}{V_0} = 0.5$, $\frac{V_1}{V_0} = \frac{V_2}{V_0} = 0.25$.

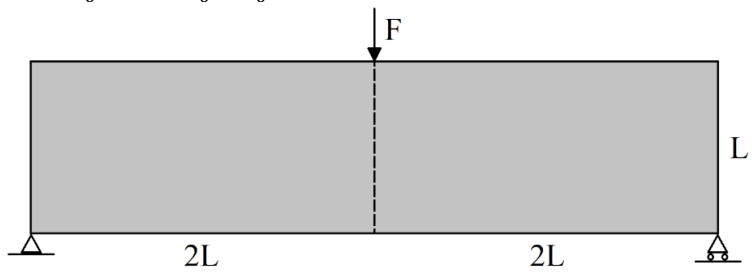


Fig. 3. Design domain with boundary conditions and loads: L = 40 mm, finite element discretization 160×40 , F = 1000 N

The test materials taken from literature [15,29] are presented in Tables 13. The optimization results are shown in Figs.7.

It can be seen that the phase with high stiffness is distributed along the edges as a result of optimization, which corresponds to the results given in the literature. However, the optimization results in this paper and the optimization results from the sources are slightly different, due to different optimization parameters and phase properties.

Optimization through alignment of the orthotropy axes along the main directions of the stress tensor is a more effective method compared to alignment along the main directions of the strain tensor. Firstly, the value of the objective function (strain energy) as a result of optimization for the first case turns out to be less. Secondly, alignment along the main directions of the stress tensor gives a more understandable result – the direction of the anisotropy axes in most cases agrees with the topology of the structure, that is, inside the "rod-like" structures remaining as a result of optimization, the direction of the orthotropy axes coincides with the direction of the outer boundary of these structures. In the case of alignment along the main directions of the strain tensor, the results are more unpredictable.

Finally, the simultaneous optimization of the material distribution, phases and orthotropy direction angle was tested on a plate. On Fig. 6, it can be seen that phase distribution has the same character as in the case of isotropic phases, and the anisotropy axes are consistent with the "rod-like" topology.

To demonstrate the advantages of the presented optimization, a comparative analysis of the results for the classic topology optimization algorithm and developed was performed. The results of optimization and comparison are presented in Table 4.

It can be seen from the table above that the use of two orthotropic phases and the alignment of the anisotropy axes leads to a decrease in compliance.

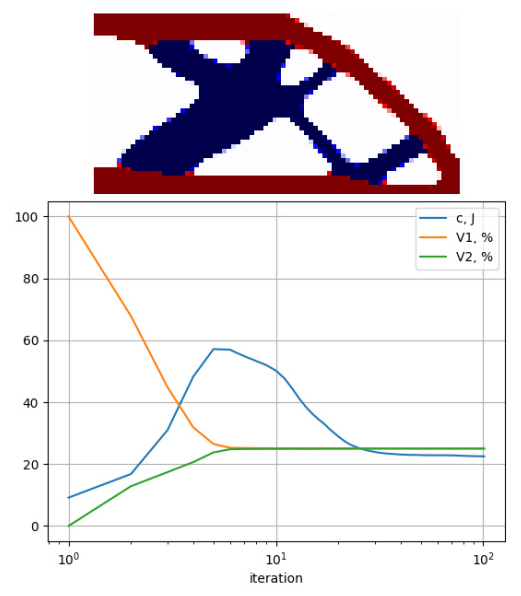


Fig. 4. Optimal distribution of isotropic phases, c = 22.49 J: red color – phase 1, blue color – phase 2

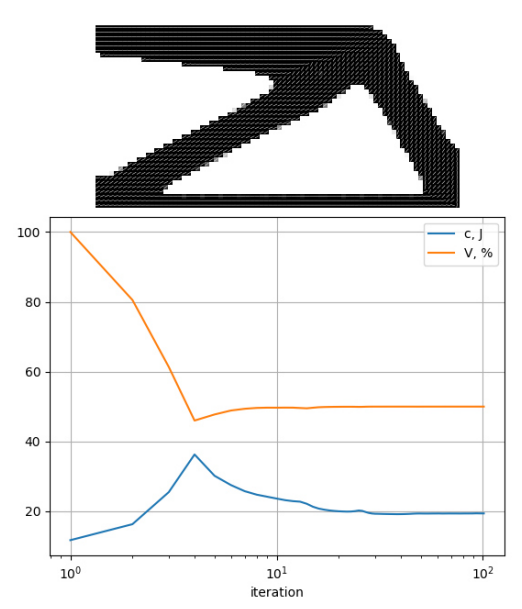


Fig. 5. Optimal distribution of orthotropic material, alignment of orthotropy axes along the main directions of the stress tensor, c = 19.413 J

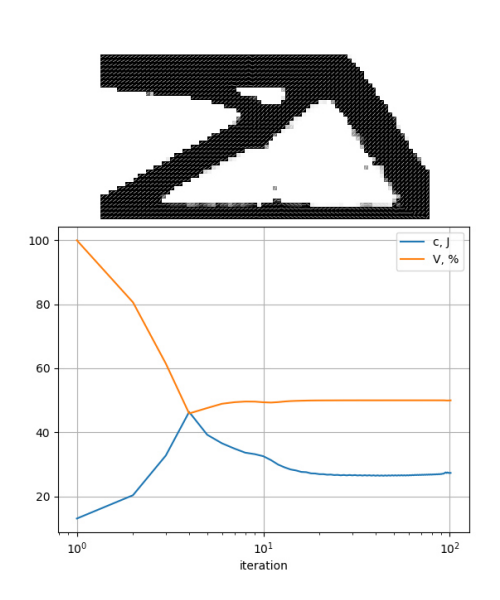


Fig. 6. Optimal distribution of orthotropic material, alignment of anisotropy axes along the main directions of the strain tensor, c = 27.317 J

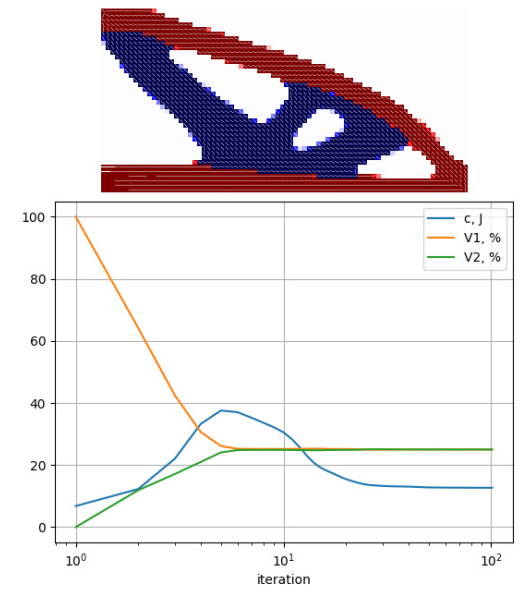


Fig. 7. Optimal distribution of orthotropic phases, alignment of anisotropy axes along the main directions of the stress tensor, $c = 12.669 \, \text{J}$: red color – phase 1, blue color – phase 2

Table 1. Properties of isotropic phases for the task of optimizing the phase distribution

E_1 , GPa	E_2 , GPa	$ u_1$	$ u_2$
200.00	100.00	0.31	0.31

Table 2. Properties of an orthotropic material for the task of optimizing the distribution of the material and the axes of orthotropy

E_x , GPa	E_y , GPa	E_z , GPa	G_{xy} , GPa	G_{yz} , GPa	G_{xz} , GPa	ν_{xy}	ν_{yz}	ν_{xz}
54.00	18.00	18.00	9.00	9.00	9.00	0.25	0.25	0.25

Table 3. Properties of orthotropic phases for the problem of optimizing the distribution of phases and axes of orthotropy

№ phase	E_x , GPa	E_y , GPa	E_z , GPa	G_{xy} , GPa	G_{yz} , GPa	G_{xz} , GPa	ν_{xy}	ν_{yz}	ν_{χ_Z}
1	108.00	18.00	18.00	9.00	9.00	9.00	0.25	0.25	0.25
2	54.00	18.00	18.00	9.00	9.00	9.00	0.25	0.25	0.25

Table 4. Comparison table of optimization results for various materials (1 – topology optimization with one orthotroic material phase, 2- topology optimization with two orthotropic material phases, 3 - topology optimization with two orthotropic material phases with orthotropy axes direction variation)

Nº material	Predicting orientation	Compliance, J	Optimal distribution
1	No	72.36	·
2	No	35.49	
2	No	28.23	
3	Yes	12.67	

Conclusions

In this paper, an algorithm for two-phase topology optimization was developed, taking into account the rotation of the axes of anisotropy (orthotropy).

The distribution of the two isotropic phases was compared with the results from open sources. Based on the results of the comparison, it can be said that the phase distributions are qualitatively the same.

The alignment of orthotropy direction angles along the main directions of the stress and strain tensor was compared. Alignment along the main directions of the stress tensor

is a more efficient method, which is why it was used in optimizing a heterogeneous material with two orthotropy phases and a void.

The developed algorithm was tested on the problem of topology optimization of the plate. An optimal distribution of the material with two orthotropic phases and a void was obtained, in which the phase distribution was similar to the isotropic case, and the orthotropy axes were consistent with a "rod-like" topology.

References

- 1. Zegard T, Paulino GH. Bridging topology optimization and additive manufacturing. *Struct. Multidiscip. Optim.* 2016;53(1): 175–192.
- 2. Zegard T, Paulino GH. GRAND Ground structure based topology optimization on arbitrary 2D domains using MATLAB. *Struct. Multidiscip. Optim* 2014;50(5): 861–882.
- 3. Robbins J, Owen SJ, Clark BW, Voth TE. An efficient and scalable approach for generating topologyly optimized cellular structures for additive manufacturing. *Addit. Manuf.* 2016;12: 296–304.
- 4. Dewhurst P, Srithongchai S. An investigaton of minimumweight dual-material symmetrically loaded wheels and torsion arms. *J. Appl. Mech.* 2005;72(2): 196–202.
- 5. Borovkov AI, Maslov LB, Zhmaylo MA, Tarasenko FD, Nezhinskaya LS. Elastic properties of additively produced metamaterials based on lattice structures. *Materials Physics Mechanics*. 2023;51(7): 42–52.
- 6. Borovkov AI, Maslov LB, Zhmaylo MA, Tarasenko FD, Nezhinskaya LS, Finite element analysis of elastic properties of metamaterials based on triply periodic minimal surfaces. *Materials Physics Mechanics*. 2024;52(2): 63–81.
- 7. Gaynor AT, Meisel NA, Williams CB, Guest JK. Multiple-material topology optimization of compliant mechanisms created via polyjet threedimensional printing. *J. Manuf. Sci. Eng.* 2014;136(6): 061015.
- 8. PolyJet Materials: A rangle of possibilities. Stratasys. 2016.
- 9. Bendsoe MP, Martin P. Topology optimization: theory, methods and applications. Berlin: Springer; 2003.
- 10. Svanberg K. The method of moving asymptotes—a new method for structural optimization. *International Journal for Numerical Methods in Engineering*. 1987;24(2): 359–373.
- 11. Bendsøe MP. Optimal shape design as a material distribution problem. Struct. Optim. 1989;1: 193-202.
- 12. Zhou M, Rozvany GIN. The COC algorithm, Part II: topology, geometrical and generalized shape optimization. *Comput. Methods Appl. Mech. Engrg.* 1991;89(1–3): 309–336.
- 13. Li M, Deng Y, Zhang H, Wong SHF, Mohamed A, Zheng Y, Gao J, Yuen TYP, Dong B, Kuang JS. Topology optimization of multi-material structures with elastoplastic strain hardening model. *Structural and Multidisciplinary Optimization*. 2021;64(3): 1141–1160.
- 14. Sigmund O, Torquato S. Design of materials with extreme thermal expansion using a three-phase topology optimization method. *J. Mech. Phys. Solids*. 1997;45(6): 1037–1067.
- 15. Sigmund O. Design of multiphysics actuators using topology optimization—Part I: Two-material structures. *Comput. Methods Appl. Mech. Engrg.* 2001;190(49–50): 6577–6604.
- 16. Taheri AH, Hassani B. Simultaneous isogeometrical shape and material design of functionally graded structures for optimal eigenfrequencies. *Comput. Methods Appl. Mech. Engrg.* 2014;277: 46–80.
- 17. Stegmann J, Lund E. Discrete material optimization of general composite shell structures. Internat. J. Numer. *Methods Engrg.* 2005;62(14): 2009–2027.
- 18. Sigmund O. Design of multiphysics actuators using topology optimization Part II: Two-material structures. *Comput. Methods Appl. Mech. Engrg.* 2001;190(49–50): 6605–6627.
- 19. Gibiansky LV, Sigmund O. Multiphase composites with extremal bulk modulus. *J. Mech. Phys. Solids*. 2000;48(3): 461–498.
- 20. Vantyghem G, Boel V, Steeman M, Corte WD. Multi-material topology optimization involving simultaneous structrual and thermal analyses. *Struct. Multidiscip. Optim.* 2019;59: 731–743.
- 21. Kazemi H, Vaziri A, Norato JA. Multi-material topology optimization of lattice structures using geometry projection. *Comput. Methods Appl. Mech. Engrg.* 2020;363: 112895.
- 22. Wu C, Fang J, Li Q. Multi-material topology optimization for thermal buckling criteria. *Comput. Methods Appl. Mech. Engrg.* 2019;346: 1136–1155.

- 23. Luo Y, Niu Y, Li M, Kang Z. A multi-material topology optimization approach for wrinkle-free design of cable-suspended membrane structures. *Comput. Mech.* 2017;59: 967–980.
- 24. Zobacheva AY, Nemov AS, Borovkov AI, Novokshenov AD, Khovaiko MV, Ermolenko NA. Design and simulation of additive manufactured structures of three-component composite material. *Materials Physics and Mechanics*. 2017;34(1): 51–58.
- 25. Zhou KM, Li X. Topology optimization of structures under multiple load cases using a fiber-reinforced composite material model. *Comput. Mech.* 2006;38(2): 163–170.
- 26. Gea H, Luo J. On the stress-based and strain-based methods for predicting optimal orientation of orthotropic materials. *Struct Multidiscip Optim*. 2004;26(3–4): 229–234.
- 27. Pedersen P. Examples of density, orientation, and shape-optimal 2D-design for stiffness and/or strength with orthotropic materials. *Structural and Multidisciplinary Optimization*. 2004;26(1–2): 37-49.
- 28. Zhou K, Li X. Topology optimization for minimum compliance under multiple loads based on continuous distribution of members. *Structural and Multidisciplinary Optimization*. 2008;37(1): 49–56.
- 29. Stegmann J, Lund E. Discrete material optimization of general composite shell structures. *International Journal for Numerical Methods in Engineering*. 2005;62(14): 2009–2027.
- 30. Ansola R, Canales J, Tarrago J, Rasmussen J. On simultaneous shape and material layout optimization of shell structures. *Structural and Multidisciplinary Optimization*. 2002;24(3): 175–184.
- 31. Thurier PF, Lesieutre GA, Frecker MI, Adair JH. A two-material topology optimization method for structures under steady thermo-mechanical loading. *Journal of Intelligent Material Systems and Structures*. 2019;30(11): 1717-1726.
- 32. Shen Y, Branscomb D. Orientation optimization in anisotropic materials using gradient descent method. *Composite Structures*. 2019;234: 111680.

About Author

Aleksei D. Novokshenov D Sc

Candidate of Technical Sciences
Associate Professor (Peter the Great St. Petersburg Polytechnic University, St. Petersburg, Russia)

Denis V. Vershinin

Engineer (Peter the Great St. Petersburg Polytechnic University, St. Petersburg, Russia)

Ilia I. Abdulin

Engineer (Peter the Great St. Petersburg Polytechnic University, St. Petersburg, Russia)

Submitted: June 13, 2023 Revised: October 31, 2023 Accepted: March 25, 2024

Variants of physical equations in a curvilinear coordinate system and their comparison based on mixed FEM

R.Z. Kiseleva ¹², N.A. Kirsanova ², A.P. Nikolaev ¹, Yu.V. Klochkov ¹,

V.N. Yushkin ¹, ¹

ABSTRACT

In arbitrary curvilinear coordinate system under elastoplastic deformation, a comparative analysis of three variants of the defining equations at the loading step was performed. In the first variant, the equations of the theory of plastic flow were used, according to which the strain increment had been divided into elastic and plastic parts. The cumbersomeness of the algorithm for obtaining expressions for the components of the plastic strain increments tensor in an arbitrary curvilinear coordinate system is shown, which leads to the lack of the possibility of obtaining the matrix dependence of physical equations at the loading step. In the second variant, to obtain plastic strain increments, the hypothesis of their proportional dependence on the components of the stress increments deviator was used. The defining equations were also obtained by summation of the elastic strains increment and plastic strains increment. In the third variant, the hypothesis of the division of strain increments into elastic and plastic parts was not used. The physical equations were written using the assumption that there was a proportional dependence between the components of the strain increment deviators and stress increment deviators. Using the example of calculating the shell of revolution, the preference of the third variant of the defining equations for elastoplastic deformation is shown.

KEYWORDS

shell of revolution • physical nonlinearity • hexahedral finite element • mixed functional • mixed FEM implementation **Acknowledgements**. This work was performed within the State assignment of Federal Scientific Research Center "Crystallography and Photonics" of Russian Academy of Sciences.

Citation: Kiseleva RZ, Kirsanova NA, Nikolaev AP, Klochkov YuV, Yushkin VN. Variants of physical equations in a curvilinear coordinate system and their comparison based on mixed FEM. *Materials Physics and Mechanics*. 2024;52(3): 33–43.

http://dx.doi.org/10.18149/MPM.5232024_4

Introduction

When calculating structures taking into account elastoplastic deformations, it is necessary to take into account the behavior of the material, including the formation of residual deformations. Determining the values of the stress-strain state during deformation beyond the elastic limit makes it possible to establish the maximum load and assign a safety factor. Therefore, calculations of structural elements taking into account zones of elastoplastic deformation are an urgent engineering problem for mechanical engineering, aircraft structures, hydraulic structures, etc. Currently, the most used theories for finding the strength parameters of deformed objects are the deformation theory of plasticity and the theory of plastic flow [1–15]. Numerical implementation of the defining equations of the theories of plasticity is widely carried out using the finite element method (FEM) in the

¹ Volgograd State Agrarian University, Volgograd, Russia

² Financial University under the Government of the Russian Federation, Moscow, Russia

[™] rumia1970@yandex.ru

displacement method formulation [16-23] and in the mixed formulation [22,24-30]. Widely used theories of plasticity (the theory of small elastoplastic deformations and the theory of plastic flow) use the hypothesis of dividing strain increments into elastic and plastic parts. In the theory of plastic flow, for the components of the plastic strain increment tensor are determined based on the assumption of their proportionality to the components of the total stress deviator with the coefficient of proportionality, which is a function of the stress intensity increment. To obtain physical equations at the loading step, it is necessary to represent the stress intensity increment through the increments of the components of the stress increment tensor, which is very difficult in a curvilinear coordinate system. The authors considered three variants of defining equations as physical ratios. In the first variant, equations of the theory of plastic flow were used. In the second variant, defining relations were used based on the assumption proposed by the authors about the proportional relation between the components of the plastic strain increments tensor and the components of the stress increments deviator. In the third variant, the defining equations were obtained without dividing the strain increments into elastic and plastic parts. The proportionality assumption was applied directly to the strain increments and stress increments deviator components. The coefficient of proportionality turned out to be a function of the tangent modulus of the strain diagram. For the numerical implementation of the equations, mentioned above, a hybrid finite element developed by the authors with nodal unknowns in the form of displacement increments and stress increments was used.

Materials and Methods

Relations of the theory of plastic flow

According to this theory, strain increments at the loading step consist of elastic strain increments $\Delta \varepsilon_{ij}^{p}$ and plastic strain increments $\Delta \varepsilon_{ij}^{p}$:

$$\Delta \varepsilon_{ij} = \Delta \varepsilon_{ij}^e + \Delta \varepsilon_{ij}^p. \tag{1}$$

Elastic strain increments are determined by Hooke's law [5–7]:

$$\Delta \varepsilon_{ij}^e = \frac{1}{2\mu} \Delta \sigma_{ij} - \frac{\lambda}{2\mu} g_{ij} \frac{1 - 2\nu}{E} P_{\Delta\sigma}; \quad (i, j = 1, 2, 3), \tag{2}$$

where λ , μ are the Lamé parameters, ν is the Poisson's ratio, $\Delta\sigma_{ij}$ are normal and tangential stresses increments, g_{ij} are the covariant components of the metric tensor at the loading step, E is the elastic modulus, $P_{\Delta\sigma} = \Delta\sigma_{mn}g^{mn} = \Delta\sigma^{mn}g_{mn}$ is the first invariant of the stress increments tensor.

The components of the plastic strain increments tensor in the theory of flow are determined [1] based on the hypothesis of a proportional relation between the components of the plastic strain increments tensor and the components of the stress deviator:

$$\Delta \varepsilon_{ij}^{p} = \frac{3}{2} \frac{\Delta \varepsilon_{i}^{p}}{\sigma_{i}} \quad \left(\sigma_{ij} - \frac{1}{3} g_{ij} P_{\sigma}\right), \tag{3}$$

where $\Delta \varepsilon_i^p$ is the increment of the plastic strain intensity, σ_i is the stress intensity; $P_{\sigma} = \sigma_{ij} g^{ij} = \sigma^{ij} g_{ij}$.

The value of the intensity of plastic strain increments included in Eq. (3) is determined by the difference:

$$\Delta \varepsilon_i^p = \Delta \varepsilon_i - \Delta \varepsilon_i^e = \frac{\Delta \sigma_i}{E_k} - \frac{\Delta \sigma_i}{E_1},\tag{4}$$

where $\Delta \varepsilon_i^p$, $\Delta \sigma_i$ are the increments of the intensities of plastic strain and stress increments, E_1 is the modulus of the initial section of the strain diagram, E_{κ} is the tangent modulus at the considered point of the strain diagram.

Relations (3) taking into account Eq. (4) are written as:

$$\Delta \varepsilon_{ij}^p = \Delta \sigma_i \frac{1}{\sigma_i} \left(\frac{1}{E_k} - \frac{1}{E_1} \right) \left(\sigma_{ij} - \frac{1}{3} g_{ij} P_{\sigma} \right). \tag{5}$$

To obtain relations between the values $\Delta \varepsilon_{ij}^p$ and $\Delta \sigma_{ij}$ the value $\Delta \sigma_i$ should be presented generally like:

$$\Delta \sigma_i = \frac{\partial \sigma_i}{\partial \sigma_{kl}} \Delta \sigma_{kl},\tag{6}$$

where the stress intensity is determined in a curvilinear coordinate system by the expression [5]:

$$\sigma_i = \sqrt{\frac{3}{2} S^{ij} S_{ij}}. (7)$$

The components of the stress deviator included in Eq. (7) are determined by the following formulas [5]:

$$S_{ij} = \sigma_{ij} - \frac{1}{3} g_{ij} \sigma_{mn} g^{mn}; \quad S^{ij} = g^{im} g^{in} S_{mn}.$$
 (8)

Expression (6) taking into account Eq. (7) will take the form:

$$\Delta\sigma_{i} = \frac{\sqrt{3}}{2\sqrt{2}} \frac{1}{\sigma_{i}} \frac{\partial}{\partial \sigma_{kl}} \left(S^{ij} S_{ij} \right) \Delta\sigma_{kl}. \tag{9}$$

The plastic strain increments (5) taking into account Eq. (9) will be written as:

$$\Delta \varepsilon_{ij}^p = \gamma_1 \frac{\partial}{\partial \sigma_{kl}} \left(S^{ij} S_{ij} \right) \Delta \sigma_{kl}, \tag{10}$$

where $\gamma_1 = \frac{\sqrt{3}}{2\sqrt{2}} \frac{1}{\sigma_i^2} \left(\frac{1}{E_{\rm K}} - \frac{1}{E_1}\right) \left(\sigma_{ij} - \frac{1}{3}g_{ij}P_{\sigma}\right)$.

By summation of Eqs. (2) and (10), the matrix is formed:

$$\{\Delta\varepsilon\} = \{C_1^{\Pi}\}\{\Delta\sigma\},\$$

$$6\times 1 \qquad 6\times 6 \qquad 6\times 1$$
(11)

where

Due to the cumbersomeness of expressing the derivative in relation (9), the work on forming the matrix relation (11) in an arbitrary curvilinear coordinate system was not carried out in this research.

The second variant of plastic flow

It is proposed to determine the plastic strain increments based on the hypothesis of their proportionality to the components of the stress increments deviator [24]:

$$\Delta \varepsilon_{ij}^{p} = \frac{3}{2} \frac{\Delta \varepsilon_{i}^{p}}{\Delta \sigma_{i}} \left(\Delta \sigma_{ij} - \frac{1}{3} g_{ij} P_{\Delta \sigma} \right). \tag{12}$$

When taking Eq. (4) into account, Eq. (12) will be written in the form:

$$\Delta \varepsilon_{ij}^{p} = \frac{3}{2} \left(\frac{1}{E_{K}} - \frac{1}{E_{1}} \right) \left(\Delta \sigma_{ij} - \frac{1}{3} g_{ij} P_{\Delta \sigma} \right). \tag{13}$$

By summation of Eqs. (2) and (13), the relation is formed:

$$\Delta \varepsilon_{ij} = \left[\frac{1}{2\mu} + \frac{3}{2} \left(\frac{1}{E_{\kappa}} - \frac{1}{E_{1}} \right) \right] \Delta \sigma_{ij} - g_{ij} P_{\Delta \sigma} \left[\frac{1}{2\mu} \frac{1 - 2\nu}{E} - \frac{1}{2} \left(\frac{1}{E_{\kappa}} - \frac{1}{E_{1}} \right) \right], \tag{14}$$

as the matrix:

$$\{\Delta \varepsilon\} = \begin{bmatrix} C_2^{\Pi} \end{bmatrix} \{\Delta \sigma\}. \tag{15}$$

It should be noted that when obtaining the components of the plastic strain increment tensor, the hypothesis of the incompressibility of the material during plastic deformation was accepted.

The third variant of physical relations at the loading step

The relations between the stress and strain increments are obtained based on the assumption of a proportional relation between the components of the deviators of the stress and strain increments without dividing the increments of strain into elastic and plastic parts:

$$\Delta \varepsilon_{ij} - \frac{1}{3} g_{ij} P_{\Delta \varepsilon} = \frac{3}{2E_{\nu}} (\Delta \sigma_{ij} - \frac{1}{3} g_{ij} P_{\Delta \sigma}), \tag{16}$$

where $P_{\Delta\varepsilon} = \Delta\varepsilon_{mn}g^{mn}$ is the first invariant of the strain increments tensor.

The relation between the values of $P_{\Delta\varepsilon}$ and $P_{\Delta\sigma}$ should be determined experimentally in the form of functional dependence $P_{\Delta\varepsilon} = \phi P_{\Delta\sigma}$. It is assumed in this research that the relation between the first invariants of the strain increments tensors and stress increments in the process of elastic and plastic deformation remains unchanged:

$$P_{\Delta\varepsilon} = P_{\Delta\sigma} \frac{1 - 2\nu}{E}.\tag{17}$$

After substituting Eq. (17) into Eq. (16), the strain increments through the stress increments can be written in the form:

$$\Delta \varepsilon_{ij} = \frac{3}{2E_{K}} \Delta \sigma_{ij} - \psi g_{ij} \cdot P_{\Delta \sigma},$$
where $\Psi = \frac{1}{2E_{K}} - \frac{1}{3} \frac{1-2\nu}{E}.$ (18)

Using Eq. (18), a matrix dependence is formed:

$$\{\Delta \varepsilon\} = \begin{bmatrix} \mathsf{C}_3^{\mathsf{I}} \end{bmatrix} \{\Delta \sigma\}. \tag{19}$$

Shell geometry

The radius vector of an arbitrary point located at a distance *t* from the middle surface is written by the expression:

$$\mathbf{R}^{0t} = \mathbf{R}^0 + t\mathbf{a}^0, \tag{20}$$

where $\mathbf{R}^0 = x\mathbf{i} + r(x)\sin\theta\mathbf{j} + r(x)\cos\theta\mathbf{k}$ is the radius vector of the corresponding point of the middle surface of the shell of revolution, \mathbf{a}^0 is the normal to middle surface, t is the distance of a point from the middle surface.

At an arbitrary point, the basis vectors are determined by differentiation Eq. (20):

$$\boldsymbol{g}_{m}^{0} = \boldsymbol{R}_{m}^{0t} = \boldsymbol{R}_{m}^{0} + t\boldsymbol{a}^{0}. \tag{21}$$

The derivatives with respect to x, θ , t of the basis vectors of the point M^{0t} are determined by the components in the same basis [23]:

$$\{\boldsymbol{g}^{0}_{,x}\} = [m]\{\boldsymbol{g}^{0}\}; \quad \{\boldsymbol{g}^{0}_{,\theta}\} = [n]\{\boldsymbol{g}^{0}\}; \quad \{\boldsymbol{g}^{0}_{,t}\} = [l]\{\boldsymbol{g}^{0}\},$$

$$\text{where } \{\boldsymbol{g}^{0}_{,\lambda}\}^{T} = \{\boldsymbol{g}^{0}_{,\lambda}, \boldsymbol{g}^{0}_{2,\lambda}, \boldsymbol{g}^{0}_{3,\lambda}\}; \quad \lambda = x, \theta, t.$$

$$(22)$$

The displacement of the shell point M^{0t} at the loading step is determined by the vector:

$$\Delta V = \Delta v^i \boldsymbol{g}_i^0. \tag{23}$$

Derivatives (23) of the vector will be written as:

$$\Delta V_{,\lambda} = f_{\lambda}^{i} \boldsymbol{g}_{i}^{0}, \tag{24}$$

where

$$f_1^1 = \Delta v_{,x}^1 + \Delta v^1 m_{11} + \Delta v^2 m_{21} + \Delta v^3 m_{31};$$

$$f_3^3 = \Delta v_{,t}^3 + \Delta v^1 l_{13} + \Delta v^2 l_{23} + \Delta v^3 l_{33}.$$
(25)

When the shell of rotation is deformed in a geometrically linear formulation, an arbitrary point M^{0t} will take the position M^t , determined by the radius vector:

$$\mathbf{R} = \mathbf{R}^{0t} + \Delta \mathbf{V}. \tag{26}$$

The basis vectors of the point M^t are determined by the differentiation Eq. (26):

$$\boldsymbol{g}_i = \boldsymbol{g}_i^0 + \Delta \boldsymbol{V}_{,i}. \tag{27}$$

The strain increments at the loading step are determined by the difference in the covariant components of the metric tensors [5]:

$$\Delta \varepsilon_{ij} = \frac{1}{2} (g_{ij} - g^0_{ij}) = \frac{1}{2} (\boldsymbol{g}_i^0 \cdot \Delta \boldsymbol{V}_{,j} + \boldsymbol{g}_j^0 \cdot \Delta \boldsymbol{V}_{,i}). \tag{28}$$

The strain increments $\Delta \varepsilon_{ij}$ taking into account Eqs. (24) and (25) could be presented through the vector components (23) in a matrix:

$$\{\Delta \varepsilon\} = [L]\{\Delta v\},\tag{29}$$

where $\{\Delta v\}^{\mathrm{T}} = \{\Delta v^1 \ \Delta v^2 \Delta v^3\}$ is the string of the displacement vector, [L] is the matrix of differential and algebraic operators.

Strain matrix of the finite element at the loading step

A hexahedral finite element with eight nodal points w = i, j, k, l, m, n, p, h, the strain matrix of which is obtained in a mixed FEM formulation when choosing as nodal unknowns in the form of displacement increments and stress increments. The coordinates of the hexahedron through the coordinates of the nodes were determined by trilinear functions of local coordinates ξ , η , ζ , varying within $-1 \leq \xi$, $\eta \zeta \leq 1$.

$$\lambda = \{ f(\xi, \eta, \zeta) \}^T \{ \lambda_y \}, \tag{30}$$

where λ is a global coordinate x, θ , t, $\{\lambda_y\}^T$ is the string of nodal coordinate values λ .

Displacement increments were also approximated using Eq. (30):

$$\{\Delta v\} = [A] \{\Delta v_{y}\},\$$

$$_{3\times 1} = [A] \{\Delta v_{y}\},\$$

$$_{3\times 24} = [A] \{\Delta v_{y}\},\$$

$$_{3\times 1} = [A] \{\Delta v_{y}\},\$$

$$_{3\times 24} = [A] \{\Delta v_{y}\},\$$

$$_{3\times 1} = [A] \{\Delta v_{y}\},\$$

$$_{3\times 1} = [A] \{\Delta v_{y}\},\$$

$$_{3\times 24} = [A] \{\Delta v_{y}\},\$$

$$_{3\times 1} = [A] \{\Delta v_{y}\},\$$

$$_{3\times 24} = [A] \{\Delta v_{y$$

where $\left\{\Delta v_y\right\}^T = \left\{\Delta v^{1i} \dots \Delta v^{1h} \Delta v^{2i} \dots \Delta v^{2h} \Delta v^{3i} \dots \Delta v^{3h}\right\}$ is the string of hexahedral nodal displacement.

Taking Eq. (31) into account, strains (29) will be written by the matrix expression:

$$\{\Delta \varepsilon\} = [L] [A] \{\Delta v_y\} = [B] \{\Delta v_y\}.$$
(32)

Stress increments in the vicinity of the internal point of the hexahedral are approximated by Eq. (30):

$$\Delta \sigma_{sr} = \{ f(\xi, \eta, \zeta) \}^T \{ \Delta \sigma_{sr}^w \},$$
where
$$\{ \Delta \sigma_{sr}^w \}^T = \{ \Delta \sigma_{sr}^i \Delta \sigma_{sr}^j \Delta \sigma_{sr}^k \Delta \sigma_{sr}^l \Delta \sigma_{sr}^m \Delta \sigma_{sr}^n \Delta \sigma_{sr}^p \Delta \sigma_{sr}^h \}.$$

$$(33)$$

Using Eq. (33), the matrix relation is formed [8]:

$$\{ \Delta \sigma_{sr} \} = [S] \{ \Delta \sigma_{y} \},$$
where $\{ \Delta \sigma_{sr} \}^{T} = \{ \Delta \sigma_{11} \Delta \sigma_{22} \Delta \sigma_{33} \Delta \sigma_{12} \Delta \sigma_{13} \Delta \sigma_{23} \};$

$$\{ \Delta \sigma_{y} \}^{T} = \{ \Delta \sigma_{11}^{i} \Delta \sigma_{11}^{j} \Delta \sigma_{11}^{k} \Delta \sigma_{11}^{l} \Delta \sigma_{11}^{m} \Delta \sigma_{11}^{n} \Delta \sigma_{11}^{n} \Delta \sigma_{11}^{n} ...$$

$$(34)$$

$$\{ \Delta \sigma_{y} \}^{T} = \{ \Delta \sigma_{11}^{i} \Delta \sigma_{11}^{j} \Delta \sigma_{11}^{k} \Delta \sigma_{11}^{l} \Delta \sigma_{11}^{m} \Delta \sigma_{11}^{n} \Delta \sigma_{11}^{n} ...$$

$$\dots \Delta \sigma_{23}^{i} \Delta \sigma_{23}^{j} \Delta \sigma_{23}^{k} \Delta \sigma_{23}^{l} \Delta \sigma_{23}^{m} \Delta \sigma_{23}^{m} \Delta \sigma_{23}^{m} \Delta \sigma_{23}^{m} \Delta \sigma_{23}^{l} \}.$$

To obtain the stress-strain state matrix at the loading step, a mixed functional was used [25]:

$$\Pi \equiv \int_{V} \{\Delta \sigma^{sr}\}^{T} [L] \{\Delta v\} dV - \frac{1}{2} \int_{V} \{\Delta \sigma^{sr}\}^{T} [C_{\kappa}^{\Pi}] \{\Delta \sigma_{sr}\} dV - \frac{1}{2} \int_{S} \{\Delta v\}^{T} \{\Delta q\} dS - \int_{S} \{\Delta v\}^{T} \{q\} dS + \int_{V} \{\sigma^{sr}\}^{T} \{\Delta \varepsilon\} dV; \quad (\kappa = 1, 2, 3). \tag{35}$$

Taking into account approximating Eqs. (31), (32) and (34), Eq. (35) will be written as:

$$\Pi \equiv \left\{ \Delta \sigma_{y} \right\}^{T} \int_{V^{48} \times 6}^{[S]} \left[\begin{matrix} G \\ 6 \times 6 \end{matrix} \right]^{T} \left[\begin{matrix} B \\ 24 \times 1 \end{matrix} \right] dV \left\{ \Delta v_{y} \right\} - \frac{1}{2} \left\{ \Delta \sigma_{y} \right\}^{T} \int_{V^{48} \times 3}^{[S]} \left[\begin{matrix} G \\ 6 \times 6 \end{matrix} \right]^{T} \left[\begin{matrix} G \\ 6 \times 48 \end{matrix} \right] dV \left\{ \Delta \sigma_{y} \right\} - \frac{1}{2} \left\{ \Delta v_{y} \right\}^{T} \int_{S}^{[A]} \left[\begin{matrix} A \\ 24 \times 3 \end{matrix} \right]^{T} \left\{ A \\ 24 \times 3 \end{matrix} \right] dS - \left\{ \Delta v_{y} \right\}^{T} \int_{S}^{[A]} \left[\begin{matrix} A \\ 24 \times 3 \end{matrix} \right]^{T} \left\{ A \\ 24 \times 3 \end{matrix} \right] dS + \left\{ \Delta v_{y} \right\}^{T} \int_{V}^{[B]} \left[\begin{matrix} B \\ 24 \times 6 \end{matrix} \right]^{T} \left\{ \sigma_{ST}^{ST} \right\} dV,$$

$$\text{where the following relation is used } \left\{ \Delta \sigma_{ST}^{ST} \right\} = \left[\begin{matrix} G \\ 6 \times 1 \end{matrix} \right] \left\{ \sigma_{ST}^{ST} \right\}.$$

By varying Eq. (36) according to the nodal unknowns, the stress-strain state matrix [K] is formed at the loading step [8]:

$$[K] \{Z_y\} = \{F_y\},\$$

$$_{72 \times 72},_{72 \times 1},_{72 \times 1}$$

$$_{72 \times 1}$$
(37)

where $\left\{Z_y\right\}^T = \left\{\left\{\Delta\sigma_y\right\}^T \left\{\Delta v_y\right\}^T\right\}$ is the vector of finite element nodal unknowns; $\left\{F_y\right\}^T = \left\{\left\{0\right\}^T : \left\{\Delta f_q\right\}^T + \left\{R\right\}^T\right\}$ is the vector of nodal loads with residual $\left\{R\right\}^T$.

Using the developed strain matrix of a hexahedral finite element, it is possible to perform calculations during elastoplastic deformation with any hardening law, except for the horizontal section of the strain diagram ($E_k = 0$).

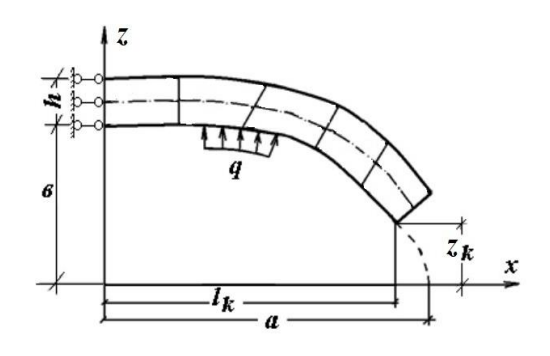
Results and Discussion

Example 1. The stress state of a shell of revolution with the middle surface of a truncated ellipsoid (Fig. 1) under the influence of internal pressure was considered. The following input data was used: a = 0.15 m; $\theta = 0.10$ m; h = 0.01 m; $l_k = 0.14$ m; $z_k = 0.0359$ m; $E = 2.10^5$ MPa; v = 0.3.

When discretizing the shell, the bases of the hexahedral elements were located in the shell surfaces located at distances $t = t_1$ and $t = t_2$ from the middle surface. The edges of the elements accepted the normals to the middle surface.

The strain diagram was accepted with a section of nonlinear hardening (Fig. 2) with the following values of its characteristics: $\sigma_{iT}=200$ MPa; $\varepsilon_{iT}=0.866667\cdot 10^{-3}$; $\varepsilon_{ik}=0.019$; $\sigma_{ik}=400$ MPa.

The function $\sigma_i = f(\varepsilon_i)$ is taken in the form of a parabola $\sigma_i = a_1 \varepsilon_i^2 + b_1 \varepsilon_i + c_1$ with numerical values of the constants: a = -6612835.5282 MPa; b = 242231.47902 MPa; c = 1795.0330258 MPa.



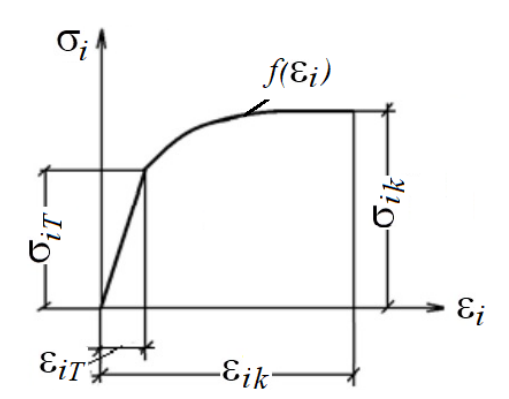


Fig. 1. Design diagram of a truncated ellipsoid

Fig. 2. Material strain diagram

To verify the convergence of the computational process based on the finite element used for different quantities, the problem was solved for elastic strain.

The function $\sigma_i = f(\varepsilon_i)$ is taken in the form of a parabola $\sigma_i = a_1 \varepsilon_i^2 + b_1 \varepsilon_i + c_1$ with numerical values of the constants: a = -6612835.5282 MPa; b = 242231.47902 MPa; c = 1795.0330258 MPa.

To verify the convergence of the computational process based on the finite element used for different quantities, the problem was solved for elastic strain.

The numerical values of normal stresses at internal pressure q = 8 MPa (elastic strain) in the initial section (S = 0.0) and the end section of the elliptical shell are given in Table 1 for various options for discretizing the structure along the meridional coordinate S (number of nodes NM) and along shell wall thickness h (number of nodes NT). Table 1 shows the normal stresses of the internal and external fibers.

Table 1. Values of normal stresses of the internal and external fibers, where σ_{11}^{in} , σ_{11}^{ex} are the meridional stresses of the internal and external fibers and σ_{22}^{in} , σ_{22}^{ex} are the circumferential stresses in internal and external fibers

or tire inte	of the meeting and external hoers and ozzyozz are the encamerential stresses in internal and external hoers									
NM	Stresses, MPa									
× NT	σ_{11}^{in}	σ_{22}^{in}	σ_{11}^{ex}	σ^{ex}_{22}	σ_{11}^{in}	σ_{22}^{in}	σ^{ex}_{11}	σ^{ex}_{22}		
20×3	32.18	65.97	34.06	60.61	2.05	62.65	1.08	46.90		
40×5	32.08	65.86	34.22	60.60	0.64	62.43	0.367	47.12		
80×7	32.05	65.83	34.28	66.60	0.18	62.36	0.113	47.15		
6UX/			S = 0.0	•		S	= 16.06 cm			

Table 1 shows the values of physical stresses obtained using Hooke's law (2). Analysis of the results given in Table 1 indicates the convergence of the computational process and emphasizes the tendency towards zero meridional stresses in the end section (S = 16.06 cm).

Example 2. The structure shown in example 1 was loaded with pressure q = 45.6 MPa for a different number of steps ($n_s = 10, 20, 40, 80$). The calculation results based on Eqs. (15) and (19) turned out to be almost identical.

Meridional and circumferential stresses in internal $(\sigma_{11}^{in}, \sigma_{22}^{in})$ and external fibers $(\sigma_{11}^{ex}, \sigma_{22}^{ex})$ of the support section, as well as stress intensity $(\sigma_i^{in}, \sigma_i^{ex})$ based on Eq. (19) are given in Table 2.

Table 2. Values of meridional and circumferential stresses in the internal and external fibers of the support

section, and stress intensity											
	Stresses, MPa										
n _s	σ_{11}^{in}	σ_{22}^{in}	σ_i^{in}	σ_i^{ex}	σ^{ex}_{22}	σ_i^{ex}					
10	158.19	340.19	319.18	249.67	418.11	355.56					
20	160.97	343.45	327.56	215.71	367.71	310.98					
40	161.22	343.77	333.43	223.05	380.12	327.36					
80	162.36	345.88	336.72	216.65	369.98	319.58					

section, and stress intensity

Analysis of the results of Table 2 indicates the convergence of the computational process with an increase in the number of loading steps.

Meridional and circumferential stresses along the thickness of the shell support section are given in Table 3 under the load q = 45.6 MPa and $n_s = 40$.

Table 3. Values of meridional and circumferential stresses along the thickness of the shell support section

σ_{11} , MPa	161.22	170.99	178.54	187.85	196.65	205.61	223.05
σ ₂₂ , MPa	343.77	349.08	352.42	356.99	362.09	365.82	380.12

Diagrams of meridional (σ_{11}^{in}) and circumferential (σ_{22}^{in}) stresses are presented in Figs. 3 and 4 respectively. Numerical values of circumferential stresses shown in Fig. 4 are in adequate agreement with the numerical values of meridional stresses.

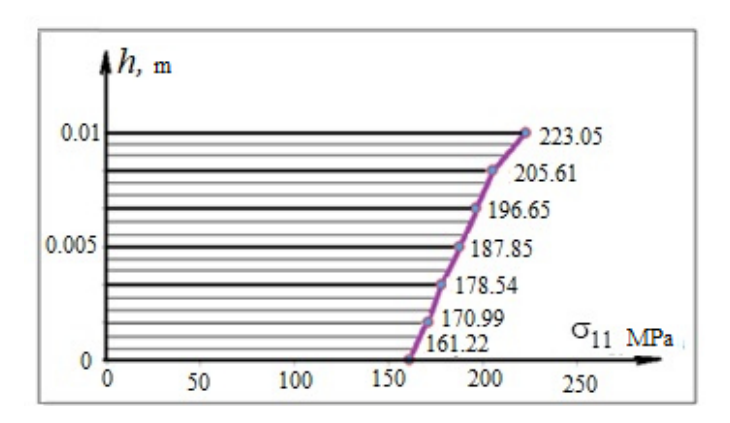


Fig. 3. Diagram of meridional stresses σ_{11} along the height of the support section

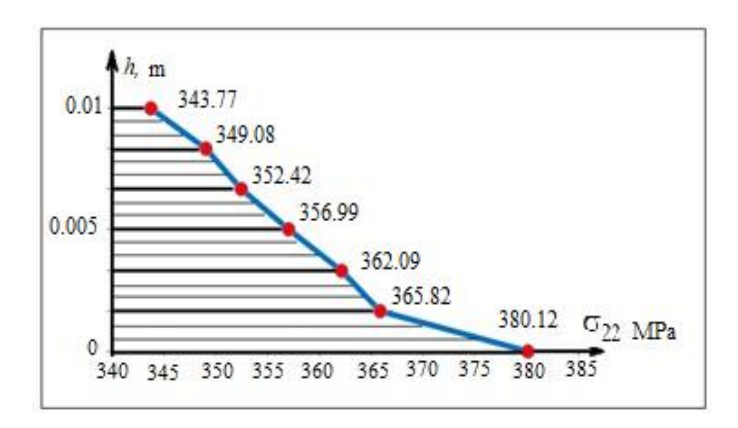


Fig. 4. Diagram of circumferential stresses σ_{22} of the support section

Table 4. Values of meridional and circumferential stresses in the internal and external fibers along the

engui of the mendian arc													
Stresses,		Length of meridian <i>S</i> , m											
MPa	0.00	1.16	3.38	5.19	7.03	10.98	12.06	13.22	13.72	14.24	14.79	15.4	16.06
σ_{11}^{in}	161.22	160.29	161.09	159.08	156.27	144.30	135.55	117.86	106.79	91.31	70.62	41.28	-0.014
σ_{22}^{in}	343.77	341.67	339.76	331.62	319.41	290.67	284.24	280.08	280.17	277.79	276.19	275.29	274.25
σ_i^{in}	333.43	331.39	329.36	322.28	312.00	286.34	280.74	276.52	277.12	275.95	277.01	282.28	294.63
σ_{11}^{ex}	223.05	219.91	207.46	192.69	172.94	110.58	88.83	67.77	58.64	51.57	42.361	29.10	1.365
σ^{ex}_{22}	380.12	377.38	362.98	363.61	346.49	293.49	287.99	274.81	275.65	270.61	275.55	275.38	274.31
σ_i^{ex}	327.36	324.53	311.09	310.69	296.18	252.12	251.61	243.90	247.64	245.02	253.12	258.15	269.64

length of the meridian arc

Table 4 shows the values of meridional and circumferential stresses, as well as stress intensities along the length of the meridian, in the internal and external fibers of the shell.

Based on the results of Table 4, graphs of meridional σ_{11} , circumferential σ_{22} and stress intensity σ_i were constructed (Fig. 5).

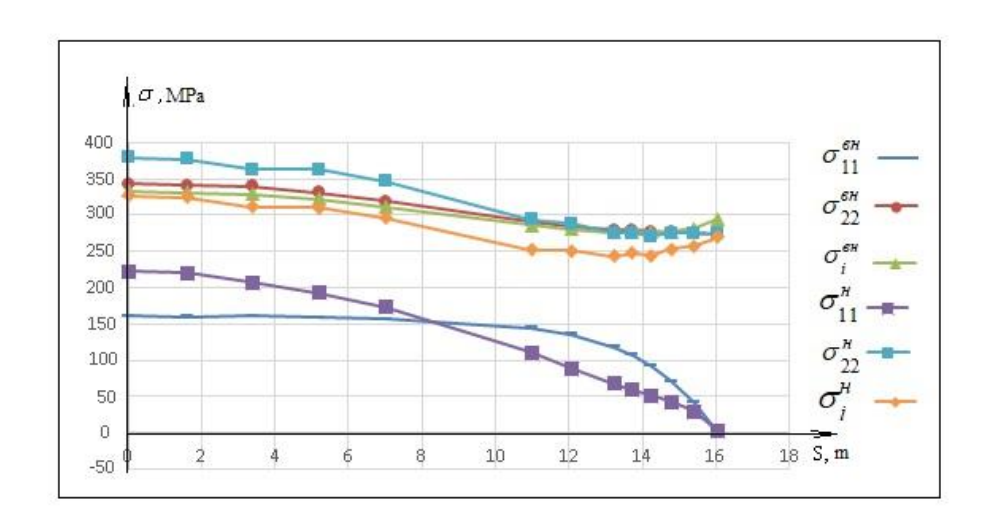


Fig. 5. Graphs of changes in meridional and circumferential stresses in fibers along the length of the meridian arc

From the values of stress intensities in the internal and external fibers on Fig. 5, it is clear that under conditions of plastic strain the material is near the surfaces. And since the meridional (σ_{11}) and circumferential (σ_{22}) stresses are tensile, it means that the material between the surfaces is under conditions of plastic strain. There are no areas of elastic strain at q = 45.6 MPa along the section thickness.

Based on Fig. 3 for meridional stresses, a static check of the equilibrium condition of the structure was performed (Fig. 1) $\sum \mathbf{x} = Q_q - Q_\sigma = 0$, where Q_σ is a stress endeavor; Q_q is a pressure endeavor q.

The error is $\delta=0.6$ %. From the values of stress intensities in the internal and external fibers in Fig. 5, it can be seen that the entire body of the shell is under conditions of plastic strain $\sigma_i>\sigma_{iT}=200$ MPa along the entire thickness.

Conclusions

In the second variant of the physical equations (Eq. (14)) the following relations are accepted $P_{\Delta\varepsilon}=P_{\Delta\varepsilon}^e+P_{\Delta\varepsilon}^p=\frac{1-2\nu}{E}+0$, in other words, it is assumed that during elastoplastic deformation ($\sigma_i>\sigma_{iT}$) the first invariant of the strain increment tensor changes according to the law of elastic deformation.

In the third variant of the defining equations (Eq. (18)) the relations $P_{\Delta\varepsilon}=P_{\Delta\varepsilon}^e+P_{\Delta\varepsilon}^p=\phi P_{\Delta\sigma}$ are used, which can be accepted either on the basis of experiment or on the basis of some hypothesis. In the first and second variants of the defining equations, the value $P_{\Delta\varepsilon}^p=0$, and the value $P_{\Delta\varepsilon}^p=\frac{1-2\nu}{E}$ is used in the increments of elastic deformation throughout the entire process of elasto-plastic deformation.

In this work, in order to compare the variants of the defining equations, the expression $P_{\Delta\varepsilon}=P_{\Delta\varepsilon}^e+P_{\Delta\varepsilon}^p=\frac{1-2\nu}{E}$, is used, in which the results of the calculation of the presented example based on the second and third variants of the physical equations turned out to be almost identical.

When calculating structures for which the material dependence $P_{\Delta\varepsilon} = \phi P_{\Delta\sigma}$ is not linear, the third variant of physical equations should be used.

References

- 1. Malinin MM. Applied Theory of Plasticity and Creep. Moscow: Mashinostroenie Publ.; 1975. (In-Russian)
- 2. Golovanov AI, Sultanov LU. *Mathematical models of computational nonlinear mechanics of deformable media*. Kazan: Kazan State University; 2009. (In-Russian)
- 3. Petrov VV. Nonlinear Incremental Structural Mechanics. Moscow: Infra-Inzheneriya Publ.; 2014. (In-Russian)
- 4. Levin VA. Nonlinear Computational Mechanics of Strength, Vol. 1: Models and methods. Formation and development of defects. Moscow: Fizmatlit Publ.; 2015. (In-Russian)
- 5. Sedov LI. Continuum Mechanics. Moscow: Nauka Publ.; 1976. (In-Russian)
- 6. Samul VI. Fundamentals of the theory of elasticity and plasticity. Moscow: Vysshaya shkola Publ.; 1982. (In-Russian)
- 7. Demidov SP. Theory of elasticity. Moscow: Vysshaya shkola Publ.; 1979. (In-Russian)
- 8. Galimov KZ, Paimushin VN, Teregulov IG. Foundations of the nonlinear theory of shells. Kazan: Fan Publ.; 1996. (In-Russian)
- 9. Krivoshapko SN. On opportunity of shell structures in modern architecture and building. *Structural Mechanics of Engineering Constructions and Buildings*. 2013;1: 51–56. (In-Russian)
- 10. Reissner E. Linear and Nonlinear Theory of Shells. *Thin-Shell Structures: Theory, Experiment and Design*. New Jersey: Prentice Hall; 1974.
- 11. Levin VA, Vershinin AV. *Nonlinear Computational Mechanics of Strength, Vol. 2: Numerical methods. Parallel computing on a computer.* Moscow: Fizmatlit Publ.; 2015. (In-Russian)
- 12. Aldakheel F, Wriggers P, Miehe C. A modified Gurson-type plasticity model at finite strains: Formulation, numerical analysis and phase-field coupling. *Computational Mechanics*. 2018;62, 815–833.
- 13. Aldakheel F, Miehe C. Coupled thermomechanical response of gradient plasticity. *International Journal of Plasticity*. 2017;91: 1–24.
- 14. Aldakheel F. Micromorphic approach for gradient-extended thermo-elastic-plastic solids in the logarithmic strain space. *Continuum Mechanics Thermodynamics*. 2017;29: 1207–1217.
- 15. Sultanov LU. Analysis of finite elasto-plastic strains. Medium kinematics and constitutive equations. *Lobachevskii Journal of Mathematics*. 2016;37: 787–793.
- 16. Bathe KJ. Finite element procedures. New Jersey: Prentice Hall; 1996.
- 17. Golovanov AI, Tyuleneva ON, Shigabutdinov AF. Finite element method in statics and dynamics of thinwalled structures. Moscow: Fizmatlit Publ.; 2006. (In-Russian)
- 18. Wriggers P, Hudobivnik B. A low order virtual element formulation for finite elasto-plastic deformations. *Computer Methods in Applied Mechanics and Engineering*. 2017;327: 459–477.

- 19. Da Veiga LB, Lovadina C, Mora D. A Virtual Element Method for elastic and inelastic problems on polytope meshes. *Computer Methods in Applied Mechanics and Engineering*. 2017;295: 327–346.
- 20. Tutyshkin ND, Zapara MA. Constitutive relations of the tensor theory of plastic damageability of metals. In: *Problemy prochnosti, plastichnosti i ustojchivosti v mekhanike deformiruemogo tverdogo tela: Materialy VII mezhdunarodnogo nauchnogo simpoziuma, Tver', 16-17 dekabrya 2010 goda.* Tver: TvGTU Publ.. 2011. p.216–219. (In-Russian)
- 21. Il'ushin AA. Plasticity: Elasto-plastic deformation. St.-Peterburg: Lenand Publ.; 2018. (In-Russian)
- 22. Dzhabrailov ASh, Nikolaev AP, Klochkov YuV, Gureyeva NA. Finite element algorithm for implementing variants of physically nonlinear defining equations in the calculation of an ellipsoidal shell. *Materials Physics and Mechanics*. 2022;50(2): 319–330.
- 23. Dzhabrailov ASh, Nikolaev AP, Klochkov YuV, Gureyeva NA, Ishchanov TR. Calculation of an Elliptic Cylindrical Shell Outside Elastic Limits Based on the FEM with Various Forms of Defining Equations. *Journal of Machinery Manufacture and Reliability*. 2020;49: 518–529.
- 24. Gureeva NA, Kiseleva RZ, Nikolaev AP. Nonlinear deformation of a solid body on the basis of flow theory and realization of FEM in mixed formulation. *IOP Conference Series: Materials Science and Engineering.* 2019:675: 012059.
- 25. Gureeva NA, Klochkov YuV, Nikolaev AP, Yushkin VN. Stress-strain state of shell of revolution analysis by using various formulations of three-dimensional finite elements. *Structural Mechanics of Engineering Constructions and Buildings*. 2020;16(5): 361–379.
- 26. Magisano D, Leonetti L, Garcea G. Advantages of the mixed format in geometrically nonlinear analysis of beams and shells using solid finite elements. *International Journal for Numerical Methods Engineering*. 2016:109(9): 1237–1262.
- 27. Liguori F, Madeo A, Garcea G. A mixed finite-element formulation for the elasto-plastic analysis of shell structures. *Theoretical and Applied Mechanics*. 2023;26: 227–232.
- 28. Leonetti L, Le CV. Plastic collapse analysis of Mindlin–Reissner plates using a composite mixed finite element. *International Journal for Numerical Methods in Engineering*. 2016;105: 915–935.
- 29. Magisano D, Garcea G. Fiber-based shakedown analysis of three-dimensional frames under multiple load combinations: Mixed finite elements and incremental-iterative solution. *International Journal for Numerical Methods in Engineering*. 2020;121: 3743–3767.
- 30. Klochkov YuV, Pshenichkina VA, Nikolaev AP, Vakhnina OV, Klochkov MYu. Stress-strain state of elastic shell based on mixed finite element. *Magazine of Civil Engineering*. 2023;4(120): 12003.

About Author

Rumia Z. Kiseleva D SC

Candidate of Technical Sciences Associate Professor (Volgograd State Agrarian University, Volgograd, Russia)

Natalya A. Kirsanova 堕

Doctor of Physical and Mathematical Sciences

Associate Professor (Financial University under the Government of the Russian Federation, Moscow, Russia)

Anatoliy P. Nikolaev D Sc

Doctor of Technical Sciences

Associate Professor (Volgograd State Agrarian University, Volgograd, Russia)

Yuriy V. Klochkov D Sc

Doctor of Technical Sciences, Professor

Head of the Laboratory for Higher Mathematics (Volgograd State Agrarian University, Volgograd, Russia)

Yushkin V.N. (1) Sc

Candidate of Technical Sciences

Associate Professor (Volgograd State Agrarian University, Volgograd, Russia)

Submitted: November 27, 2023

Revised: December 18, 2023

Accepted: May 9, 2024

Synthesis and tensile behavior of Al7475-nano B₄C particles reinforced composites at elevated temperatures

G.L. Chandrasekhar ^{1,2} [™], Y. Vijayakumar ³, M. Nagaral ⁴, ¹ A. Rajesh ⁵, K. Manjunath ⁶,

R. Vara Prasad Kaviti 7, V. Auradi 8, 100

- ¹ Sri Sai Ram College of Engineering, Karnataka, India
- ² Cambridge Institute of Technology, Karnataka, India
- ³ JNN College of Engineering, Karnataka, India
- ⁴ Aircraft Research and Design Centre, Hindustan Aeronautics Limited, Karnataka, India
- ⁵ New Horizon College of Engineering, Karnataka, India
- ⁶ SEA College of Engineering and Technology, Karnataka, India
- ⁷ Brindavan College of Engineering, Karnataka, India
- 8 Siddaganga Institute of Technology, Karnataka, India
- [™] chandrasekhar.gotur@gmail.com

ABSTRACT

Materials with superior mechanical and wear properties, high strength, high stiffness, and low weight are necessary for modern technology. Mechanical characteristics of metal matrix composites are crucial to their potential use as structural materials. The current research focuses on the preparation of Al7475 alloy with 400 to 500 nm sized B4C a composite using a liquid metallurgy technique. Al7475 alloy was used to make composites with 2, 4, 6, 8 and 10 wt. % of B4C particles. Microstructural analysis was performed on the produced composites using SEM and EDS. Density, hardness, ultimate strength, yield strength, and elongation as a percentage were all measured as per ASTM norms. Further, tensile tests were conducted at room temperature, 50°C and 100°C elevated temperatures. SEM images showed that the boron carbide particles were evenly dispersed throughout the Al7475 alloy. EDS spectrums verified that Al7475 alloy contains boron carbide particles. By incorporating dual particles into the matrix, the density of Al alloy composites was lowered. Al7475 alloy with B4C composites exhibited superior tensile properties at room and elevated temperatures as compared to the base alloy.

KEYWORDS

Al7475 alloy • B₄C particles • microstructure • density • tensile behavior

Citation: Chandrasekhar GL, Vijayakumar Y, Nagaral M, Rajesh A, Manjunath K, Vara Prasad Kaviti R, Auradi V. Synthesis and tensile behavior of Al7475-nano B₄C particles reinforced composites at elevated temperatures. *Materials Physics and Mechanics*. 2024;52(3): 44–57. http://dx.doi.org/10.18149/MPM.5232024_5

Introduction

Similar to other composites, metal matrix composites (MMCs) consist of at least two chemically and physically different phases that are dispersed in a way that confers properties not present in either phase alone. Many scientists simply refer to these materials as "light metal matrix composites". Recent decades have seen significant progress in the development of light metal matrix composites, allowing for their deployment in the most critical applications. In a commercial setting, aluminium matrix composites (AMCs) perform admirably. Due to their low density, high strength,

outstanding creep resistance, high damping capacity, and amazing dimensional stability, metal matrix nanocomposites of aluminium have been the topic of extensive research in recent years [1,2].

Aluminium and its derivatives are now in the mechanical generation stage of MMC production, having exceeded the previous lattice materials. The creation of low-cost Albased MMCs that are reinforced with hard and delicate materials including SiC, Al_2O_3 , ZrO_2 , Graphite, and Mica have been a key focus of study. Boron carbide filaments and particles are widely recognized as being of exceptional quality [3]. Aluminium-ceramic multi-material composites produced using different methods are good examples of inexpensive, application-specific manufactured materials [4,5].

Metal matrix composites (MMCs) are a broad category of materials with the goal of improving many different characteristics. Although the grid can be constructed from any metal or alloy, research has focused mostly on the more easily modified mechanical properties of the lighter basic metals. Improvements in quality and reliability [6,7] have thus far been the driving forces for MMC development. By incorporating various filler components into metal grids, significant improvements can be made. As a result of these upgrades, the grids now have a higher damping limit, lighter segments, better wear resistance, warmer development, and higher temperature capacity. Metals are preferred due to their many useful qualities, including their low production cost, malleability, high heat and electrical conductivity, etc.

Since the properties of metal matrix composites (MMCs) may be modified by adding different reinforcements, they find widespread application in cutting-edge sectors including the aerospace and automotive industries. Particulate-reinforced metal composites have recently attracted attention due to their high specific strength and specific stiffness in either room temperature or increased temperature applications. Micro-structural factors of the reinforcement, such as form, size, orientation, distribution, volume, and weight, are known to have a major impact on the elastic properties of a metal matrix composite [8,9].

Aluminium alloys show great promise as matrix materials due to their high specific strength and stiffness. However, their short lifespan limits their applicability. The aerospace and automotive industries make extensive use of particulate reinforced aluminium matrix composites because of their superior mechanical and tribological properties in comparison to those of regular alloys. In order to develop high-quality, inexpensive MMCs [10,11], scientists are investigating Al-based compounds reinforced with hard and soft materials such as SiC, Al_2O_3 , B_4C , ZrO_2 , tungsten carbide, graphite, and mica.

The mechanical and other qualities of aluminium alloy can be improved by using ceramic particles as reinforcement, and this has been demonstrated. Most of the time, ceramics are used for the reinforcement in MMCs, and these reinforcements can be broadly classified as either continuous or discontinuous. They are known as continuous (fibre) reinforced composites and discontinuous (non-fiber) reinforced composites, respectively, for the MMCs they yield. Continuous fibres, short fibres (chopped fibres, not always the same length), whiskers, particle, and wire (only for metal) are the five main groups into which they can be further classified [12,13]. With the exception of wires, most reinforcing materials are ceramics, specifically oxides, carbides, and nitrides. These are

put to use because they combine excellent strength and stiffness in both cold and hot conditions.

Mechanical properties of Al7475 MMCs reinforced with nano B₄C particles manufactured through the stir casting method are poorly understood, however. Aluminium boron carbide composites are becoming increasingly significant as lightweight materials are required for new industrial applications. In light of these findings, it is suggested that Al7475 nano B₄C composites with different concentrations of B₄C particles be developed. The goal of this research is to use the liquid metallurgy method to develop Al7475 alloy with 2 to 10 wt. % of B₄C composites and examine the mechanical properties of composites. Tensile characteristics are analyzed between a 50 and 100 °C temperature range. In the present research an attempt has been made to develop Al7475 alloy with 400 to 500 nano sized B₄C composites using advanced novel two stage stir casting process. In the preparation of metal composites using oxide, carbide or nitride ceramic particles in the metal, always wettability between matrix and reinforcement is a major concern. This novel two stage melt stir method helped to develop uniformly distributed particles in the matrix.

Experimental details

Materials used

The main alloying element in 7475-alloy is zinc, making it a precipitation hardening aluminium alloy. 7475-O (annealed) and 7475-T6 (solutionized and artificially aged) are two popular pre-tempered grades, and 7475-T651 (solutionized, stress-relieved stretched and artificially aged) is another. In Table 1, we can see the Al7475 ingot that was analyzed here.

Table 1. Chemical composition of the Al7475 alloy used in the present study

Elements	Zn	Mg	Si	Mn	Cu	Fe	Cr	Ti	Al
Weight, %	5.70	2.50	1.50	0.06	1.20	0.12	0.22	0.06	Bal

As a wrought product and primary matrix material, Al7475 belongs to the 7000 class of aluminium alloys and features a high zinc and magnesium content. Al7475 is favored among aluminium alloys due to its low density (2.8 g/cm³) and great machinability (it can be formed into many shapes, such as jet engine components, structural components, and tubing). Age hardenable, strength, corrosion resistance, and superior weldability are all benefits of the materials with high zinc and magnesium content. The elements that make up Al7475 alloy are shown in Table 1.

The nanoB₄C employed here is a secondary reinforcement particle with a diameter of 400 to 500 nm. It was purchased from Reinste Delhi. Nano B₄C is a popular material among scientists and engineers because of its high mechanical and tribological qualities, as well as its other unique traits, such as its hardness, its ability to support a catalyst, and its use as a neutron absorber. B₄C is used to reinforce aluminium because of the metal's low density (it's lighter than the matrix material, thus it helps save weight) and because B₄C has a high melting point (up to 2950 °C) and good chemical and thermal stability. As a result, the low-cost stir casting technology has gained popularity among consumers interested in B₄C reinforced aluminium matrix composites.

Table 2. Physical properties of boron carbide [14]

Physical property	Specification
Crystallography	Rhombohedral
Color	Black
Specific gravity	2.52
Knoop100 hardness	2800
Melting point, °C	2950

Particles of boron carbide have unusually high hardness, low density, and good wear resistance. Carbon and boron oxide are reduced in an electric furnace to form boron carbide. The black powder is first ground into a fine powder and then pressed at temperatures above 2000 °C to solidify it. Tables 2 and 3 list the material and mechanical properties of boron carbide, respectively.

Table 3. Mechanical properties of boron carbide [14]

Density, gm /cm³)	2.52
Melting point, °C	2445
Young's modulus, GPa	450 - 470
Thermal conductivity (at 25 °C), W/m-K	30 - 42
Hardness (Knoop 100g), kg/mm ²	2900 - 3580

Because of its low cost and suitability for mass manufacturing, the stir casting technique is used to manufacture metal matrix nano composites. Stir casting was used to create nano-composites with 2, 4, 6, 8, and 10 wt. % of B₄C particles, respectively. The necessary quantity of B₄C and the cast iron die are initially warmed to 500 °C. However, the Al7475 was heated to 750 °C in an electric furnace after being weighed and deposited in a graphite crucible. After the Al7475 alloy has melted completely, a degassing powder called solid hexachloroethane (C₂Cl₆) [15] was added to the molten melt in order to expel the undesirable adsorbed gases. A zirconium-coated mechanical stirrer is dipped into the hot melt, creating a visible vortex while the stirrer spins at 300 revolutions per minute. The nano ceramic particles and the right amount of K_2TiF_6 were fed into the vortex at a consistent rate once the melt has reached the suitable temperature. The nano B₄C and K_2TiF_6 combination was stirred continuously before and after each pouring stage to ensure that the nano particles are evenly dispersed throughout the melt without cluster. The molten metal was put into a cast iron die that had been preheated, and then stirred for a while.

To prepare the metal matrix composites usually ceramic reinforcements in the form of oxides, nitrides and carbides are used. The maximum 15 wt. % of reinforcement can be used to synthesize the metal base composites, beyond this is very difficult to have good wettability between the matrix and reinforcement. So, one can use any combination of weight percentage below 15 wt. % to fabricate the composites, it may be 2, 4, 6, 8 and 10 or 4 and 8 or 3, 6, 9 and 12 wt. %. In the present study, it is considered 2 to 10 wt. % in steps of 2 wt. %. Al7475 - 10 wt. % of B₄C composites exhibited lesser ductility as compared to 8 wt. % of B₄C reinforced composites; hence in this study 10 wt. % was used as a maximum wt. % to fabricate the Al7475 alloy composites. Rashmi et al. [16] studied the impact of 4 and 8 wt. % of nano and micron particles of B₄C composites. Al7075 alloy

with 8 wt. % of nano B_4C composites shown improved properties with slight decrease in the ductility, if more wt. % of boron carbide content in the matrix, decreases the ductility of the composites. Angadi et al. [17] investigated the various properties of 2.5 to 5 wt. % of B_4C reinforced Al2011 composites. Al2011 with 5 wt. % of boron carbide composites once again exhibited high properties with slight reduced elongation. Hence, the higher weight percentage of carbide particles reduces the ductility of the composites. Ductility is an important property of materials it should not be lesser.

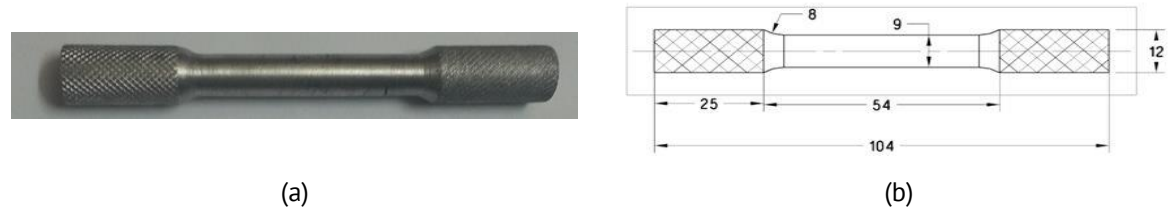


Fig. 1. Photograph (a) and dimensions (in mm) of a tensile test specimen

For the purpose of characterization, the synthesized Nano composites were machined to ASTM standards. After confirming the presence of B and C components and the homogeneous distribution of particles in the matrix using SEM, the mechanical behavior of as cast Al7475 alloy and its nano composites is evaluated using ASTM standards. Figure 1(a) shows the tensile test specimen used as per ASTM E8 standard. Figure 1(b) demonstrates the block diagram of the tensile test specimen with dimensions as per ASTM E8 standard.

Results and Discussion

Microstructural studies

The manufactured nano composite's reinforcing pattern and uniform distribution of nano particles are inspected using a scanning electron microscope. Emery papers of progressively finer grits (starting with 220 grit SiC paper) were used to smooth up a segment of the casted specimen's cut section. Keller's reagent (HCL+ HNO₃+HF+Water) was used to etch the samples after they were manually polished to better highlight the microstructure [18,19].

Scanning electron microscopy (SEM) images of as cast Al7475 alloy are displayed in Fig. 2(a). Figure 2(b-f) demonstrates 2 to 10 wt. % of nanoB $_4$ C reinforced composites. SEM images show that secondary phase nanoparticles are dispersed uniformly throughout the Al7475 alloy matrix with no evidence of agglomeration. Furthermore, the characteristics of Al7475 alloy are improved by the excellent interfacial bonding between the B $_4$ C and the alloy matrix.

Figure 3(a) displays EDS spectra of as cast Al7475 alloy, while Fig. 3(b-f) displays EDS spectra of Al7475 alloy reinforced with 2 to 10 wt. % of nano B_4C particulates. Elements such as Zn, Fe, Mg, Cu, Si, Cr, and Ti are depicted in an Al matrix in Fig. 3(a). Energy dispersive spectroscope spectra of Al7475 alloy with 2, 4, 6, 8, and 10 wt. % B_4C nano composites are shown in Fig. 3(b-f). All of the spectra show that boron (B) and carbon (C) are present in the Al7475 alloy, in addition to the expected Al, Zn, Cu, and Si.

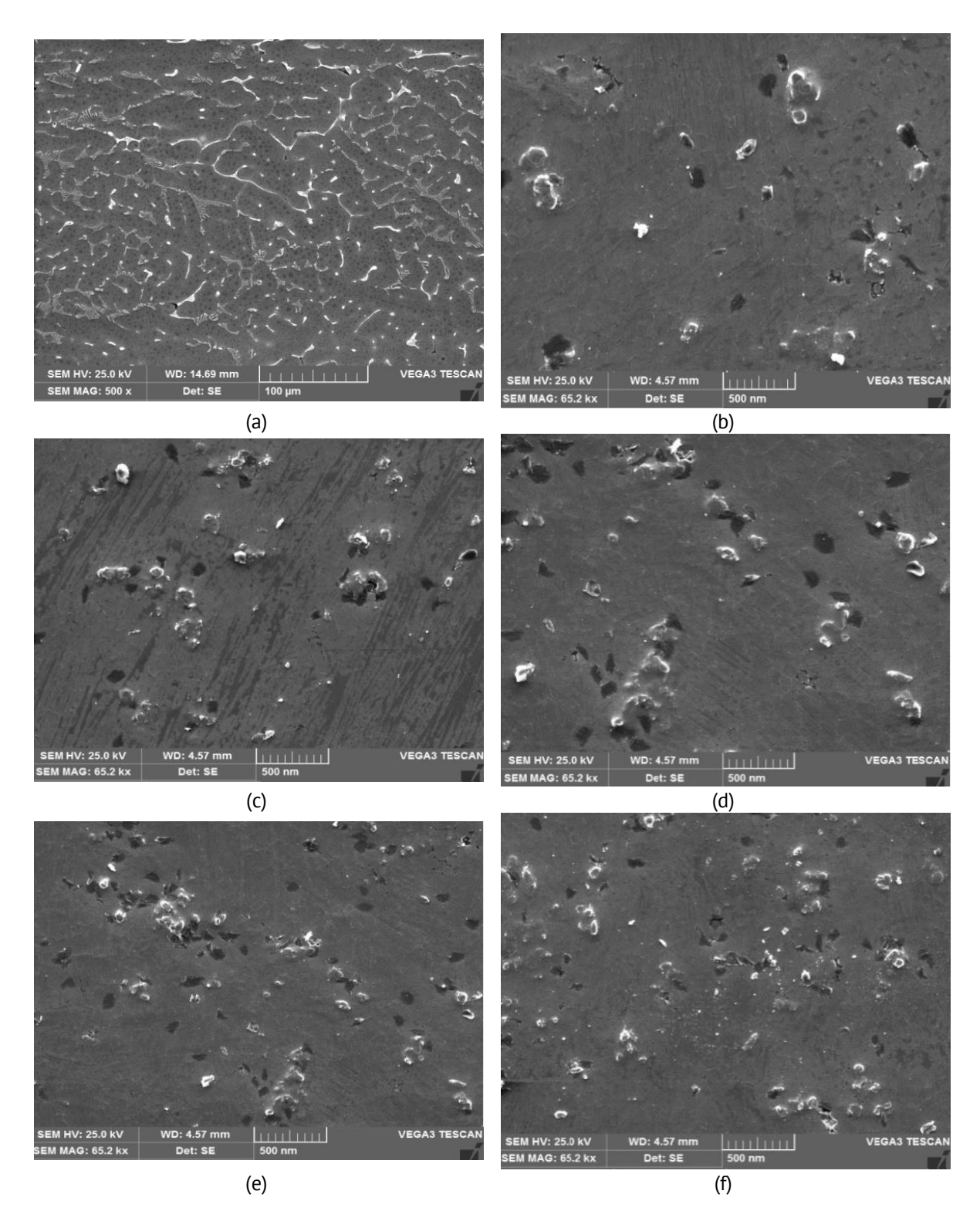


Fig. 2. SEM images of (a) As cast Al7475 alloy, (b) Al7475-2% B_4C , (c) Al7475-4% B_4C , (d) Al7475-6% B_4C , (e) Al7475-8% B_4C , (f) Al7475-10% B_4C nano composites

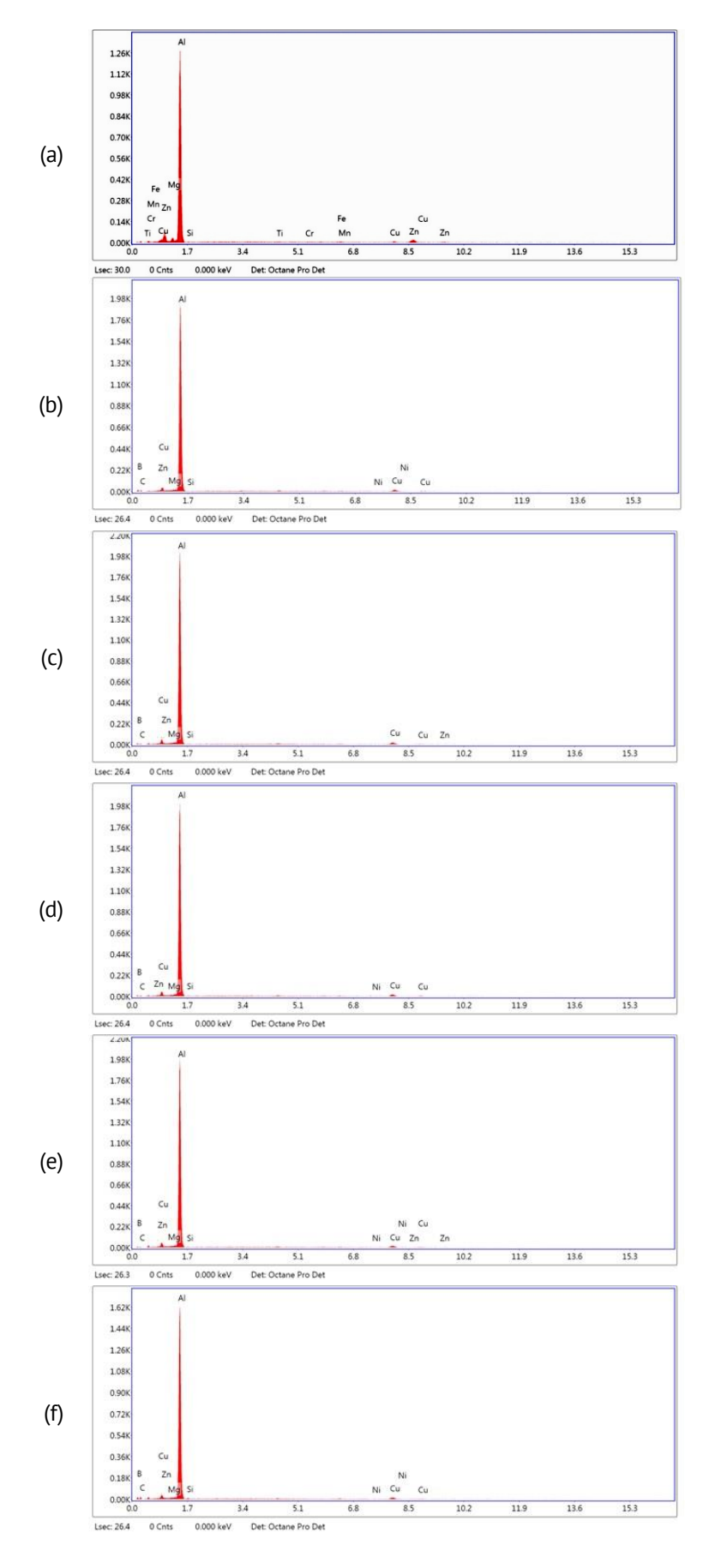
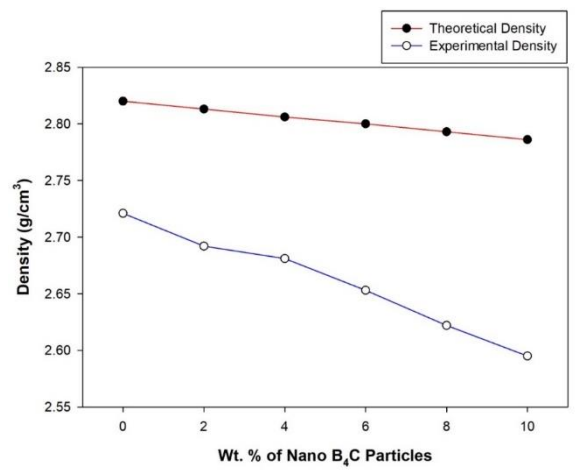


Fig. 3. EDS spectrums of (a) as cast Al7475 alloy, (b) Al7475-2% B_4C , (c) Al7475-4% B_4C , (d) Al7475-6% B_4C , (e) Al7475-8% B_4C , (f) Al7475-10% B_4C nano composites

Density measurements

Figure 4 shows a comparison of the theoretical and experimental densities of as cast Al7475 alloy to Al7475 alloy with 2, 4, 6, 8, and 10 wt. % of nano sized B_4C composites. The density of Al7475 is 2.82 g/cm³, while that of boron carbide is 2.52 g/cm³. When Al7475 is reinforced with 2 wt. % nano B_4C , the composite's overall density decreases because the B_4C density is lower than the Al7475 alloy. When 4, 6, 8, or 10 wt. % of B_4C particles are added to Al7475 alloy, the composite typically has a lower density than the original/base aluminium alloy. Furthermore, the difference between the theoretical and experimental densities can be seen to be smaller than expected [20,21]. Boron carbides' ability to reduce material density agrees with findings from competing studies.



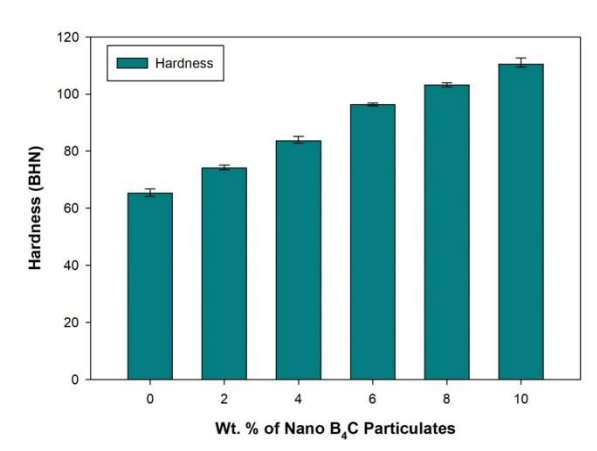


Fig. 4. Theoretical and experimental densities of Al7475 alloy with nano B₄C composites

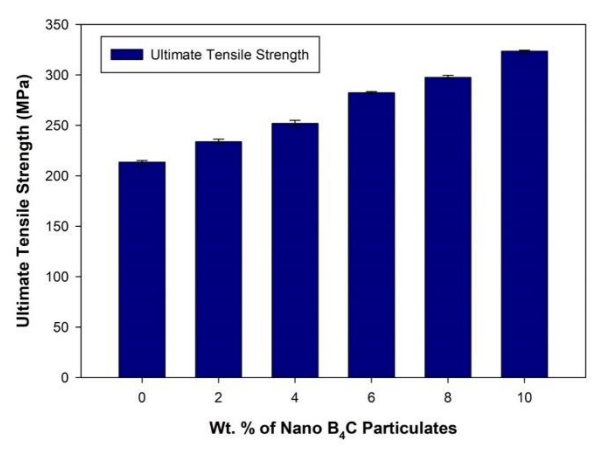
Fig. 5. Hardness of Al7475 alloy and its nano B₄C composites

Hardness measurements

One way to characterize a material's hardness is by measuring its resistance to plastic deformation. The hardness of as cast Al7475 alloy and Al7475 alloy with nanoB₄C composites containing 2, 4, 6, 8, and 10 wt. % is measured using a Brinell hardness testing machine equipped with a 5 mm ball indenter, an applied force of 250 kgf, and a dwell period of 30 seconds for each sample at different locations. As can be seen in Fig. 5, the durability of composites greatly exceeds that of their as-cast counterparts as the percentage of nano B₄C in the composites increases. The increasing trend in hardness can be attributed to the B₄C particles, which are dispersed uniformly and add to the hardness of the composite by blocking the progress of dislocations within the matrix. The findings are consistent with those of other researchers, which may be due in large part to the intrinsic link between the matrix and reinforcement [22,23].

Tensile properties

Figures 6–8 show the ultimate tensile strength of unreinforced Al7475, Al7475 reinforced with 2 wt. % B_4C , Al7475 reinforced with 4 wt. % B_4C , Al7475 reinforced with 6 wt. % B_4C , Al7475 reinforced with 8 weight percent B_4C , and Al7475 reinforced with 10 wt. % B_4C at room temperature and at 50 and 100 °C, respectively.



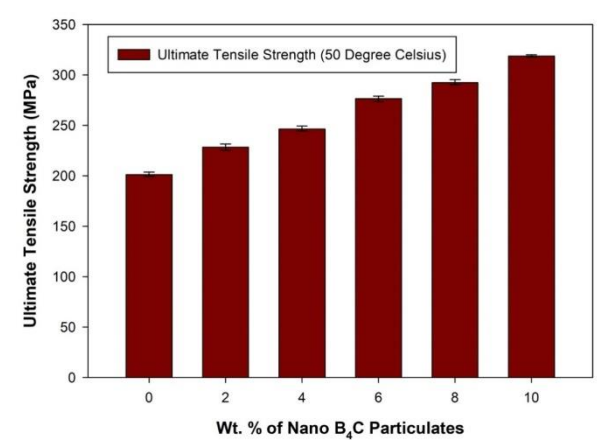


Fig. 6. UTS of Al7475 alloy and its nano B₄C composites at room temperature

Fig. 7. UTS of Al7475 alloy and its nano B₄C composites at 50 °C

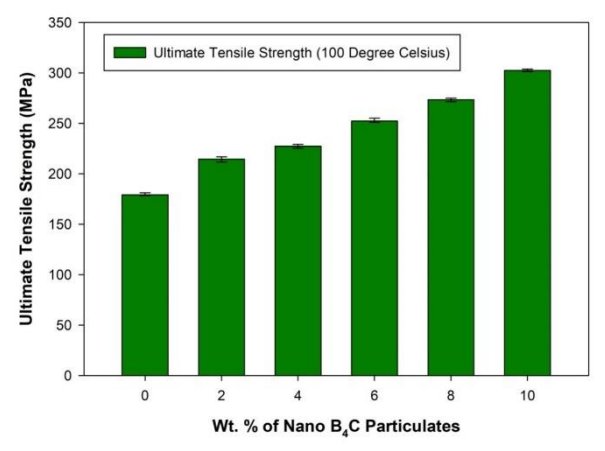
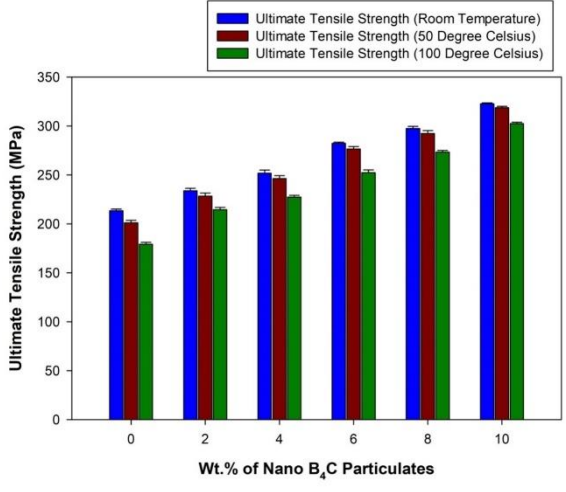


Fig. 8. UTS of Al7475 alloy and its nanoB₄C composites at 100 °C

Figure 6 displays the room-temperature ultimate tensile strength of Al7475 alloy and its nano B₄C reinforced composites, respectively. When Al7475 alloy is as cast, its maximal tensile strength is 212.43 MPa. Nano B₄C particles added at quantities between 2 and 10 % increased the UTS of Al7475 alloy. The following are the UTS values: The tensile strength of Al7475 alloy at 2% B₄C is 234.17 MPa, at 4 % B₄C it is 251.67 MPa, at 6 % B₄C it is 282.47 MPa, at 8 % B₄C it is 298.03 MPa, and at 10 % B₄C it is 322.53 MPa. The UTS of Al7475 alloy is enhanced by 52.8 % when nano B₄C is added at a concentration of 10 wt. %. Nanoparticle inclusion has resulted in increased ultimate strength, primarily as a result of reinforcing tougher particles in the soft matrix. During testing, strengthening particles work to prevent the matrix from undergoing plastic deformation because they are, by definition, stronger and more rigid than the matrix. However, the distribution of the boron carbide particles throughout the Al7475 alloy matrix is essential for preventing the matrix from deforming plastically [24,25].

Composites supplemented with 2–10 % nano boron carbide particles from Al7475 alloy exhibit higher ultimate tensile strength at 50 and 100 °C, as shown in Figs. 7 and 8. Increasing the percentage of reinforcement particles from 2 to 10 wt. % enhances the UTS of Al7475 alloy at both 50 and 100 °C, as shown by the graphs. The increased UTS of Al7475 alloy at high temperatures is extremely useful in a wide variety of applications. With UTS of

201.37 MPa at 50 °C and 179.80 MPa at 100 °C, Al7475 alloy possesses impressive properties as cast. After incorporating 10 wt. % nano boron carbide particles, the UTS increases to 318.87 MPa at 50 °C and 302.5 MPa at 100 °C. In both the 50 and 100 °C test conditions, the UTS of Al7475 alloy nano B_4C composites is greater than that of the base matrix. Nanoparticle-reinforced composites are advantageous mainly because to their resistance to plastic deformation. At 50 °C, the UTS of the Al7475 alloy rose by 58.26 %.



Yield Strength (Room Temperature)
Yield Strength (90 Degree Celsius)
Yield Strength (100 Degree Celsius)

250

250

4

Wt.% of Nano B₄C Particulates

Fig. 9. Comparison of UTS of Al7475 alloy and its nano B₄C composites at room temperature and elevated temperatures

Fig. 10. Comparison of YS of Al7475 alloy and its nano B₄C composites at room temperature and elevated temperatures

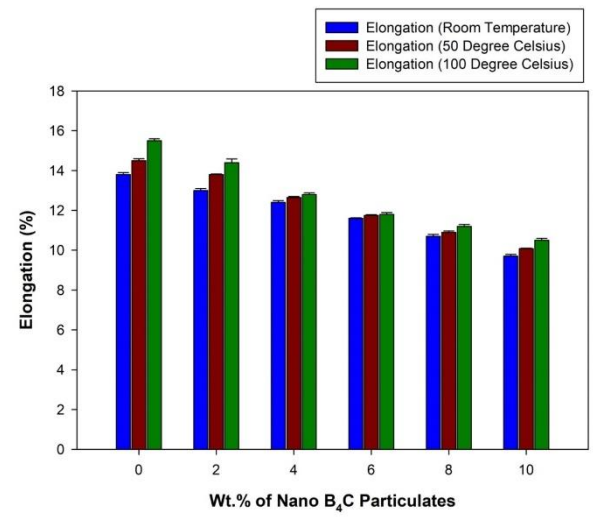


Fig. 11. Comparison of elongation of Al7475 alloy and its nano B₄C composites at room temperature and elevated temperatures

Ultimate tensile strength comparisons at room temperature and increased temperatures (50 and 100 °C) for Al7475 alloy and various wt. % of B_4C reinforced composites are shown in Fig. 9. As cast alloy has a UTS of 212.43 MPa at room temperature; at 50 and 100 °C, the UTS is 201.37 MPa (50 °C) and 179.80 MPa (100 °C), respectively. The as cast Al7475 alloy's UTS decreases from ambient temperature to higher temperatures. More plastic deformation of alloy occurs at higher temperatures, which is the primary cause of this decrease in UTS.

Furthermore, Fig. 9 shows that the UTS is enhanced both at room temperature and at elevated temperatures as the weight percentage of B_4C particles is increased from 2 to 10 wt. %. UTS values for composites of Al7475 - 2 wt. % of B_4C reinforcement at room temperature (RT), $50^{\circ}C$, and $100^{\circ}C$, respectively, are 234.17, 228.4, and 214.13 MPa. As cast alloy has a UTS of 212.43 MPa at room temperature. The UTS of Al7475 alloy is enhanced by the addition of 2 wt. % of nanoparticles in all situations at ambient temperature as well as at increased temperatures. Furthermore, the ultimate strength of as cast Al7475 alloy and its composites decreases from room temperature to $100^{\circ}C$. The softening of the material caused by exposure to high temperatures is responsible for most of the drop in UTS. The ultimate strength of the Al7475 alloy without any particles is 212.43 MPa at room temperature, this ultimate strength has been improved to 322.53 MPa with 10 wt. % of B_4C particles in the Al7475 alloy. Al7475 - 10 wt. % of B_4C composites exhibited an improvement of 51.82 % in the ultimate tensile strength at room temperature.

Yield strength comparisons at room temperature and increased temperatures (50 and 100 °C) between Al7475 alloy and various wt. % of B_4C reinforced composites are shown in Fig. 10. As cast alloy has YS of 173.83 MPa at room temperature; similarly, it has YS of 169.57 MPa (at 50 °C) and 157.73 MPa (at 100 °C) in test settings. As cast Al7475 alloy has a lower YS at high temperatures than at ambient temperature. When heated, alloy undergoes increased plastic deformation, leading to a drop in YS.

Furthermore, as shown in Fig. 10, increasing the proportion of B_4C particles from 2 to 10 wt. % improves YS at both room temperature and higher temperatures. The YS values of composites made from Al7475 alloy and 2 wt. % of B_4C reinforcement were 196.4 MPa at RT, 192.2 MPa at 50 °C, and 173.47 MPa at 100 °C. The addition of 2 wt. % of nano particles improves the YS of Al7475 alloy under all conditions, including at room temperature and higher temperatures. The yield strength of as cast Al7475 alloy and its composites diminishes from 0 to 100 °C. This decrease in YS can be traced back to the material softening as a result of prolonged contact to high temperatures [26,27].

Figure 11 displays the elongation as a percentage of the initial length at room temperature and high temperature for Al7475 alloy and nano boron carbide reinforced composites, respectively. As can be seen in Fig. 11 the ductility of Al7475 alloy is diminished when hard boron carbide particles are added to it. Experiments conducted at room temperature reveal a 13.83 % stretch in as cast Al7475 alloy. In addition, nano B_4C reinforced composites at 10 wt. % for Al7475 alloy have a value of 9.73 %. From the plot it is observed that as the testing temperature increases from RT to 100 °C, there is increase in the elongation due to the higher temperature.

Figure 12 represents SEM images of tensile fractured surfaces of Al7475 alloy and Al7475 with 10 wt. % of B_4C reinforced composites at room temperature and at 100 °C temperatures tensile test specimens. Figure 12(a) is the tensile fractured surface of Al7475 alloy at room temperature test conducted specimen. This shows grains and void dimples. Further, the fracture surface of Al7475 alloy at 100 °C testing environment exhibited the elongated grains, which is mainly due to improved ductility at higher temperature. Figure 12(c-d) are representing the tensile fractured surfaces of Al7475 alloy with 10 wt. % of B_4C composites. These samples surfaces are showing combined brittle and ductile mode of fracture due to presence of hard particles [28].

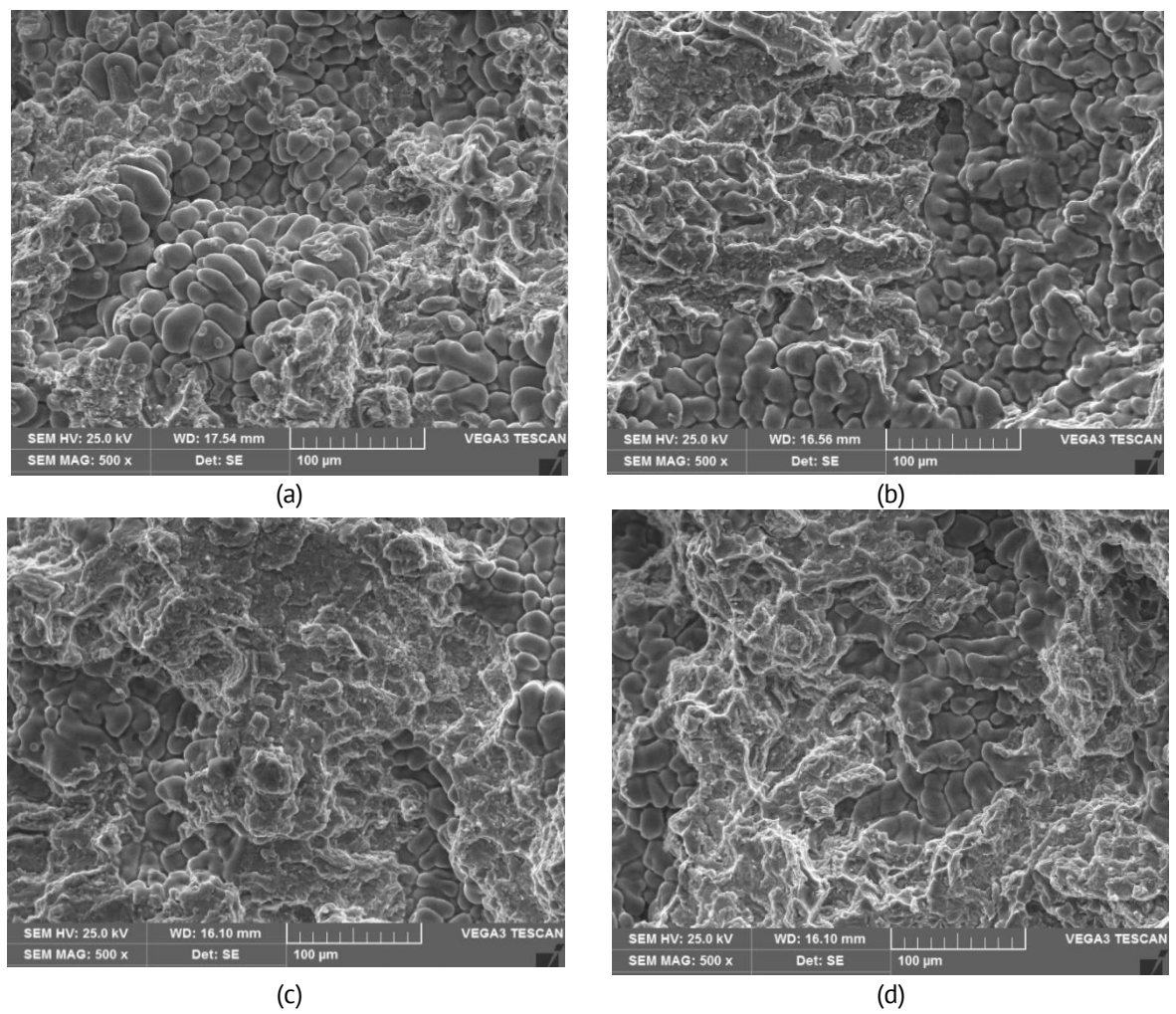


Fig. 12. Tensile fractured SEM of (a) Al7475 alloy at room temperature, (b) Al7475 alloy at 100 °C, (c) Al7475 – 10 wt. % of B_4C composites at room temperature, (d) Al7475 – 10 wt. % of B_4C composites at 100 °C

Conclusions

The stir cast method is suitable for producing Al7475 alloy with B₄C particles of nano in size and MMCs of 2 to 10 wt. %. Scanning electron microscopy images show that B₄C particles are evenly dispersed across the Al7475 alloy. This study analyzed the EDS patterns of composites made from Al7475 alloy and B₄C particles at 2 to 10 wt. %. The presence of boron and carbon elements in Al7475 alloy with B₄C composites are confirmed by EDS spectrums. The incorporation of B₄C particles reduced the density of Al7475 alloy composites. Further, theoretical and experimental densities are very nearer to each other, which indicate the proper casting method of Al7475 alloy and B₄C composites. The hardness of Al7475 alloy has increased with the incorporation of B₄C particles. The highest hardness is observed in the case of Al7475 alloy with 10 wt. % of B₄C composites. The ultimate strength of the Al7475 alloy without any particles is 212.43 MPa at room temperature, this ultimate strength has been improved to 322.53 MPa with 10 wt. % of B₄C particles in the Al7475 alloy. Ultimate and yield strengths of Al7475 alloy have enhanced with the 2 to 10 wt. % of boron carbide particles reinforced addition. Improvements in the UTS and YS with 10 wt. % of B₄C particles in Al7475 alloy is 51.8 and 61.6 % respectively. Further, UTS and YS values of as cast Al7475

alloy and its 2 to 10 wt. % of boron carbide composites decreased at elevated 50 and $100\,^{\circ}$ C. The ductility of Al7475 alloy has been slightly reduced with the incorporation of boron carbide particles in the Al7475 alloy matrix. The ductility has been improved in the case of elevated temperatures as compared to the room temperature experimental values. Tensile fractured surfaces at elevated temperatures exhibited larger and elongated grains. Metal composites with B_4C shown combined brittle and ductile mode of fracture behavior.

References

- 1. Suresh S, Moorthi NSV, Vettivel SC, Selvakumar N, Jinu GR. Effect of graphite addition on mechanical behavior of Al6061-TiB₂ hybrid composites using acoustic emission. *Materials Science and Engineering A*. 2014;612: 16–27.

 2. Siddesh KNG, Shivashankar GS, Basavarajappa S, Suresh R. Some studies on mechanical and machining accounts of the composite of the
- characteristics of Al2219/n-B₄C/MoS₂nano hybrid metal matrix composites. *Measurement*. 2017;107: 1–11.
- 3. Veeresh Kumar GB, Gude VC, Mandadi SV, Jayarami RK, Nagaral M, Naresh K. Effects of addition of Titanium Diboride and Graphite Particulate Reinforcements on Physical, Mechanical and Tribological properties of Al6061 Alloy based Hybrid Metal Matrix Composites. *Advances in Materials and Processing Technologies*. 2022;8(2): 2259–2276.
- 4. Ruixiao Z, Jing C, Yitan Z, Kei A, Chaoli M. Fabrication and characterization of hybrid structured Al alloy matrix composites reinforced by high volume fraction of B_4C particles. *Materials Science and Engineering A.* 2014;601: 20–28. 5. Sekar K, Allesu K, Joseph MA. Effect of heat treatment in tribological properties of A356 aluminium alloy reinforced with Al_2O_3 nano particles by combination effect of stir and squeeze casting method. *Applied Mechanics and Materials*. 2014;592-594: 968–971.
- 6. Umanath K, Selvamani ST, Palanikumar K, Raphael T, Prashanth K. Effect of sliding distance on dry sliding wear behavior of Al6061-SiC-Al $_2$ O $_3$ hybrid composite. In: *Proceedings of International Conference on Advances in Mechanical Engineering*. 2013. p.749–75.
- 7. Ramchandra M, Abhishek A, Siddeshwar P, Bharathi V. Hardness and wear resistance of ZrO₂ nano particle reinforced Al nano composites produced by powder metallurgy. *Procedia Materials Science*. 2015;10: 212–219.
- 8. Dhanalakshmi P, Mohansundararaju N, Venkatkrishnan PG. Preparation and mechanical characterization of stir cast hybrid Al7075 Al₂O₃ B₄C metal matrix composites. *Applied Mechanics and Materials*. 2014;592–594: 705-710.
- 9. Devnani GL, Shishir S. Effect of nano fillers on the properties of natural fiber reinforced polymer composites. *Materials Today Proceedings*. 2018;18: 647–654.
- 10. Mohammad N, Behnam L, Zohreh S. Evaluation of the microstructure and wear behavior of AA6063-B₄C/TiB₂ mono and hybrid composite layers produced by friction stir processing. *Surface & Coatings Technology*. 2016;285: 1–10.
- 11. Amir P, Agnieszka W, Gaulthier R, Dayangku N, Valeria N. A comprehensive analysis of extrusion behavior, microstructural evolution and mechanical properties of 6063 Al-B₄C composites produced by semisolid stir casting. *Materials Science and Engineering Materials A*. 2018;721: 28–37.
- 12. Narasimha MI, VenkataRao D, BabuRao J. Microstructure and mechanical properties of aluminium fly ash nano composites made by ultrasonic method. *Materials and Design*. 2012;35: 55–65.
- 13. Omyma E, Fathy A. Effect of SiC particle on the physical and mechanical properties o extruded Al matrix composites. *Materials and Design*. 2014;54: 348–353.
- 14. Murali MR, Kempaiah UN, Manjunatha B, Madeva N, Auradi V. Processing and wear behavior optimization of B₄C and rice husk ash dual particles reinforced ADC12 alloy composites using Taguchi method. *Materials Physics and Mechanics*. 2022;50(2): 304–318.
- 15. VijayaRamnath B, Elanchezhian C, Jaivignesh M, Rajesh S, Parswajinan A. Siddique Ahmed Ghias Evaluation of mechanical properties of aluminium alloy—alumina—boron carbide metal matrix composites. *Materials and Design*. 2014;58: 332–338.
- 16. Rashmi PS, Hemanth RT, Nagaral M, Nithin K, Auradi V. Effect of B_4C particles addition on the mechanical, tensile fracture and wear behavior of Al7075 alloy composites. *Journal of Bio-and Tribo-Corrosion*. 2024;10(2): 32.
- 17. Angadi SB, Nagaral M, Pilankar V, Yarnalkar P, Purohit B, Shewale S. Assessment of mechanical behavior and microstructure of micro boron carbide particles reinforced al2011 alloy metal matrix composite for aerospace applications. *International Journal of Vehicle Structures & Systems (IJVSS)*. 2023;15(2): 251–257.

- 18. Hong SJ, Kim HM, Huh D, Suryanarayana C, Chun BS. Effects of Clustering on the Mechanical Properties of SiC Particulate Reinforced Aluminum Alloy 2024 Metal Matrix Composites. *Material Science and Engineering A.* 2003;347: 198–204.
- 19. Madeva N, Vijaykumar H, Auradi V, Kori SA. Influence of Two-Stage Stir Casting Process on Mechanical Characterization and Wear Behavior of AA2014-ZrO₂ Nano-composites. *Transactions of the Indian Institute of Metals*. 2018;71: 2845–2850.
- 20. Meijuan L, Kaka M, Lin J, Hanry H, Enrique L, Lianmeng Z, Julie S. Synthesis and mechanical behavior of nanostructured Al5083-TiB₂ metal matrix composites. *Materials Science and Engineering A.* 2016;656: 241–248.
- 21. Yogesh P, Chapgaon AN. Effect of volume fraction of Al_2O_3 on tensile strength of aluminium 6061 by varying stir casting furnace parameters: A review. *International Research Journal of Engineering and Technology*.2017;4(10): 1351–1355.
- 22. Fazil N, Venkataraman V, Nagaral M. Mechanical characterization and wear behavior of aerospace alloy AA2124 and micro B₄C reinforced metal composites. *Journal of Metals, Materials and Minerals*. 2020:30(4): 97–105. 23. Vijayakumar R, AnanthaPadmanabham KC, Chandrasekhar GL, Roopa RN, Manjunatha, HemanthRaju T,
- Udayashankar S. Synthesis and Characteristics of Heat Treated Al6061-Zirconium Dioxide Metal Matrix Composites. *Journal of The Institution of Engineers (India): Series D.* 2023;104: 795–804.
- 24. Suresh R. Comparative study on dry sliding wear behavior of mono (Al2219/B₄C) and hybrid (Al2219/B₄C/Gr) metal matrix composites using statistical technique. *Journal of the Mechanical Behavior of Materials*. 2020;29(1): 57–68.
- 25. Nagaral M, Auradi V, Parashivamurthy KI, Kori SA, Shivananda BK. Synthesis and characterization of Al6061-SiC-graphite composites fabricated by liquid metallurgy *Materials Today Proceedings*. 2018;5(1): 2836–2843.
- 26. Balaraj V, Nagaraj K, Nagaral M, Auradi V. Influence of Al_2O_3 and B_4C dual particles addition on the mechanical characterization of Al6061 alloy hybrid metal composites for automobile applications. *International Journal of Vehicles Structures and Systems*. 2021:13(5): 1–8.
- 27. Anjan KB, Hanumantharayappa CP, Chethana CR, Chnadrasekhar SB, Latha SB, Nagaral M, Suresh R. Synthesis and mechanical characterization of Si_3N_4 reinforced copper-tin matrix composites. *Journal of Mechanical Behavior of Materials*. 2021:30(1): 199–206.
- 28. Subhashchandra SG, Mahadev S, Nagaral M, Shashidhar S, Auradi V. Microstructural evolution and mechanical behavior of 90 micron sized B_4C particulates reinforced Al2219 alloy composites. *Materials Today Proceedings*. 2021:45(7): 7138–7142.

About Authors

G.L. Chandrasekhar Sc

Research Scholar (Sri Sai Ram College of Engineering, Karnataka, India)

Y. Vijayakumar Sc

PhD, Professor (JNN College of Engineering, Karnataka, India)

Madeva Nagaral D Sc

PhD, Manager (Design) (Aircraft Research and Design Centre, Hindustan Aeronautics Limited, Karnataka, India)

A. Rajesh

PhD, Professor (New Horizon College of Engineering, Karnataka, India)

K. Manjunath

PhD, Professor (SEA College of Engineering and Technology, Karnataka, India)

R. Vara Prasad Kaviti

PhD, Professor (Brindavan College of Engineering, Karnataka, India)

Virupaxi Auradi 📵 Sc

PhD, Associate Professor (Siddaganga Institute of Technology, Karnataka, India)

Submitted: April 15, 2024 Revised: May 28, 2024 Accepted: June 11, 2024

Unique properties of the Al-0.5Fe-0.3Cu alloy, obtained by casting into an electromagnetic crystallizer, after equal-channel angular pressing and cold drawing

A.E. Medvedev 1 , 0 O.O. Zhukova 1, V.U. Kazykhanov 1, A.F. Shaikhulova 1, 0

M.M. Motkov ², ¹⁰ V.N. Timofeev ², N.A. Enikeev ^{1,3}, ¹⁰ M.Yu. Murashkin ^{1,3}, ¹⁰

ABSTRACT

This paper examines the effect of equal-channel angular pressing (ECAP) and subsequent cold drawing (CD) on the microstructure and properties of the Al-0.5Fe-0.3Cu (wt. %) alloy produced by electromagnetic casting (EMC). The high rate of crystallization of the alloy ensured the formation of a solid solution of copper in the aluminum matrix, while iron was completely bound in intermetallic particles of the Al-Fe and Al-Fe-Cu types. A distinctive feature of ECAP processing followed by CD is the presence of signs of both ECAP and CD in the structure of the processed alloy. Moreover, the syncretic effect of two deformation methods, implementing different deformation schemes, led to the appearance of features that were absent in the alloy structures after ECAP or after CD. Presence of the unique ultra-fine grained (UFG) microstructure, formed as a result of the combined ECAP+CD treatment, led to an increase in the tensile strength of wires made of the Al-0.5Fe-0.3Cu alloy to 342 MPa while maintaining a relatively high electrical conductivity of 55.5 % IACS. Compared to the commercial scale alloys, the wire (with a UFG structure) from the Al-0.5Fe-0.3Cu alloy demonstrates either equal (6000 series alloys) or improved (8000 series alloys) mechanical strength and electrical conductivity. Introduction of copper into Al-0.5Fe alloy, obtained using the EMC method, allows to even further improve the strength-conductivity combination of this alloy.

KEYWORDS

aluminum alloy • Al-Fe-Cu • electromagnetic crystallization • equal-channel angular pressing cold drawing • UFG microstructure • electrical conductivity • strength • thermal stability

Acknowledgements. The research was supported by the Russian Science Foundation grant No. 20-79-10133, https://rscf.ru/project/20-79-10133/. The research part of the work was carried out on the equipment of the Core Facility Centre "Nanotech" of Ufa University of Science and Technology.

Citation: Medvedev AE, Zhukova OO, Kazykhanov VU, Shaikhulova AF, Motkov MM, Timofeev VN, Enikeev NA, Murashkin MYu. Unique properties of the Al-0.5Fe-0.3Cu alloy, obtained by casting into an electromagnetic crystallizer, after equal-channel angular pressing and cold drawing. *Materials Physics and Mechanics*. 2024;52(3): 58–72.

http://dx.doi.org/10.18149/MPM.5232024 6

Introduction

The development of the industrial and technical complex requires new materials, while traditionally used aluminum alloys are close to exhausting the resource for further improving their characteristics [1]. Nevertheless, aluminum remains, due to its availability and a combination of attractive properties, one of the most popular materials, and the task of modern metal science is to find new ways of producing and processing aluminum alloys [2,3].

¹ Ufa University of Science and Technology, Ufa, Russia

² Siberian Federal University, Krasnoyarsk, Russia

³ Saint-Petersburg State University, Saint-Petersburg

Improvement of mechanical performance of aluminum alloys can be achieved in several ways - by alloying, by thermal and deformation treatment, as well as by modification of casting methods [4–6]. However, with almost any method of increasing the strength of aluminum alloys, their electrical conductivity is inevitably lost [5–7]. This is due to the fact that the same structural mechanisms that lead to increased strength (increased dislocation density, increased density of grain boundaries, the presence of strengthening particles, the presence of a solid solution of alloying elements in aluminum) simultaneously negatively affect electrical conductivity. An important point is that the absolute values of the contributions of the above mechanisms are different, and by selecting them in a special way, it is possible to ensure an increase in mechanical strength without a significant loss of electrical conductivity [8].

In this regard, the creation of low-alloyed alloys is of particular importance, since the influence of alloying elements on the structures is more significant, the higher the concentration of these elements [9,10]. Maximum reduction in the concentration of alloying elements and a competent approach to structural mechanisms can provide the required level of physical and mechanical properties.

Relatively recently, alloys of the Al-Fe system have gained a significant interest [11]. New methods for producing these alloys, as well as their maximum availability due to the low cost of components, have led to the fact that their use is permitted as materials for household electrical wiring [12,13]. In addition to being cheap, such materials are also subject to requirements for mechanical strength, electrical conductivity, and thermal stability. This set of properties is achievable by creating certain structures in the material, namely, a relatively small grain size, the presence of strengthening intermetallic particles and the absence of a solid solution. Alloys of this system are also attractive because the solubility of iron in aluminum at room temperature is no more than 0.005 wt. %, which transforms these alloys into the category of an alloy with no solubility of alloying elements in the solid state, which means that the contribution of the solid solution to the increase in electrical resistance will be minimal or equal to zero [14].

In addition to Al-Fe alloys, the advancement of this system with the addition of copper is also of interest. Al-Fe alloys are already quite well studied, which prompts the search for new materials and combinations of alloying elements. Copper additions have a positive effect on the strength of alloys without significantly affecting their electrical conductivity. Copper, unlike iron, forms a solid solution with aluminum, which allows a more flexible approach to the issue of heat treatment and decomposition of the solid solution/formation of intermetallic precipitates [15,16].

In addition to the selected chemical composition, the structure of the material in its initial state also plays an important role. If the cast billet is subsequently subjected to deformation processing, then to obtain a relatively small average grain size in the original billet, conditions must be created for this [17]. In addition, the initial workpiece should not contain large gradients in the chemical composition and inhomogeneities in the distribution of structural elements, since such features may not be eliminated by deformation treatment and remain in the final product.

A relatively new method for producing aluminum alloys is casting in an electromagnetic crystallizer [18,19]. The main advantage of this method is the high (10^3-10^4K/s) cooling rate of the melt, which ensures nonequilibrium crystallization

conditions. In addition, the method itself makes it possible to obtain a workpiece that is uniform in chemical composition and size and distribution of structural elements. Thus, it becomes possible to form highly dispersed particles of the second phases and a supersaturated solid solution already in cast workpieces, homogeneously distributed in the aluminum matrix [20].

The third way to obtain outstanding properties is the currently widely known methods of severe plastic deformation [21,22]. Techniques such as high-pressure torsion [23], equal-channel angular pressing [24,25] and their variations make it possible to achieve large degrees of deformation in materials and obtain nonequilibrium structures (minimum grain size, supersaturated solid solution), which would be impossible to obtain using classical methods. Such alloy microstructures, in combination with subsequent heat treatment, make it possible to realize the best balance of physical and mechanical properties in semifinished products and products [26,27].

In the previous study, authors have stablished that combined deformation treatment including SPD methods positively affects the mechanical properties of the Al-Fe-Cu system alloys [28]. Particularly, stripes of the Al-0.5Fe-0.3Cu produced by EMC and subjected to the ECAP with the subsequent cold rolling demonstrated formed UFG microstructure providing the UTS of 300 MPa along with the electrical conductivity of the 56 % IACS. Since the form of a wire is preferable for the materials in the electrical industry, the combination of the ECAP and cold drawing was studied in the current work.

In this work, three approaches are used to create a conductive aluminum alloy with unique properties. The workpieces of economically alloyed Al-0.5Fe-0.3Cu alloy (wt. %) obtained by frontier technique of casting in an electromagnetic crystallizer were subjected to two-stage deformation processing, including equal-channel angular pressing and cold drawing. Samples of wire with a diameter of 3 mm obtained by this treatment were subjected to annealing at 230 °C for 1 hour to test its thermal stability. The physical and mechanical properties of the wire samples produced in this work are compared with the properties of conductive wires made from commercial alloys for electrical purposes, as well as from Al-Fe system alloys produced by casting in EMC, which do not contain copper.

Materials and Methods

In order to study the effect of electromagnetic casting and subsequent deformation treatment the experimental Al-0.5Fe-0.3Cu wt. % alloy was produced. Its samples in the form of thin rods of a diameter of 10 mm were obtained by continuous casting in an electromagnetic mold. The chemical composition of the alloy samples is presented in Table 1. In terms of the content of alloying elements and impurities, it is close to the AA8030 alloy [29], widely used in electrical engineering. Conventionally, wire rod of such alloys is produced by the method of continuous casting and rolling (CCR) [30].

Table 1. Chemical composition of alloys of the Al-Fe system (wt. %)

Alloy	Cu	Fe	Si	Σ (Mn, Cr, Zn)	Al
Al-0.5Fe-0.3Cu	0.30	0.50	0.02	< 0.01	Res.
AA8030 [29]	0.15 - 0.20	0.35 - 0.45	0.07	< 0.03	Res.

Samples of wire rod of the Al-Fe-Cu alloy were made on the basis of primary aluminum grade A85 (not less than 99.85 wt. % Al), copper grade M00k (not less than 99.9 wt. % Cu), as well as Fe80Al20 alloy in proportions selected to match the required Fe and Cu concentrations. After the melt temperature reached more than 800 °C, continuous casting was carried out in an EMC installation at a speed of 12.4 mm/s.

Some of the obtained wire rod samples were subjected to two-stage deformation treatment, including SPD by equal-channel angular pressing (ECAP) and subsequent cold drawing (CD), and the other part was subjected to deformation only by cold drawing.

Using an ARTA-120 wire-cutting machine, square samples measuring $10 \times 10 \times 100$ mm were made from cast semifinished products and subjected to two-stage deformation processing.

At the first stage, the samples were deformed using the ECAP method in equipment with a channel coupling angle of 120° , in the B_C mode, at room temperature. The number of processing cycles was 4. Similar processing conditions are used to form the UFG structure in low-alloy aluminum alloys [31–33]. As a result of SPD processing, samples with a cross-section of 10×10 mm and a length of up to 80 mm were obtained.

At the second stage, the samples were subjected to cold deformation on a laboratory drawing machine with a draw ratio of 13.5 (relative compression \sim 75 %). As a result of CD, wire samples with a diameter of 3 mm were obtained. Samples of the original wire rod were also subjected to CD using similar conditions.

The heat resistance of wire samples was assessed in accordance with the requirements of the IEC 62641:2023 standard [34]. To do this, after cold treatment, some of the samples were annealed at a temperature of 230 °C for 1 hour, followed by cooling in air. Annealing was carried out in a Nabertherm B180 furnace.

The microstructure was studied using scanning electron microscopy (SEM) on a Tescan Mira microscope at an accelerating voltage of 10-20 kV in back-scattered (BSE) and secondary electrons (SE) modes.

The microstructure was studied using transmission electron microscopy (TEM) on a JEOL JEM 2100 microscope at an accelerating voltage of 200 kV. Before the study, the samples were subjected to electropolishing by double-jet polishing of thin foils on a Struers Tenupol-5 unit using a solution of 20 % nitric acid and 80 % methanol. Polishing was carried out at a solution temperature of -20 °C and a voltage of 20 kV. The studies were carried out on three foils per condition to obtain statistically reliable data. Images were obtained in bright field (BF) and dark field (DF) modes.

To obtain statistically reliable results, tensile tests were carried out on three samples for each state, on a universal dynamometer Instron 5982 at room temperature and a strain rate of 10^{-3} s⁻¹ (for initial samples and after deformation by the ECAP method) in accordance with GOST 1487-94 and at a speed of 100 mm/min (for wire samples after cold drawing) in accordance with GOST 10446-80. Based on the test results, the values of the yield strength (σ_{YS}), ultimate tensile strength (σ_{UTS}) and elongation to failure (δ) were determined. Tensile test samples after ECAP had the dimensions of $1 \times 1 \times 4$ mm, after cold drawing – the shape of cylinders of 3 mm diameter and 100 mm length.

X-ray diffraction (XRD) analysis was conducted with a Bruker D2 Phaser diffractometer using $CuK\alpha$ radiation. Values of lattice parameter were calculated via the Rietveld refinement method using MAUD software [31].

Electrical conductivity (ω) was determined with an error of \pm 2 % by the eddy current method on samples after ECAP and by the four-point bridge method on samples after drawing [35]. The electrical conductivity relative to annealed copper (International Annealed Copper Standard, % IACS) was calculated using Eq. (1):

$$IACS = \frac{\omega_{Al}}{\omega_{Cu}} \times 100\% \tag{1}$$

where ω_{Al} is the measured electrical conductivity of the Al alloy, ω_{Cu} is the electrical conductivity of annealed chemically pure copper (58 MS/m).

Results and Discussion

Microstructural assessment

Figure 1 shows images of the microstructure of the Al-0.5Fe-0.3Cu alloy formed in the original wire rod after EMC casting. The dark gray phase is the aluminum matrix, the light phase is intermetallic particles. The structure is very similar to one observed before in Al-Fe [36], Al-La-Ce [17] and Al-Fe-Cu [28] system alloys produced by casting into electromagnetic mold.

The average size of a dendritic cell is $5.7 \pm 0.9 \, \mu m$. Based on the previous research it means that the crystallization rate was not less than 10^3 K\s [18]. It is known from the literature that in alloys of the Al-Fe system, during nonequilibrium crystallization, both metastable phases such as Al₂Fe and Al₆Fe and a stable phase Al₁₃Fe₄ can be formed [36–38]. However, the studied alloy also contains copper, which can form a solid solution in aluminum with a maximum equilibrium concentration at room temperature of about 0.3 wt. % and form double phases like Al₂Cu and/or ternary Al-Fe-Cu phases, the most prevalent of which is Al₇Cu₂Fe [39–41].

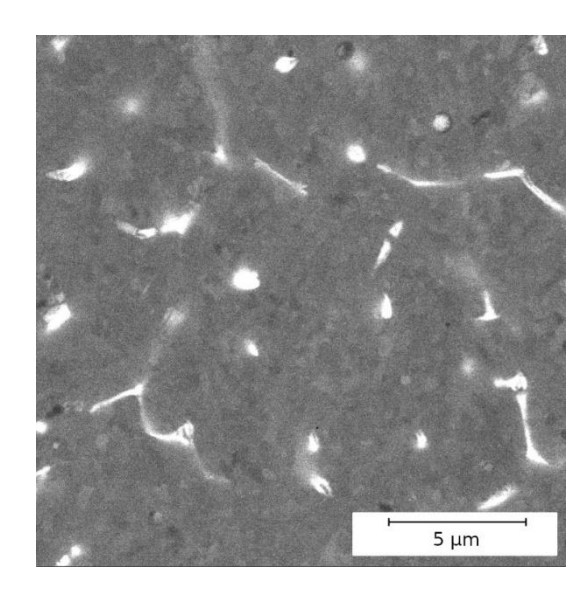


Fig. 1. Microstructure of the Al-0.5Fe-0.3Cu alloy in the initial state, SEM, BSE [41]

According to previous studies, almost all Fe is concentrated in intermetallic particles, which is expected, given its low solubility in aluminum [8,14]. Due to the high rate of crystallization of the alloy, part of the Cu is in the solid solution of aluminum and can also be part of some intermetallic particles [42].

Judging by the results of XRD analysis, which were previously carried out by authors on alloys of the Al-Fe system, obtained by a similar casting method [37,38], it can be assumed that the particles of the double phase of iron aluminide belong to the metastable Al₂Fe phase. While the lattice parameter of the Al-0.5Fe alloy practically does not change due to ECAP (from 4.0507±0.0001 Å to 4.0503±0.0001 Å) [37], the lattice parameter of the Al-0.5Fe-0.3Cu alloy due to ECAP decreases from 4.0522 ± 0.0001 to 4.0498 ± 0.0001 Å. The data obtained indicate the retention of a solid solution of copper in aluminum in the alloy after casting in the EMC, as well as the presence in the composition, in addition to the double phase of iron aluminide, of a ternary phase, presumably Al₇Cu₂Fe [43]. Copper, when dissolved in a solid solution of aluminum, reduces its lattice parameter, which can be seen in the material under study. According to literature data [8,14], the maximum concentration of a solid solution of copper in aluminum at room temperature is about 0.3 wt. %, so theoretically all the copper could dissolve in aluminum. According to the literature data, the ECAP has a rather weak effect on the formation of a solid solution, so it could be safely assumed that not all copper is dissolved in the solid solution after ECAP [44].

Figure 2 shows the microstructure of a sample of the Al-0.5Fe-0.3Cu alloy after deformation by ECAP. The intermetallic network formed by the plates of intermetallic phases is deformed and becomes curved due to deformation and loses its continuity. Fragmentation of intermetallic particles also occurs. The average grain/structural element size is 1350 ± 70 nm in length and 700 ± 40 nm in width, the average size of intermetallic particles is 650 ± 50 nm. Despite the fact that ECAP belongs to SPD methods, it usually does not lead to phase transformations in aluminum alloys of this or similar alloying systems [31,45], suggesting their absence in this case. Figure 2(b) shows black voids in the middle of intermetallic particles. This could be attributed either to fragmentation of the particles during the ECAP and formation of the micropores (similar effect was observed in [46]), or to the effect of the particles "falling out" from the sample during the electropolishing. Since this effect was previously observed on samples prepared by mechanical polishing, authors are inclined to the state that these voids are the result of the deformation of the relatively soft aluminium matrix by the fragmented intermetallic particles.

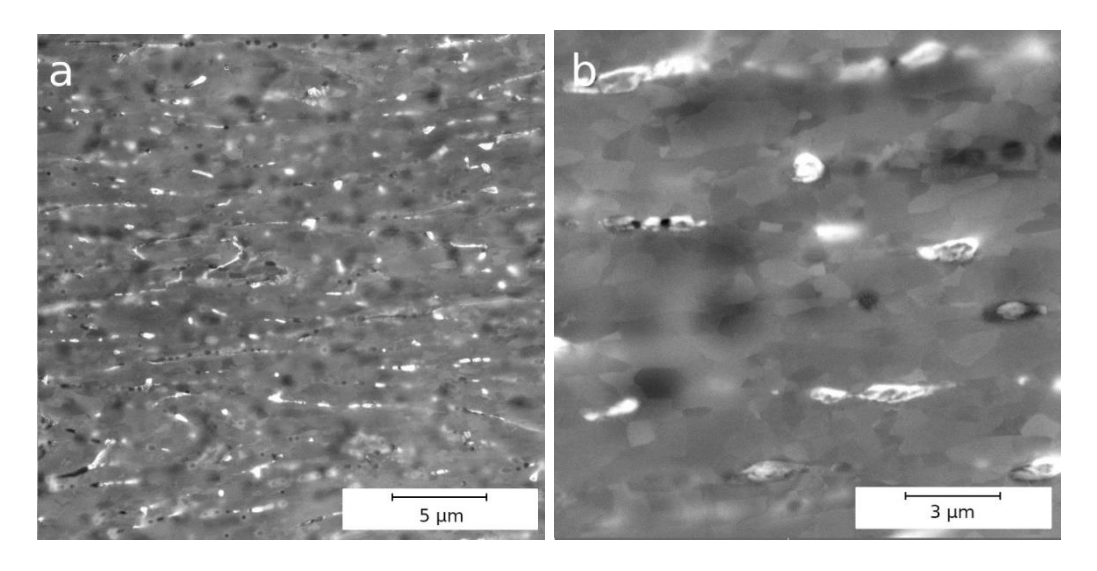


Fig. 2. Microstructure of the Al-0.5Fe-0.3Cu alloy in the state after ECAP: (a) 2kx, (b) 5kx, SEM, BSE

After ECAP, the consequent deformation treatment of the alloy in the form of cold drawing took place. Figure 3 shows the microstructure of the Al-0.5Fe-0.3Cu alloy after combined ECAP and CD. The material in this state was successively subjected to deformation with tangential (ECAP) and normal (CD) stresses, affecting its microstructure. Both grains and intermetallic particles experience the fragmentation during CD. Thus, according to SEM data, the average size of intermetallic particles after ECAP and CD in decreased to 380 ± 45 nm, the average grain width - to 350 ± 15 nm with the simultaneous average grain length increase up to 2850 ± 290 nm. The decrease in size of the major structural features, such as average grain size and average particle size, was facilitated by both the deformation accumulated during ECAP and the preliminary fragmentation of intermetallic particles and their denser distribution in the volume of the material.

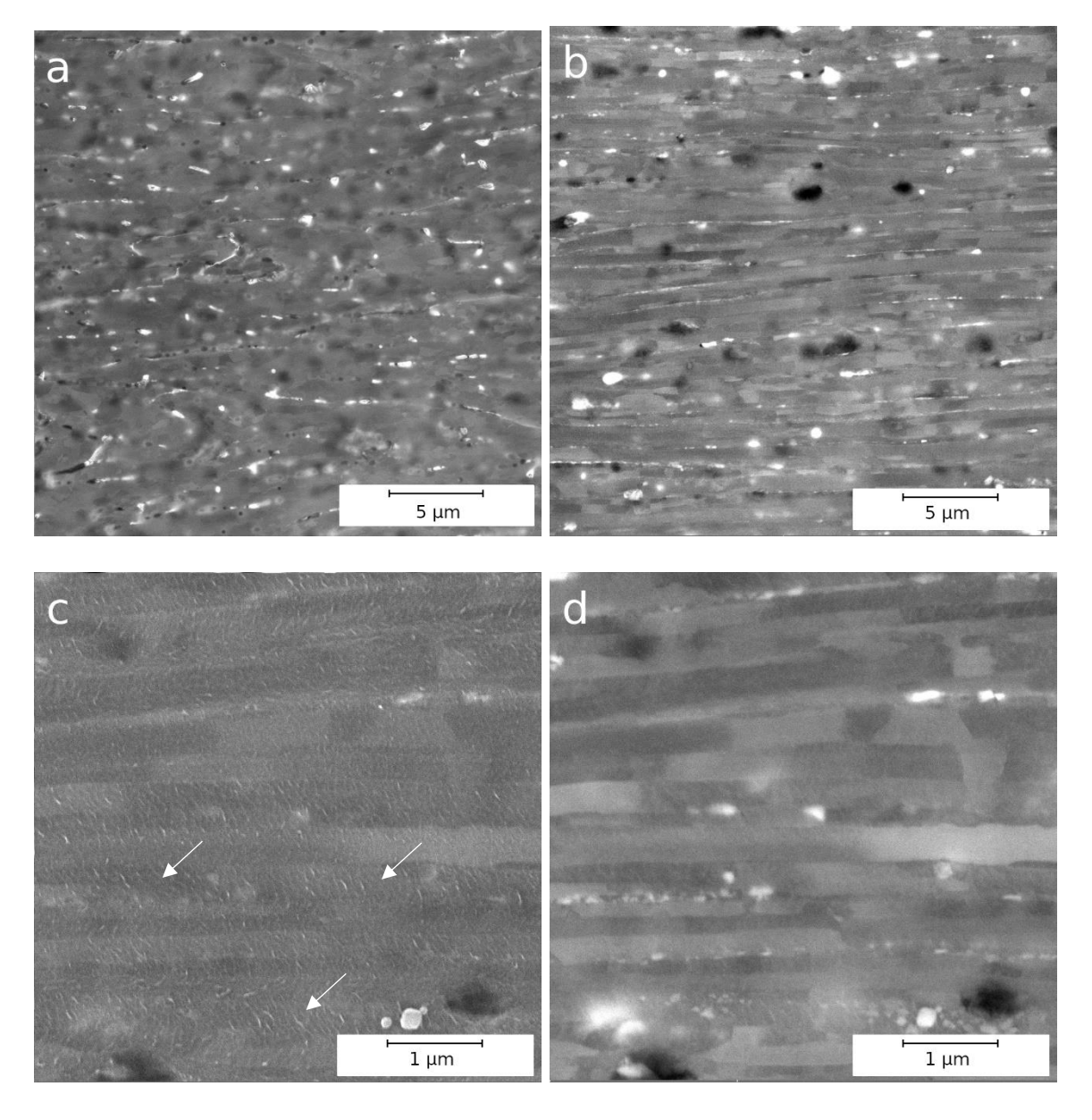


Fig. 3. Microstructure of the Al-0.5Fe-0.3Cu alloy after ECAP+CD, obtained in different SEM modes: (a,c) backscattered electrons, 2kx, (b,d) secondary electrons, 10kx. Secondary electrons mode allows to highlight the surface relief of the sample. White arrows indicate the deformation bands

Another effect introduced by the combined ECAP+CD treatment is a characteristic relief on the surface of samples for microscopy. It consists of the presence of bright stripes located within the grain boundaries and oriented at an angle of 45° relative to the direction of deformation (Fig. 3(c)). These structural elements are visible only in secondary electrons and are not visible in back-scattered electrons, from which two conclusions can be drawn: first, these bands are not particles of a different phase relative to the grains, and second, they appear on the surface of the sample. Most likely, these are shear bands formed during the localization of deformation in the aluminum matrix as a result of combined deformation treatment according to schemes that implement shear (ECAP) and normal (CD) deformation [25].

Figure 4 shows the microstructure of the Al-0.5Fe-0.3Cu alloy after cold drawing. The structure is qualitatively similar to that observed in the ECAP+CD state (Fig. 3).

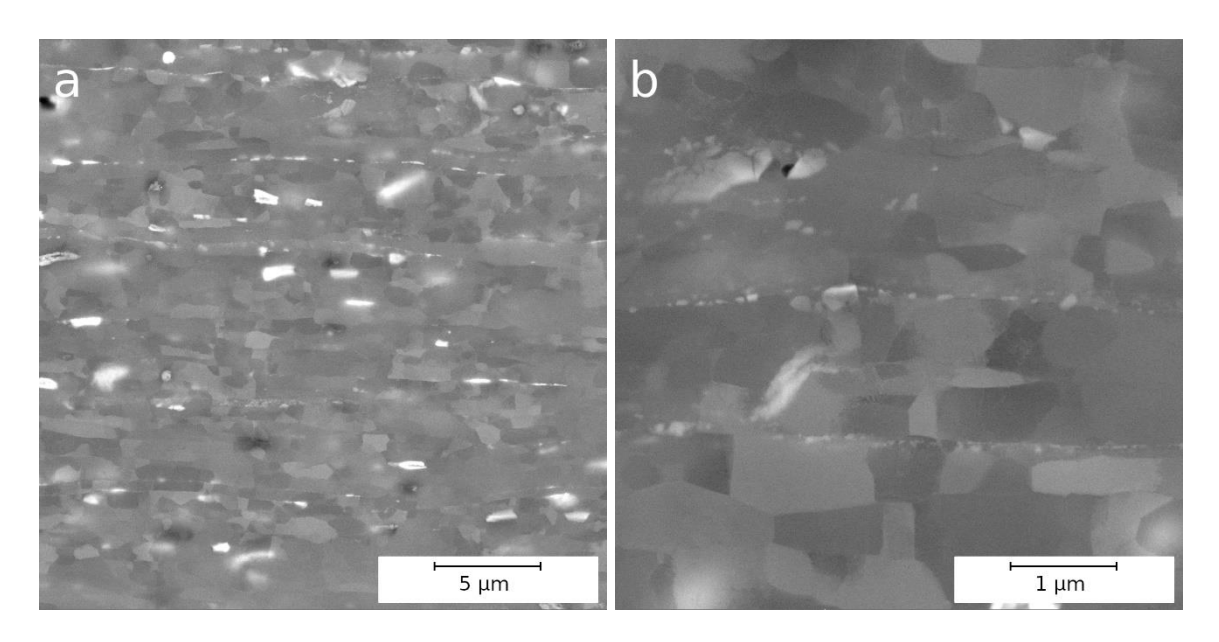


Fig. 4. Microstructure of the Al-0.5Fe-0.3Cu alloy after CD: (a) 2kx, (b) 10kx, BSE, SEM

The arrangement of layers of intermetallic particles along the grain boundaries is noticeably less dense than after ECAP +CD (Fig. 3). This effect is facilitated by the absence of the preliminary fragmentation of clusters of intermetallic particles during ECAP (like in the case of ECAP+CD), providing fewer barriers for the grain boundary migration and resulting in wider grain - due to CD of the materials in the initial state the grains acquired an elongated shape with an average length of 2750 ± 400 nm and an average width of 650 ± 20 nm, while grains after ECAP, having roughly the same length, are about 2 times narrower. The fragmentation of the intermetallic particles occurs during the CD, resulting in the formation of the linear particles clusters oriented in the direction of deformation (Fig. 4(b)). The average size of intermetallic particles in CD state is 390 ± 80 nm.

It should also be noted that the segregations/clusters of intermetallic particles, although they acted as barriers to the migration of grain boundaries, were not the only obstacle to their migration - the grain boundaries of the aluminum matrix also line up in lines parallel to the direction of deformation (Fig. 4(b)).

The abovementioned observations are confirmed by the TEM results. Figure 5 shows the microstructure of the Al-0.5Fe-0.3Cu alloy after cold drawing in longitudinal (Fig. 5(a,b)) and cross-sections (Fig. 5(c,d)). Images of a longitudinal section show segregations of intermetallic particles along grain boundaries elongated in the direction of deformation. These segregations act as obstacles to the migration of grain boundaries. Segregation of particles along grain boundaries are also observed in the cross-section.

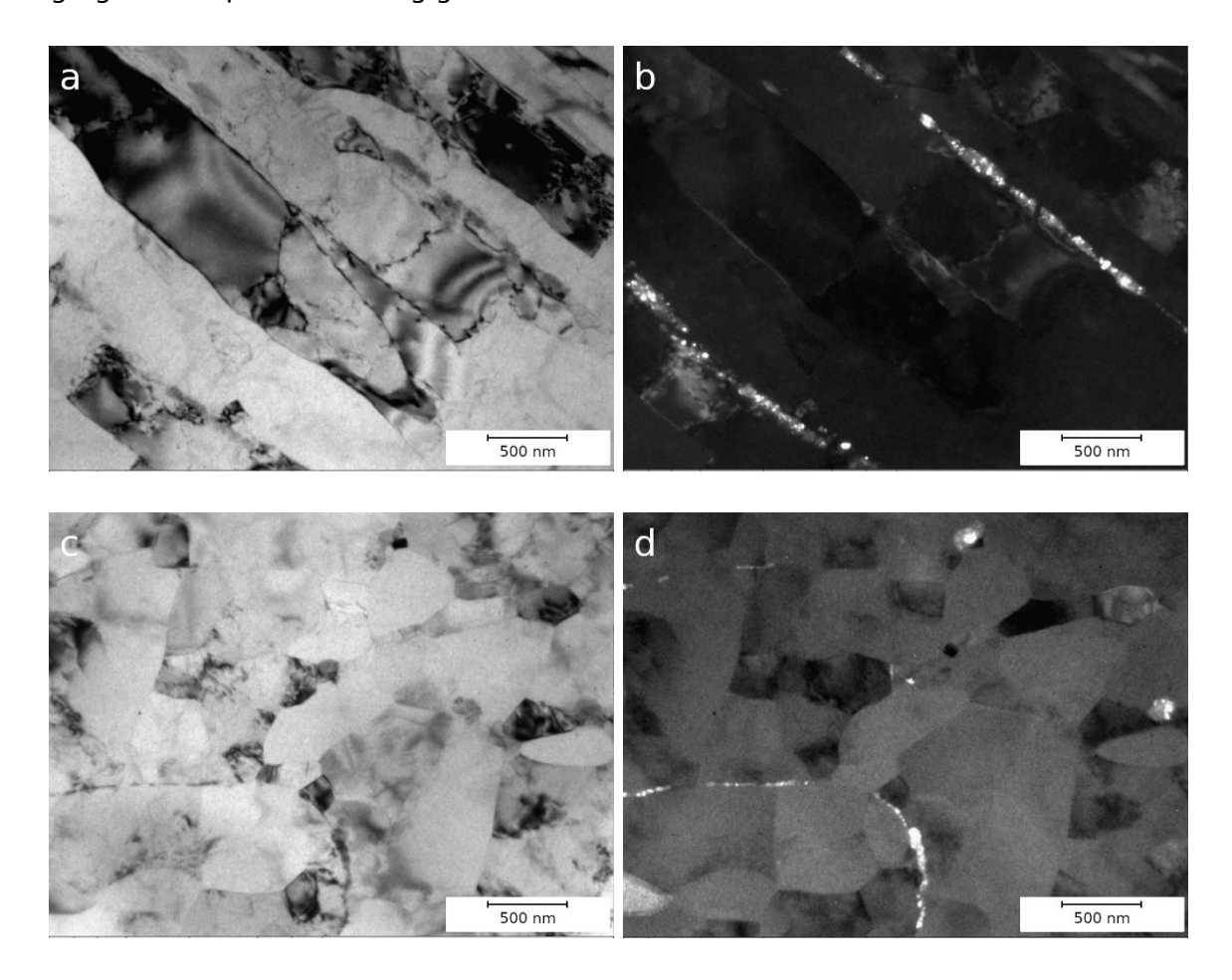


Fig. 5. Microstructure of Al-0.5Fe-0.3Cu alloy in cold drawing state, longitudinal ((a) - BF, (b) - DF) and cross section ((c) - BF, (d) - DF), TEM

Overall, the implementation of the ECAP before the CD results in the qualitatively and quantitively different microstructure in comparison to the single CD treatment. ECAP+CD provides narrower grain with more even distribution of the intermetallic particles within the material, although the size of the particle remains the same.

According to previously published studies, the smaller grain should provide the higher level of the yield stress since it shortens the free path of the dislocations [26]. Rough estimation of the grain size impact on the mechanical strength of the material shows that ECAP + CD state should have 25 MPa higher yield stress than CD state, which is confirmed, considering the error value, in the Table 2.

Physical and mechanical properties of Al-0.5Fe-0.3Cu alloy

The mechanical properties and electrical conductivity of the Al-0.5Fe-0.3Cu alloy are presented in Table 2. According to the data given below, in the initial state the Al-0.5Fe-0.3Cu alloy is characterized by low strength indicators (ultimate strength 106 MPa) with a fairly high level of electrical conductivity (about 56%IACS) and elongation to failure (about 34 %).

Table 2. Physical and mechanical properties of the Al-0.5Fe-0.3Cu alloy

State	Electrical properties	Mec	Mechanical properties		
	IACS, %	σ_{YS} , MPa	$\sigma_{ t UTS}$, MPa	δ, %	
Before and after ECAP					
Initial (cast)	56.1±0.4	72.0±8.0	106.0±4.0	33.7±6.5	
ECAP	54.8±0.2	181.0±12.0	214.0±15.0	13.7±2.8	
ECAP+CD	55.5±0.3	234.0±19.0	342.0±6.0	2.7±0.5	
CD	55.8±0.4	230.0±7.0	260.0±5.0	2.5±0.2	
After CD and annealing at 230°C for 1h					
ECAP+CD+230 °C	58.5±0.3	146.0±16.0	163.0±15.0	7.2±3.7	
CD+230 °C	58.0±0.1	174.0±3.0	200.0±3.0	3.2±0.3	
Wire made from Al-0.5Fe and 6101 Al-Mg-Si alloys					
8000 series alloys [29]	60.6	-	103.0-152.0	-	
Al-0.5Fe EMC + CD [37]	58.4	170.0±12.0	204.0±14.0	5.3±0.2	
Al-0.5Fe EMC + CD+230°C [37]	59.2	175.0±11.0	200.0±16.0	4.0±0.4	
6000 series alloys [47]	57.4-52.5	-	245.0-342.0	3.0-3.5	
6101 ECAP-C +AA+CD [31]	56.4	-	364.0	3.5	
Stripes					
Al-0.5Fe-0.3Cu EMC + ECAP + Cold rolling [28]	55.9±0.7	267.0±6.0	309.0±4.0	13.8±0.9	

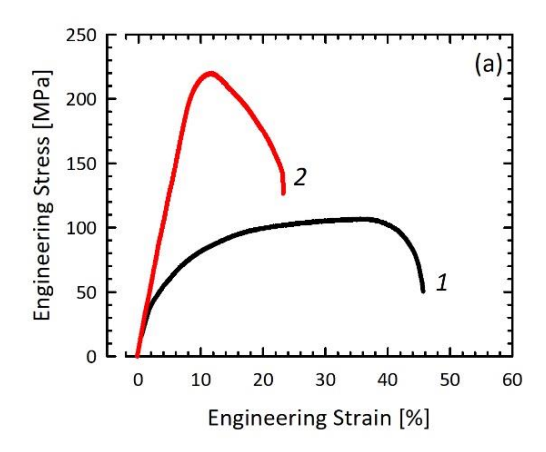
In case of the studied materials, ECAP generally leads to a lower level of structural defects than cold drawing resulting in a lower level of ultimate tensile strength (214 MPa). The electrical conductivity value, however, is higher in the cold-drawn state, which can be explained by the possible formation of a solid solution of copper in aluminum during ECAP due to the diffusion of copper into the aluminum matrix under the influence of large stress fields and shear deformation. As a result of the combined processing of ECAP + CD, a wire was obtained that is characterized by a high (as after drawing) level of electrical conductivity and a significantly increased (even more than after ECAP) level of tensile strength. The relative elongation to failure, however, is at the level of the wire after cold drawing and is very small (Table 2).

Table 2 also shows the strength and electrical conductivity values of some commercial alloys for comparison. Thus, wire from the Al-0.5Fe-0.3Cu alloy after combined ECAP + CD treatment in terms of strength and electrical conductivity is at the level of heat-resistant wire made from 6101 alloy by the same deformation scheme,

making it affordable alternative to the Al-Mg-Si alloys. Commercially produced wires from 6000 and 8000 series alloys, as well as wires made from electromagnetically cast Al-0.5Fe alloy, while having slightly higher level of electrical conductivity, demonstrate notably (about 1.5 times) lower mechanical strength compared to the wires produced from electromagnetically cast Al-0.5Fe-0.3Cu alloy with use of ECAP+CD.

Alloys made from these systems are subject to thermal stability requirements. Thermal stability is tested by annealing at 230 °C for 1 hour, which is equivalent to operating at 150 °C for 40 years [34].

Engineering stress-strain curves of the alloy in deformed states and after annealing are presented in Fig. 6. It would be fair to say that every studied state has ductile character of the deformation and failure. This is surprising considering that the presence of the Cu in aluminium alloy may result in the embrittlement of the latter.



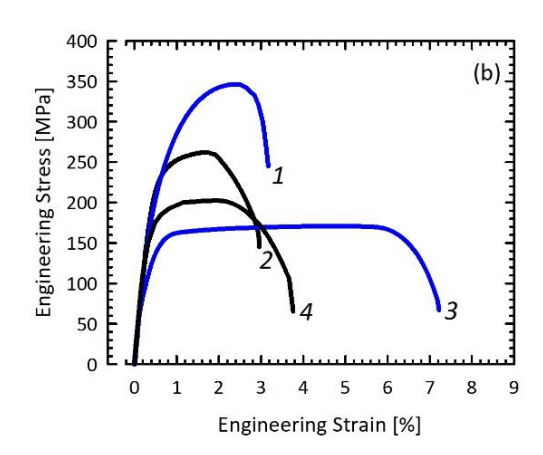


Fig. 6. Engineering stress-strain curves of alloy samples in the EMC and ECAP states (a): 1 – EMC, 2 – ECAP; as well as samples in the form of a wires (b): 1 – ECAP+CD, 2 – CD, 3 – ECAP+CD+230°C, 4 – CD+230°C

The mechanical properties and electrical conductivity of the alloy after annealing at 230 °C for 1 hour are also presented in Table 2. Annealing leads to softening of alloys both after cold drawing and after a combination of equal-channel angular pressing and cold drawing [48]. The drop in the level of ultimate strength in the alloy after drawing was 23 %, in the alloy after combined processing – 52 %. None of these states can be considered thermally stable, since the drop of the UTS was more than 10 %. As for absolute values, the alloy after combined processing softened significantly more than after drawing. At the same time, there was an increase in the relative elongation to failure and electrical conductivity. Similar processes occurred in the alloy after cold drawing, but the decrease in strength and increase in ductility are much less pronounced. The electrical conductivity in both states is comparable and amounts to 58–58.5 % IACS, exceeding the electrical conductivity of the starting material.

Conclusions

In this work, a two-stage deformation treatment was carried out, including equal-channel angular pressing and cold drawing, of an Al-0.5Fe-0.3Cu alloy produced by casting in an electromagnetic crystallizer. During the work, the following conclusions were drawn:

- 1. The method of casting in an electromagnetic crystallizer makes it possible to form the microstructure of the alloy at a high crystallization rate. The resulting microstructure is characteristic of aluminum alloys with limited solubility of components in the solid state after casting in an EMC.
- 2. During the ECAP a solid solution of copper in aluminum is formed. Iron is bound in intermetallic Al_2Fe , Al_6Fe and $Al_{13}Fe_4$ phases. Copper atoms are also bound in either double (Al_2Cu) or triple (Al_7Cu_2Fe) intermetallic phases.
- 3. The combined treatment of ECAP + CD leads to the formation of a structure in the Al-0.5Fe-0.3Cu alloy that is different from one formed as a result of CD. The main difference is the decreased grain width and the presence of the shear bands within them in the ECAP+CD state. This structural difference resulted in the 25 % increased UTS of the wire in the ECAP+CD state relative to the CD sate with the similar values of the electrical conductivity and elongation to failure.
- 4. The strength level of wire made from the Al-0.5Fe-0.3Cu alloy after ECAP + CD exceeds that of thermally resistant alloys of the 6000 and 8000 series, as well as the Al-0.5Fe alloy produced by casting in an electromagnetic crystallizer. As a result of the combined ECAP + CD processing, a tensile strength level of 342 MPa and an electrical conductivity level of 55.5 % IACS are achieved, which is comparable to the similar characteristics of the commercial alloy 6101 subjected to ECAP-Conform processing followed by cold drawing.
- 5. According to the standards for conductive wires made of aluminum alloys, wire made of Al-0.5Fe-0.3Cu alloy after heat treatment and ECAP + CD cannot be considered thermally stable, since the loss of strength after heat treatment is more than 10 % in both cases. However, after annealing equivalent to operating at 150 °C for 40 years, both wires have an electrical conductivity of at least 58 % IACS and a strength of at least 160 MPa.

References

- 1. Polmear I, StJohn D, Nie JF, Qian M. Light Alloys: Metallurgy of the Light Metals. 5th ed. Elsevier; 2017.
- 2. Jawalkar CS, Kant S. A Review on use of Aluminium Alloys in Aircraft Components. *I-Manager's Journal on Material Science*. 2015;3(3): 33–38.
- 3. Verma RP, Kumar Lila M. A short review on aluminium alloys and welding in structural applications. *Mater. Today Proc.* 2021;46: 10687–10691.
- 4. Jini Raj R, Panneer Selvam P, Pughalendi M. A Review of Aluminum Alloys in Aircraft and Aerospace Industry Aerodynamic. *Journal of Huazhong University of Science and Technology*. 2021;50(4): 4512.
- 5. Liu CH, Chen J, Lai YX, Zhu DH, Gu Y, Chen JH. Enhancing electrical conductivity and strength in Al alloys by modification of conventional thermo-mechanical process. *Mater. Des.* 2015;87: 1–5.
- 6. Lin G, Zhang Z, Wang H, Zhou K, Wei Y. Enhanced strength and electrical conductivity of Al-Mg-Si alloy by thermo-mechanical treatment. *Materials Science and Engineering A*. 2016;650: 210–217.
- 7. Yang Y, Nie J, Mao Q, Zhao Y. Improving the combination of electrical conductivity and tensile strength of Al 1070 by rotary swaging deformation. *Results in Physics*. 2019;13: 102236.
- 8. Mondolfo LF. Aluminum Alloys Structure and Properties. Elsevier; 1976.

Crystallizer. *Physics of Metals and Metallography*. 2020;121: 173–179.

- 9. Deng Z, He H, Liu K, Tao X, Shang Z, Gong Z, Wang X. The influence of natural aging on the precipitation behavior of the low-alloy content Al-Zn-Mg aluminum alloys during subsequent artificial aging and related mechanisms. *Materials Science and Engineering: A.* 2024;891: 145954.
- 10. Deng P, Mo W, Ouyang Z, Ling K, Luo B, Bai Z. Microstructural evolution and corrosion mechanism of micro-alloyed 2024 (Zr, Sc, Ag) aluminum alloys. *Corros Sci.* 2023;224: 111476.
- 11. Jiang H, Li S, Zhang L, He J, Zheng Q, Song Y, Li Y, Zhao J. The influence of rare earth element lanthanum on the microstructures and properties of as-cast 8176 (Al-0.5Fe) aluminum alloy. *J. Alloys Compd.* 2021;859: 157804.
- 12. Fadeeva VI, Leonov AV, Khodina LN. Metastable phases in mechanically alloyed Al-Fe system. *Materials Science Forum.* 1995;179–181: 397–402.
- 13. Sasaki TT, Ohkubo T, Hono K. Microstructure and mechanical properties of bulk nanocrystalline Al-Fe alloy processed by mechanical alloying and spark plasma sintering. *Acta Mater.* 2009;57: 3529–3538.
- 14. Mondolfo LF, Zmeskal O. Engineering metallurgy. New York: McGraw-Hill Book Co., Inc.; 1955.
- 15. Chen P, Fan X, Yang Q, Zhang Z, Jia Z, Liu Q. Creep behavior and microstructural evolution of 8030 aluminum alloys compressed at intermediate temperature. *Journal of Materials Research and Technology*. 2021;12:1755–1761.
- 16. Jiang X, Zhang Y, Yi D, Wang H, Deng X, Wang B. Low-temperature creep behavior and microstructural evolution of 8030 aluminum cables. *Mater. Charact.* 2017;130: 181–187.
- 17. Mogucheva AA, Zyabkin DV, Kaibyshev RO. Effect of annealing on the structure and properties of aluminum alloy Al 8% MM. *Met. Sci Heat Treat*. 2012;53: 450–454.
- 18. Belov N, Murashkin M, Korotkova N, Akopyan T, Timofeev V. Structure and properties of Al-0.6 Wt.%Zr wire alloy manufactured by direct drawing of electromagnetically cast wire rod. *Metals*. 2020;10(6): 769.
- 19. Belov N, Akopyan T, Korotkova N, Murashkin M, Timofeev V, Fortuna A. Structure and properties of ca and zr containing heat resistant wire aluminum alloy manufactured by electromagnetic casting. *Metals*. 2021;11(2): 236. 20. Korotkova NO, Belov NA, Timofeev VN, Motkov MM, Cherkasov SO. Influence of Heat Treatment on the Structure and Properties of an Al–7% REM Conductive Aluminum Alloy Casted in an Electromagnetic
- 21. Kvackaj T, Bidulska J, Fujda M, Kocisko R, Pokorny I, Milkovic O. Nanostructure formation and properties in some Al alloys after SPD and heat treatment. Materials Science Forum 2010;633–634: 273–302. https://doi.org/10.4028/www.scientific.net/MSF.633-634.273
- 22. Wawer K, Lewandowska M, Kurzydlowski KJ. Improvement of mechanical properties of 7475 aluminium alloy by the combination of SPD processing and annealing. *Materials Science Forum*. 2011;690: 311–314.
- 23. Cubero-Sesin JM, In H, Arita M, Iwaoka H, Horita Z. High-pressure torsion for fabrication of high-strength and high-electrical conductivity Al micro-wires. *J. Mater Sci.* 2014;49: 6550–6557.
- 24. Xu C, Schroeder S, Berbon PB, Langdon TG. Principles of ECAP-Conform as a continuous process for achieving grain refinement: Application to an aluminum alloy. *Acta Mater*. 2010;58: 1379–1386.
- 25. Raab GJ, Valiev RZ, Lowe TC, Zhu YT. Continuous processing of ultrafine grained Al by ECAP-Conform. *Materials Science and Engineering A.* 2004;382(1–2): 30–34.
- 26. Valiev RZ, Murashkin M, Sabirov I. A nanostructural design to produce high-strength Al alloys with enhanced electrical conductivity. *Scr. Mater.* 2014;76: 13–16.
- 27. Sabirov I, Murashkin MY, Valiev RZ. Nanostructured aluminium alloys produced by severe plastic deformation: New horizons in development. *Materials Science and Engineering A*. 2013;560: 1–24.
- 28. Medvedev AE, Zhukova OO, Kazykhanov VU, Shaikhulova AF, Motkov MM, Timofeev VN, Enikeev NA, Murashkin MYu. Influence of Cu alloying on the microstructure and properties of the Al-Fe alloy, produced by electromagnetic casting and subjected to equal-channel angular pressing. To be published in *Physics of Metals and Metallography*. [Preprint] 2024.
- 29. ASTM International. ASTM B800-05(2021). *Standard Specification for 8000 Series Aluminum Alloy Wire for Electrical Purposes—Annealed and Intermediate Tempers*. West Conshohocken, PA, USA: ASTM International; 2021.
- 30. Beliy DI. Aluminum alloys for conductors of cable products. *Cables and Wires*. 2012;332: 8–15. (In Russian)
- 31. Murashkin M, Medvedev A, Kazykhanov V, Krokhin A, Raab G, Enikeev N, Valiev RZ. Enhanced mechanical properties and electrical conductivity in ultrafine-grained Al 6101 alloy processed via ECAP-conform. *Metals*. 2015;5: 2148–2164.
- 32. Djavanroodi F, Ebrahimi M. Effect of die parameters and material properties in ECAP with parallel channels. *Materials Science and Engineering A*. 2010;527(29–30): 7593–7599.

- 33. Kawasaki M, Sklenička V, Langdon TG. An evaluation of creep behavior in ultrafine-grained aluminum alloys processed by ECAP. *J Mater Sci.* 2010;45: 271–274.
- 34. European Standard IEC 62641:2023. *Conductors for overhead lines Aluminium and aluminium alloy wires for concentric lay stranded conductors*. 2022.
- 35. International Standard IEC 60468:1974. Method of measurement of resistivity of metallic materials. 1974.
- 36. Medvedev A, Murashkin M, Enikeev N, Medvedev E, Sauvage X. Influence of morphology of intermetallic particles on the microstructure and properties evolution in severely deformed al-fe alloys. *Metals*. 2021;11(5): 815.
- 37. Medvedev AE, Zhukova OO, Fedotova DD, Murashkin MYu. The mechanical properties, electrical conductivity, and thermal stability of a wire made of Al–Fe alloys produced by casting into an electromagnetic crystallizer. *Frontier Materials & Technologies*. 2022;3: 96–105. (In Russian)
- 38. Medvedev A, Zhukova O, Enikeev N, Kazykhanov V, Timofeev V, Murashkin M. The Effect of Casting Technique and Severe Straining on the Microstructure, Electrical Conductivity, Mechanical Properties and Thermal Stability of the Al–1.7 wt.% Fe Alloy. *Materials*. 2023;16(8): 3067.
- 39. Fu X, Wang R, Zhu Q, Wang P, Zuo Y. Effect of annealing on the interface and mechanical properties of Cu-Al-Cu laminated composite prepared with cold rolling. *Materials*. 2020;13(2): 369.
- 40. Draissia M, Debili M-Y. Study of solid-solution hardening in binary aluminium-based alloys. *Central European Journal of Physics*. 2005;3: 395-408.
- 41. Kaloshkin SD, Tcherdyntsev VV, Danilov VD. Preparation of Al-Cu-Fe quasicrystalline powdered alloys and related materials by mechanical activation. *Crystallography Reports*. 2007;52: 953–965.
- 42. Selyutina NS. Influence of Mg and Cu on the dynamic yield stress of aluminium alloys. *Materials Physics and Mechanics*. 2021;47(3): 408–415.
- 43. Zhang X, Zhang H, Kong X, Fu D. Microstructure and properties of Al-0.70Fe-0.24Cu alloy conductor prepared by horizontal continuous casting and subsequent continuous extrusion forming. *Transactions of Nonferrous Metals Society of China*. 2015;25(6): 1763–1769.
- 44. Masuda T, Sauvage X, Hirosawa S, Horita Z. Achieving highly strengthened Al-Cu-Mg alloy by grain refinement and grain boundary segregation. *Materials Science and Engineering: A.* 2020;793: 139668.
- 45. Medvedev AE, Zhukova OO, Kazykhanov VU, Shaikhulova AF, Enikeev NA, Timofeev VN, et al. On the effect of ECAP and subsequent cold rolling on the microstructure and properties of electromagnetically cast Al–Fe alloys. *International Journal of Lightweight Materials and Manufacture*. 2022;5(4): 484–495.
- 46. Medvedev AE, Murashkin My, Enikeev NA, Bikmukhametov I, Valiev RZ, Hodgson PD, Lapovok R. Effect of the eutectic Al-(Ce,La) phase morphology on microstructure, mechanical properties, electrical conductivity and heat resistance of Al-4.5(Ce,La) alloy after SPD and subsequent annealing. *Journal of Alloys and Compounds*. 2019;796: 321-330.
- 47. European Standard EN 50183:2002. *Conductors for overhead lines Aluminium-magnesium-silicon alloy wires*. 2002. 48. Semenov BN, Smirnov IV, Sudenkov YV, Tatarinova NV. Effect of heat treatment on the mechanical properties of ultrafine-grained aluminium. *Materials Physics and Mechanics*. 2015;24(4): 319–324.

About Author

Andrey E. Medvedev D Sc

Candidate of Physical and Mathematical Sciences Senior Researcher (Ufa University of Science and Technology, Ufa, Russia)

Olga O. Zhukova Sc

Engineer (Ufa University of Science and Technology, Ufa, Russia)

Vil U. Kazykhanov Sc

Candidate of Technical Sciences Senior Researcher (Ufa University of Science and Technology, Ufa, Russia)

Aygul F. Shaikhulova D Sc

Candidate of Technical Sciences Lead Researcher (Ufa University of Science and Technology, Ufa, Russia)

Mikhail M. Motkov D Sc

Candidate of Technical Sciences Associate Professor (Siberian Federal University, Krasnoyarsk, Russia)

Viktor N. Timofeev Sc

Doctor of Physical and Mathematical Sciences Professor (Siberian Federal University, Krasnoyarsk, Russia)

Nariman A. Enikeev D Sc

Doctor of Physical and Mathematical Sciences Professor (Ufa University of Science and Technology, Ufa, Russia)

Maxim Yu. Murashkin D Sc

Candidate of Technical Sciences Senior Researcher (Ufa University of Science and Technology, Ufa, Russia) Submitted: June 4, 2024 Revised: June 20, 2024 Accepted: July 8, 2024

Outstanding ductility of high-strength ultrafine-grained aluminium at cryogenic temperatures

T.S. Orlova [™], ¹⁰ D.I. Sadykov, ¹⁰

loffe Institute, St. Petersburg, Russia

[™] orlova.t@mail.ioffe.ru

ABSTRACT

By decreasing the temperature of the tensile tests from 293 to 77 K, a drastic increase in ductility (elongation to failure \sim 40 % and uniform elongation \sim 25 %) was demonstrated for the first time, along with an increase in strength (yield stress \sim 235 MPa and ultimate tensile strength \sim 265 MPa) for ultrafine-grained aluminium structured by combination of equal-channel angular pressing and cold rolling with subsequent annealing. The increase in ductility at 77 K is accompanied by an increase in the strain hardening coefficient. The physical reasons for the significant increase in ductility at 77 K are discussed in comparison with the peculiarities of microstructure. The obtained combination of ductility and strength opens up prospects for the use of this material at cryogenic temperatures, as well as the application of cryogenic temperatures for the formation of its products of complex shapes.

KEYWORDS

aluminium • ultrafine-grained structure • ductility • strength • cryogenic temperatures

Citation: Orlova TS, Sadykov DI. Outstanding ductility of high-strength ultrafine-grained aluminium at cryogenic temperatures. *Materials Physics and Mechanics*. 2024;52(3): 73–79. http://dx.doi.org/10.18149/MPM.5232024_7

Introduction

Grain refinement by severe plastic deformation (SPD) methods is widely used to increase the strength of aluminium and its alloys [1-6]. As a result of such processing, an ultrafinegrained (UFG) structure is formed, with an average grain size usually ranging from 100 to 1000 nm, depending on the SPD method used, processing parameters, and the chemical composition of the specific alloy [1]. The most widely used SPD methods currently are equal-channel angular pressing (ECAP), high-pressure torsion (HPT), and accumulative roll bonding [1,3,7-9]. The formation of UFG structure leads to a significant (several times) increase in strength, however, ductility is significantly reduced [1,7,10]. The reduction in ductility greatly complicates the processing of such materials and, consequently, limits their industrial application. The traditional method for increasing ductility is a suitable annealing at specific temperatures and durations. However, the increase in ductility in this case is accompanied by grain growth and, consequently, leads to significant decrease in strength [11,12]. The thermal stability of UFG materials decreases with increase in their chemical purity and decrease in grain size, which leads to decrease in strength when using, for example, hot pressing for the manufacture of products from them. Previously, we suggested a new approach to achieve significant increase in ductility at room temperature (RT) while maintaining high strength of UFG Al (99.6 wt. %), structured by the HPT method [13]. This approach presents the use of a special deformation-heat treatment (DHT), consisting of low-temperature annealing and 74 T.S. Orlova, D.I. Sadykov

additional small HPT deformation at RT. As a result of such DHT, a good combination of strength (yield stress $\sigma_{0.2} \sim 130$ MPa and ultimate tensile strength $\sigma_{\rm UTS} \sim 180$ MPa) and ductility (elongation to failure $\delta \sim 34$ % and uniform elongation $\delta_1 \sim 19$ %) at RT was achieved for HPT Al [14]. As was shown, the increase in ductility of HPT Al after such DHT is due to increase in the degree of non-equilibrium of high-angle grain boundaries through their relaxation and subsequent introduction of additional density of extrinsic dislocations into them [15,16]. However, such DHT did not ensure high ductility in UFG Al, in which the UFG structure was formed by a combination of ECAP and cold rolling (CR) methods [17]. As a result of structuring aluminium by the combination of ECAP and CR methods with subsequent annealing at 150 °C for 1 h, remarkable strength ($\sigma_{0.2} \sim 182$ MPa, $\sigma_{\rm UTS} \sim 212$ MPa) was achieved and thermal stability of properties up to 150 °C, at least [17]. At the same time, δ was equal to ~ 9.6 %, and δ_1 was only ~ 1.2 %, indicating low formability of this material at RT.

In the present work, it has been shown that deformation at cryogenic temperatures (77 K) of samples structured by the combination of ECAP and CR methods followed by annealing (T = 150 °C, t = 1 h), provides a drastic increase in ductility accompanied by increase in strength. The achieved ductility, primarily uniform elongation, indicate the prospects of using Al structured in this way for products operating at low temperatures, as well as for deformation treatments of this material under cryogenic temperature conditions.

Materials and Methods

Commercially pure Al (A7E, 99.7 wt. % Al) was chosen for the study. The UFG structure was formed by combination of ECAP (4 passes, via route B_{c} , the angle between channels is 90°) and CR (total thickness reduction \sim 90 %), followed by annealing at T = 150 °C for 1 h (Al ECAP+CR+AN state). Mechanical properties were studied by uniaxial tensile tests using the blade-shaped samples with a gauge size of $2.0 \times 1.0 \times 6.0 \text{ mm}^3$ (the gauge length was oriented along the rolling direction). Tensile tests were carried out on a Shimadzu AG-50kNX testing machine with a constant strain rate of $5 \times 10^{-4} \, \text{s}^{-1}$ at RT, as well as in liquid nitrogen (at 77 K). At least three samples were tested for each state and temperature. The yield stress ($\sigma_{0.2}$), ultimate tensile strength (σ_{UTS}), elongation to failure (δ) and uniform elongation (δ_1) were determined from the obtained stress-strain curves. The microstructure of samples was studied by transmission electron microscopy (TEM) using a JEOL 2100 microscope at an accelerating voltage of 200 kV. TEM studies were carried out in the plane marked in red in Fig. 1(a), which is formed by the rolling direction (RD) and the direction normal to the rolling plane (ND). Analysis of the obtained microstructure images was carried out using ImageJ software. Samples for TEM studies were prepared by mechanical polishing followed by twin-jet electropolishing in solution of nitric acid (25 %) in methanol at -25 °C at an operating voltage of 25 V.

Results and Discussion

A typical TEM image of the microstructure is shown in Fig. 1(a). Based on a series of TEM images obtained, grain sizes were measured using ImageJ software. The size of each grain was determined by estimating the diameter of a circle equivalent in area to each individual grain. The grain size distribution obtained on the basis of ~ 100 grains is shown in Fig. 1(b). The average grain size is (d_G) ~ 665 nm. According to data obtained by electron backscatter diffraction, such structure contains predominantly (67 %) high-angle grain boundaries [17]. Despite the annealing at 150 °C, dislocations are clearly visible in some grains (Fig. 1(a)). According to X-ray diffraction analysis, the dislocation density in the Al_ECAP+CR+AN state is $\sim 1.6 \times 10^{12}$ m⁻² [17].

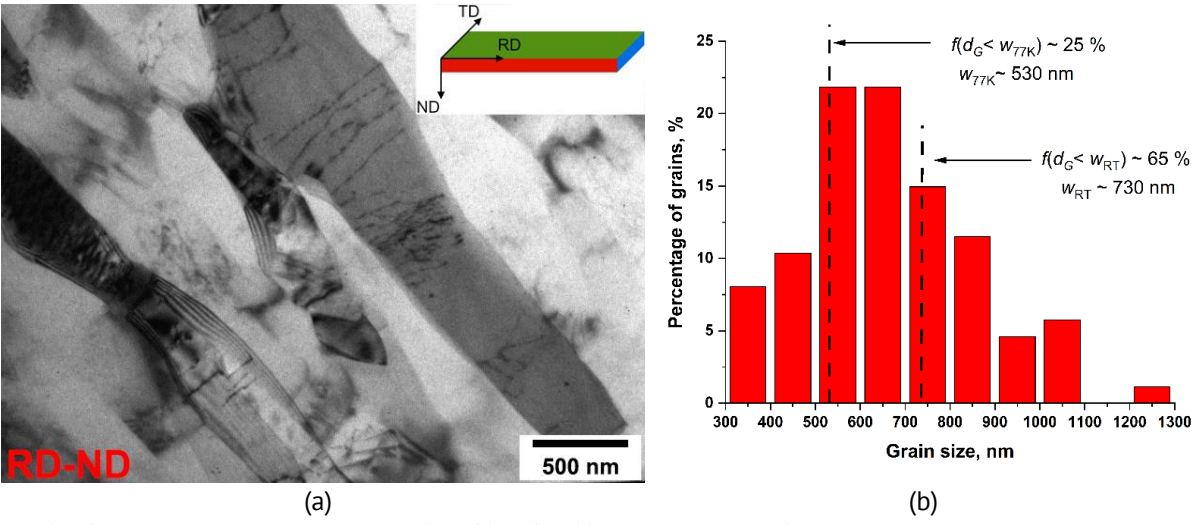


Fig. 1. (a) – typical TEM image of Al_ECAP+CR+AN samples in RD-ND plane with indication of the sample orientation relative to the rolling direction RD; ND and TD – normal and transverse directions, respectively; (b) – statistical grain size distribution for Al_ECAP+CR+AN. w_{RT} , w_{77K} – the steady-state subgrain size at RT and 77 K, respectively (see the explanation in the text); $f(d_G < w_{RT})$, $f(d_G < w_{77K})$ – fractions of grains with the grain size d_G smaller than w_{RT} and w_{77K} , respectively

Figure 2 shows the stress-strain curves of the Al_ECAP+CR+AN samples at RT and 77 K. For comparison, the stress-strain curve of Al in the initial coarse-grained state (CG) at RT is also presented. The mechanical characteristics of the Al_ECAP+CR+AN samples at RT are similar to those we obtained previously [17]. As is seen (Fig. 2), the strength characteristics of the material in the UFG state Al_ECAP+CR+AN significantly exceed those in the initial CG state. In the UFG state, compared to the CG state, the value of $\sigma_{0.2}$ increased from ~ 35 to ~ 185 MPa, and the value of σ_{UTS} increased from ~ 50 to ~ 215 MPa. The value of δ at RT drops by 4 times, from ~ 40 % in the CG state to δ ~ 10 % in the UFG state. The uniform elongation becomes very low (δ_1 ~ 1 %), which indicates the localization of deformation in UFG Al immediately after the onset of plastic flow. However, the Al_ECAP+CR+AN samples demonstrate excellent ductility at 77 K (curve 3 in Fig. 2): δ reaches ~ 40 %, and uniform elongation is ~ 25 %, which exceeds δ_1 at RT by ~ 25 times. The increase in ductility of UFG Al at 77 K is accompanied by a noticeable increase in the strength (by ~ 1.3 times). The values of $\sigma_{0.2}$ and σ_{UTS} increased from ~ 185 to ~ 235 MPa and from ~ 215 to ~ 265 MPa, respectively.

76 T.S. Orlova, D.I. Sadykov

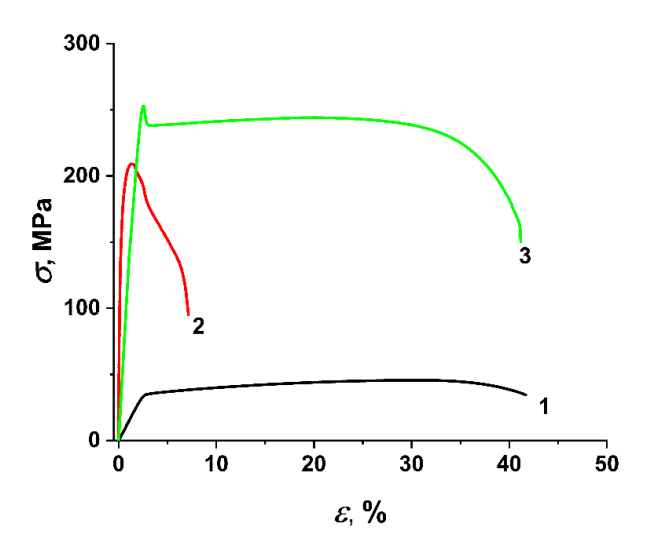


Fig. 2. Stress-strain curves of Al in the CG state (1) and in the UFG state Al_ECAP+CR+AN (2, 3) at RT (1, 2) and 77 K (3)

Figure 3 shows the stress-strain curves in true coordinates and the corresponding dependences of strain hardening coefficient ($\theta = d\sigma_{tr}/d\epsilon_{tr}$, where σ_{tr} is true stress and ϵ_{tr} is true strain) on true strain for UFG Al in the Al_ECAP+CR+AN state at different deformation temperatures.

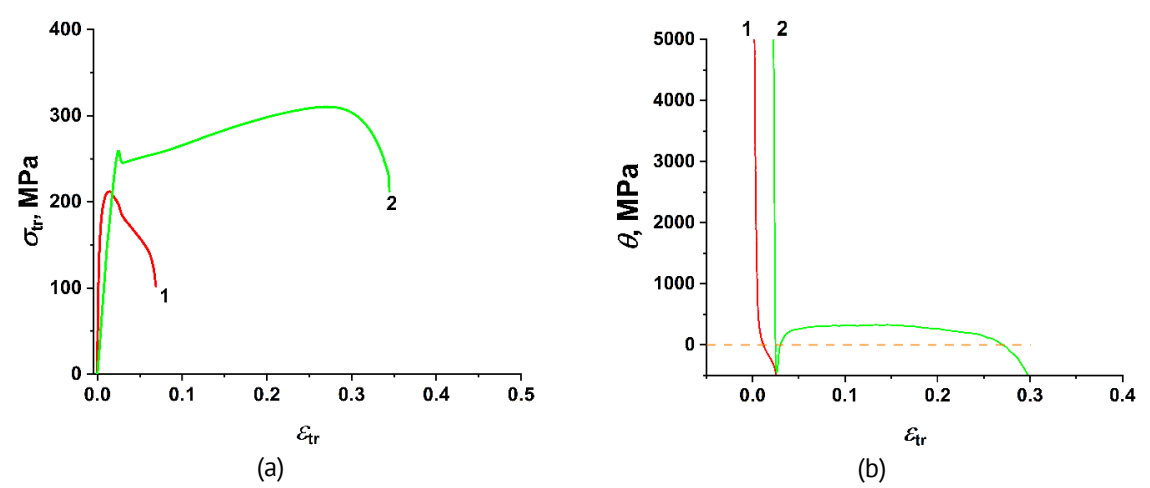


Fig. 3. (a) – true stress-strain curves of Al_ECAP+CR+AN at RT (curve 1) and 77 K (curve 2); (b) – the strain hardening coefficient as a function of true strain for Al_ECAP+CR+AN at RT (curve 1) and 77K (curve 2)

As is seen, the value of θ at RT sharply decreases to negative values when the strain is very small, that indicates low ability of UFG Al to strain hardening. At 77 K, the Al_ECAP+CR+AN samples show strain hardening (θ > 0) until a large strain of ~ 25 % is reached (Fig. 3(b)). The high ductility of Al in the Al_ECAP+CR+AN state at 77 K opens up prospects for using this material to form products of complex shapes. High ductility at cryogenic temperature (77 K) was also demonstrated by UFG Al structured only by the CR method (Al_CR) [18]. However, Al_CR showed significantly lower strength at RT: $\sigma_{0.2}$ ~ 134 MPa and σ_{UTS} ~ 140 MPa, which are 1.35 and 1.5 times lower, respectively, than the such characteristics of Al_ECAP+CR+AN. At 77 K, both strength characteristics ($\sigma_{0.2}$ and σ_{UTS}) of Al_CR are also approximately 1.3 times lower than those of Al_ECAP+CR+AN. UFG

Al structured only by ECAP also has lower strength ($\sigma_{0.2} \sim 150$ MPa and $\sigma_{UTS} \sim 180$ MPa) and low ductility ($\delta_1 \sim 3.9$ % and $\delta \sim 14$ %) at RT [19]. The yield stress of UFG Al samples structured by HPT is ~ 1.4 times lower compared to $\sigma_{0.2}$ of Al_ECAP+CR+AN samples. For UFG Al structured by HPT, no increase in ductility is observed at 77 K compared to that at RT [20]. At 77 K, the ductility of Al_HPT is $\delta \sim 19$ % with uniform elongation $\delta_1 \sim 1$ % in both states: with and without subsequent annealing at T = 150 °C for t = 1 h [20]. Thus, comparison of mechanical properties of Al_ECAP+CR+AN and UFG Al structured by other SPD methods at RT shows that the Al ECAP+CR+AN samples have the best strength.

As is known, at large plastic deformation a subgrain structure develops in the initial CG material as a result of the rearrangement of dislocations accumulated during deformation [21,22]. When the strain reaches a critical value, the stationary regime of dynamic equilibrium of the nucleation and annihilation of dislocations is established, and a steady-state subgrain size w is reached. According to [23], the steady-state subgrain size is determined as:

$$w = k_W \frac{bG}{\sigma_{tr}^{max}},\tag{1}$$

where k_w is a constant in the range 10–30, G is the shear modulus, b is the value of Burgers vector and σ_{tr}^{max} is the maximum true stress obtained from the stress-strain curves in true coordinates.

It is known that the value of the parameter w decreases with decreasing temperature and increasing strain rate [24,25]. At low temperatures, dynamic recovery (annihilation of dislocations and rearrangement of the dislocation structure) is suppressed, which contributes to a greater accumulation of dislocations during deformation. As a consequence, the free path of mobile dislocations decreases. The level of flow stress increases, that can promote the activation of additional sources of dislocations, leading to an overall increase in dislocation density. These dislocations can interact with each other and form a cell/subgrain dislocation structure with a lower w compared to the case of deformation at RT [24]. According to [18,22], the grain size d_G in a UFG structure relative to the parameter w at a given temperature and strain rate can play a decisive role in determining the overall deformation behavior of the material. In UFG alloys with a predominant grain size $d_G < w$, dislocations emitted from grain boundaries will glide to the opposite boundary (in the absence of any obstacles) and be embedded into it. Such dynamics of dislocations leads to a very slight or almost complete absence of strain hardening of the material, the rapid achievement of instability state (localization of deformation) in accordance with the Considère criterion: $\sigma = \theta$ [26,27], and, consequently, to low tensile ductility, primarily to low uniform elongation. In a UFG structure with a grain size $d_G > w$, emitted dislocations can interact with each other, accumulate, and form a cell/subgrain structure and, as a result, promote strain hardening.

In the present work, we estimated the parameter w for UFG Al_ECAP+CR+AN for deformation conditions at RT (w_{RT}) and 77 K (w_{77K}) according to Eq. (1). Using the values of G = 26 GPa at RT and 29.2 GPa at 77 K for Al [28], b = 0.286 nm [29] and the widely used value $k_w = 20$ for Al [30], as well as corresponding values of σ_{tr}^{max} determined from true stress – true strain diagrams (Fig. 3(a)), the values of $w_{RT} \approx 730$ nm and $w_{77K} \approx 530$ nm were obtained.

A comparison of the estimated w-values with the experimentally obtained grain size distribution for UFG Al in the Al_ECAP+CR+AN state (Fig. 1(b)) shows that the majority of

78 T.S. Orlova, D.I. Sadykov

grains (fraction of grains $f \approx 65$ %) have a size d_G smaller then w_{RT} , therefore, at RT the accumulation of dislocations during deformation can occur mainly only in ~ 35 % of grains, that explains the low ductility at RT (Fig. 2). At the same time, the majority of grains (~ 75 %) meet the criterion $d_G > w_{77K}$; therefore, at 77 K, deformation with the accumulation of dislocations can occur in them promoting noticeable strain hardening, which is observed experimentally (Fig. 3) and explains the drastic increase in ductility at the cryogenic temperature (Fig. 2).

Conclusions

Thus, it was shown that UFG aluminium structured by a combination of ECAP and CR methods followed by annealing ($T=150~^{\circ}$ C, t=1~h) demonstrates drastic increase in ductility at 77 K compared with the ductility at RT. The values of δ and δ_1 increased respectively from ~ 10 % and ~ 1 % at RT to ~ 40 % and ~ 25 % at 77 K, while the strength also increased, reaching values of $\sigma_{0.2}$ ~ 235 MPa and σ_{UTS} ~ 265 MPa at 77 K. The achieved large uniform elongation opens up prospects for the use of cryogenic temperatures for molding products of complex shapes from such high-strength UFG aluminum, as well as its use for operation at cryogenic temperatures. It was shown that the increase in ductility, both elongation to failure and uniform elongation at 77 K, is associated with an increase in the strain hardening coefficient with decreasing deformation temperature and a high fraction of grains with sizes exceeding the characteristic steady-state subgrain size at 77 K.

References

- 1. Edalati K, Ahmed AQ, Akrami S, Ameyama K, Aptukov V, Asfandiyarov RN, Ashida M, Astanin V, Bachmaier A, Beloshenko V, Bobruk EV, Bryła K, Cabrera JM, Carvalho AP, Chinh NQ, Choi IC, Chulist R, Cubero-Sesin JM, Davdian G, Demirtas M, Zhu YT. Severe plastic deformation for producing superfunctional ultrafine-grained and heterostructured materials: An interdisciplinary review. *Journal of Alloys and Compounds*. 2024;1002: 174667.
- 2. Valiev RZ, Alexandrov IV, Kawasaki M, Langdon TG. Ultrafine-Grained Materials. Cham: Springer; 2024.
- 3. Karami S, Piroozi B, Borhani E. Fatigue-induced microstructure evolution and ratcheting behavior of ultrafine-grained (UFG) pure aluminum processed by accumulative roll bonding (ARB). *Materials Characterization*. 2023;196: 112578.
- 4. Lanjewar H, Naghdy S, Vercruysse F, Kestens LA, Verleysen P. Severe plastically deformed commercially pure aluminum: Substructure, micro-texture and associated mechanical response during uniaxial tension. *Materials Science and Engineering: A.* 2019;764: 138195.
- 5. Mohammadi A, Enikeev NA, Murashkin MYu, Arita M, Edalati K. Examination of inverse Hall-Petch relation in nanostructured aluminum alloys by ultra-severe plastic deformation. *Journal of Materials Science & Technology*. 2021;91:78–89.
- 6. Evstifeev AD, Smirnov IV. Effect of annealing and additional deformation on the microstructure and mechanical properties of ultrafine-grained Al5083 alloy. *Materials Physics and Mechanics*. 2023;95(3): 20–28. 7. Edalati K, Bachmaier A, Beloshenko VA, Beygelzimer Y, Blank VD, Botta WJ, Bryła K, et al. Nanomaterials by severe plastic deformation: review of historical developments and recent advances. *Materials Research Letters*. 2022;10(4): 163–256.
- 8. Awasthi A, Sathish Rao U, Saxena KK, Dwivedi RK. Impact of equal channel angular pressing on aluminium alloys: An overview. *Materials Today: Proceedings*. 2022;57: 908–912.
- 9. Zhilyaev AP, Torres MJ, Cadena HD, Rodriguez SL, Calvo J, Cabrera JM. The effect of pre-annealing on the evolution of the microstructure and mechanical behavior of aluminum processed by a novel SPD method. *Materials*. 2020;13(10): 2361.
- 10. Chen X, Wang W, Wang M, Huang G, Zhang J, Pan F. Optimizing the strength and ductility of pure aluminum laminate via tailoring coarse/ultrafine grain layer thickness ratio. *Journal of Materials Research and Technology.* 2023;27: 7394–7406.

- 11. Huang T, Shuai L, Wakeel A, Wu G, Hansen N, Huang X. Strengthening mechanisms and Hall-Petch stress of ultrafine grained Al-0.3%Cu. *Acta Materialia*. 2018;156: 369–378.
- 12. Chen X, Wang W, Yang H, Huang G, Xia D, Tang A, Jiang B, Han HN, Pan F. Microstructure evolution, mechanical properties and deformation characteristics of ultrafine-grained annealed pure aluminum. *Materials Science and Engineering: A.* 2022;846: 143320.
- 13. Fu H, Zhou X, Xue H, Li X, Lu K. Breaking the purity-stability dilemma in pure Cu with grain boundary relaxation. *Materials Today.* 2022;55: 66–73.
- 14. Mavlyutov AM, Latynina TA, Murashkin MYu, Valiev RZ, Orlova TS. Effect of annealing on the microstructure and mechanical properties of ultrafine-grained commercially pure Al. *Physics of the Solid State*. 2017;59(10): 1970–1977.
- 15. Orlova TS, Skiba NV, Mavlyutov AM, Valiev RZ, Murashkin MY, Gutkin MY. Hardening by annealing and implementation of high ductility of ultra-fine grained aluminum: experiment and theory. *Reviews On Advanced Materials Science*. 2018;57(2): 224–240.
- 16. Orlova TS, Sadykov DI, Kirilenko DA, Lihachev AI, Levin AA. The key role of grain boundary state in deformation-induced softening effect in Al processed by high pressure torsion. *Materials Science and Engineering: A.* 2023;875: 145122.
- 17. Sadykov DI, Medvedev AE, Murashkin MYu, Enikeev NA, Kirilenko DA, Orlova TS. Influence of ultrafine-grained structure parameters on the annealing-induced hardening and deformation-induced softening effects in pure Al. *International Journal of Lightweight Materials and Manufacture*. 2024;7(2): 221–232.
- 18. Wang R, Liu W, Hao Y, Yao M. Mechanism of considerable strain hardening in ultrafine-grained pure aluminum sheets at cryogenic temperatures. *Materials Science and Engineering: A.* 2023;862: 144481.
- 19. Yu CY, Sun PL, Kao PW, Chang CP. Mechanical properties of submicron-grained aluminum. *Scripta Materialia*. 2005;52(5): 359–363.
- 20. Orlova TS, Mavlyutov AM, Gutkin MYu. Suppression of the annealing-induced hardening effect in ultrafine-grained Al at low temperatures. *Materials Science and Engineering: A.* 2021;802: 140588.
- 21. Tian YZ, Gao S, Zhao LJ, Lu S, Pippan R, Zhang ZF, Tsuji N. Remarkable transitions of yield behavior and Lüders deformation in pure Cu by changing grain sizes. *Scripta Materialia*. 2018;142: 88–91.
- 22. Kumar N, Mishra RS, Huskamp CS, Sankaran KK. Critical grain size for change in deformation behavior in ultrafine grained Al-Mg-Sc alloy. *Scripta Materialia*. 2011;64(6): 576–579.
- 23. Li YJ, Zeng XH, Blum W. Transition from strengthening to softening by grain boundaries in ultrafine-grained Cu. *Acta Materialia*. 2004;52(17): 5009–5018.
- 24. Huang F, Tao NR. Effects of strain rate and deformation temperature on microstructures and hardness in plastically deformed pure aluminum. *Journal of Materials Science & Technology*. 2011;27(1): 1–7.
- 25. Huang Y, Prangnell PB. The effect of cryogenic temperature and change in deformation mode on the limiting grain size in a severely deformed dilute aluminium alloy. *Acta Materialia*. 2008;56(7): 1619–1632.
- 26. Kozlov EV, Glazer AM, Koneva NA, Popova NA, Kurzina IA. Fundamentals of plastic deformation of nanostructured materials. Moscow: FIZMATLIT; 2016. (In Russian)
- 27. Backofen WA. Deformation processing. Boston: Addison-Wesley Educational Pub; 1972.
- 28. Cheng W, Liu W, Fan X, Yuan S. Cooperative enhancements in ductility and strain hardening of a solution-treated Al-Cu-Mn alloy at cryogenic temperatures. *Materials Science and Engineering: A.* 2020;790: 139707.
- 29. Anderson PM, Hirth JP, Lothe J. *Theory of dislocations*. 3rd ed. Cambridge: Cambridge University Press; 2017.
- 30. Wang BB, Xie GM, Wu LH, Xue P, Ni DR, Xiao BL, Liu YD, Ma ZY. Grain size effect on tensile deformation behaviors of pure aluminum. *Materials Science and Engineering: A.* 2021;820: 141504.

About Author

Tatiana S. Orlova D Sc

Doctor of Physical and Mathematical Sciences Principal Researcher (Ioffe Institute, St. Petersburg, Russia)

Dinislam I. Sadykov 🗓 Sc

Junior Researcher (loffe Institute, St. Petersburg, Russia)

Submitted: May 27, 2024 Revised: June 18, 2024 Accepted: July 9, 2024

The effect of high-temperature annealing on the properties of bulk β -Ga₂O₃ obtained in different growth atmospheres

V.A. Spiridonov [™], [©] D.I. Panov, [©] A.Yu. Ivanov, [©] D.A. Bauman, [©] A.E. Romanov, [©]

ITMO University, St. Petersburg, Russia

□ vladspiridonov@itmo.ru

ABSTRACT

The work presents the results of the experiments on annealing in air of bulk crystals of gallium oxide grown in $Ar+O_2$ and CO_2 atmospheres at a temperature of 1400 °C. The annealing time was 5 hours; the time to reach the temperature was 3.5 hours; the cooling time was 20 hours. Annealed samples show increasing of transmission in infrared area of electromagnetic spectrum and decreasing of width of X-ray rocking curve which means the reduction of the number of defects in crystals. Full width at half maximum of rocking curve for annealed samples was almost the same for both atmospheres: FWHMa = 84 arcsec for sample grown in $Ar+O_2$ atmosphere and FWHMa = 80 arcsec for sample grown in CO_2 , which means that after annealing, the quality of the samples became comparable, despite the initial difference.

KEYWORDS

 β -Ga₂O₃ • bulk crystal • annealing • optical spectroscopy • XRD

Acknowledgements. This study was supported by the Russian Science Foundation, project no. 24-12-00229.

Citation: Spiridonov VA, Panov DI, Ivanov AYu, Bauman DA, Romanov AE. The effect of high-temperature annealing on the properties of bulk β -Ga₂O₃ obtained in different growth atmospheres. *Materials Physics and Mechanics*. 2024;52(3): 80–85.

http://dx.doi.org/10.18149/MPM.5232024 8

Introduction

Recently, the theme of ultra-wide bandgap (UWBG) semiconductors has been gaining big attention [1–4]. The term UWBG is commonly used to denote semiconductors with a larger band gap E_g than traditional wide bandgap semiconductors such as silicon carbide (E_g =3.2eV [5]) and gallium nitride (E_g =3.4 eV [6]). Usually, compounds III-V (BN, AlN, AlGaN), diamond and compounds based on gallium oxide are considered as UWBG. The bulk crystal of gallium oxide (β -Ga₂O₃) is a semiconductor with a band gap of about 4.8 eV [7,8], with excellent electrical characteristics, such as large breakdown electric field of about 8 MV/cm theoretically [9] and about 3.8 MV/cm in the device [10], high radiation resistance [11] and relatively high electron mobility (up to 200 cm²V⁻¹s⁻¹ [12]). One of the main advantages of gallium oxide over other UWBG semiconductors is the possibility of fabricating bulk crystals by liquid phase growth methods such as the Czochralski method [13–19] and the edge-defined film-fed growth (EFG) method [20–25] used in the industry.

Experiments on the annealing of bulk β -Ga₂O₃ crystals have shown that annealing in an oxygen-containing atmosphere leads to an increase in optical transmission in the IR region and a drop in the concentration of charge carriers [26–28]. During annealing without oxygen, for example in nitrogen [28] or in vacuum [29], the reverse processes occur — the concentration of carriers increases, transmission decreases.

Previous experiments have shown that increasing the oxygen concentration in the growth atmosphere improves the quality of crystals [30,31], as well as high-temperature annealing in an oxygen-containing atmosphere [26–28,31–33]. In addition, experiments have shown that the properties of the crystal after annealing change significantly at an annealing temperature of 1200 °C and above [31,33]. In this paper, the effect of annealing on gallium oxide crystals grown in different growth atmospheres is evaluated.

Experimental setup and methodology

For this study bulk single crystals of gallium oxide were grown in the industrial facility "Nika-3" (production of EZAN, Russia) using the Czochralski method as described in our previous work [30]. An iridium crucible was used to form the melt. β -Ga₂O₃ crystals were used as seeds. Ga₂O₃ powder with a purity of 99.999 % (5N) was used as a starting material for the formation of the melt. The growths were conducted in an argon atmosphere with the addition of 5 vol. % of oxygen and in CO₂ atmosphere at a pressure of 1.4 bar.

For the studies plane-parallel plates with thicknesses of 1 mm were cut from crystal boule along the cleavage plane (100).

Annealing was conducted in a shaft furnace at a temperature of 1400 °C for 5 hours (the time to reach the temperature was 3.5 hours, the cooling time was 20 hours) in air. Sample for annealing was placed on sapphire substrate in corundum crucible.

Results and Discussion

The main difficulties in obtaining gallium oxide from the melt are the high melting point (1795–1820 °C [16,34]) and melt decomposition into volatile forms during growth in an atmosphere with oxygen deficiency [16]. The decomposition of the gallium oxide melt can be described by the following reactions:

$$2Ga_2O_3 \rightarrow 4GaO\uparrow + O_2\uparrow \tag{1}$$

$$4GaO \rightarrow 2Ga_2O\uparrow + O_2\uparrow \tag{2}$$

$$2Ga_2O \rightarrow 4Ga\uparrow + O_2\uparrow \tag{3}$$

With crystal growth, decomposition leads to a lack of oxygen in the melt, which in turn leads to a violation of stoichiometry in the grown crystal and the formation of oxygen vacancies in crystal. Vacancies in β -Ga₂O₃ lead, for example, to an increase in optical absorption in the IR region of the spectrum [35].

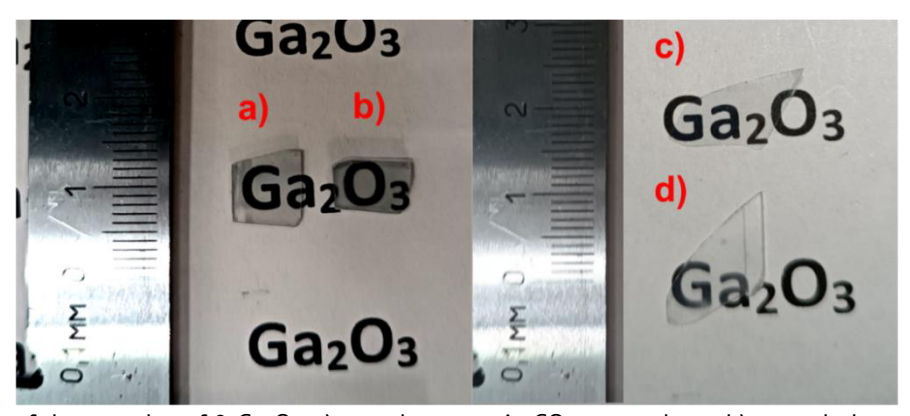


Fig. 1. Photo of the samples of β-Ga₂O₃: a) sample grown in CO₂ atmosphere; b) annealed sample grown in CO₂ atmosphere; c) sample grown in Ar+O₂ atmosphere

After annealing, the sample became visually cloudy (Fig. 1), which indicates a change in the morphology of its top surface, presumably due to diffusion processes. For further experiments, a rough surface layer 0.1 mm thick was exfoliated from each annealed sample and the measurements were carried out on the remaining part of the samples.

Figure 2 shows the normalized transmission spectra of samples. The graph shows that annealing led to an increase in transmission in the IR region of the spectrum, which means a decrease in the number of absorbing centers that can be oxygen vacancies [35]. There is also a strong difference between samples grown in $Ar+O_2$ and in CO_2 atmosphere, due to the almost five times higher [31] oxygen concentration in the growth atmosphere, which reduces the volatilization of oxygen from the melt [16].

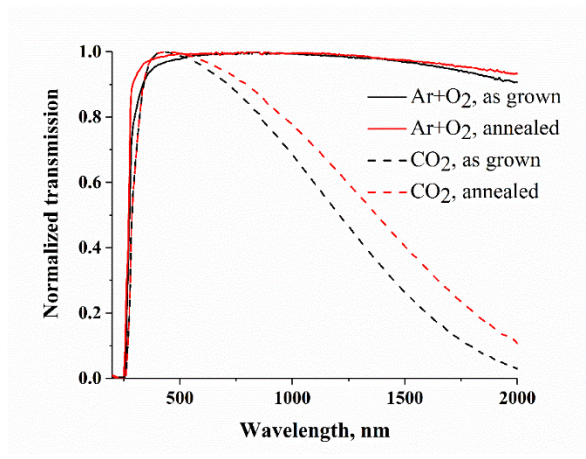


Fig. 2. Normalized transmission spectra of samples of β -Ga₂O₃. Solid line – samples grown in Ar+O₂ atmosphere, dashed line - samples grown in CO₂ atmosphere

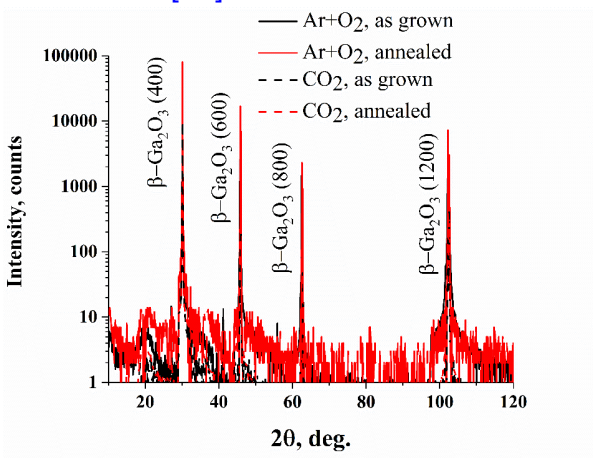


Fig. 3. XRD 2θ-spectra of annealed and non-annealed samples of β-Ga₂O₃. Solid line – samples grown in Ar+O₂ atmosphere, dashed line - samples grown in CO₂ atmosphere

XRD spectra (Fig. 3) showed the presence of peaks corresponding to the (100) plane of the β -Ga₂O₃ and showed no phase changes between samples. Figures 4 and 5 present normalized rocking curves of samples for peak (400). For sample grown in the Ar+O₂ atmosphere we can see significant reduction in the full width at half maximum (FWHM) of the rocking curve (RC) from FWHM_{na} = 208 arcsec for the non-annealed sample to FWHM_a = 84 arcsec for the annealed one.

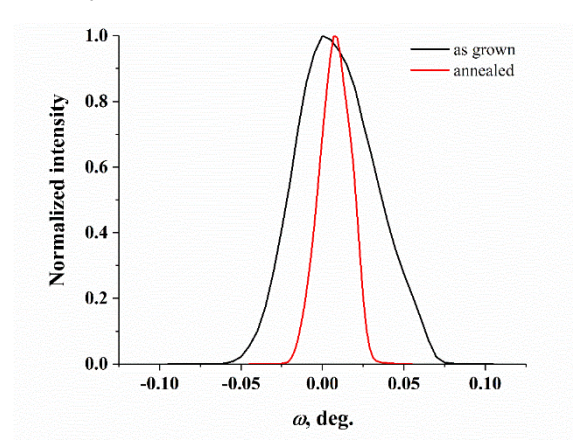


Fig. 4. Rocking curve ω for the peak (400) of annealed and non-annealed samples of β-Ga₂O₃ grown in Ar+O₂ atmosphere. FWHM_{na}=208 arcsec, FWHM_a= 84 arcsec

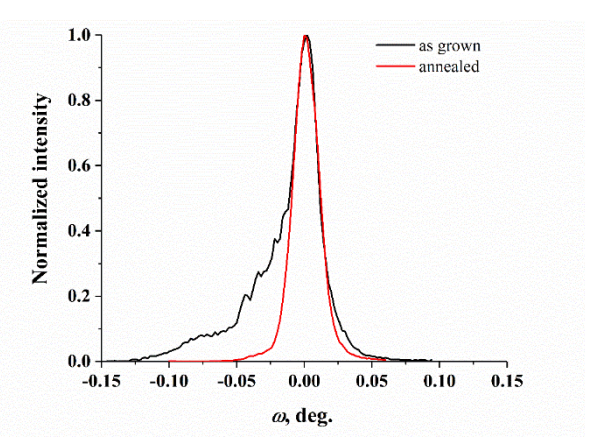


Fig. 5. Rocking curve ω for the peak (400) of annealed and non-annealed samples of β-Ga₂O₃ grown in CO₂. FWHM_{na}=82 arcsec, FWHM_a=80 arcsec

Together with the visible change in the morphology of the sample surface after annealing, we can say about the movement of defects on to the surface and an increase in the bulk crystalline quality.

For the sample grown in CO_2 before annealing, a wide tail is observed on the RC, which indicates the presence of defect blocks in the crystal. The RC of the non-annealed sample can be decomposed by gaussians to the three peaks (see Fig. 6), similar to how it was done in [36], which means the presence of multiple disoriented blocks. After annealing, this tail disappears, which shows a decrease in the number of defects i.e., an improvement in crystal quality. The FWHM of RC after annealing correspond to the FWHM of strongest peak at the RC of the non-annealed sample.

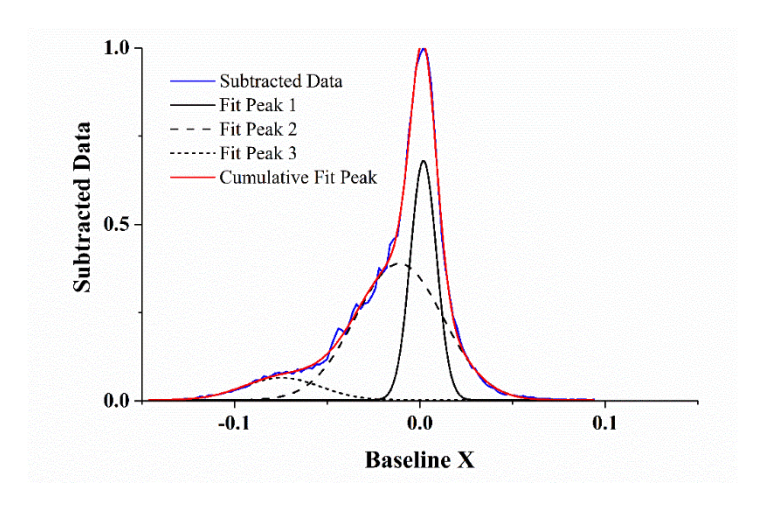


Fig. 6. Decomposition of rocking curve ω for the peak (400) of non-annealed sample β-Ga $_2$ O $_3$ grown in CO $_2$ atmosphere by gaussians

Conclusions

The work showed that annealing of β -Ga₂O₃ bulk crystals in air at 1400 °C for 5 hours leads to an increase in transmission in the infrared region of the electromagnetic spectrum and a decrease in the width of the rocking curve, which indicates a decrease in the number of defects in crystal. As has been shown in [35] oxygen vacancies can serve as absorption centers in a gallium oxide. Thus, the increase in transmittance in the IR region can be explained by a decrease in the concentration of oxygen vacancies during annealing in an oxygen-containing atmosphere (in air). RC shows that after annealing FWHM is almost same for samples grown in CO₂ and Ar+O₂ (95:5 vol. %) atmosphere, which means that after annealing, the quality of the sample obtained in the atmosphere of CO₂, which was initially lower, became comparable to the quality of the sample obtained in the atmosphere of Ar+O₂. In general, it can be concluded that annealing leads to a significant improvement in the quality of the samples regardless of the growth atmosphere, although the sample grown in CO₂ still shows higher absorbance in IR range of electromagnetic spectrum.

References

- 1. Tsao JY, Chowdhury S, Hollis MA, Jena D, Johnson NM, Jones KA, Kaplar RJ, Rajan S, Van de Walle CG, Bellotti E, Chua CL, Collazo R, Coltrin ME, Cooper JA, Evans KR, Graham S, Grotjohn TA, Heller ER, Higashiwaki M, Islam MS, Juodawlkis PW, Khan MA, Koehler AD, Leach JH, Mishra UK, Nemanich RJ, Pilawa-Podgurski RCN, Shealy JB, Sitar Z, Tadjer MJ, Witulski AF, Wraback M, Simmons JA. Ultrawide-Bandgap Semiconductors: Research Opportunities and Challenges. *Advanced Electronic Materials*. 2018;4(1): 160.
- 2. Wong MH, Bierwagen O, Kaplar RJ, Umezawa H. Ultrawide-bandgap semiconductors: An overview. *Journal of Materials Research*. 2021;36(23): 4601–4615.
- 3. Woo K, Bian Z, Noshin M, Martinez RP, Malakoutian M, Shankar B, Chowdhury S. From wide to ultrawide-bandgap semiconductors for high power and high frequency electronic devices. *J. Phys. Mater.* 2024;7(2): 022003.
- 4. Feng T, Zhou H, Cheng Z, Larkin LS, Neupane MR. A Critical Review of Thermal Boundary Conductance across Wide and Ultrawide Bandgap Semiconductor Interfaces. *ACS Appl Mater Interfaces*. 2023;15(25): 29655–29673.
- 5. Patrick L, Hamilton DR, Choyke WJ. Growth, Luminescence, Selection Rules, and Lattice Sums of SiC with Wurtzite Structure. *Phys Rev.* 1966;143(2): 526–536.
- 6. Levinshtein ME, Rumyantsev SL, Shur MS. *Properties of Advanced Semiconductor Materials: GaN, AIN, InN, BN, SiC, SiGe*. John Wiley & Sons; 2001.
- 7. Orita M, Ohta H, Hirano M, Hosono H. Deep-ultraviolet transparent conductive β-Ga2O3 thin films. *Appl. Phys. Lett.* 2000;77(25): 4166–4168.
- 8. Panov DI, Spiridonov VA, Zakgeim DA, Kremleva AV, Bauman DA, Romanov AE, Bougrov VE. Growth Technology and Optical Properties of Bulk Crystalline Gallium Oxide. *Rev. Adv. Mater. Tech.* 2020;2(3): 51–55.
- 9. Zhang J, Shi J, Qi DC, Chen L, Zhang KHL. Recent progress on the electronic structure, defect, and doping properties of Ga2O3. *APL Materials*. 2020;8(2): 020906.
- 10. Green AJ, Chabak KD, Heller ER, Fitch RC, Baldini M, Fiedler A, Irmscher K, Wagner G, Galazka Z, Tetlak SE, Crespo A, Leedy K, Jessen GH. 3.8-MV/cm Breakdown Strength of MOVPE-Grown Sn-Doped β-Ga2O3 MOSFETs. *IEEE Electron Device Letters*. 2016;37(7): 902–905.
- 11. Bauman DA, Borodkin AI, Petrenko AA, Panov DI, Kremleva AV, Spiridonov VA, Zakgeim DA, Silnikov MV, Odnoblyudov MA, Romanov AE, Bougrov VE. On improving the radiation resistance of gallium oxide for space applications. *Acta Astronautica*. 2021;180: 125–129.
- 12. Singh R, Lenka TR, Panda DK, Velpula RT, Jain B, Bui HQT, Nguyen HPT. The dawn of Ga2O3 HEMTs for high power electronics A review. *Materials Science in Semiconductor Processing*. 2020;119: 105216.
- 13. Shimamura K, Villora E. Czochralski-Based growth and characteristics of selected novel single crystals for optical applications. *Acta Physica Polonica A*. 2013;124(2): 265–273.
- 14. Blevins JD, Thomson D, Stevens K, Foundos G. Growth of single crystal beta-gallium oxide (β-Ga2O3) semiconductor material. In: *Proceedings of the CSMANTECH*. Indian wells, CA, USA; 2017. p.22–25.
- 15. Vasil'tsiv VI, Zakarko YaM. Effects of electron capture by impurity centers on the luminescent parameters of β-Ga2O3:Cr crystals. *J. Appl. Spectrosc.* 1983;39(3): 1037–1041.
- 16. Galazka Z, Uecker R, Irmscher K, Albrecht M, Klimm D, Pietsch M, Brützam M, Bertram R, Ganschow S, Fornari R. Czochralski growth and characterization of β-Ga2O3 single crystals. *Crystal Research and Technology*. 2010;45(12):1229–1236.
- 17. Tomm Y, Reiche P, Klimm D, Fukuda T. Czochralski grown Ga2O3 crystals. *Journal of Crystal Growth*. 2000;220(4): 510–514.

 18. Panov DI, Spiridonov VA, Zakgeim DA, Kremleva AV, Bauman DA, Romanov AE, Bougrov VE. Growth
- technology and characterization of bulk crystalline gallium oxide. *J. Phys: Conf. Ser.* 2020;1695(1): 012024. 19. McCloy JS, Jesenovec J, Dutton BL, Pansegrau C, Remple C, Weber MH, Swain S, McCluskey M, Scarpulla
- M. Growth and defect characterization of doped and undoped β-Ga2O3 crystals. In: *Oxide-based Materials and Devices XIII*. San Francisco, California, United States: SPIE; 2022. p.21–39.
- 20. Nakai K, Nagai T, Noami K, Futagi T. Characterization of defects in β-Ga2O3 single crystals. *Jpn. J. Appl. Phys.* 2015;54(5):051103. 21. Kuramata A, Koshi K, Watanabe S, Yamaoka Y, Masui T, Yamakoshi S. High-quality β-Ga2O3 single crystals grown by edge-defined film-fed growth. *Jpn. J. Appl. Phys.* 2016;55(12): 1202A2.
- 22. Tang H, He N, Zhang H, Liu B, Zhu Z, Xu M, Chen L, Liu J, Ouyang X, Xu J. Inhibition of volatilization and polycrystalline cracking, and the optical properties of β -Ga2O3 grown by the EFG method. *CrystEngComm*. 2020;22(5): 924–931.
- 23. Zhang S, Lian X, Ma Y, Liu W, Zhang Y, Xu Y, Cheng H. Growth and characterization of 2-inch high quality β-Ga2O3 single crystals grown by EFG method. *J. Semicond*. 2018;39(8): 083003.
- 24. Mu W, Jia Z, Yin Y, Hu Q, Li Y, Wu B, Zhang J, Tao X. High quality crystal growth and anisotropic physical characterization of β-Ga2O3 single crystals grown by EFG method. *Journal of Alloys and Compounds*. 2017;714:453–458.

- 25. Bauman DA, Panov DIu., Spiridonov VA, Kremleva AV, Asach AV, Tambulatova EV, Sakharov AV, Romanov AE. High quality β-Ga2O3 bulk crystals, grown by edge-defined film-fed growth method: Growth features, structural, and thermal properties. *Journal of Vacuum Science & Technology A*. 2023;41(5): 053203.
- 26. Li P, Han X, Chen D, Sai Q, Qi H. Effect of air annealing on the structural, electrical, and optical properties of V-doped β-Ga2O3single crystals. *Journal of Alloys and Compounds*. 2022;908: 164590.
- 27. Irmscher K, Galazka Z, Pietsch M, Uecker R, Fornari R. Electrical properties of β-Ga2O3 single crystals grown by the Czochralski method. *Journal of Applied Physics*. 2011;110(6): 063720.
- 28. Tadjer MJ, Freitas JA, Culbertson JC, Weber MH, Glaser ER, Mock AL, Mahadik NA, Schmieder K, Jackson E, Gallagher JC, Feigelson BN, Kuramata A. Structural and electronic properties of Si- and Sn-doped (–201) β-Ga2O3 annealed in nitrogen and oxygen atmospheres. *J. Phys. D: Appl. Phys.* 2020;53(50): 504002.
- 29. Okada A, Nakatani M, Chen L, Ferreyra RA, Kadono K. Effect of annealing conditions on the optical properties and surface morphologies of $\overline{(201)}$ -oriented β -Ga2O3 crystals. *Applied Surface Science*. 2022;574: 151651.
- 30. Bauman DA, Panov DIu, Zakgeim DA, Spiridonov VA, Kremleva AV, Petrenko AA, Brunkov PN, Prasolov ND, Nashchekin AV, Smirnov AM, Odnoblyudov MA, Bougrov VE, Romanov AE. High-Quality Bulk β-Ga2O3 and β-(Al x Ga1-x)2O3 Crystals: Growth and Properties. *Physica Status Solidi (a*). 2021;218(20): 2100335.
- 31. Galazka Z, Irmscher K, Uecker R, Bertram R, Pietsch M, Kwasniewski A, Naumann M, Schulz T, Schewski R, Klimm D, Bickermann M. On the bulk β -Ga2O3 single crystals grown by the Czochralski method. *Journal of Crystal Growth*. 2014;404: 184–191.
- 32. Zhang N, Liu H, Sai Q, Shao C, Xia C, Wan L, Feng ZC, Mohamed HF. Structural and electronic characteristics of Fe-doped β-Ga2O3 single crystals and the annealing effects. *J. Mater. Sci.* 2021;56(23): 13178–13189.
- 33. Jesenovec J, Weber MH, Pansegrau C, McCluskey MD, Lynn KG, McCloy JS. Gallium vacancy formation in oxygen annealed β-Ga2O3. *Journal of Applied Physics*. 2021;129(24): 245701.
- 34. Schneider SJ, Waring JL. Phase Equilibrium Relations in the Sc2O3-Ga2O3 System. *J. Res. Natl. Bur. Stand. A Phys. Chem.* 1963;67A(1): 19–25.
- 35. Dong L, Jia R, Xin B, Peng B, Zhang Y. Effects of oxygen vacancies on the structural and optical properties of β-Ga2O3. *Sci Rep.* 2017;7(1): 40160.
- 36. Bauman DA, Panov DYu, Spiridonov VA, Ivanov AYu, Sakharov AV, Rodin SN, Prasolov ND, Romanov AE. Ob uspeshnom opyte gomoepitaksii sloyev β-Ga2O3 na sobstvennykh podlozhkakh. *Pisma v ZhTF*. 2024;50(7): 43–46. (In Russian)

About Author

Vladislav A. Spiridonov 🗓 Sc

Researcher (ITMO University, St. Petersburg, Russia)

Dmitrii I. Panov D SC

Candidate of Physical and Mathematical Sciences Senior Researcher (ITMO University, St. Petersburg, Russia)

Andrey Yu. Ivanov 📵 Sc

Junior Researcher (ITMO University, St. Petersburg, Russia)

Dmitrii A. Bauman 🗓 Sc

Candidate of Physical and Mathematical Sciences Associate Professor (ITMO University, St. Petersburg, Russia)

Alexey E. Romanov D Sc

Doctor of Physical and Mathematical Sciences Leading Professor (ITMO University, St. Petersburg, Russia) Submitted: April 5, 2024 Revised: June 4, 2024 Accepted: July 30, 2024

Influence of aluminum shell on the process of devitrification of amorphous titanium nanoparticles: molecular dynamics simulation

G.M. Poletaev 1,2, D Y.Y. Gafner 2, D S.L. Gafner 2, D I.V. Zorya 3, D

Y.V. Bebikhov 4, DA.S. Semenov 4, D

ABSTRACT

Using molecular dynamics modeling, a study of the amorphous nanoparticle devitrification process of titanium during heating at a rate of $5\cdot10^{11}$ K/s in vacuum conditions and with the presence of aluminum shell was conducted. It was shown that the presence of an aluminum shell leads to a significant increase in the nanoparticle devitrification temperature of titanium – for the considered particle sizes (with diameter from 1.75 to 11 nm) the difference was approximately 200 K. In addition, it was discovered that in vacuum conditions, crystalline embryos are primarily formed near the surface of the particle, while in the presence of an aluminum shell, they are formed, on the contrary, first in the volume of the particle. Thus, according to the results of molecular dynamics modeling, a decrease in the size of titanium particles and the presence of an aluminum shell increase the temperature range for the existence of the amorphous phase of titanium.

KEYWORDS

molecular dynamics • nanoparticle • devitrification • crystallization • amorphous metal

Acknowledgements. The study was funded by the Russian Science Foundation (project No. 23-12-20003, https://rscf.ru/project/23-12-20003/) with parity financial support from the Government of the Republic of Khakassia.

Citation: Poletaev GM, Gafner YY, Gafner SL, Zorya IV, Bebikhov YV, Semenov AS. Influence of aluminum shell on the process of devitrification of amorphous titanium nanoparticles: molecular dynamics simulation. *Materials Physics and Mechanics*. 2024;52(3): 86–95.

http://dx.doi.org/10.18149/MPM.5232024_9

Introduction

In the last few decades, metallic nanoparticles have garnered substantial interest due to their distinctive physical, chemical, and optical attributes, which stem from a high percentage of free surface as well as quantum-mechanical and topological effects [1]. Besides crystalline metallic nanoparticles, there is currently a surge in interest for particles with an amorphous structure [2–5]. Amorphous particles contain atoms that are in a non-equilibrium state and possess a greater Gibbs free energy compared to atoms in a crystal. These particles exhibit a unique electronic structure, which makes them a promising candidate, particularly in the field of catalysis [6–8]. Furthermore, amorphous metals, also known as metallic glasses, boast an unusual combination of magnetic and mechanical properties, characterized by high strength, plasticity, and toughness [9,10].

¹ Khakass State University, Abakan, Russia

² Polzunov Altai State Technical University, Barnaul, Russia

³ Siberian State Industrial University, Novokuznetsk, Russia

⁴ Polytechnic Institute of North-Eastern Federal University, Mirny, Russia

[□] gmpoletaev@mail.ru

In the exploration of techniques for creating and manipulating metallic nanoparticles, significant emphasis is placed on regulating the phase state, dimensions, and morphology of the particles, as these factors play a crucial role in determining their beneficial characteristics [11–14]. Consequently, investigations into the stability of phase states, the mechanisms governing phase transitions in nanoparticles, and the variables impacting the kinetics of these transitions and the temperature at which they occur are gaining heightened significance.

Presently, it is established that the melting temperature of nanoparticles tends to decrease as their size diminishes, a phenomenon attributed to the increasing ratio of surface area to volume. This trend has been substantiated through experimental studies [15–17] and computer modeling [18–21]. Additionally, computer simulations have demonstrated that the crystallization temperature during cooling from the melt is contingent upon the size and shape of the particles, which is directly related to the ratio of surface area to volume. This temperature decreases as the proportion of surface area to volume increases [19–22].

Furthermore, the mechanism and kinetics of the devitrification process in nanoparticles, which involves the loss of their amorphous state due to crystallization during heating, remain largely unexplored. The objective of this research is to investigate the devitrification process of amorphous titanium nanoparticles at the atomic level, utilizing molecular dynamics modeling in both vacuum conditions and within an aluminum shell. The additional consideration of the influence of the aluminum shell is related to the solution of the problem of reducing the temperature of initiation of the high-temperature synthesis reaction in the Ti-Al system in mixtures subjected to preliminary mechanochemical activation [23-25]. During mechanochemical activation, so-called mechanocomposites are formed, which represent a matrix of a more plastic component (in this case aluminum), in which nanoscale particles of a more brittle component of the mixture (titanium) are located [24,25]. Such a system is characterized by a high degree of non-equilibrium due to a high concentration of defects and even the presence of an amorphous phase, which is formed as a result of intense deformation. It is noted that the beginning of the burning reaction in such a non-equilibrium system begins at temperatures significantly lower than the melting temperature of aluminum [24,25].

One of the advantages of computer modeling is the ability to study the influence of one of the factors (presence of high density of grain boundaries, dislocations, internal stresses, amorphous state) on the process being studied. In [26,27], it was shown that the amorphous state of aluminum leads to a lower degree of intensification of mutual diffusion than the amorphous state of titanium. However, with increasing temperature, devitrification of the amorphous phase of titanium can obviously occur and its effect on ignition will be minimal. At the same time, the presence of the Ti-Al interface can affect the devitrification temperature and increase the temperature range of existence of the amorphous phase. The above issue, in addition to the study of amorphous nanoparticles of titanium in a vacuum, is also considered in this work.

Description of the model

To model the interatomic interactions within the Ti-Al system, EAM potentials from [28] were employed, which were derived through comparisons with experimental data and *ab initio* calculations for various properties and structures of metals Ti, Al, and intermetallides Ti₃Al and TiAl. These potentials have demonstrated their efficacy in various studies and have been successfully validated for a broad spectrum of mechanical and structural-energetic properties of Ti-Al alloys [26−31]. In particular, the potentials used by us show good agreement with experimental data on the melting temperature of Ti and Al: in molecular dynamics modeling, they turned out to be equal to 1995 and 990 K, respectively (reference values: 1943 and 933 K).

In the initial stage, a titanium particle was created by excising a sphere of the required size from an ideal crystal. The particle sizes considered ranged from 1.75 to 11 nm. For particles with a diameter below 1.75 nm, pinpointing the onset of crystallization proved challenging, while for particles with a diameter exceeding 11 nm, the impact of the free surface was already relatively small. Free space was simulated around the particle, that is, free boundary conditions and the NPT canonical ensemble were used. Temperature regulation was achieved using a Nose-Hoover thermostat. The time step for integration in the molecular dynamics method was set to 1 fs.

To simulate the aluminum layer around the titanium particle, a shell was created that contained approximately the same number of atoms as the particle. Initially, the shell was also cut out of an aluminum crystal. The thickness of the shell was sufficient, and further increasing it did not affect the results.

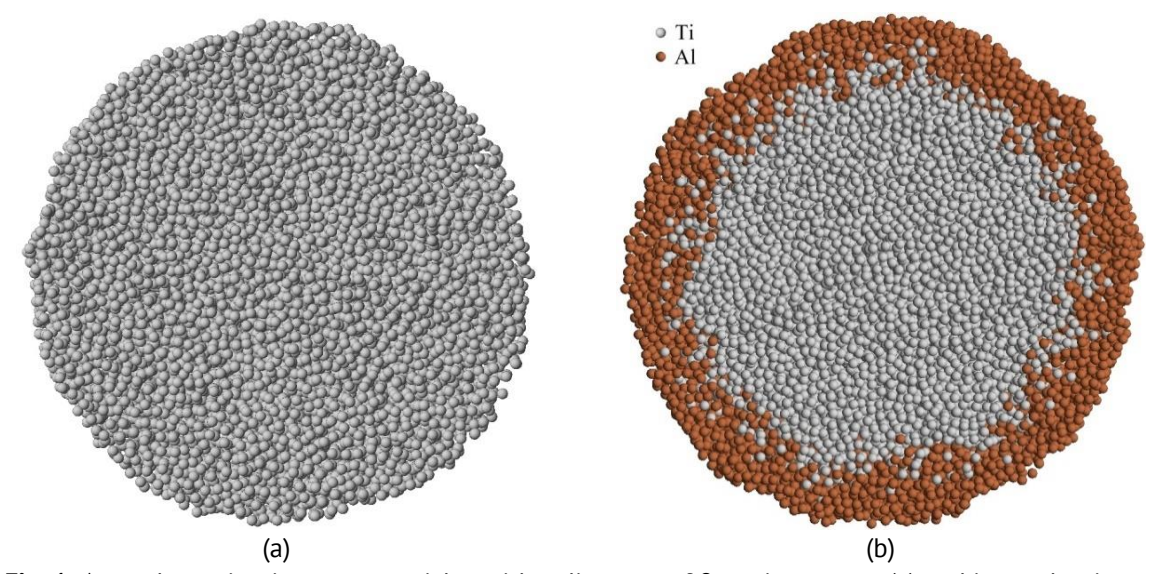


Fig. 1. Amorphous titanium nanoparticles with a diameter of 9 nm in vacuum (a) and in an aluminum shell (b). Particle cross-sections are shown

To produce the amorphous structure of the particles, ultra-fast cooling (with a cooling rate of approximately 10^{16} – 10^{17} K/s) was implemented, following the melting of the particles via heating to 3000 K. At such a rapid cooling rate, homogeneous crystallization is unable to occur, resulting in the formation of an amorphous structure. The quality of the amorphous structure was assessed using radial distribution diagrams

of atoms and the average energy of atoms within the nanoparticle (with further details provided in the subsequent section). Furthermore, the destruction of the crystalline structure of the particles, as well as their crystallization, were typically discernible both visually and through the use of a crystalline phase visualizer. Examples of slices of amorphous titanium particles with a diameter of 9 nm in a vacuum and in an aluminum shell are shown in Fig. 1.

For particles of each size, heating was simulated at a constant rate of $5\cdot10^{11}$ K/s. In similar tasks using molecular dynamics simulation, the rate of temperature change is usually set from 10^{11} to 10^{13} K/s [19–22]. In [20–22], it was shown that temperature change rates of $5\cdot10^{12}$ K/s are already sufficient for homogeneous crystallization to occur. However, the lower the speed, the more accurately the temperature of the phase transition onset can be determined. On the other hand, the longer the computer experiment, the higher the mutual diffusion at the Ti-Al interface, which also affects the accuracy of determining the sintering temperature. According to our previous works [20,21], the speed in the range of $5\cdot10^{11}$ – 10^{12} K/s turned out to be optimal in this case.

Simulation of devitrification was carried out with gradual heating from 700 to 1300 K for titanium particles without a shell and from 800 to 1400 K in the case of the presence of a shell. In both cases, the simulation duration was 1.2 ns.

Results and Discussion

The average potential energy of titanium atoms was chosen as the main characteristic of the nanoparticle structure state. Figure 2 shows the dependencies of the average energy of titanium atoms on temperature for particles with diameters of 7 and 9 nm in vacuum and in an aluminum shell. Dotted lines also show the dependencies for a monocrystalline particle.

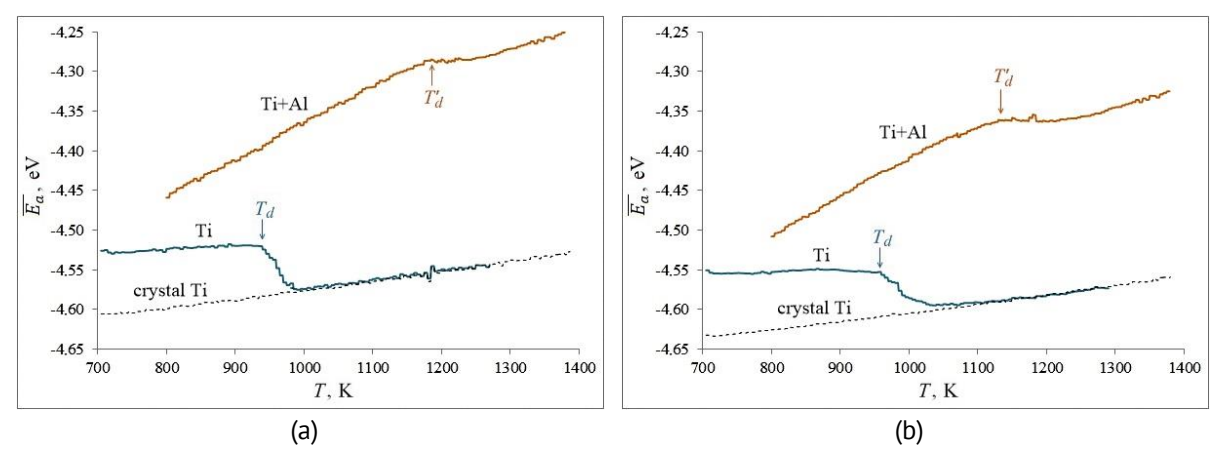


Fig. 2. Dependences of the average potential energy of Ti atoms on temperature during heating at a rate of $5 \cdot 10^{11}$ K/s of an amorphous Ti particle in vacuum and in an aluminum shell: (a) with a diameter of 7 nm; (b) with a diameter of 9 nm. The dotted line shows the dependence for a single-crystal particle. T_d – devitrification temperature of an amorphous particle in vacuum, T'_d – in an aluminum shell

The sharp drops in the average energy of atoms on the graphs correspond to the phase transition — devitrification of amorphous particles during heating. As is known, phase transitions of melting-crystallization do not occur instantly, the crystal-liquid front

moves at a finite speed, which depends on temperature and usually amounts to several tens of meters per second [32,33]. In connection with this, the temperature of melting was determined by the moment of the onset of the phase transition (shown by arrows on the graph).

For particles in vacuum (lower graphs in Fig. 2), devitrification began at a temperature of approximately 940 K for a 7 nm diameter particle and 930 K for a 9 nm diameter particle. These values are higher than experimental ones: according to [34], for alloys with a high titanium content this temperature is about 700 - 800 K. However, it is known that in the molecular dynamics model a relatively long process of nucleation of crystallization centers is required and the beginning of this process is "delayed" at gradual change in temperature, and the higher the rate of temperature change, the higher the "delay" [20–22]. In addition, the potential used has some error in describing the devitrification process, which also affects the determination of the transition temperature.

After devitrification and crystallization of the entire particle in vacuum, the average energy of the atoms almost coincided with the energy of the single-crystalline particle. The considered rate of temperature increase was low enough to form a minimum density of defects during crystallization. If grain boundaries were formed, then, as a rule, they were low-energy — with a high density of coinciding nodes, often twins.

The graphs showing the change in average energy of titanium atoms for particles in an aluminum shell are located above in Fig. 2. This is because some titanium atoms diffused into the aluminum, and the potential energy of these atoms is higher than in the particle's bulk. The greater slope of the dependencies compared to those for particles in vacuum is also explained by diffusion. During the devitrification process of titanium particles in an aluminum shell, the decrease in the average energy of titanium atoms is significantly smaller compared to particles in vacuum, again due to the contribution of diffused titanium atoms in aluminum. After crystallization, the energy growth with increasing temperature became less intense, and the slopes of the dependencies decreased. This is explained by the reduction in the intensity of mutual diffusion in the crystalline state of titanium.

The presence of an aluminum shell, as shown in Fig. 2, significantly affects the devitrification temperature – it begins at a much higher temperature: approximately 1180 and 1130 K for particles with diameters of 7 and 9 nm, respectively.

To quantify the impact of the free surface of nanoparticles on their melting temperature, a mathematical formula is frequently employed, which assumes that the variation in the phase transition temperature is directly proportional to the ratio of the surface area to the volume of the particle. In the case of a spherical particle, this change should be proportional to $N^{-1/3}$ or d^{-1} , where N represents the number of atoms in the particle, and d is its diameter. For the devitrification temperature, we adopted the same assumption, incorporating a correction δ to account for the finite thickness of the surface layer of the particle or the diffusion zone in the case of an aluminum shell [20,21,31]:

$$T_d(d) = T_d^0 - \frac{A}{d - \delta} \tag{1}$$

Here T_d and T_d^0 are the devitrification temperatures of the particle and bulk material; A is a parameter responsible for the degree of influence of the particle surface on its devitrification.

To construct approximation curves for the devitrification temperature of titanium nanoparticles in vacuum and in an aluminum shell, we utilized Eq. (1) and plotted them as dashed lines in Fig. 3. The markers in the figure represent the values derived from our model, which align quite well with the approximation curves. This agreement provides compelling evidence for the dominant influence of the interface, whether it be the free surface or the interphase boundary, in the devitrification process of nanoparticles. Values for Eq. (1) for titanium particles in vacuum: $T_d^0 = 850 \text{ K}$, $A_d = -600 \text{ K} \cdot \text{nm}$, $\delta = 0.4 \text{ nm}$; in an aluminum shell: $T_d^0 = 980 \text{ K}$, $A_d = -970 \text{ K} \cdot \text{nm}$, $\delta = 1.4 \text{ nm}$.

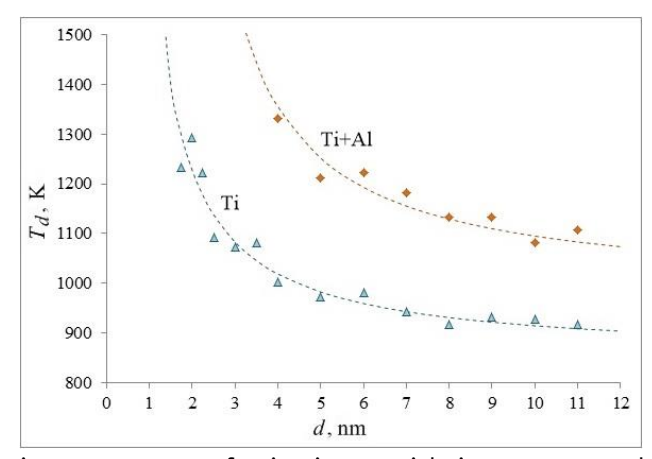


Fig. 3. The devitrification temperature of a titanium particle in a vacuum and in an aluminum shell depending on its diameter. Markers – model results, dotted lines – approximation

As can be seen, the influence of the aluminum shell on the devitrification temperature of titanium particles is quite significant – in the case of its presence, the devitrification temperature is approximately 200 K higher than for particles in vacuum. When considering the diffusion zone and the blurring of the particle boundary, the value of δ increased by 1 nm, which roughly corresponds to the picture observed during modeling.

The value of A in Eq. (1) – the parameter responsible for the degree of influence of the particle boundary on the change in devitrification temperature compared to a massive sample – turned out to be negative. This means that if the melting temperature of nanoparticles decreases with a decrease in particle size, the devitrification temperature, on the contrary, increases. This can be explained as follows. The potential wells in which atoms are located on the surface or near defects are less deep and wider, blurred, due to less regular arrangement of neighboring atoms, thermal vibrations, and diffusion. Therefore, the presence of defects and interfaces reduces the probability of the nucleation of crystallization centers. However, on the other hand, the formation of these centers requires a certain mobility of atoms, that is, self-diffusion, which is more intense near the surface. This is well seen in Fig. 4, where the crystallization mechanism during devitrification was studied using a crystal phase visualizer. This visualizer determines the belonging of each atom to a certain crystalline structure based on the analysis of the

arrangement of neighboring atoms. In this case, a Ti atom was considered to belong to the hcp or fcc lattice if more than 75 % of its nearest neighbors (in this case, the number of nearest neighbors for atoms on the surface is approximately two times less than in the volume) were located close to the nodes of an ideal hcp or fcc crystal (accounting for thermal expansion) within a specified tolerance of 25 % from the radius of the first coordination sphere. Ti atoms that did not meet these conditions were considered to belong to an amorphous structure. It should be noted that the values of 75 and 25% were variable.

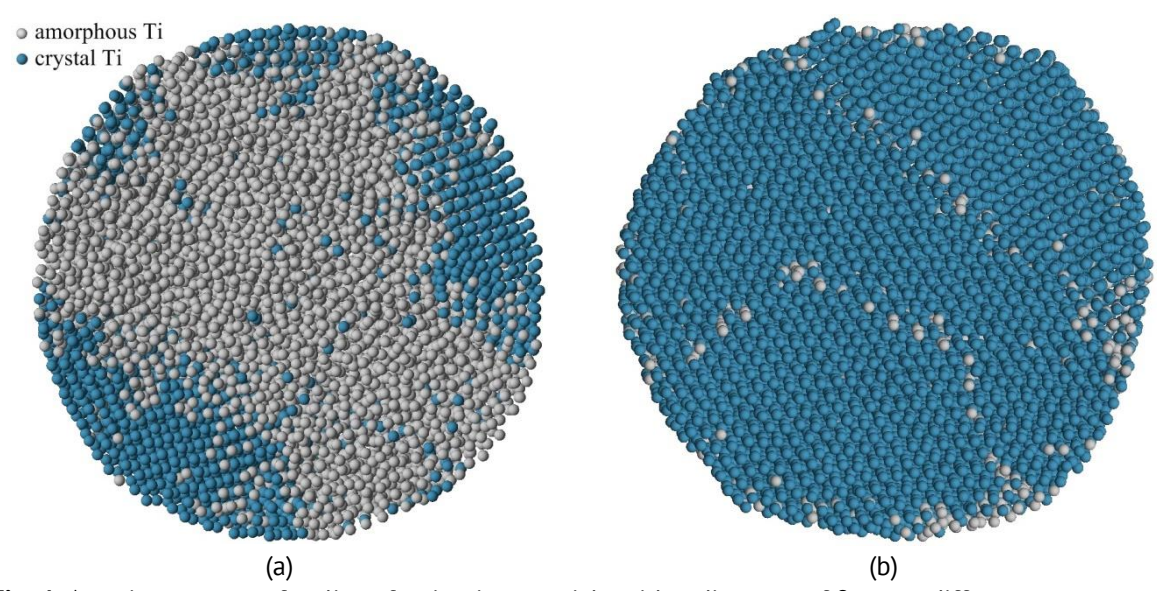


Fig. 4. Atomic structure of a slice of a titanium particle with a diameter of 9 nm at different moments of the devitrification process: (a) at the moment of formation of crystallization centers when the temperature reaches 890 K; (b) after the completion of crystallization. Green color highlights atoms with a nearest environment corresponding to a crystalline structure, gray – amorphous

As can be seen in Fig. 4, the formation of a crystalline structure occurs during devitrification from the surface, which is explained by a relatively larger contribution of self-diffusion near the surface in this case. After crystallization in the volume of the particle, as shown in the example, three grains were formed, separated by grain boundaries with relatively low energy (high density of coinciding nodes).

In the case of having an aluminum shell, the devitrification mechanism changed drastically (Fig. 5) – crystallization nuclei were formed not near the boundary but, typically, within the core of the titanium particle. Here, the factor of high mobility near the boundary disappears, and the formation of relatively deeper and narrower potential wells in the core of the particle takes precedence. Additionally, aluminum atoms, along with the presence of a diffusion zone, lead to the blurring of potential wells and a decrease in the likelihood of crystallization nuclei appearing near the interfacial boundary.

As for the aluminum shell, it was in an amorphous state throughout the entire heating simulation. When the starting bimetallic particles were created, it suddenly melted and cooled along with the Ti core (Fig. 1(b)). The devitrification of the Ti core upon subsequent heating occurred at a temperature above the melting point of aluminum.

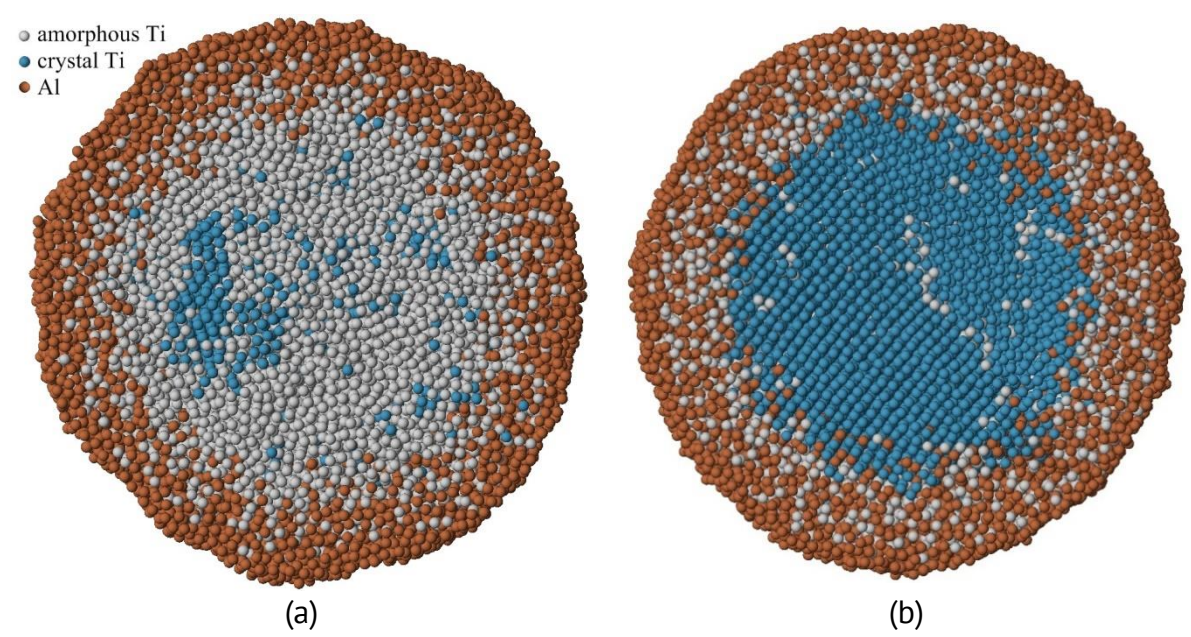


Fig. 5. Atomic structure of a slice of a titanium particle with a diameter of 9 nm in an aluminum shell at different moments of the devitrification process: (a) at the moment of formation of crystallization centers when the temperature reaches 1120 K; (b) after the completion of crystallization

The obtained result, i.e., the increase in the temperature range of the amorphous phase of metal nanoparticles in the shell of another metal, can likely be qualitatively extended to other binary systems. Moreover, a more significant influence of the shell on the increase in the devitrification temperature is probably expected with a greater difference in the radii of atoms of the two metals.

Conclusions

The molecular dynamics method was used to study the devitrification process of titanium nanoparticles in vacuum and in an aluminum shell during heating at a rate of $5\cdot10^{11}$ K/s. The investigation revealed that the devitrification temperature, in comparison to a massive sample, exhibits an inverse proportionality to the particle diameter, with a correction that accounts for the finite width of the surface layer or diffusion zone in the case of an aluminum shell. As the particle size diminishes, leading to an increased proportion of atoms in close proximity to the boundary, the devitrification temperature rises. The presence of an aluminum shell significantly increases the devitrification temperature of titanium nanoparticles – for the considered particle sizes, the difference was about 200 K. Thus, reducing the size of titanium particles and the presence of an aluminum shell increase the temperature range of the existence of the amorphous phase of titanium. The mechanisms of crystalline phase formation in particles in vacuum and in an aluminum shell differ significantly: in the first case, crystalline nuclei are formed near the surface, while in the second, on the contrary, in the volume of the particle.

References

- 1. Schwarz JA, Lyshevski SE, Contescu CI. (eds.) *Dekker encyclopedia of nanoscience and nanotechnology*. Third ed. Boca Raton: CRC Press; 2014.
- 2. Liang S-X, Zhang LC, Reichenberger S, Barcikowski S. Design and perspective of amorphous metal nanoparticles from laser synthesis and processing. *Physical Chemistry Chemical Physics*. 2021;23: 11121–11154.
- 3. Sun J, Sinha SK, Khammari A, Picher M, Terrones M, Banhart F. The amorphization of metal nanoparticles in graphitic shells under laser pulses. *Carbon*. 2020;161: 495–501.
- 4. He DS, Huang Y, Myers BD, Isheim D, Fan X, Xia G-J, Deng Y, Xie L, Han S, Qiu Y, Wang Y-G, Luan J, Jiao Z, Huang L, Dravid VP, He J. Single-element amorphous palladium nanoparticles formed via phase separation. *Nano Research*. 2022;15: 5575–5580.
- 5. Qian Y, Silva A, Yu E, Anderson CL, Liu Y, Theis W, Ercius P, Xu T. Crystallization of nanoparticles induced by precipitation of trace polymeric additives. *Nature Communications*. 2021;12: 2767.
- 6. Pei Y, Zhou G, Luan N, Zong B, Qiao M, Tao F. Synthesis and catalysis of chemically reduced metalmetalloid amorphous alloys. *Chemical Society Reviews*. 2012;41: 8140–8162.
- 7. Jia Z, Wang Q, Sun L, Wang Q, Zhang LC, Wu G, Luan JH, Jiao ZB, Wang A, Liang SX, Gu M, Lu J. Metallic glass catalysts: attractive in situ self-reconstructed hierarchical gradient structure of metallic glass for high efficiency and remarkable stability in catalytic performance. *Advanced Functional Materials*. 2019;29: 1807857.
- 8. Chen Q, Yan Z, Guo L, Zhang H, Zhang L-C, Wang W. Role of maze like structure and Y_2O_3 on Al-based amorphous ribbon surface in MO solution degradation. *Journal of Molecular Liquids*. 2020;318: 114318.
- 9. Yang BJ, Yao JH, Zhang J, Yang HW, Wang JQ, Ma E. Al-rich bulk metallic glasses with plasticity and ultrahigh specific strength. *Scripta Materialia*. 2009;61: 423–426.
- 10. Schroers J, Johnson WL. Ductile bulk metallic glass. *Physical Review Letters*. 2004;93: 255506.
- 11. Wagener P, Jakobi J, Rehbock C, Chakravadhanula VSK, Thede C, Wiedwald U, Bartsch M, Kienleand L, Barcikowski S. Solvent-surface interactions control the phase structure in laser-generated iron-gold coreshell nanoparticles. *Scientific Reports*. 2016;6: 23352.
- 12. Ziefub AR, Reichenberger S, Rehbock C, Chakraborty I, Gharib M, Parak WJ, Barcikowski S. Laser fragmentation of colloidal gold nanoparticles with high-intensity nanosecond pulses is driven by a single-step fragmentation mechanism with a defined educt particle-size threshold. *The Journal of Physical Chemistry C.* 2018;122: 22125–22136.
- 13. Amikura K, Kimura T, Hamada M, Yokoyama N, Miyazaki J, Yamada Y. Copper oxide particles produced by laser ablation in water. *Applied Surface Science*. 2008;254: 6976–6982.
- 14. Barcikowski S, Compagnini G. Advanced nanoparticle generation and excitation by lasers in liquids. *Physical Chemistry Chemical Physics*. 2013;15: 3022–3026.
- 15. Buffat P, Borel J-P. Size effect on the melting temperature of gold particles. *Physical Review A*. 1976;13: 2287.
- 16. Allen GL, Bayles RA, Gile WW, Jesser WA. Small particle melting of pure metals. *Thin Solid Films*. 1986;144: 297–308.
- 17. Castro T, Reifenberger R, Choi E, Andres RP. Size-dependent melting temperature of individual nanometer-sized metallic clusters. *Physical Review B*. 1990;42: 8548.
- 18. Chepkasov IV, Gafner YY, Vysotin MA, Redel LV. A study of melting of various types of Pt-Pd nanoparticles. *Physics of the Solid State*. 2017;59: 2076–2081.
- 19. Qi Y, Cagin T, Johnson WL, Goddard III WA. Melting and crystallization in Ni nanoclusters: the mesoscale regime. *The Journal of Chemical Physics*. 2001;115: 385–394.
- 20. Poletaev GM, Bebikhov YV, Semenov AS. Molecular dynamics study of the formation of the nanocrystalline structure in nickel nanoparticles during rapid cooling from the melt. *Materials Chemistry and Physics*. 2023;309: 128358.
- 21. Poletaev GM, Gafner YY, Gafner SL. Molecular dynamics study of melting, crystallization and devitrification of nickel nanoparticles. *Letters on Materials*. 2023;13(4): 298–303.
- 22. Nguyen TD, Nguyen CC, Tran VH. Molecular dynamics study of microscopic structures, phase transitions and dynamic crystallization in Ni nanoparticles. *RSC Advances*. 2017;7: 25406–25413.
- 23. Boldyrev VV, Tkacova K. Mechanochemistry of solids: past, present, and prospects. *Journal of Materials Synthesis and Processing*. 2000;8: 121–132.
- 24. Filimonov VY, Loginova MV, Ivanov SG, Sitnikov AA, Yakovlev VI, Sobachkin AV, Negodyaev AZ, Myasnikov AY. Peculiarities of phase formation processes in activated Ti+Al powder mixture during

transition from combustion synthesis to high-temperature annealing. *Combustion Science and Technology*. 2020;192: 457–470.

- 25. Loginova MV, Yakovlev VI, Filimonov VY, Sitnikov AA, Sobachkin AV, Ivanov SG, Gradoboev AV. Formation of structural states in mechanically activated powder mixtures Ti+Al exposed to gamma irradiation. *Letters on Materials*. 2018;8: 129–134.
- 26. Poletaev GM, Bebikhov YV, Semenov AS, Sitnikov AA. Molecular dynamics investigation of the effect of the interface orientation on the intensity of titanium dissolution in crystalline and amorphous aluminum. *Journal of Experimental and Theoretical Physics.* 2023;136(4): 477–483.
- 27. Poletaev GM, Bebikhov YV, Semenov AS, Sitnikov AA, Yakovlev VI. Molecular dynamics study of the dissolution of titanium nanoparticles in aluminum. *Materials Physics and Mechanics*. 2023;51(5): 9–15.
- 28. Zope RR, Mishin Y. Interatomic potentials for atomistic simulations of the Ti-Al system. *Physical Review B*. 2003;68: 024102.
- 29. Kim Y-K, Kim H-K, Jung W-S, Lee B-J. Atomistic modeling of the Ti-Al binary system. *Computational Materials Science*. 2016;119: 1–8.
- 30. Pei Q-X, Jhon MH, Quek SS, Wu Z. A systematic study of interatomic potentials for mechanical behaviours of Ti-Al alloys. *Computational Materials Science*. 2021;188: 110239.
- 31. Poletaev G, Gafner Y, Gafner S, Bebikhov Y, Semenov A. Molecular dynamics study of the devitrification of amorphous copper nanoparticles in vacuum and in a silver shell. *Metals*. 2023;13(10): 1664.
- 32. Chan W-L, Averback RS, Cahill DG, Ashkenazy Y. Solidification velocities in deeply undercooled silver. *Physical Review Letters*. 2009;102: 095701.
- 33. Zhang HY, Liu F, Yang Y, Sun DY. The molecular dynamics study of vacancy formation during solidification of pure metals. *Scientific Reports*. 2017;7: 10241.
- 34. Susic MV. Kinetics of devitrification (crystallization) of amorphous titanium. *Materials Chemistry and Physics*. 1985;12: 99–109.

About Authors

Gennady M. Poletaev 🗓 Sc

Doctor of Physical and Mathematical Sciences Leading Researcher (Khakass State University, Abakan, Russia) Head of Department (Polzunov Altai State Technical University, Barnaul, Russia)

Yuri Ya. Gafner 🗓 Sc

Doctor of Physical and Mathematical Sciences Head of Department (Khakass State University, Abakan, Russia)

Svetlana L. Gafner D Sc

Doctor of Physical and Mathematical Sciences Professor (Khakass State University, Abakan, Russia)

Irina V. Zorya 🗓 Sc

Doctor of Physical and Mathematical Sciences Head of Department (Siberian State Industrial University, Novokuznetsk, Russia)

Yuriy V. Bebikhov 🗓 Sc

Candidate of Physical and Mathematical Sciences
Assistant Professor (Polytechnic Institute of North-Eastern Federal University, Mirny, Russia)

Alexander S. Semenov D Sc

Doctor of Physical and Mathematical Sciences Director of the Institute (Polytechnic Institute of North-Eastern Federal University, Mirny, Russia) Submitted: February 1, 2023 Revised: March 6, 2024 Accepted: June 10, 2024

Interaction of two circular holes in an infinite plate by body force method

S.M. Badiger ^{1 ™}, D.S. Ramakrishna ²

- ¹ M.S. Ramaiah University of Applied Sciences, Bengaluru, India
- ² Jawaharlal Nehru National College of Engineering, Shivamogga, India
- [™] krishnabadiqer@yahoo.com

ABSTRACT

The body force method is used to perform stress analysis around two circular holes with equal and different sizes in an infinite plate subjected to uni-axial loading. The elasticity solution for a point force in an infinite plate is used as the fundamental solution. Traction free boundary conditions are satisfied at the midpoint of segments. Stress concentration factors obtained by body force method are compared with the results available in the literature. It is noted, accurate results are obtained with small number of segments of the discontinuity. The body force method is simple, yet robust method useful in performing stress analysis of bodies with discontinuities.

KEYWORDS

two unequal circular holes • body force method • stress concentration factor • infinite plate • uni-axial loading

Acknowledgements. The authors would like to thank Mahesh Varpe and Kiran Hubballi for their generosity and permitting to use computing facility. No external funding was received for this study.

Citation: Badiger SM, Ramakrishna DS. Interaction of two circular holes in an infinite plate by body force method. *Materials Physics and Mechanics*. 2024;52(3): 96–107.

http://dx.doi.org/10.18149/MPM.5232024_10

Introduction

In many structural applications, multiple holes are used to achieve required functionality. In applications where multiple holes exist, interaction of holes and its effect on stress concentration factor becomes important consideration to a design engineer. In this regard, interaction of two circular holes (Fig. 1) has attracted attention of many researchers. Ling [1] employed bipolar coordinates, taking advantage of double symmetry solved the problem of two equal circular holes with all around tension, longitudinal tension and transverse tension cases. Davies [2] obtained approximate solutions to the problem of two unequal circular holes employing complex variable technique. The method employed is restricted because of collocation on one of the boundaries. Haddon [3] obtained closed form solution in series form, using complex variable technique for the case of two unequal circular holes. Stress concentration factor (SCF) was computed for the case of angle α (angle between line connecting centers of the holes and the far field uniform tension) equal to 0°, 90° and 45°. Salerno [4] employed complex variable technique, Schwartz Alternating Method with successive approximations to obtain stress distribution around two unequal circular holes under equal biaxial stresses. Miyata [5] investigated stresses around two circular holes in an infinite plate subjected to biaxial tension using complex variable method with method of successive approximations. Miyata presented numerical results for uniaxial longitudinal tension and transverse tension. In a finite plate, Erickson [6] used 2D photoelasticity and obtained the optimum size and locations of multiple ancillary holes near central hole. Iwaki [7] used bipolar coordinates and obtained explicit solution for stresses around two unequal circular holes subjected to far-field uniform tension, uniform internal pressure and uniform shearing stresses along a hole. Horii [8] used method of pseudotractions and obtained SCF around (a) two circular holes (b) three circular holes in a row (c) infinite row of equal circular holes in an infinite plate under uniaxial longitudinal tension and transverse tension. This method was also used to obtain stress intensity factor (SIF) in the case of (a) two cracks and (b) infinite rows collinear/parallel cracks. Duan [9] used integral equation technique to study (a) hole to edge dislocation interaction (b) hole to hole interaction (c) hole to free boundary interaction. Chiang [10] obtained SCF around two unequal circular holes using a numerical method which resembles the method of fundamental solutions for longitudinal tension and transverse tension cases. To study the interaction between existing major holes (three holes) and the "defense" hole system (addition of two, four smaller holes) in a plate under uniaxial tension, Meguid [11] conducted analytical, finite element analysis and photoelastic tests. For the problem of two circular holes in plane stress and uniform internal pressure inside the holes, Hoang [12] derived explicit expression for the stress distribution near holes. Ukadgaonker [13] investigated SCF around two unequal circular holes in an infinite plate under longitudinal tension and transverse tension cases using Schwarz Alternating Method. Kuo [14] studied degenerate scale problem of the infinite plane containing two equal circular holes. Zeng [15] obtained optimal shape of two closely spaced holes under biaxial loading using differential-evolution algorithm to compute coefficients of mapping function. Mohan [16] performed stress analysis of rectangular plates with two symmetrical circular holes under uniaxial tension for two material types (PLA, PLA/15%carbon) and compared results from experiments and finite element method. Gandilyan [17] solved the problem of two equal holes in a plane subjected to biaxial tension using bipolar coordinates and series expansion taking into account the effects of surface elasticity. Patel [18] obtained expression for tangential stress concentration factor around an elliptical hole in a large rectangular plate subjected to linearly varying in-plane loading on two opposite edges. Yang [19] designed 5 crack models and studied the propensity of forming the hook pattern. Simulations were carried out for the two borehole case employing the 5 models using the T-stress at the crack tip and the incremental crack growth method is adopted to simulate the crack propagation paths. Ma [20] proposed solution to elastoplastic problem of an infinite medium containing two equal circular holes. The preconditions followed are the two plastic regions formed are disconnected with each other, and each plastic region can completely surround each hole. The influences of the separation distance between the two holes and the loads on the plastic regions were analyzed. Maksymovych [21] studied stress concentration at closely placed holes in wing bearing area of anisotropic plate. Asymptotic formula for stresses near holes was employed, implementation of the approach was carried out using Boundary Integral equation method and method of least squares.

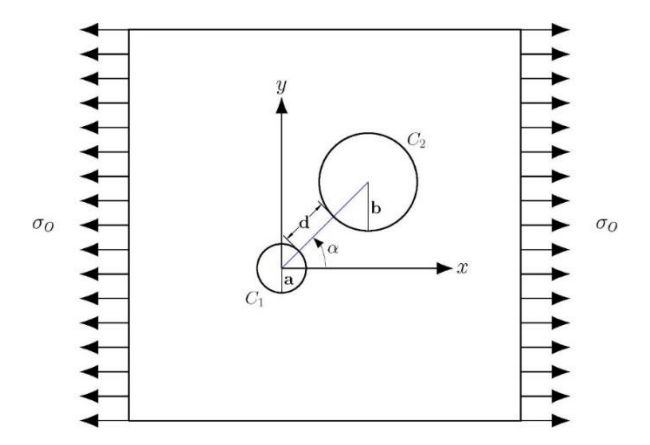


Fig. 1. Two circular holes in an infinite plate under uniaxial tension

The body force method has been used in the present work to examine the interaction of two circular holes in isotropic infinite plate under uni-axial tension. Ratio of diameters (b/a) is varied from 1 to 10, ratio of distance between holes to diameter a, (d/a) is varied from 0.4 to 10 and angle (α) between the line joining two centers and direction of uniaxial tension is varied from 0° to 90°. In the next section description of body force method is provided. In the "Body force method applied to two circular holes" section, application of body force method is discussed. In the "Numerical results and Discussion" section, numerical results along with plots, discussion and comparison with data from literature are presented followed by concluding remarks in the "Conclusions" section.

Body force method

Nisitani [22-24] originally proposed the body force method (BFM) which is a boundary integral type approach helpful in performing stress analysis. Detailed account of BFM can be found in [25]. In using BFM, actual discontinuity (for e.g. circular hole) present in an infinite plate is visualized as an imaginary condition, i.e. infinite plate with a hole is treated as a plate without hole. The hole is visualized as an imaginary curve divided into M number of segments forming its boundary. In order to achieve traction free boundary condition at the boundary of the imaginary curve, at the midpoints of segments on its periphery, body force densities (ρ_{xi}, ρ_{vi}) are applied. Influence coefficients are computed from the equations of stress field in an infinite plate due to a point force and the boundary conditions of traction free at the midpoint of each segment are applied and body force densities are obtained. At each given point in the plate, stress produced is computed by a linear combination of the body force densities.

The stresses at location (x, y) in an infinite plate, due to concentrated point force **X** and **Y** acting at (ξ, η) are as follows.

$$\sigma_x^X = -F l \{ (3+\nu)l^2 + (1-\nu)m^2 \} X, \tag{1}$$

$$\sigma_y^X = F l \{ (1 - \nu)l^2 - (1 + 3\nu)m^2 \} X, \tag{2}$$

$$\sigma_{x}^{X} = -F l \{ (3 + \nu)l^{2} + (1 - \nu)m^{2} \} X,$$

$$\sigma_{y}^{X} = F l \{ (1 - \nu)l^{2} - (1 + 3\nu)m^{2} \} X,$$

$$\tau_{xy}^{X} = -F m \{ (3 + \nu)l^{2} + (1 - \nu)m^{2} \} X,$$
(3)

$$\sigma_x^Y = -F \, m \, \{ (1+3\nu)l^2 - (1-\nu)m^2 \, \} \, Y, \tag{4}$$

$$\sigma_y^Y = -F \, m \left\{ (1 - \nu)l^2 + (3 + \nu)m^2 \right\} Y, \tag{5}$$

$$\tau_{xy}^{Y} = -F l \{ (1 - \nu)l^2 + (3 + \nu)m^2 \} Y, \tag{6}$$

where

$$l = \frac{x - \xi}{y},\tag{7}$$

$$m = \frac{y - \eta}{y},\tag{8}$$

$$F = \frac{1}{4\pi y (l^2 + m^2)^2}. (9)$$

The effect of point force X or Y applied at (ξ,η) are computed from stress fields and these form the influence coefficients. As the relations $-d\xi=a\sin\theta\,d\theta$ and $d\eta=b\cos\theta\,d\theta$ prevail along the ellipse $(\xi=a\cos\theta\,,\eta=b\sin\theta)$, the coefficients can be expressed as:

$$\sigma_{xM}^{XN} = \int_{N} \sigma_{x}^{X}(\xi, \eta, x, y) \ b \cos \theta \ d\theta \ at \ X = 1, \tag{10}$$

$$\sigma_{yM}^{XN} = \int_{N}^{X} \sigma_{y}^{X}(\xi, \eta, x, y) \ b \cos \theta \ d\theta \ at \ X = 1, \tag{11}$$

$$\tau_{xyM}^{XN} = \int_{N} \tau_{xy}^{X}(\xi, \eta, x, y) \ b \cos \theta \ d\theta \ at \ X = 1, \tag{12}$$

and

$$\sigma_{xM}^{YN} = \int_{N} \sigma_{x}^{Y}(\xi, \eta, x, y) \ a \sin \theta \ d\theta \ at \ Y = 1, \tag{13}$$

$$\sigma_{vM}^{YN} = \int_{N} \sigma_{v}^{Y}(\xi, \eta, x, y) \ a \sin \theta \ d\theta \ at \ Y = 1, \tag{14}$$

$$\tau_{xyM}^{YN} = \int_{N} \tau_{xy}^{Y}(\xi, \eta, x, y) \ a \sin \theta \ d\theta \ at \ Y = 1, \tag{15}$$

where \int_{N} represents integration of the N-th interval.

The Influence Coefficients σ_{xM}^{XN} , σ_{xM}^{YN} , σ_{yM}^{XN} , σ_{yM}^{YN} , τ_{xyM}^{XN} , τ_{xyM}^{YN} are the stresses at the mid-point of the M-th interval due to a body force on the N-th interval having unit body force densities ($\rho_x = 1$ or $\rho_y = 1$).

Applying the boundary conditions which result in stress-free midpoints for each interval lead to:

$$\sum_{N=1}^{MM} \rho_{xN} \left(\sigma_{xM}^{XN} \cos \varphi_M + \tau_{xyM}^{XN} \sin \varphi_M \right) + \sum_{N=1}^{MM} \rho_{yN} \left(\sigma_{xM}^{YN} \cos \varphi_M + \tau_{xyM}^{YN} \sin \varphi_M \right) = -\sigma_0 \cos \varphi_M, \tag{16}$$

$$\sum_{N=1}^{MM} \rho_{xN} \left(\tau_{xyM}^{XN} \cos \varphi_M + \sigma_{yM}^{XN} \sin \varphi_M \right) + \sum_{N=1}^{MM} \rho_{yN} \left(\tau_{xyM}^{YN} \cos \varphi_M + \sigma_{yM}^{YN} \sin \varphi_M \right) = 0, \tag{17}$$

where ρ_{xN} , ρ_{yN} represent body force densities acting on the N-th interval along x and y direction respectively, σ_0 stress at infinity along x-direction and φ_M represents the angle between the x-axis and the ellipse's normal at the midpoint of the M-th interval: $\varphi_M = \tan^{-1}\left(\frac{a}{b}\tan\theta_M\right)$. Equations (16) and (17) results in 2M linear equations in 2M unknowns ρ_{xN} , ρ_{yN} .

A set of linear equations result from Eqs. (16) and (17) in matrix form is Ax = b, where A is a square matrix (size $2M \times 2M$) known as influence coefficient matrix (ICM) due to terms inside the brackets, x is body force density column vector and column vector b is the right hand side of Eqs. (16) and (17) representing traction due to applied uni-axial far field load.

The linear combination of the influence coefficients and body force densities at arbitrary point Q(x, y) in an infinite plate is employed to calculate the stresses at Q(x, y).

$$\sigma_{x} = \sum_{N=1}^{MM} \left(\rho_{xN} \sigma_{xP}^{XN} + \rho_{yN} \sigma_{xP}^{YN} \right) + \sigma_{0}, \tag{18}$$

$$\sigma_{y} = \sum_{N=1}^{MM} (\rho_{xN} \sigma_{yP}^{XN} + \rho_{yN} \sigma_{yP}^{YN}), \tag{19}$$

$$\tau_{xy} = \sum_{N=1}^{MM} (\rho_{xN} \tau_{xyP}^{XN} + \rho_{yN} \tau_{xyP}^{YN}). \tag{20}$$

Radial, hoop and shear stresses are computed using appropriate stress transformation.

Body force method applied to two circular holes

Two circular holes are divided into 4 segments, at the midpoint of each segments, body force densities (ρ_{xi} , ρ_{yi}) are applied. This arrangement is shown in Fig. 2. Influence coefficient matrix (ICM) takes the following form:

$$A = \begin{bmatrix} A_{11} & A_{12} \\ A_{22} & A_{22} \end{bmatrix}, \tag{21}$$

where A_{11} is the ICM (obtained from Eqs. (16) and (17) of circular hole C_1 due to body force densities ((ρ_{x1} , ρ_{y1}) to (ρ_{x4} , ρ_{y4})) applied on the segments of circular hole C_1 . A_{12} is the ICM (obtained from Eqs. (16) and (17)) of circular hole C_1 due to body force densities ((ρ_{x5} , ρ_{y5}) to (ρ_{x8} , ρ_{y8})) applied on the segments of circular hole C_2 . A_{21} is the ICM (obtained from Eqs. (16) and (17)) of circular hole C_2 due to body force densities ((ρ_{x1} , ρ_{y1})) to (ρ_{x4} , ρ_{y4})) applied on the segments of circular hole C_1 . A_{22} is the ICM (obtained from Eqs. (16) and (17)) of circular hole C_2 due to body force densities ((ρ_{x5} , ρ_{y5}) to (ρ_{x8} , ρ_{y8})) applied on the segments of circular hole C_2 . The body force density vector and traction vector on each segment due to applied uni-axial load takes the following form:

$$\mathbf{x}^{T} = \begin{bmatrix} \rho_{x1} & \rho_{y1} & \rho_{x2} & \rho_{y2} & \rho_{x3} & \rho_{y3} & \rho_{x4} & \rho_{y4} & \rho_{x5} & \rho_{y5} & \rho_{x6} & \rho_{y6} & \rho_{x7} & \rho_{y7} & \rho_{x8} & \rho_{y8} \end{bmatrix}$$

$$\mathbf{b}^{T} = \begin{bmatrix} -\sigma_{0} \cos \varphi_{1} & 0 & -\sigma_{0} \cos \varphi_{2} & 0 & -\sigma_{0} \cos \varphi_{3} & 0 & -\sigma_{0} \cos \varphi_{4} & 0 \\ -\sigma_{0} \cos \varphi_{5} & 0 & -\sigma_{0} \cos \varphi_{6} & 0 & -\sigma_{0} \cos \varphi_{7} & 0 & -\sigma_{0} \cos \varphi_{8} & 0 \end{bmatrix}$$
(22)

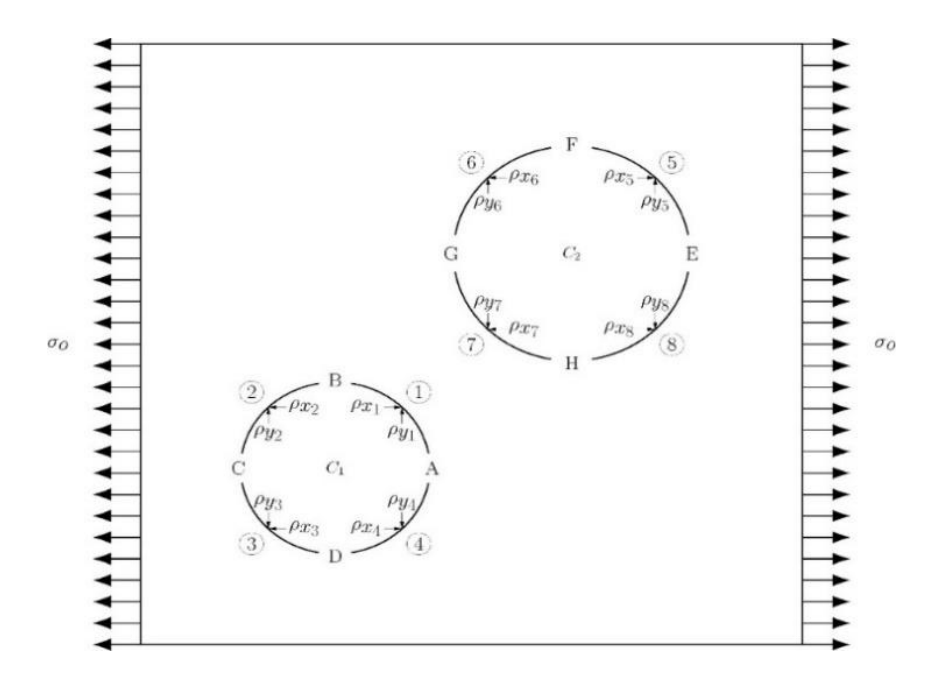


Fig. 2. An infinite plate under uni-axial tension with body force densities (ρ_{xi}, ρ_{yi}) applied at the midpoints of 4 segments of the two circular holes

Location of circular hole C_1 is fixed with center at (0,0) and radius a=1 is held constant, circular hole C_2 with center at (x_{c_2},y_{c_2}) and radius b is varied. Values of radius b are varied from 1 to 10. Center to center distance l is related to radii of circular holes using the relation l=a+d+b. The values of l are chosen such that the ratio d/a varies from 0.4 to 10. Angle α is varied from 0° to 90°. Both circular holes (C_1, C_2) are divided into 4 segments.

Numerical results and Discussion

A geometric configuration is first chosen (values of a, b, d, α , σ_o), Cartesian stresses are then computed (using Eqs. (18)–(20)) in the vicinity of the circular holes. Using stress transformation relationships, radial, hoop and shear stresses are computed. Hoop stress is extrapolated on the boundaries of the holes. Maximum value of hoop stress (occurring on the boundary of either of the holes) is identified and stress concentration factor (SCF) is computed. Figure 3 shows hoop stress variation along the boundary of holes (C_1 , C_2) for configuration a = 1 mm, $\sigma_o = 1$ MPa and $\alpha = 45^\circ$. Hoop stress varies in sinusoidal form on the hole boundary. SCF is computed for various values of b, d, α with uni-axial far field stress $\sigma_o = 1$ MPa and plots drawn are shown in Figs. 4–9.

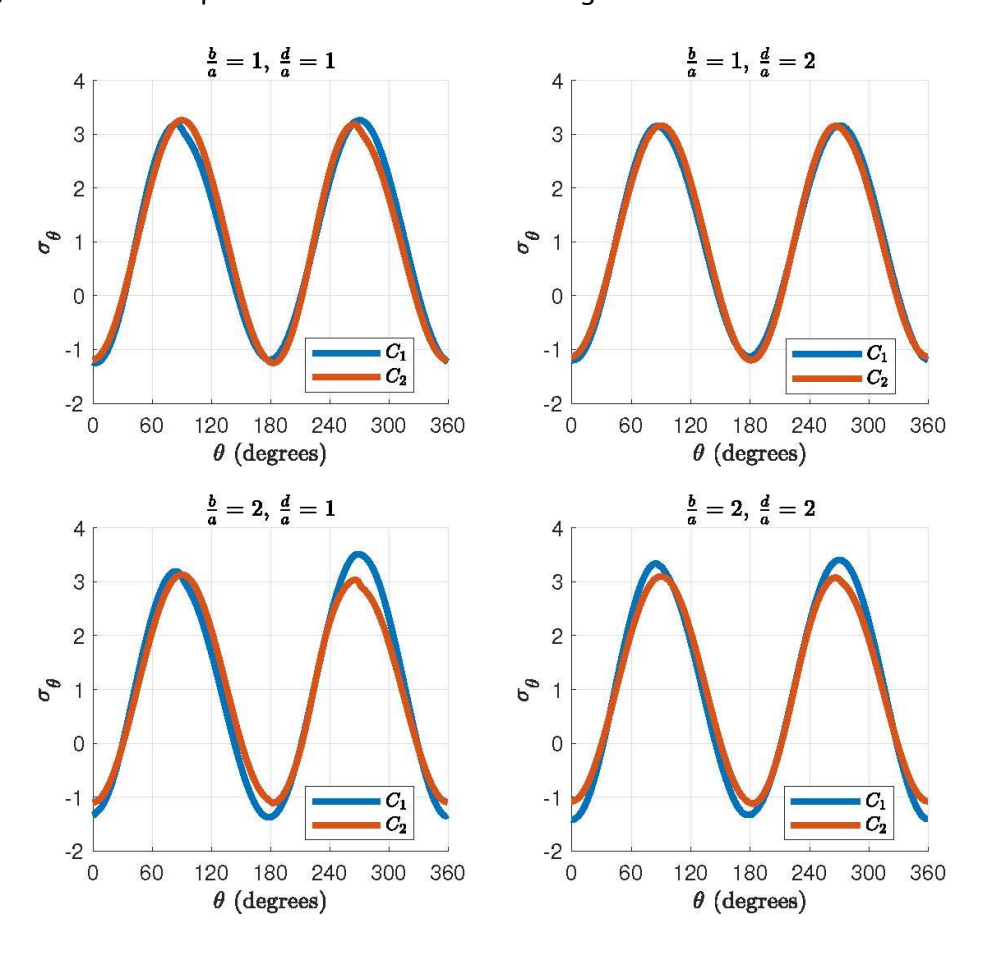


Fig. 3. Hoop stress variation on the hole boundary (C₁, C₂) for angle $\alpha = 45^{\circ}$

Figure 4 shows plots of variation of SCF with angle α . These plots are generated at fixed values of ratio $^b/_a$ and the individual curves correspond to a particular value of the ratio $^d/_a$ as shown in the legend. The value of SCF remains well below 2.65 when two circular holes are equal in diameter, located farthest away from each other irrespective of the angle α . The value of SCF remains close to 3.0 when $b \geq 2a$ and angle α does not exceeds 30°. Maximum value of SCF shifts from 78° to 90° with increase in ratio $^b/_a$ and shortest hole distance.

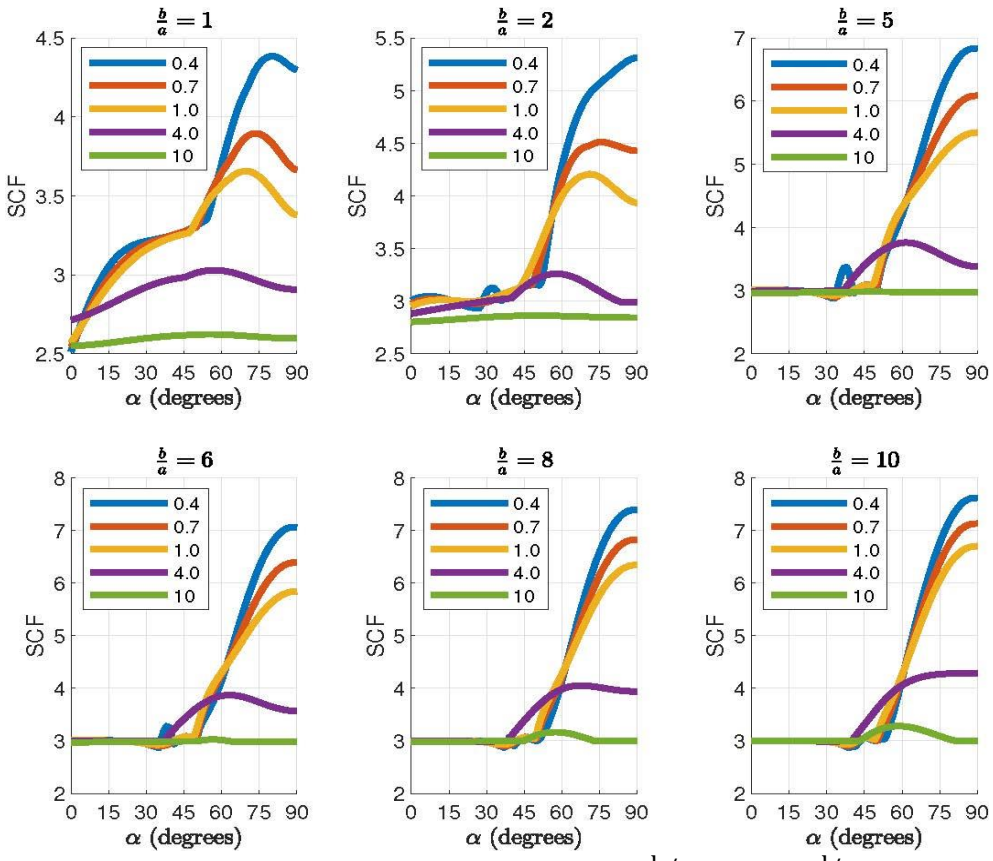
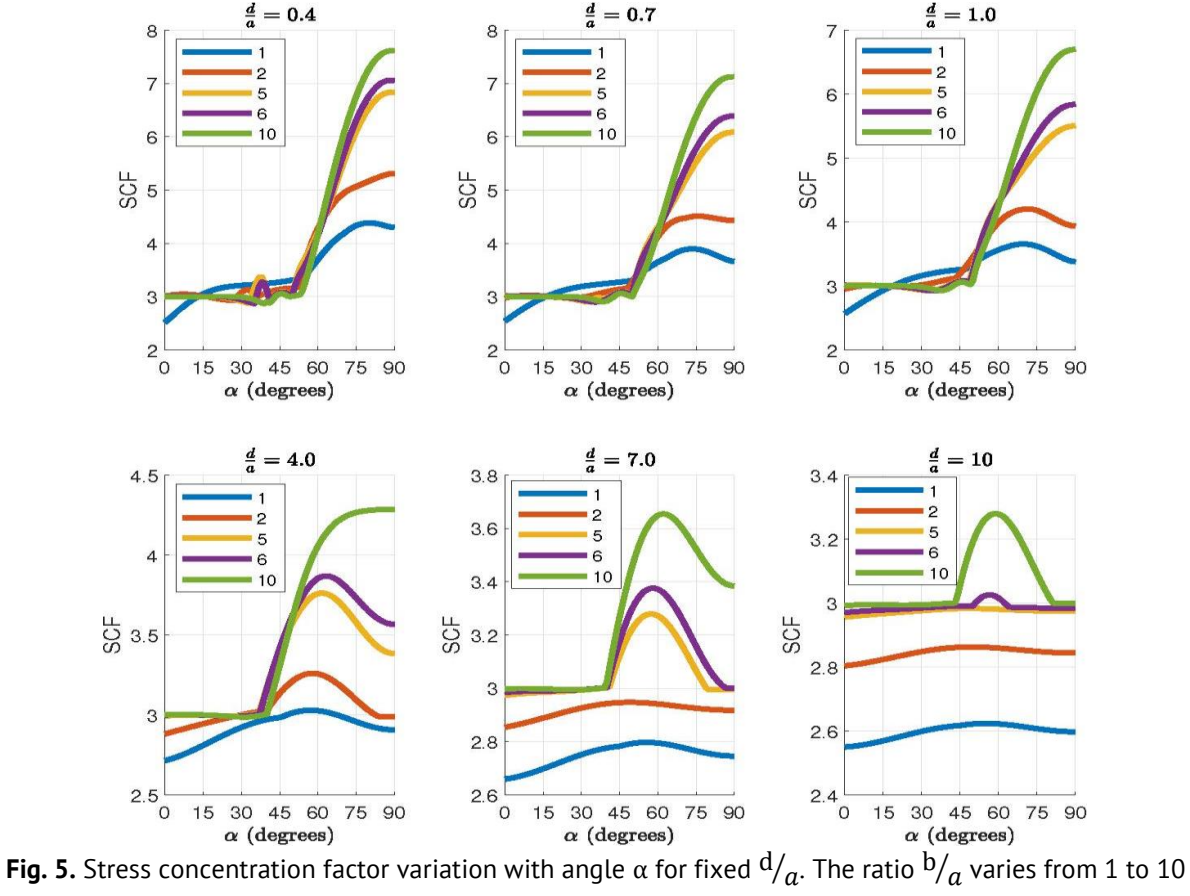


Fig. 4. Stress concentration factor variation with angle α for fixed $^b/_a$. The ratio $^d/_a$ varies from 0.4 to 10



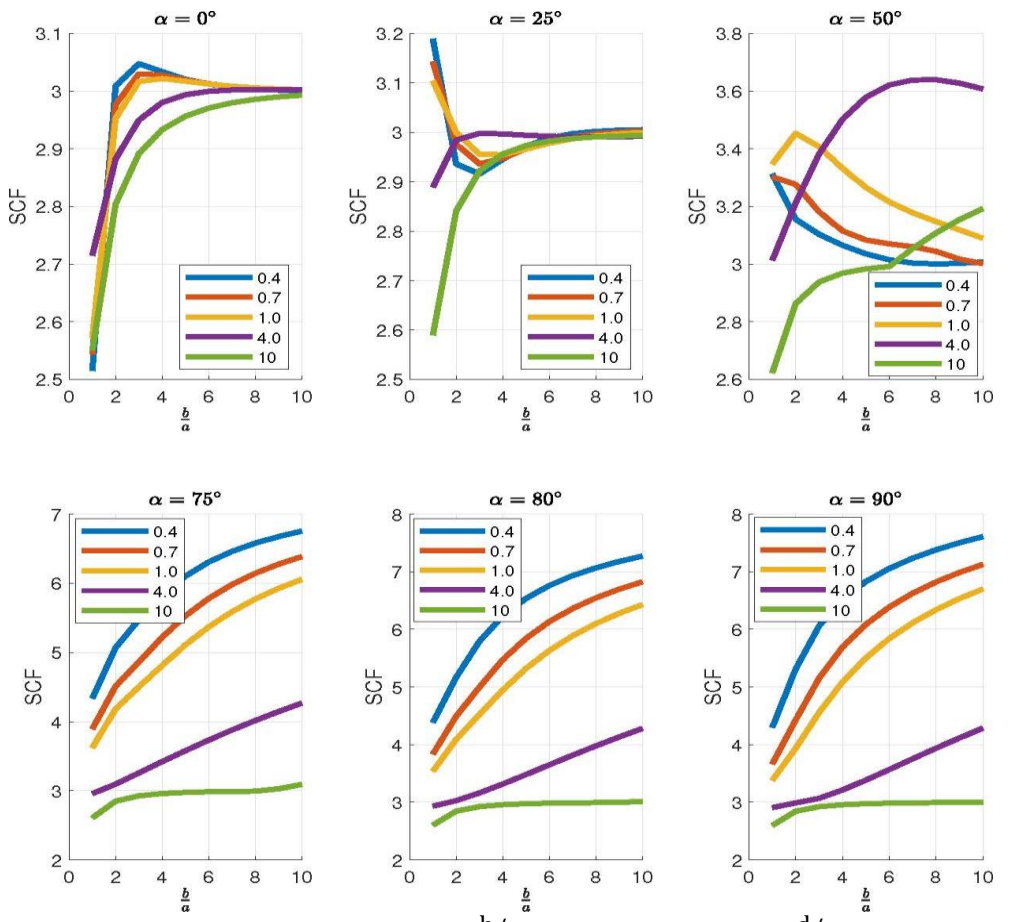


Fig. 6. Stress concentration factor variation with $^b/_a$ for fixed angle α . Ratio $^d/_a$ varies from 0.4 to 10

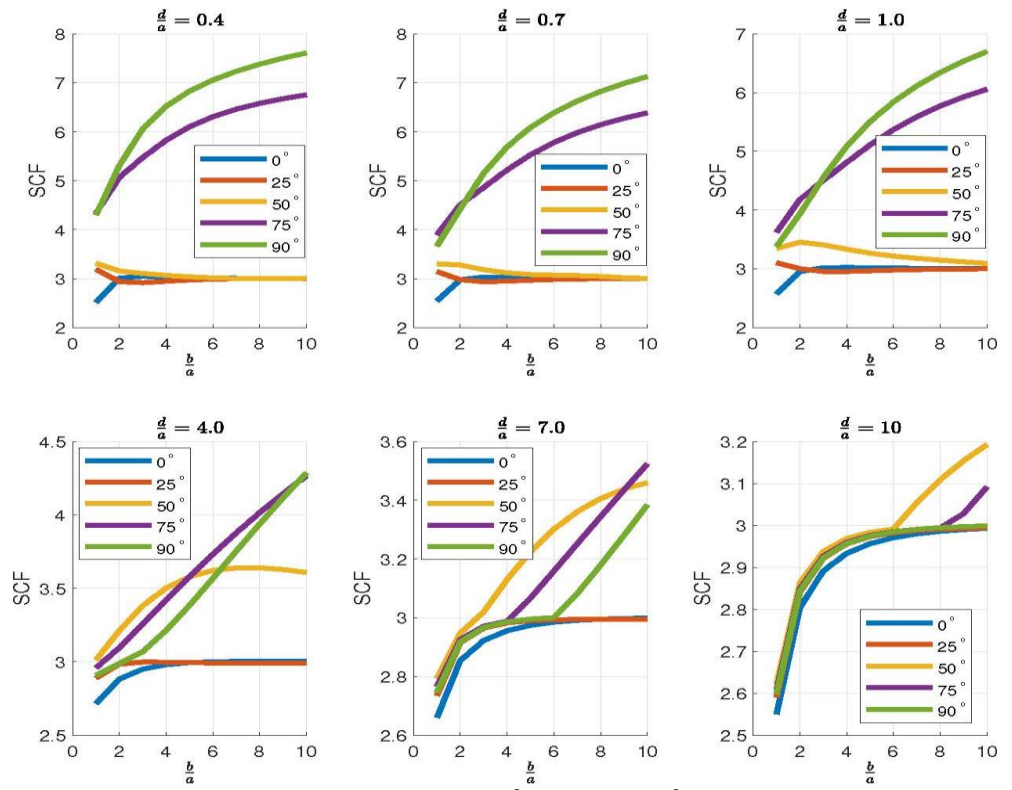
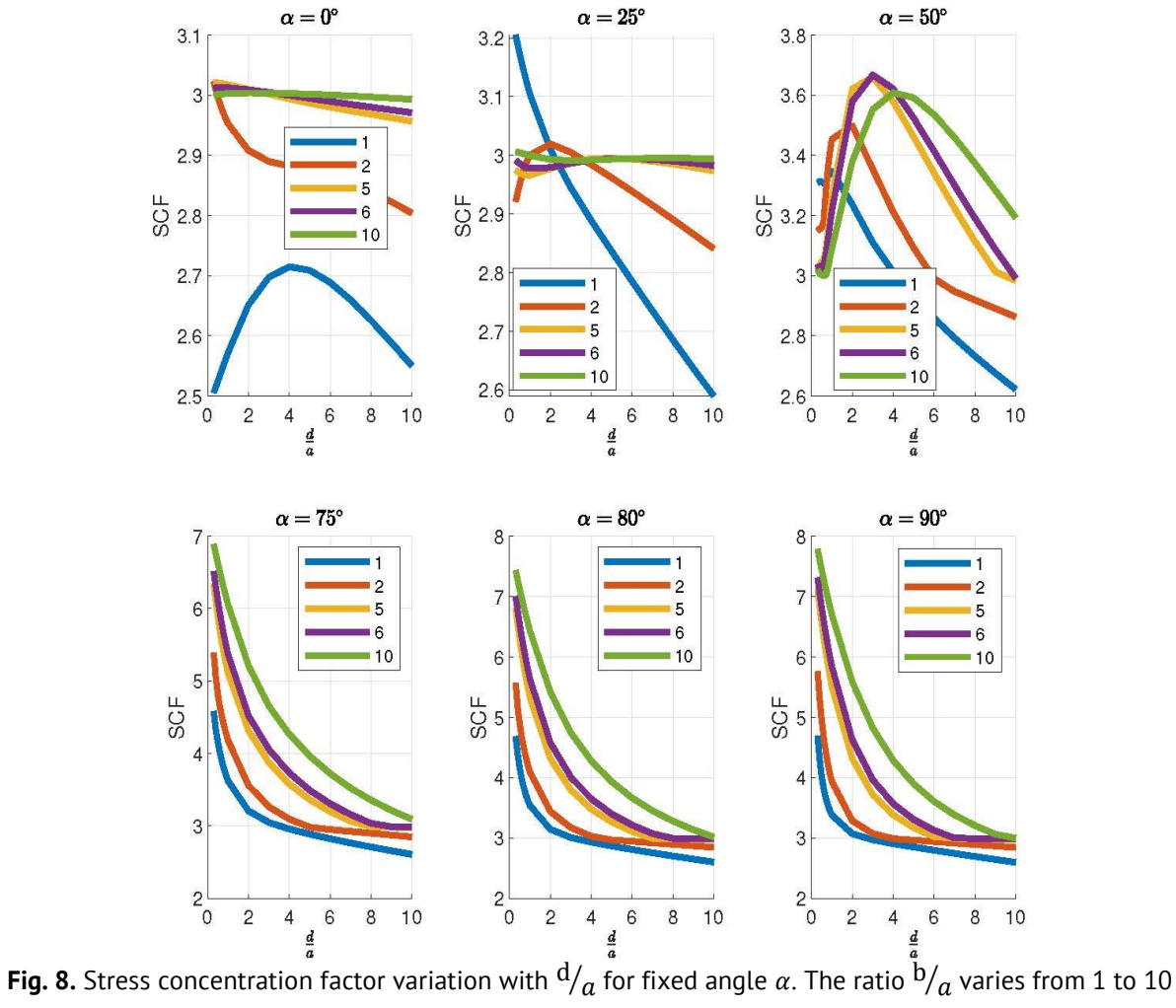


Fig. 7. Stress concentration factor variation with $^{\rm b}/_a$ for fixed $^{\rm d}/_a$. Angle α varies from 0° to 90°



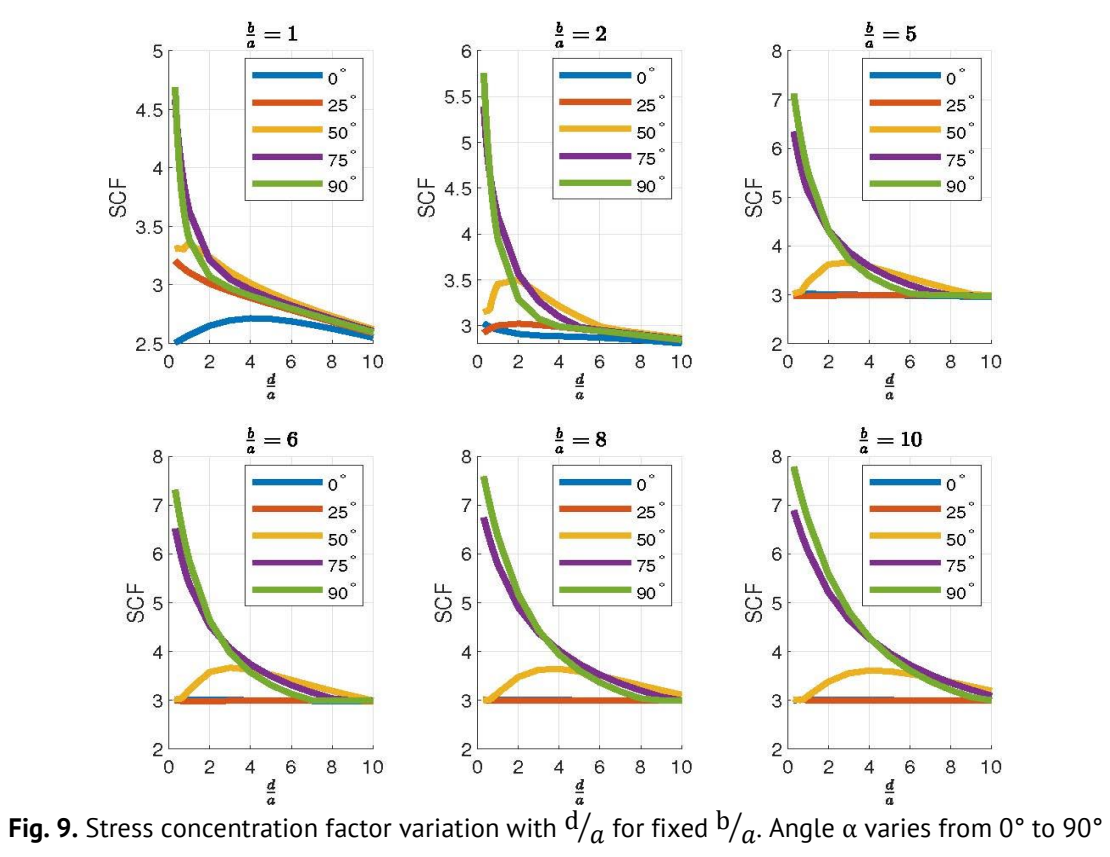


Figure 5 shows plots of variation of SCF with angle α . These plots are generated at fixed values of ratio $^d/_a$ and the individual curves correspond to a particular value of the ratio $^b/_a$ as shown in the legend. With value of angle α from 35° to 55°, SCF increases monotonically for shorter center distances.

Figure 6 shows plots of variation of SCF with ratio $^b/_a$. These plots are generated at fixed values of angle α and the individual curves correspond to a particular value of the ratio $^d/_a$ as shown in the legend. With value of angle $\alpha \geq 55^\circ$, SCF increases monotonically for shorter center distances.

Figure 7 shows plots of variation of SCF with ratio $^b/_a$. These plots are generated at fixed values of ratio $^d/_a$ and the individual curves correspond to a particular value of angle α as shown in the legend. The value of SCF remains below 3 for $b \leq 6a$ irrespective of the angle α .

Figure 8 shows plots of variation of SCF with ratio $^d/_a$. These plots are generated at fixed values of angle α and the individual curves correspond to a particular value of the ratio $^b/_a$ as shown in the legend. The lower three subplots confirm "With value of angle $\alpha \geq 55^\circ$, SCF increases monotonically for shorter center distances".

Figure 9 shows plots of variation of SCF with ratio $^d/_a$. These plots are generated at fixed values of ratio $^b/_a$ and the individual curves correspond to a particular value of angle α as shown in the legend. SCF remains close to 3 for the ratio $^d/_a$ closer to 10.

From these graphs, we can note maximum value of SCF decreases with decrease in angle α , increase in ratio $^d/_a$, decrease in ratio $^b/_a$. Minimum value of SCF increases with increase in angle α , decrease in ratio $^d/_a$, increase in ratio $^b/_a$. The lowest values of SCF occur (2.515) at angle $\alpha=0^\circ$, ratio $^b/_a=1$ and $^d/_a=0.4$. The highest values of SCF occur (7.61) at angle $\alpha=89^\circ$, ratio $^b/_a=10$ and $^d/_a=0.4$.

Table 1. Stress concentration factor with angle \propto =	0°
--	----

THE LY SHIESS CONCENTRATION RECEST WITH LANGUE TO					
b/a	d/a	VGU [13]	Chiang [10]	BFM	FEM
1	1	2.658	2.625	2.602	2.682
			2.623 [1]		
			2.650 [3]		
1	2	2.787	2.703	2.675	2.752
			2.703 [1]		
			2.715 [3]		
1	3	2.864	2.772	2.746	2.813
1	4	2.907	2.825	2.798	2.863
			2.825 [1]		
			2.827 [3]		
2	1	2.556	2.924	2.991	2.961
3	1	2.404	2.982	3.019	3.021
4	1	2.255	2.993	3.001	3.035

In order to validate the results obtained from BFM, SCF values available in the literature and results of the finite element analysis (FEM) has been included in the Tables 1 and 2. Table 1 shows SCF values from [1,3,10,13] with BFM and FEM for angle $\alpha = 0^{\circ}$. Computed SCF value from BFM are closer to values from [1,3,10]. SCF values from

[13] are lower than other estimation for b > a. Table 2 shows SCF values from [1,3,10,13] with BFM and FEM for angle $\alpha = 90^{\circ}$. Computed SCF value from BFM are closer to values from [1,3,10]. SCF values from [13] are lower than other estimation for b > a.

Table 2. Stress	Concentration	factor with	angle $\propto = 90^{\circ}$

b/a	d/a	VGU [13]	Chiang [10]	BFM	FEM
1	1	3.97	3.264	3.242	3.316
			3.264 [1]		
			3.264 [3]		
1	2	3.481	3.066	3.092	3.108
			3.066 [1]		
			3.066 [3]		
1	3	-	3.034	3.042	3.076
1	4	3.182	3.02	3.017	3.062
			3.020 [1]		
			3.020 [3]		
2	1	3.966	4.051	3.912	4.112
3	1	3.611	4.854	4.620	4.899
4	1	3.618	5.537	5.204	5.583

Conclusions

Body Force Method is used to compute SCF around two circular holes in an infinite plate subjected to uniaxial loading along x-direction. The values of SCF obtained by using BFM closely match with the values of SCF available in the literature. BFM is simple, yet robust method useful in performing stress analysis of bodies with discontinuities. Accurate results are obtained with small number of segments of the discontinuity.

Maximum stress concentration factor is 7.61 which occurs when angle $\alpha = 89^{\circ}$, ratio of hole diameters b/a = 10 and ratio of distance between holes to diameter d/a = 0.4. It is found that maximum value of stress concentration factor decreases with decrease in angle α , decrease in ratio of hole diameters b/a, increase in ratio of distance between holes to diameter d/a.

Minimum stress concentration factor is 2.515 which occurs when angle $\alpha=0^\circ$, ratio of hole diameters b/a=1 and ratio of distance between holes to diameter d/a=0.4. It is found that minimum value of stress concentration factor increases with increase in angle α , increase in ratio of hole diameters b/a, decrease in ratio of distance between holes to diameter d/a. The value of SCF can be maintained ≤ 3 if angle $\alpha \leq 30^\circ$ and $b \geq 2a$.

References

- 1. Ling CB. On the Stresses in a Plate Containing Two Circular Holes. J. Appl. Phys. 1948;19(77): 77 82.
- 2. Davies GAO, Hoddinott JR. Stresses in a Plate Pierced by two Unequal Circular Holes. *The Journal of the Royal Aeronautical Society*. 1963;67(631): 451–452.
- 3. Haddon RAW. Stresses in an Infinite Plate with Two Unequal Circular Holes. *The Quarterly Journal of Mechanics and Applied Mathematics*. 1967;20(3): 277–291.
- 4. Salerno VL, Mahoney JB. Stress Solution for an Infinite Plate Containing Two Arbitrary Circular Holes Under Equal Biaxial Stresses. *J. Eng. Ind.* 1968;90(4): 656–665.

- 5. Miyata H. Finite elastic deformations of an infinite plate perforated by two circular holes under biaxial tension. *Ing. Arch.* 1970;39: 209–218.
- 6. Erickson PE, Riley WF. Minimizing stress concentrations around circular holes in uniaxially loaded plates. *Experimental Mechanics*. 1978;18: 97 100.
- 7. Iwaki T, Miyao K. Stress concentrations in a plate with two unequal circular holes. *International Journal of Engineering Science*. 1980;18(8): 1077–1090.
- 8. Horii H, Nemat-Nasser S. Elastic fields of interacting inhomogeneities. *International Journal of Solids and Structures*. 1985;21(7): 731–745.
- 9. Duan ZP, Kienzler R, Herrmann G. An integral equation method and its application to defect mechanics. *Journal of the Mechanics and Physics of Solids*. 1986;34(6): 539–561.
- 10. Chiang CR. A numerical method for solving elasticity problems: Application to the problems of an infinite plate containing two circular holes. *Computers & Structures*. 1988;30(5): 1199–1205.
- 11. Meguid SA, Gong SX. Stress concentration around interacting circular holes: a comparison between theory and experiments. *Engineering Fracture Mechanics*. 1993;44(2): 247–256.
- 12. Hoang SK, Abousleiman YN. Extended Green's Solution for the Stresses in an Infinite Plate with Two Equal or Unequal Circular Holes. *J. Appl. Mech.* 2008;75(3): 031016.
- 13. Ukadgaonker VG. Theory of Elasticity and Fracture Mechanics. Delhi: PHI Learning Pvt. Ltd; 2015.
- 14. Kuo SR, Kao SK, Huang YL, Chen JT. Revisit of the degenerate scale for an infinite plane problem containing two circular holes using conformal mapping. *Applied Mathematics Letters*. 2019;92: 99–107.
- 15. Zeng X, Lu A, Wang S. Shape optimization of two equal holes in an infinite elastic plate. *Mechanics Based Design of Structures and Machines*. 2020;48(2): 133–145.
- 16. Mohan AE, Habeeb HA, Abood AH. Experimental and modeling stress concentration factor (SCF) of a tension poly lactic acid (PLA) plate with two circular holes. *Periodicals of Engineering and Natural Sciences*. 2019;7(4): 1733–1742.
- 17. Gandilyan DV, Ustinov KB. Influence of surface effects on stress state in a body with two circular holes. *J. Phys.: Conf. Ser.* 2020; 1474: 012014.
- 18. Patel A, Desai CK. Stress concentration around an elliptical hole in a large rectangular plate subjected to linearly varying in-plane loading on two opposite edges. *Theoretical and Applied Fracture Mechanics*. 2020;106: 102432.
- 19. Yang L, Wang Q, Xu L, Yang R, Chao YJ. Fracture path of cracks emigrating from two circular holes under blasting load. *Theoretical and Applied Fracture Mechanics*. 2020;108: 102559.
- 20. Ma Y, Lu A, Cai H, Zeng X. An analytical method for determining the plastic regions around two circular holes in an infinite medium. *Applied Mathematical Modelling*. 2021;89(1): 636–653.
- 21. Maksymovych M, Lazorko A, Maksymovych O, Dmitriiev O. Research of Stress Concentration at Closely Placed Holes in Wing Bearing Area in Anisotropic Platesю *Diagnostyka*. 2022;23(4): 2022402.
- 22. Nisitani H. Solutions of notch problems by body force method. In: Sih GC. (ed.) *Mechanics of Fracture, Volume 5*. Alphen aan den Rijn: Noordhoff Intern Publ.; 1978. p.1–68.
- 23. Nisitani H, Saimoto A. Short History of Body Force Method and its Application to Various Problems of Stress Analysis. *Materials Science Forum.* 2003;440–441: 161–168.
- 24. Chen D, Nisitani H. Body force method. *International Journal of Fracture*. 1997;86: 161–189.
- 25. Fraga WE, Hewitt RL. *Implementation of Nisitani's Body Force Method for the Solution of Notch Problems*. National Aeronautical Establishment, NAE-AN-17, NRC NO. 22831 Ottawa; 1983.

About Author

Shrikrishna M. Badiger 📵 Sc

Assistant Professor (M.S. Ramaiah University of Applied Sciences, Bengaluru, India)

Daivajna Subbarayappa Ramakrishna Sc

PhD, Professor (Jawaharlal Nehru National College of Engineering, Shivamogga, India)

Submitted: March 12, 2024 Revised: April 22, 2024 Accepted: June 6, 2024

The role of the hydrostatic pressure under dynamic fracture of rocks

ABSTRACT

In this study, within the context of the structural-temporal approach, the dynamic effects of the strength characteristics of rocks arising due to hydrostatic pressure are analysed. The key idea of the proposed approach is the introduction of the incubation time parameter for describing material fracture processes, which is interpreted as the main measure of material response. Theoretical velocity dependencies of the fracture toughness for marble and granite, subjected to different values of external hydrostatic pressure, as well as for dry and wet sandstones, are predicted based on the proposed approach. The calculated incubation times for marble and granite are allowed to establish a linear function between incubation time and hydrostatic pressure. The obtained values of incubation times are compared according to the velocity dependencies of the fracture toughness and the velocity dependencies of the strength of rocks differing in external hydrostatic pressure or moisture level. It is shown that the incubation time depending on the external hydrostatic pressure or on the moisture of rocks is similarly changed.

KEYWORDS

dynamic fracture toughness • hydrostatic pressure • structural-temporal approach • fracture incubation time loading rate

Acknowledgements. The study was supported by the Ministry of Science and Higher Education of the Russian Federation, Agreement number No. 075-15-2022-1114. Sections "Introduction", "Modes I fracture toughness in a wide range of the loading rate", "Dependence of dynamic fracture toughness on loading rate" were performed by N.S. Selyutina at the support of the Russian Science Foundation (RSF No. 22-11-00091), Yu.V. Petrov performed his part of the work with the support of the Ministry of Science and Higher Education of the Russian Federation (project No. 124041500007-4)Yu.V. Petrov performed his part of the work with the support of the Ministry of Science and Higher Education of the Russian Federation (project No. 124041500007-4).

Citation: Selyutina NS, Igusheva LA, Petrov YV. The role of the hydrostatic pressure under dynamic fracture of rocks. *Materials Physics and Mechanics*. 2024;52(3): 108–120. http://dx.doi.org/10.18149/MPM.5232024_11

Introduction

The strength characteristics of rocks with a change of moisture content depending on the static or dynamic deformation mode are increased or are decreased. Dry and wet rocks were tested in different ranges of strain rates on a split Hopkinson–Kolsky bar tests: limestone $(10^2-10^3 \text{ s}^{-1})$ [1], sandstone $(10^1-10^2 \text{ s}^{-1})$ [2], tuff $(10^0-10^1 \text{ s}^{-1})$ [3,4], granite $(10^0-10^1 \text{ s}^{-1})$ [3,5]. Dynamic experiments on rocks [1–5], showed, that the dynamic and static strength of dry rock is greater than wet rock. A comparison of the strength of granite [5] under static loads and high-speed deformation of $\dot{\varepsilon} \sim 10^2 \text{ s}^{-1}$ revealed that the highest dynamic strength of wet granite and the highest static strength of dry granite (Fig. 1) were observed. A significant increase in the tensile strength of wet rock under dynamic loading in comparison with the static loading is explained by the presence of hydrostatic

¹ St. Petersburg State University, St. Petersburg, Russia

² Institute for Problems in Mechanical Engineering of the Russian Academy of Sciences, St. Petersburg, Russia

[™] nina.selutina@gmail.com

pressure (confining pressure) in water-saturated samples, which has a different effect on static strength and dynamic strength at high strain rates. Under static loading conditions, the effect of hydrostatic pressure of the contained liquid in wet rocks reduces their strength characteristics in comparison with dry rocks. The static fracture toughness of the limestone [6,7], the granite [7,8], the marble [7], the sandstone [9,10] by the external hydrostatic pressure of the liquid in the rock was increased. The hydrostatic pressure effect on dynamic strength characteristics of rock was also considered in works [11–14]. In this paper, the mechanism of the influence of hydrostatic pressure on the strength characteristics of rocks under high-speed deformation is studied in detail.

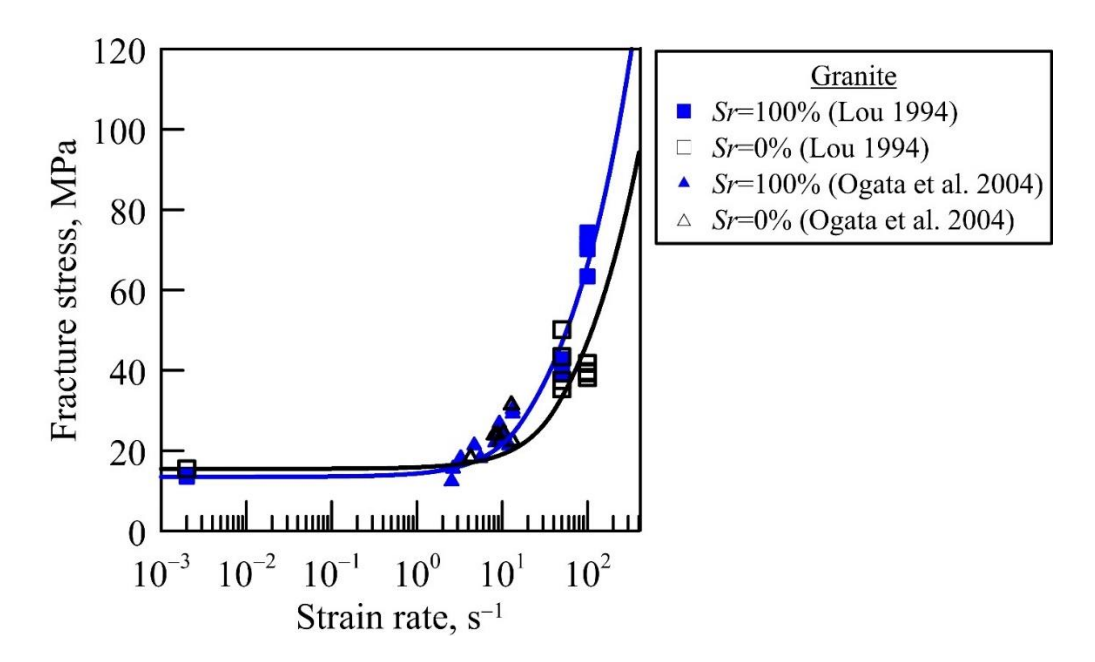


Fig. 1. Speed dependencies of fracture stress of granite [3,5] with different saturation ratio (Sr), predicted on the basis of the structural-temporal approach in study [15]

In [16–19], the competition effects of the rate dependences of the concrete strength with different levels of water saturation were observed. In [20], the hydrostatic pressure effect was considered in the context of the incubation time criterion. Using this criterion, the rate dependences of strength in [20] were predicted and calculated rate sensitivity parameters, called the characteristic relaxation times, were compared. The advantage of the incubation time criterion compared to other dynamic approaches [21–25] is the use of parameters that are invariant to the applied loading rate. It was found that the greater the incubation time for saturated concrete, the greater the dynamic strength in terms of critical stress. A significant (in several times) increase of incubation time values for saturated concrete samples is revealed.

In the paper, the rate dependences of the fracture toughness of rocks with different external hydrostatic pressure and water saturation levels are studied based on the structural-time approach [26-29]. A pattern has been revealed between hydrostatic pressure and incubation time.

Incubation time criterion of fracture

General formulation

Let us consider the fracture criterion proposed in [26-29] which is used to describe the brittle fracture of materials. The general form of the incubation time criterion is as follows:

$$\frac{1}{\tau} \int_{t-\tau}^{t} \left(\frac{F(t')}{F_c} \right)^{\alpha} dt' \le 1, \tag{1}$$

where τ is the incubation time associated with the dynamics of the relaxation process prior to fracture, F(t) is the intensity of the local force field that causes fracture of the medium, and F_c is the static limit of the local force field. The fracture time t- corresponds to the condition for achieving equality in inequality (1), i.e., when the left side of inequality (1) becomes equal to 1. The parameter α characterizes the sensitivity to the intensity of the force field causing fracture.

Fracture criterion (1) implies the existence of the incubation period, preceding a macroscopic break of the material. In this case, an incubation process is an essential factor of the fracture process and takes place both in cases of quasi-static and fast impact loads. Due to the presence of the fracture incubation period, some specific effects do happen under dynamic loading. Among those effects is a well-known strain-rate dependency of strength. As one of the simplest interpretations of the fracture incubation time, let us consider an example of fracture caused by a slow $(t_* >> \tau)$ linearly growing fracture toughness $K(t) = \dot{K} t H(t)$, where $\dot{K} = \text{const}$ and H(t) is the Heaviside step function. Substituting F(t) = K(t) into (1) we can calculate the time to fracture $t_* = \sigma_c/\dot{\sigma} + 0.5\tau$ and a value of the critical stress intensity factor at the moment of fracture $K_* = K(t_*) = K_c + 0.5 \,\dot{\sigma} \,\tau$, where $K_c = F_c$ is the tabulated value of the material static fracture toughness. In the case of very slow stress growth $(\dot{K}\tau)/K_c << 1$, the ultimate stress does not differ much from the static strength $\sigma_* \approx K_c$. The obtained expressions show that according to (1) the material remains intact at the moment when the static strength limit is achieved $t_c = K_c/\dot{K}$. It is crucial that before the onset of the macroscopic rupture of the material, preparatory processes having a characteristic temporal period τ evolve in the material structure (Fig. 2).

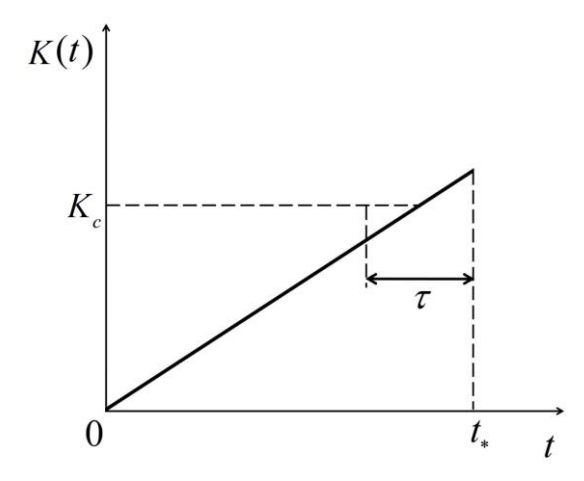


Fig. 2. Temporal dependence of stress for slow linear loading

The main feature of the approach is the introduction of the incubation time as a property of the material. This property is due to the preparatory relaxation processes of the evolution of microdefects in the material structure associated with microcracking. The key role of τ in the interpretation of the fracture process at different external loading rates is described in detail in [27,28].

The structural-temporal approach (1) can be used for both problems of crack propagation and problems of fracture of initially undamaged media that do not a priori contain macrocracks or sharp notches.

Modes I fracture toughness in a wide range of the loading rate

Using the structural-temporal approach, we derive the fracture condition for a three-point bending experiment (Fig. 3), to construct the strain rate dependences of the mode I fracture toughness. According to [30], the relationship between the dynamic force applied to the specimen and the mode I fracture toughness in three-point bending tests is linear:

$$K_I(t) = Y_I(\beta) \frac{P(t)\sqrt{\pi a_I}}{2RB},\tag{2}$$

where P(t) is time dependence of loading force in the specimen, $Y(\beta)$ is the dimensionless geometric factor, determined in the case of three-point bending test in the study [11] as $Y(\beta) = 0.4670 + 3.9094\beta - 8.7634\beta^2 + 16.845\beta^3$, $\beta = a_l/R$, s is the distance between two supporting pins, R is the specimen radius, a_l is the notch length, B is the specimen thickness. Taking into account Eq. (2), criterion (1) is rewritten in the following form:

$$Y_{I} \frac{\sqrt{\pi a_{I}}}{2RB} \frac{1}{\tau_{I}} \int_{t-\tau_{I}}^{t} P(s) ds \le K_{IC}, \tag{3}$$

where K_{IC} is the static mode I fracture toughness, τ_I is the fracture incubation time under the mode I fracture toughness limit condition.

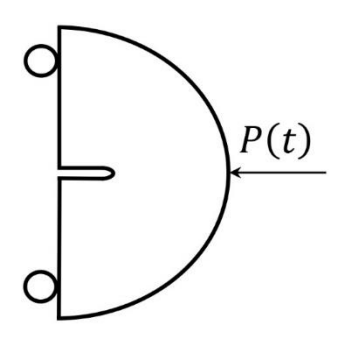


Fig. 3. Three-point bending test configuration for a notched semi-circular specimen

Here we use the experimental data on three-point bending of semicircular specimens of sandstone [31] and granite [11], where the time dependence of the applied force P(t) changes linearly:

$$P(t) = \dot{P}tH(t),\tag{4}$$

where \dot{P} is the force growth rate, and H(t) is the Heaviside function.

For linear loading (4) we plot the rate dependence of the mode I fracture toughness. Considering that the condition of equality (3) determines the time to fracture in the

specimen, we can calculate the dependence of the moment of fracture on the mode I

fracture toughness rate
$$\dot{K}_{I}$$
 ($\dot{K}_{I}=Y_{I}(\beta)\frac{\dot{P}(t)\sqrt{\pi a_{I}}}{2RB}$):
$$t_{*}(\dot{K}_{I}) = \begin{cases} \frac{K_{Ic}}{\dot{K}_{I}} + \frac{\tau_{I}}{2}, & t_{*} > \tau_{I}, \\ \sqrt{\frac{2K_{Ic}\tau_{I}}{\dot{K}_{I}}}, & t_{*} \leq \tau_{I}, \end{cases}$$
(5)

and substitute the resulting dependence into the dynamic mode I fracture toughness $K_{ID} = K_I (t^*)$:

$$K_{Id}(\dot{K}_{I}) = \begin{cases} K_{Ic} + \frac{1}{2}\dot{K}_{I}\tau_{I}, & t_{*} > \tau_{I}, \\ \sqrt{2K_{Ic}\tau_{I}\dot{K}_{I}}, & t_{*} \leq \tau_{I}. \end{cases}$$
(6)

To construct theoretical dependences (6), it is necessary to determine the incubation time, which is estimated from experimental data by the least squares.

Modes II fracture toughness in a wide range of the loading rate

On the basis of the structural-temporal approach we lead out the fracture condition for the dynamic short core in compression test [32-34] (Fig. 4), proceeded on the split Hopkinson pressure bar tests, to plot the strain rate dependences of the mode II fracture toughness. The relationship between the dynamic force applied to the specimen and the dynamic short core in compression test [12] is linear:

$$K_{II}(t) = Y_{II}(\gamma) \frac{P(t)\sqrt{\pi a_{II}}}{DC},\tag{7}$$

where $Y_{II}(y)$ is dimensionless geometric factor, y = C/H, C is the distance between two notches, H is the specimen height, D is the specimen diameter, a_{II} is the notch length. Taking into account expression (7), criterion (1) is rewritten in the following form:

$$Y_{II} \frac{\sqrt{\pi a_{II}}}{DC} \frac{1}{\tau_{II}} \int_{t-\tau_{II}}^{t} P(s) \, ds \le K_{IIC}, \tag{8}$$

where K_{IIC} is the static mode II fracture toughness, τ_{II} is the fracture incubation time under the mode II fracture toughness limit condition.

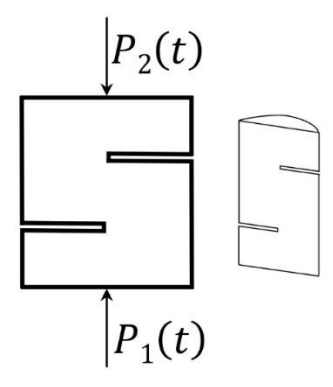


Fig. 4. Scheme of the dynamic short core in compression test [29] for a notched cylindrical specimen

Here we use the experimental data on dynamic short core in compression test of notched cylindrical specimens of marble [32], where the time dependence of the applied force P(t) changes linearly.

Similarly to the previous section, substituting Eq. (4) to the equality condition Eq. (8) we determine the dependence of the fracture moment on the rate of the mode II fracture toughness $\dot{K}_{II} = Y_{II}(\gamma) \frac{\dot{P}(t)\sqrt{\pi a_{II}}}{DC}$. Therefore, the dependence of the dynamic mode II fracture toughness $K_{IID} = K_{II}(t)$ on fracture toughness rate \dot{K}_{II} is given as:

$$K_{IId}(\dot{K}_{II}) = \begin{cases} K_{IIc} + \frac{1}{2} \dot{K}_{II} \tau_{II}, & t_* > \tau_{II}, \\ \sqrt{2K_{IIc} \tau_{II} \dot{K}_{II}}, & t_* \leq \tau_{II}. \end{cases}$$
(9)

Dependence of dynamic fracture toughness on loading rate

The effect of water saturation

Let us apply the criterion (3) for calculation of rate dependences of mode I fracture toughness based on experimental data of sandstone [31], obtained as a result of a static and dynamic tests in three-point bending tests with following parameters: a_l = 5 mm, B = 20 mm, R = 25 mm. In [31], values of quasi-static toughness K_{lc} = 0.51 MPa·m $^{1/2}$ for dry sandstone with a density ρ = 2374.7 kg/m³ and K_{lc} = 0.29 MPa·m $^{1/2}$ for wet sandstone with a density ρ = 2457.8 kg/m³ were presented.

Using the least squares method to the experimental data under consideration [27] according to the numerical scheme (6), estimate of the incubation time for wet τ_{l} = 0.196 ms and dry sandstone τ_{l} = 0.155 ms. Figure 5 shows the theoretical dependences of the fracture stress on the strain rate and experimental data [31] for dry and wet sandstone. Plotted theoretical dependences for dry and saturated sandstone in Fig. 5 have a good correspondence with an experimental data [31]. The dynamic and static fracture toughness of dry sandstone in the considered range of loading rate 10–100 GPa·m^{1/2}/s are greater than wet sandstone (Fig. 5), and the incubation time of wet sandstone is longer than dry sandstone. The data given in Fig. 5 indicates the fracture toughness and incubation time of wet samples approaching that of dry samples.

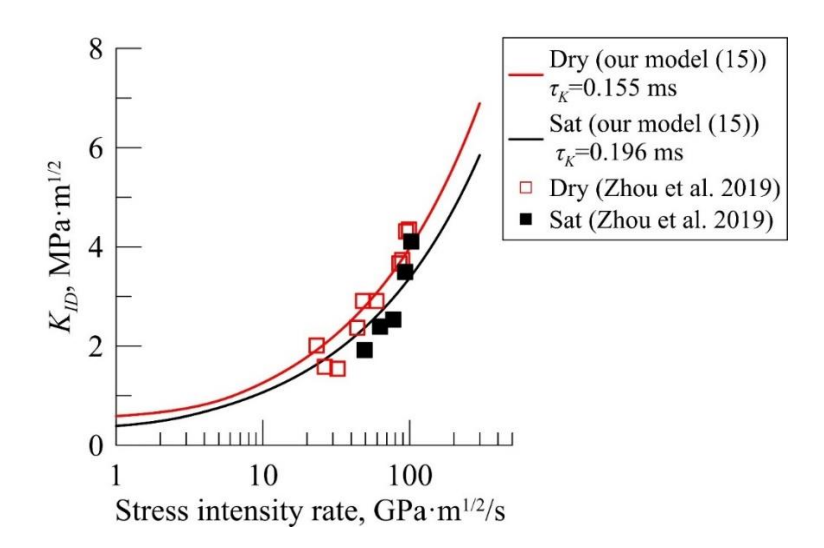


Fig. 5. The water saturation effect of sandstone on the theoretical and experimental dependencies of the fracture toughness rate based on the proposed model (6), respectively, and experimental data [28]

The opposite effect of hydrostatic pressure under static and dynamic loading is discussed in Fig. 1. The incubation time of the wet granite 21 µs (for dry granite 11.8 µs [15]) is the biggest. The reason for the decreasing static fracture toughness is the presence of additional hydrostatic fluid pressure in the voids (pores, cracks, caverns) of wet sandstone samples in comparison with dry sandstone samples. The hydrostatic pressure of liquid in voids under dynamic loads has the opposite effect on the fracture toughness of rock: the presence of liquid in voids leads to "compression" of microdefects and microcracks in the structure of the material, which slows down relaxation processes. In terms of the structural-temporal approach, this means that the incubation time of rocks with a high moisture content is greatest. In [20], using the example of rate dependences of the strength of dry and wet granite, predicted based on the structural-time approach for strength (1). The hydrostatic pressure effects are opposite at low (acceleration of relaxation processes) and high (deceleration of relaxation processes) strain rates. Despite the higher values of the dynamic fracture toughness of the dry sandstone in the considered range of loading rates of 10-100 GPa·m^{1/2}/s, the incubation time of wet sandstone (as well as wet granite) is slightly longer.

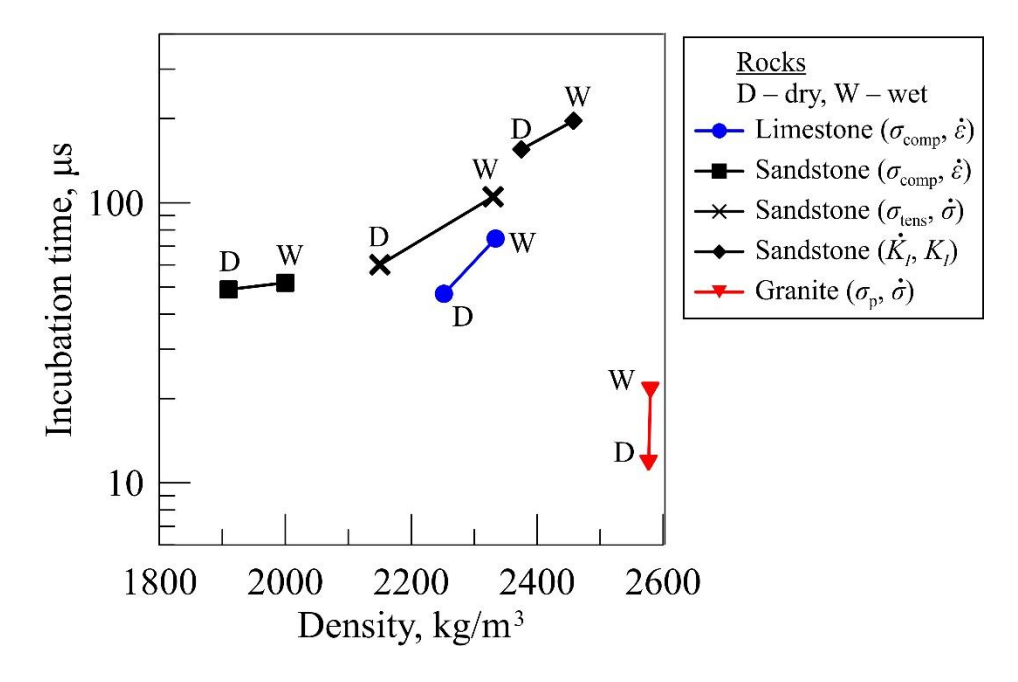


Fig. 6. Dependence of incubation time on rock density, present in results this paper for sandstone (K_l, \dot{K}_l) and papers [15,20] for limestone $(\sigma_{comp}, \dot{\varepsilon})$, sandstone $(\sigma_{comp}, \dot{\varepsilon})$, $(\sigma_{tens}, \dot{\varepsilon})$ and granite $(\sigma_{tens}, \dot{\sigma})$. References to experimental data used for calculations: limestone $(\sigma_{comp}, \dot{\varepsilon})$ – [1], sandstone $(\sigma_{comp}, \dot{\varepsilon})$ – [32], sandstone $(\sigma_{tens}, \dot{\sigma})$ – [2], sandstone (K_l, \dot{K}_l) (black diamonds) – [31], granite $(\sigma_{tens}, \dot{\sigma})$ – [3,5]

The incubation time values increase with rock density, as shown in [20]. Since water-saturated rocks have a higher density in comparison with dry rocks, they have the greatest strength under dynamic conditions. Let us plot the dependence of the incubation time on the density of the rock based on the results obtained and compare it with the results of studies [15,20]. Figure 6 shows the dependence of incubation time on density for limestone, sandstone, granite based on the results of the presented paper and papers [15,20]. The calculated incubation times for wet and dry sandstone (this section), obtained from the rate dependences of the mode I fracture toughness, are a continuation of the

linear dependence for the incubation times of sandstones. The higher the moisture content of the material, the greater the density and incubation time of the rock. As noted above, the main factor in the greater strength characteristics (strength, fracture toughness) at high strain rates for wet rock compared to dry rock is hydrostatic pressure, and not the density of the material.

Effect of external hydrostatic pressure

Based on the incubation time criterion (1), we consider the influence of external hydrostatic pressure on the rate dependences of the fracture toughness of rocks and their incubation times. Experimental data [11,12] are used to verify the criterion. In [11], the results of dynamic tests for three-point bending of the Laurentian granite, tests at various hydrostatic pressures 0, 5, 10, 15, and 20 MPa were discussed. In [11], values of quasistatic toughness $K_{Ic} = 1.5 \text{ MPa} \cdot \text{m}^{1/2}$ for granite with a density at zero hydrostatic pressure $\rho_0 = 2630 \text{ kg/m}^3$ and other parameter of tests $a_I = 5 \text{ mm}$, B = 25 mm, R = 25 mm, were presented. In [12], the dynamic fracture of marbles tested according to the scheme of dynamic short core in compression test [32–34] with five external hydrostatic pressures 0, 5, 10, 15, and 20 MPa, was examined. In [12], values of quasi-static toughness $K_{Ic} = 1.5 \text{ MPa} \cdot \text{m}^{1/2}$ for granite with a density at zero hydrostatic pressure $\rho_0 = 2630 \text{ kg/m}^3$ and other parameter of tests $a_I = 5 \text{ mm}$, B = 25 mm, R = 25 mm, R = 260.74 MN/m were presented.

Table 1. Estimated incubation times of Laurentian granite for different values of hydrostatic pressures [11] and densities

and densities			
Hydrostatic pressure, MPa	ρ, kg/m3 (Eq. (12))	τ, μs	
0	2630	100	
5	2632.6	145	
10	2635	190	
15	2637.5	235	
20	2640	295	

Table 2. Estimated incubation times of marble for different values of hydrostatic pressures [12] and densities

Hydrostatic pressure, MPa	ρ, kg/m3 (Eq. (12))	τ, μς
0	2850	25.6
5	2850.2	26.7
10	2850.4	31.3
15	2850.6	33.1
20	2850.8	33.3

In terms of the structural-temporal approach, it is assumed that the incubation time of the rock for each hydrostatic pressure is different. In terms of the structural-temporal approach, it is assumed that the incubation time of the rock for each hydrostatic pressure is different. Based on the experimental results obtained in [11,12] on the study of the dynamic fracture of Laurentian granite at various hydrostatic pressures, theoretical calculations of the rate dependences of the dynamic fracture toughness on the loading rate using the time criterion (1) are carried out. Tables 1 and 2 show the incubation times estimated by applying criterion (1) to the experimental data of granite [11] and

marble [12]. The plotted theoretical dependences of mode I fracture toughness on loading rate for granite in comparison with experimental data [11] are shown in Fig. 7. The constructed theoretical dependences of mode II fracture toughness on loading rate for marble in comparison with experimental data [12] are presented in Fig. 8. A good agreement between the experimental results and the calculations are observed.

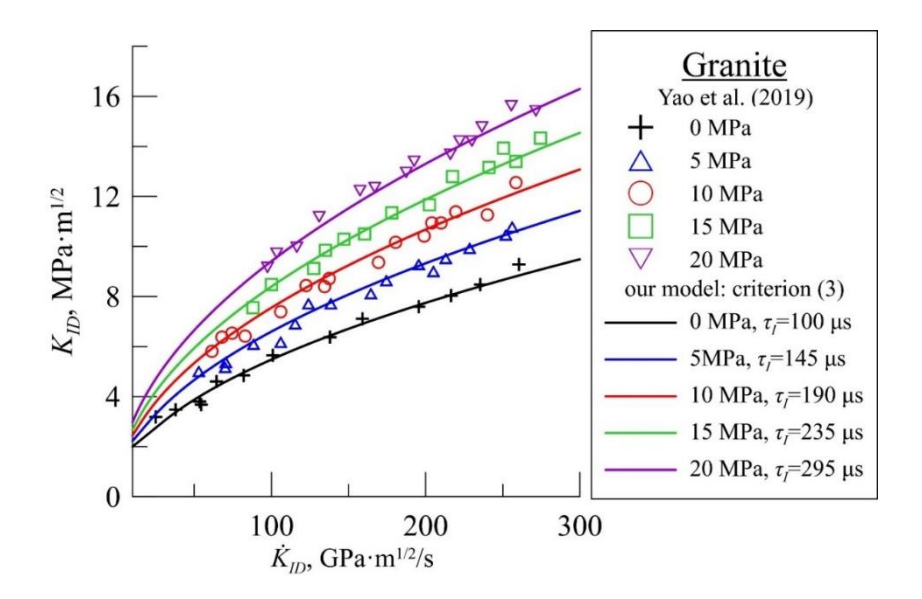


Fig. 7. Dependence of mode I fracture toughness on rate fracture toughness at different hydrostatic pressures, predicted by the incubation time criterion of fracture based on experimental data of granite [11]

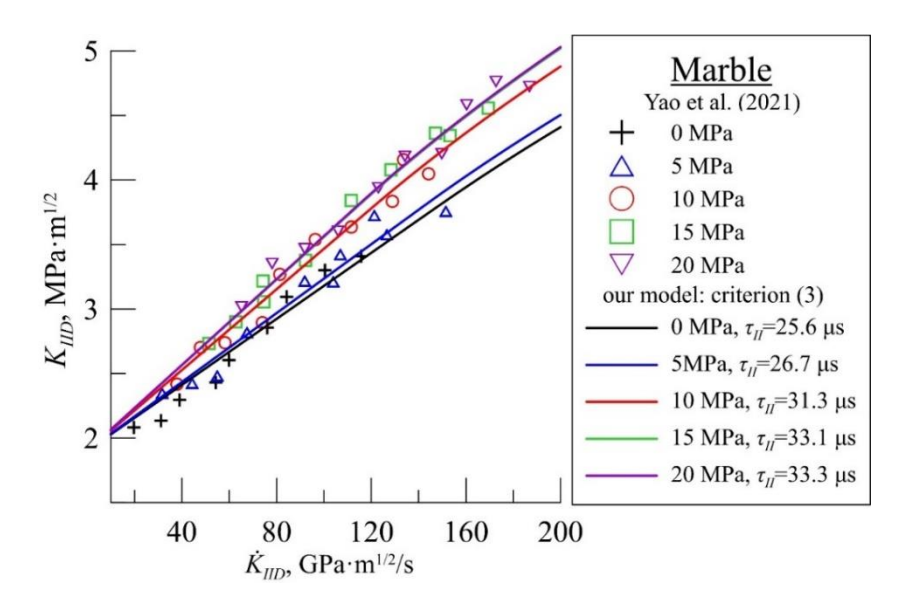


Fig. 8. Dependences of mode II fracture toughness on rate fracture toughness at different hydrostatic pressures, predicted by the incubation time criterion of fracture based on experimental data of marble [12]

The results show that the dynamic fracture toughness of mode I and mode II under hydrostatic pressure increases with loading rate. This is due to the influence of hydrostatic pressure, when, under the influence of a high strain rate, microcracks do not have time to propagate and microcracks in rocks close, which leads to an increase in dynamic fracture toughness.

Let us study the dependence of incubation time on rock density, expressing the density in terms of hydrostatic pressure. Fractional variation ϑ , associated with the action of hydrostatic pressure, is defined from the following expression:

$$\theta = \frac{(1-2\nu)}{E} 3p,\tag{10}$$

where v is the Poisson's ratio, E is the Young's modulus. According to the law of conservation of mass:

$$\rho_0 V_0 = \rho_1 V_0 (1 + \theta), \tag{11}$$

where ρ_0 is the density of rock without the action of hydrostatic pressure, ρ_1 is the density of rock with the action of hydrostatic pressure.

Tables 1 and 2 show the calculated values of rock density according to Eq. (11) at different hydrostatic pressures. Changes in rock density relative to the initial density at zero hydrostatic pressure were 0.4 % for granite and 0.02 % for marble. The observed trend of increasing incubation time is more related to hydrostatic pressure than rock density. Thus, an increase of the incubation time and the dynamic fracture toughness at high strain rates of wet rock compared to dry rock is hydrostatic pressure, and not a significant change in density (Fig. 6). Thus, an increase of the incubation time and the dynamic fracture toughness at high strain rates of wet rock compared to dry rock is related with the hydrostatic pressure, and not a significant change in density (Fig. 6).

Thus, the increase of the incubation time with rock moisture is directly related to hydrostatic pressure. This will make it possible: to explain the effect of water saturation (the previous section), to compare rocks with different static and dynamic strength characteristics and to select the optimal material with the level of water saturation for the selected deformation mode.

Fracture incubation time under hydrostatic pressure effect

Incubation time as a parameter of the speed sensitivity of a material is a significant characteristic when valuation of the dynamic strength characteristics of rocks. As hydrostatic pressure increases, the incubation time for destruction increases. Based on the results of the previous section, we will analyze the incubation time from hydrostatic pressure. Let us assume that there is a linear dependence of the incubation time on hydrostatic pressure, given by Eq. (12):

$$\tau = \tau_0 + k * p,\tag{12}$$

where τ_0 is the value of incubation time in the absence of external hydrostatic pressure (0 MPa), i.e. τ_0 = 100 µs for granite and τ_0 = 25.6 µs for marble, k is the constant proportionality factor, p is the hydrostatic pressure. Figure 9 shows the calculated values of incubation time for granite and marble corresponding to external hydrostatic pressure and the calculated linear dependencies with the estimated parameter k = 9 µs/MPa for granite and k = 0.44 µs/MPa for marble. Plotted linear dependencies according to Eq. (12) have good agreement with the incubation times.

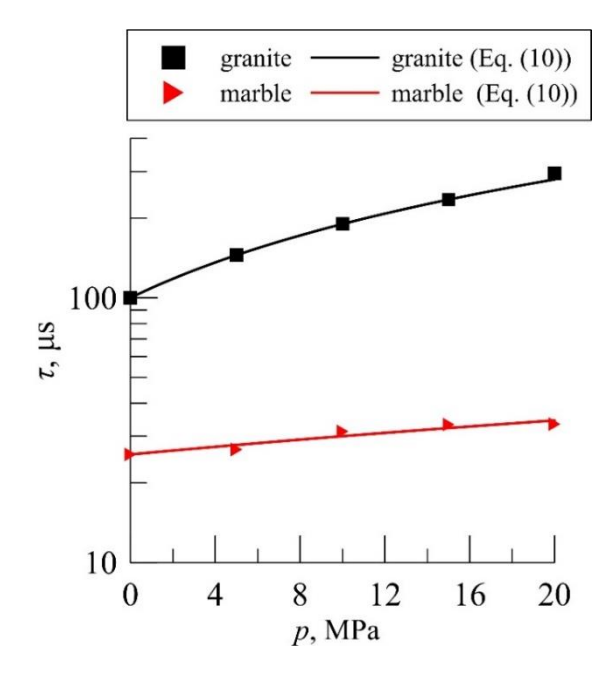


Fig. 9. Dependence of incubation time on hydrostatic pressure. References to experimental data used for calculations: granite (K_l, \dot{K}_l) (red triangles) – [11], marble (K_{ll}, \dot{K}_{ll}) – [12]

It supports the hypothesis that the difference in incubation times between rocks with different degrees of water saturation is caused by different levels of hydrostatic pressure resulting from rapid impact. Hydrostatic fluid pressure slows down the incubation process of micro-cracking, therefore, the characteristic relaxation time increases.

Conclusions

The rate dependences of fracture toughness according to mode I for sandstone and granite and according to mode II for marble were predicted based on the incubation time criterion. Theoretical dependencies of dry and saturated sandstones were plotted. The highest value of incubation time, characterizing the speed sensitivity of the material, was observed for saturated sandstone. The trend of increasing incubation time with the addition of water in rock samples depending on density was discussed in comparison with other estimated incubation times calculated from different rate dependences of strength.

On the basis of the proposed approach, the influence of hydrostatic pressure on the rate dependences of the fracture toughness of granite and marble was studied. Incubation time has been shown to increase with hydrostatic pressure and water saturation level. The linear dependence of incubation time on hydrostatic pressure was proposed. A relationship between hydrostatic pressure and saturation level for granite and marble was discussed. The dependences of incubation time on hydrostatic pressure were plotted.

Analysis of the incubation time depending on hydrostatic pressure and the level of water saturation showed that the hydrostatic pressure effects are opposite at low (acceleration of relaxation processes) and high (deceleration of relaxation processes) strain rates. The obtained estimates of incubation times can be used to determine the optimal strength properties of rocks, depending on the selected loading mode and the level of water saturation.

References

- 1. Petrov YV, Smirnov IV, Volkov GA, Abramian AK, Bragov AM, Verichev SN. Dynamic failure of dry and fully saturated limestone samples based on incubation time concept. *Journal of Rock Mechanics and Geotechnical Engineering*. 2017;9(1): 125–134.
- 2. Huang S, Xia K, Yan F, Feng X. An experimental study of the rate dependence of tensile strength softening of Longyou sandstone. *Rock Mechanics and Rock Engineering*. 2010;43: 677–683.
- 3. Ogata Y, Jung W jin, Kubota S, Wada Y. Effect of the strain rate and water saturation for the dynamic tensile strength of rocks. *Materials Science Forum*. 2004;465–466: 361–366.
- 4. Okubo S, Nishimatsu Y, He C, CHU SY. Loading rate dependency of uniaxial compressive strength of rock under water-saturated condition. *Journal of the Society of Materials Science*. 1992;41(463): 403–409.
- 5. Lou W. Dynamic fracture behaviour of dry and waterlogged granites. *Explosion and Shock Waves*. 1994;14(3): 249–254.
- 6. Al-Shayea NA, Khan K, Abduljauwad SN. Effects of confining pressure and temperature on mixed-mode (I–II) fracture toughness of a limestone rock. *International Journal of Rock Mechanics and Mining Sciences*. 2000;37(4): 629–643.
- 7. Backers T, Stephansson O, Rybacki E. Rock fracture toughness testing in Mode II—punch-through shear test. *International Journal of Rock Mechanics and Mining Sciences*. 2002;39(6): 755–769.
- 8. Hashida T, Oghikubo H, Takahashi H, Shoji T. Numerical simulation with experimental verification of the fracture behavior in granite under confining pressures based on the tension-softening model. *International Journal of Fracture*. 1993;59: 227–244.
- 9. Kataoka M, Mahdavi E, Funatsu T, Takehara T, Obara Y, Fukui K, i dr. Estimation of mode I fracture toughness of rock by semi-circular bend test under confining pressure condition. *Procedia Engineering*. 2017;191: 886–893.
- 10. Ko TY, Kemeny J. Effect of confining stress and loading rate on fracture toughness of rocks. *Rock Mechanics: Meeting Society's Challenges and Demands*. 2007; 625–629.
- 11. Yao W, Xia K, Zhang T. Dynamic Fracture Test of Laurentian Granite Subjected to Hydrostatic Pressure. *Experimental Mechanics*. 2019;59(2): 245–250.
- 12. Yao W, Xu Y, Wang C, Xia K, Hokka M. Dynamic Mode II fracture behavior of rocks under hydrostatic pressure using the short core in compression (SCC) method. *International Journal of Mining Science and Technology*. 2021;31(5): 927–937.
- 13. Yao W, Xu Y, Xia K, Wang S. Dynamic mode II fracture toughness of rocks subjected to confining pressure. *Rock Mechanics and Rock Engineering*. 2020;53: 569–586.
- 14. Lamzin DA, Bragov AM, Lomunov AK, Konstantinov AY, dell'Isola F. Analysis of the dynamic behavior of sand-lime and ceramic bricks. *Materials Physics and Mechanics*. 2019;42(6): 691–698.
- 15. Selyutina NS, Petrov YV. The water-saturation effect for concretes and rocks subjected to high strain rates. *Procedia Structural Integrity*. 2018;13: 705–709.
- 16. Cadoni E, Labibes K, Albertini C, Berra M, Giangrasso M. Strain-rate effect on the tensile behaviour of concrete at different relative humidity levels. *Materials and Structures*. 2001;34: 21–26.
- 17. Yan D, Lin G. Dynamic properties of concrete in direct tension. *Cement and Concrete Research*. 2006;36(7): 1371–1378.
- 18. Smirnov I, Konstantinov A. Evaluation of critical stresses for quasi-brittle materials at various loading rates. *Materials Physics and Mechanics*. 2020;44(2): 210–220.
- 19. Bragov AM, Konstantinov AY, Petrov YV, Evstifeev AD. Structural-temporal approach for dynamic strength characterization of rock. *Materials Physics and Mechanics*. 2015;23(1): 61–65.
- 20. Selyutina NS, Petrov YV. Fracture of saturated concrete and rocks under dynamic loading. *Engineering Fracture Mechanics*. 2020;225: 106265.
- 21. Chakraborty T, Mishra S, Loukus J, Halonen B, Bekkala B. Characterization of three Himalayan rocks using a split Hopkinson pressure bar. International *Journal of Rock Mechanics and Mining Sciences*. 2016;85: 112–118.
- 22. Steverding B, Lehnigk SH. Response of cracks to impact. *Journal of Applied Physics*. 1970;41(5): 2096–2099.
- 23. Li HB, Zhao J, Li TJ. Triaxial compression tests on a granite at different strain rates and confining pressures. *International Journal of Rock Mechanics and Mining Sciences*. 1999;36(8): 1057–1063.
- 24. Meshcheryakov Yul, Atroshenko SA. On the mesoscopic mechanisms of spall fractrure. *Materials Physics and Mechanics*. 2018;36(1): 121–130.

- 25. Grinevich DV, Buznik VM, Nyzhnyi GA, Numerical simulation of ice fracture by compression using of the discrete element method. *Materials Physics and Mechanics*. 2023;51(3): 75–87.
- 26. Petrov YV, Karihaloo BL, Bratov VV, Bragov AM. Multi-scale dynamic fracture model for quasi-brittle materials. *International Journal of Engineering Science*. 2012;61: 3–9.
- 27. Petrov YV, Gruzdkov AA, Bratov VA. Structural-temporal theory of fracture as a multiscale process. *Physical Mesomechanics*. 2012;15: 232–237.
- 28. Selyutina NS. Strain rate dependences of dynamic fracture toughness and fracture energy of rocks. *Physical Mesomechanics*. 2022;25(4): 366–372.
- 29. Lim IL, Johnston IW, Choi SK. Stress intensity factors for semi-circular specimens under three-point bending. *Engineering Fracture Mechanics*. 1993;44(3): 363–382.
- 30. Zhou Z, Cai X, Ma D, Du X, Chen L, Wang H, i dr. Water saturation effects on dynamic fracture behavior of sandstone. *International Journal of Rock Mechanics and Mining Sciences*. 2019;114: 46–61.
- 31. Jung Y, Park E, Kim H. Determination of mode II toughness of granite by using SCC test. In: *Processings of the ISRM International Symposium-EUROCK*. Ürgüp; 2016.
- 32. Schmidt RA, Huddle CW. Effect of confining pressure on fracture toughness of Indiana limestone. *International Journal of Rock Mechanics and Mining Sciences & Geomechanics Abstracts*. 1977;14(5): 289–293.
- 33. Mishra S, Meena H, Parashar V, Khetwal A, Chakraborty T, Matsagar V, i dr. High strain rate response of rocks under dynamic loading using split Hopkinson pressure bar. *Geotechnical and Geological Engineering*. 2018;36: 531–549.
- 34. Xu Y, Yao W, Zhao G, Xia K. Evaluation of the short core in compression (SCC) method for measuring mode II fracture toughness of rocks. *Engineering Fracture Mechanics*. 2020;224: 106747.

About Author

Nina S. Selyutina 🗓 Sc

Doctor of Physical and Mathematical Sciences Senior Researcher (St. Petersburg State University, St. Petersburg, Russia)

Lyudmila A. Igusheva 🗓

PhD Student (St. Petersburg State University, St. Petersburg, Russia)

Yuri V. Petrov D Sc

Doctor of Physical and Mathematical Sciences

Professor (Institute for Problems in Mechanical Engineering of the Russian Academy of Sciences, St. Petersburg, Russia)

Submitted: March 14, 2024 Revised: May 6, 2024 Accepted: May 28, 2024

Laboratory study on use of lime and waste materials in improving geotechnical properties of clay

G. Juneja ^{1 ⊠}, ¹ A. Bhardwaj ², ¹ A. Sharma ³, ¹ R.K. Sharma ²

ABSTRACT

The waste materials such as fly ash, construction demolition waste, and plastic waste are generated in tremendous quantities and are dumped haphazardly thereby causing irreparable damage to the environment. Proper utilization of these wastes particularly in the construction sector will protect the environment from their harmful effects and will prove to be economical through the preservation of precious natural resources. This paper presents an investigation on the utilization of lime, fly ash, and construction demolition waste individually and in combination with each other for the stabilization of poor soil. The utilization of plastic waste along with soil-fly ash-construction demolition waste-lime composite was further investigated. The samples for unconfined compressive strength and split tensile strength were compacted at optimum moisture content to maximum dry density, which was obtained from standard Proctor compaction tests. The samples were tested after 7 days, 28 days, and 56 days of curing periods. The results reveal that the addition of admixtures increases the unconfined compressive strength and split tensile strength, and the optimum mixes were selected based on 7 days of unconfined compressive strength. The increase in strength with the addition of admixtures depends on the type of admixture used and the formation of new minerals, which can be observed from XRD graphs. The soaked California bearing ratio tests were conducted on the optimum mixes and soil-fly ash-C&D waste-lime mix was selected as the best sub-grade material compared to other material combinations based upon economic and environmental considerations.

KEYWORDS

clay • fly ash • construction demolition waste • lime • plastic waste

Citation: Juneja G, Bhardwaj A, Sharma A, Sharma RK. Laboratory study on use of lime and waste materials in improving geotechnical properties of clay. *Materials Physics and Mechanics*. 2024;52(3): 121–144. http://dx.doi.org/10.18149/MPM.5232024_12

Introduction

The production of waste materials is increasing day by day, resulting in the requirement of a large area for disposal, which is a costly affair. The utilization of waste materials in improving the properties of soil is one of the effective methods of disposal. The waste materials used in this study are fly ash, construction demolition (C&D) waste, and plastic waste. Fly ash is a waste material produced by thermal power plants. Though the use of fly ash is growing continuously, much attention is needed to utilize more and more quantity of fly ash. Rapid infrastructure development leads to an increase in the generation of C&D waste in large quantities, the disposal of which is causing environmental and economic problems. Most of C&D waste remains unutilized hence, using this waste in improving the properties of the soil will be useful both from an economical and eco-friendly point of view. Plastic waste is produced in different ways

¹ Chandigarh Group of Colleges, Jhanjeri, Punjab, India

² National Institute of Technology, Hamirpur, Himachal Pradesh, India

³ Chandigarh University, Punjab, India

[™] juneja.gaurav@nith.ac.in

such as shopping bags, polypropylene of plastic sacks, polypropylene of carpets, and plastic bottles. Although, the reuse and recycling of plastic waste are getting attention day by day, even then only a small percentage of the total volume of plastic waste produced is being utilized and a larger amount of it is placed in disposal sites or storage. The construction of disposal sites and/or landfills will be a costly process, hence, disposal of plastic by using it in soil stabilization is one of the viable options. Soil stabilization is the process of improving the engineering and index properties of poor soils. Numerous research studies have been conducted in the past to stabilize expansive soils by using various materials and admixtures [1–4]. Though lime is not a waste material and is costly but can be utilized in soil stabilization because it leads to early and high strength gain. Thus, fly ash, C&D waste, plastic waste, and lime are chosen as stabilizing materials for improving the properties of soil.

Some research has been done on the utilization of these materials in soil stabilization. Adding the fly ash to the soil improves the engineering properties i.e. unconfined compressive strength (UCS) and California bearing ratio (CBR) of soil and is cost-effective material [5–8]. The uniaxial compression indirect (splitting) tension and flexure strength were also found to be enhanced with the addition of fly ash [5]. There is a decrease in the maximum dry density (MDD) and an increase in the value of optimum moisture content (OMC) on adding fly ash to soil [6,7]. The various properties of soil such as plasticity index, free swell, activity, swelling pressure, swell potential, etc. are found to be decreased with the addition of fly ash or fly ash-lime content [8].

Many researchers explained the consequences of lime on the engineering properties of soil, some among them are: The characteristics such as swell potential, liquid limit, plastic limit, free swell, cohesion, compaction characteristics, and modulus of elasticity are affected by the addition of lime to soil [9–14]. There is an improvement in the value of OMC, CBR value, and UCS of the mix due to the addition of lime to soils [9,11,12,14]. This is attributed to the formation of cementing minerals such as calcium aluminate hydrate (CAH), calcite, and mullite which are identified by X-ray diffraction (XRD) [10,12,13]. Initially, with the increase in lime content up to 5 %, there is an increase in the plastic limit and a decrease in the liquid limit, but beyond 5 % lime content, the Atterberg limits show negligible variations. Further, there is a decrease in the swell potential up to certain lime content, after which it accelerates its value beyond 9 and 5 % addition of lime for coarse-grained soils and fine-grained soils respectively. The unconfined compressive strength (UCS) of the composite mix increases up to a certain lime content [13].

Construction demolition waste refers to the waste generated during the demolition of structures. A lot of research in the past have been conducted in past on the utilization of recycled aggregates from concrete waste in soil stabilization and as sub-base and base course material in pavements [15–25]. Many researchers concluded that for unpaved rural roads, natural aggregates can be replaced by recycled aggregates obtained from C&D waste [19,22]. Soils blended with fine crushed concrete cubes and cement showed considerable improvement in UCS value, split tensile strength (STS), and CBR value as shown in [20].

The plastic waste when added to soil increases the peak strength, ultimate strength; energy absorption capacity, and UCS value [26,27]. Sub-grade characteristics of soil are

improved with the addition of plastic waste because of an increase in CBR value [28–30]. The addition of plastic waste increases deviator stress and changes the behavior from brittle to ductile and the penetration resistance increases with plastic waste as shown in [30].

When fly ash and lime are added in combination to poor soils, OMC, UCS, and CBR values are found to be increased whereas MDD value and the free swell were observed to be decreased which was resulted due to the flocculation and cation exchange reaction [31–33].

The use of fly ash for agricultural purposes has been studied and the existence of harmful trace elements such as Pb, Cd, Ni, etc. has been shown [34]. Further, class F fly ash alone pollutes the groundwater thereby damaging the environment but if class F fly ash is used with lime, the release of harmful metals can be prevented as shown in [35].

The addition of plastic waste to the soil-fly ash-lime mix increases the UCS value, split tensile strength, and overall toughness [36–40]. The addition of plastic waste or fiber increases the CBR value and changes the failure behavior from brittle to ductile [41–47]. Thus, the soil-fly ash-lime-plastic waste mix can be effectively utilized in geotechnical and pavement applications.

The primary objective of this paper is to reveal how waste materials such as fly ash, C&D waste, plastic waste, and lime can be used in refining the properties of soil and to investigate the strength characteristics of various material combinations such as clay-fly ash, clay-C&D waste, clay-lime, clay-fly ash-lime, clay-C&D waste-lime, clay-fly ash-C&D waste, clay-fly ash-C&D waste-lime, clay-fly ash-C&D waste-lime-plastic waste mixtures for obtaining the optimum composite in soil stabilization. Further, the use of fly ash with lime can prevent the release of harmful trace elements present in it thus minimizing the negative impact on the environment.

Experimental study

The soil (S) used in the current study was brought from a construction site near Hamirpur, Himachal Pradesh (India). The fly ash (FA) was collected from Ropar thermal power plant and construction demolition (C&D) waste was acquired from the floor finish layer of local construction. The standard specification [45] for quicklime and hydrated lime was followed for use of lime in soil stabilization.

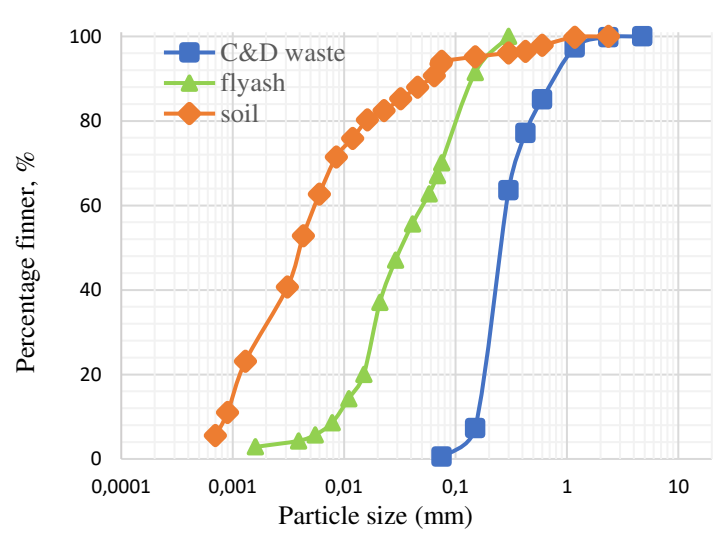


Fig. 1. Gradation curves of soil, fly ash and C&D waste

The plastic waste used in the present investigation was obtained from wasted online shopping bags, which were cut into pieces 12 mm in length and 6 mm in width. The average thickness of the plastic bags was 70 μ m. The particle size curves of soil, fly ash, and construction demolition waste is shown in Fig. 1 [48–50]. Based on the Indian soil classification system as per [51], the soil was classified as clay with high plasticity, CH. The composition of fly ash lies in the range of the class F category. The gradation curve of C&D waste reveals that most of the particles are in the fine sand range. The properties of soil, fly ash and C&D waste are shown in Tables 1–3 respectively.

Table 1. Properties of soil

Properties	Value
Natural water content, w _n , %	22.0
Specific gravity <i>G</i> [52]	2.573
Liquid limit w _L , %	51.0
Plastic limit w _p , %	23.0
Plasticity index (PI), %	28.0
Soil classification	CH
Maximum dry density ρ_d , KN/m ³	17.5
Optimum moisture content, %	16.0
Percent finer than 2 µm, %	32
Coefficient of permeability, cm/s [53]	3.337 × 10 ⁻⁸
Unconfined compressive strength after 7 days, KN/m ²	355.05
Differential free swell, % [54]	16.52
Soaked California bearing ratio, %	1.612

Table 2. Properties of fly ash

Chemical composition and index properties	Value
Silica (SiO ₂), %	59.50
Alumina (Al ₂ O ₃), %	27.10
Iron oxide (Fe ₂ O ₃), %	7.36
Calcium oxide (CaO), %	2.30
Magnesium oxide (MgO), %	0.64
Sulphur trioxide (SO ₃), %	0.85
Loss of ignition, %	2.25
Specific gravity, G [52]	1.966
Liquid limit, w _L (%)	39.5
Coefficient of uniformity, C _u	4.909
Coefficient of curvature, C _c	0.930
Indian standard soil classification	MI
Optimum moisture content, %	27.4
Maximum dry density ρ_d , KN/m ³)	12.24
Coefficient of permeability, cm/s [53]	6.6 × 10 ⁻⁵
Soaked California bearing ratio, %	4.45

Table 3. Properties of construction demolition waste

Properties	Value
Specific gravity, <i>G</i> [52]	2.57
Coefficient of uniformity C _u	1.781
Coefficient of curvature C _c	0.877
Soil classification	SP
Optimum moisture content, %	12.4
Maximum dry density, ρ_d , KN/m ³	16.75
Coefficient of permeability, cm/s [53]	4.26 × 10 ⁻⁴
Soaked California bearing ratio, %	17.07

Various tests were performed to classify the best optimum mix and best optimum arrangement for the stabilization of clayey soil. Firstly, the standard Proctor compaction tests were conducted on soil-fly ash mixes, soil-lime mixes, soil-C&D waste mixes, soil-fly ash-lime mixes, soil-fly ash-C&D waste mixes, soil-fly ash-C&D waste-lime mixes and soil-fly ash-C&D waste-lime-plastic waste mixes as per standard [55]. The results of the compaction tests detailing MDD and OMC are shown in Table 4. Based on the results, it can be concluded that the optimum mixes cannot be obtained from compaction characteristics.

Table 4. Compaction characteristics of different mixes

Mix proportions	Maximum dry density, KN/m ³	Optimum moisture content, %
S :: 100	17.50	16.00
S:FA:: 92:8	16.98	16.70
S:FA :: 88:12	16.92	16.80
S:FA :: 84:16	16.90	17.10
S:L :: 97:3	16.85	18.00
S:L :: 96:4	16.68	19.00
S:L :: 95:5	16.41	19.50
S:C&D :: 88:12	17.32	15.10
S:C&D :: 78:22	17.22	14.95
S:C&D :: 76:24	17.20	14.90
S:FA:L :: 85.8:11.7:2.5	15.90	20.00
S:FA:L :: 84.92:11.58: 3.5	15.82	20.40
S:FA:L :: 84.04:11.46:4.5	15.81	20.90
S:C&D:L :: 77.62:21.89:0.49	17.04	17.00
S: C&D:L :: 77.42:21.836:0.744	16.86	17.60
S: C&D:L :: 77.23:21.78:0.99	16.78	19.00
S: FA:C&D :: 66:17:17	16.61	17.00
S: FA:C&D :: 65:17:18	16.63	16.80
S: FA:C&D :: 64:18:18	16.62	17.50
S: FA:C&D:L:: 64.36:16.83:17.82: 0.99	16.26	19.00
S:FA:C&D: L :: 63.73:16.67:17.64:1.96	15.96	19.40
S:FA:C&D: L :: 63.12:16.5:17.47:2.91	15.80	19.80
S: FA:C&D:L:PW :: 64.25:16.79:17.78:0.98:0.2	15.96	18.60
S:FA:C&D:L:PW :: 64.11:16.76:17.75:0.98:0.4	16.08	18.60
S:FA:C&D:L: PW :: 63.97:16.73:17.72:0.98:0.6	16.03	18.60

To demonstrate the effect of C&D waste on the liquid limit of soil, tests were piloted on soil alone and on soil C&D waste mixes, as per [56]. The results of the liquid limit test are shown in Fig. 2, which designates that the liquid limit falls down with the increase in the content of C&D waste. As the percentage of C&D waste approaches 30 %, the lowering rate in liquid limit also falls down, which indicates that the optimum mix should contain between 20-30 % of C&D waste. As the liquid limit is one of the important parameters in selecting the sub-grade material, it can be established from liquid limit tests that adding C&D waste to soil can improve the performance of soil as pavement sub-grade material.

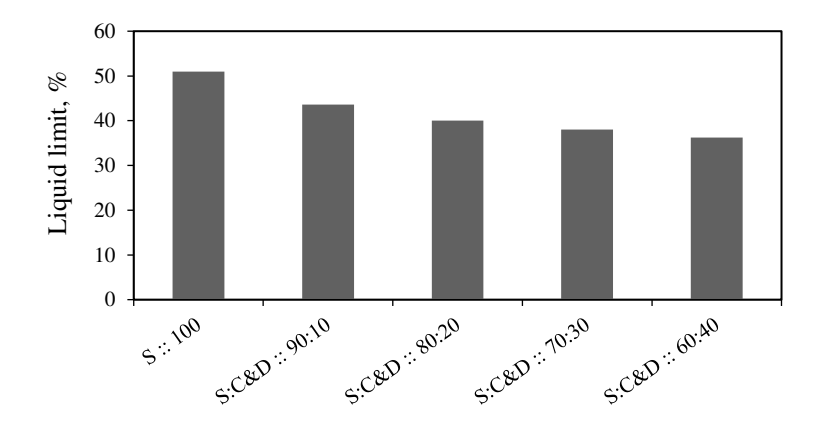


Fig. 2. Influence of addition of construction demolition waste on liquid limit of soil

The unconfined compressive strength tests were performed on numerous mix proportions to obtain the optimum composite mixes. The compaction of samples having a size of 38 mm diameter and 76 mm height was done to MDD in a standard mold at OMC. In order to avoid excess moisture loss, samples were kept in desiccators for 7, 28, and 56 days curing periods, and UCS tests were performed on these samples as per standard [57]. Two samples were prepared for every mix combination for each curing period and an average of two is presented as the UCS value. The optimum mix was chosen for that mix proportion which yielded the highest UCS value.

The split tensile strength tests were conducted as per [58] in split mold on samples of 50 mm diameter and 25 mm height prepared in a standard mold at OMC compacted to MDD. The average value of the strength of two samples for each curing period is the split tensile strength of the sample.

The CBR tests were conducted on the optimum mixes obtained from unconfined compressive strength for each combination. The sample for conducting the CBR tests was prepared according to [59]. The surcharge was placed on the sample and soaking of the sample was done for a period of 4 days. The sample was removed from the water after 4 days prior to 15 minutes before conducting the test. The testing was conducted in a CBR testing machine and the CBR value (load/standard load) was a maximum of two values obtained for 2.5 and 5 mm penetrations.

Results and Discussion

Unconfined compressive strength. Influence of adding lime, fly ash and C&D waste individually on UCS of soil

The curves of unconfined compressive strength (UCS) versus the curing period (Fig. 3) reveal that the addition of different contents of admixtures such as fly ash, lime, and C&D waste increase the UCS value of the clay. The maximum increment in UCS value is observed upon the addition of optimum content (4 %) of lime, which is attributed to the chemical reaction among soil and lime particles.

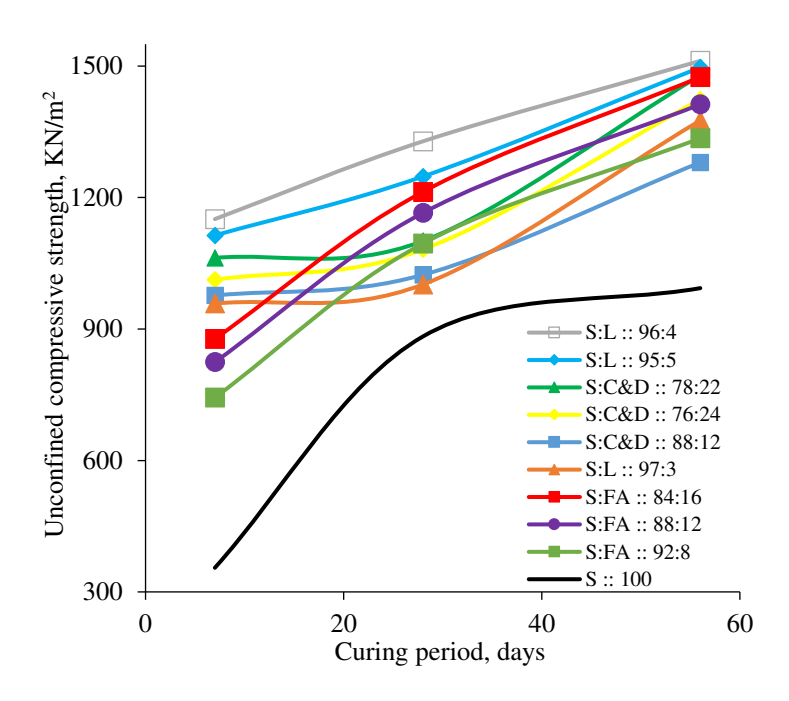


Fig. 3. Influence of addition of additives on UCS of soil with curing period

With the curing time, an increase in UCS value is noticed irrespective of the additive and additive content. The 7 days unconfined compressive strength is more on the addition of lime followed by C&D waste and fly ash. The strength increment is more for 4 % lime compared to 3 and 5 % lime content. The optimum content of lime may be taken as 4 % since a higher content of lime leads to the existence of free lime which tends to decrease the strength. Similarly, the strength of 78 % soil + 22 % C&D waste is more compared to 76 % soil + 24 % C&D waste and 88 % soil + 12 % C&D waste. The optimum content of C&D waste may be taken as 22 % at which the contents of compounds present in it are sufficient to complete the reaction and form new compounds like calciobetafite. There is no appreciable enhancement in the UCS value of soil-fly ash composite for fly ash content of more than 12 %. Hence, based on the above results, the optimum content of lime, fly ash, and C&D waste for stabilization of soil may be taken as 4, 12, and 22 % respectively. The strength gains up to 28 days curing period is more for soil-lime admixture followed by soil-fly ash admixture and soil-C&D waste admixture which indicates that the pozzolanic reaction between soil and fly ash and soil-C&D waste is relatively slow. The 28-day UCS value of 78 % soil + 22 % C&D waste is nearly the equivalent as that of 92 % soil + 8 % fly ash which indicates that C&D waste is an effective stabilization material. Initially, there is less increase in the UCS value of soil on the addition of optimum C&D waste content (up to 28 days) but increases after 56 days and is comparable with the strength value obtained upon the addition of optimum lime content. This is mainly attributed to the slow pozzolanic reaction among soil and C&D waste particles. The UCS value of soil admixed with fly ash content (16 %) increases with the curing period and is comparable with that achieved upon adding the optimum lime content after 56 days curing period. Though strength is higher for 16 % fly ash content than that for 12% content its maximum dry density is less and hence 12 % fly ash content may be taken as the optimum. This increment in strength value on adding fly ash is attributed to the pozzolanic reaction among the particles of soil and admixtures. Thus, it can be observed that when the optimum content of the admixtures – lime or C&D waste or fly ash is added; the unconfined compressive strength achieved is comparable after 56 day curing period.

The X-ray diffraction (XRD) pattern of soil (Fig. 4(a)) reveals the existence of montmorillonite, quartz, and muscovite. The presence of montmorillonite indicates that the clay is very sensitive when it comes in contact with water and has high swelling properties.

The cause of improvement in the UCS value of soil on adding lime is due to the formation of new compounds like calcite, which was observed in the X-ray diffraction pattern presented in Fig. 4(b). The further increase in the UCS value of soil on adding fly ash is attributed to the formation of new compounds like mullite observed in the X-ray diffraction pattern Fig. 4(c).

On adding C&D waste to the soil, the formation of new compounds like calciobetafite was observed in the X-ray diffraction pattern presented in Fig. 4(d), which lead to an increase in the value of unconfined strength.

The difference between the 56 days of unconfined compressive strengths of the optimum soil-lime, soil-fly ash, and soil-C&D waste mixes is negligible. This indicates that all three additives are good stabilizers when long-term strength is a governing criterion. However, since lime is a costly material, it should be used only when short-term strength is the governing criterion. Fly ash is a waste material affecting the environment adversely but utilized for various purposes already in enormous quantities. The stabilization of soil requires less quantity (12 %) of fly ash compared with C&D waste, making it as the second-best alternative. The generation of C&D waste is increasing tremendously, whereas its utilization for construction purposes is very less presently. Hence, the utilization of large quantities (22 % as compared to 12 % fly ash) of C&D waste in soil stabilization will solve the problem of its disposal. Thus, C&D waste can also be selected as a good stabilizer comparable to other materials, taking into account its strength as well as economical and environmental considerations.

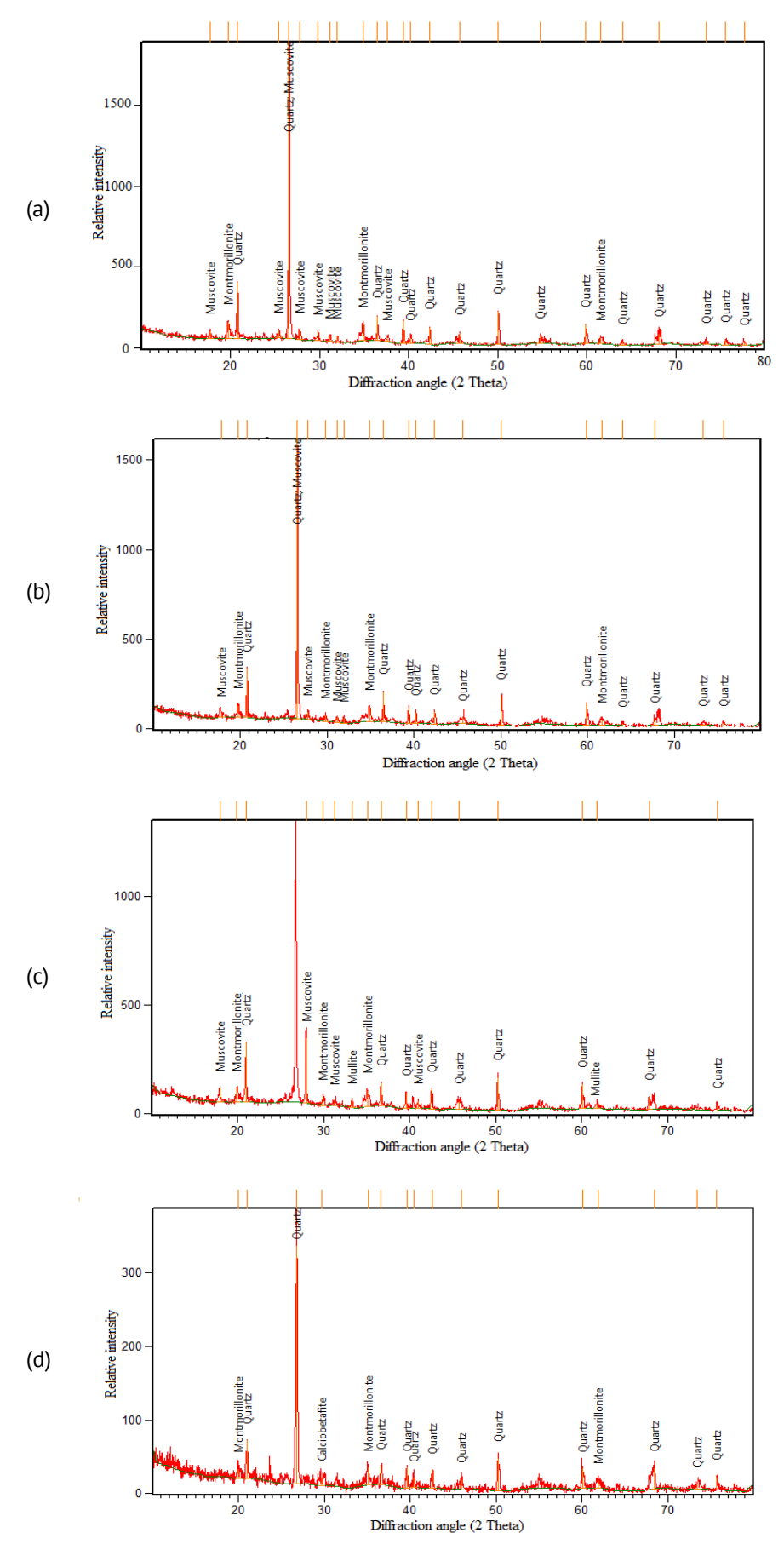


Fig. 4. XRD graph of soil (a), soil + lime (b), soil + fly ash (c), soil + C&D waste (d)

Influence of addition of fly ash and lime on UCS of soil

UCS tests were carried out on the optimum mixes soil-fly ash mix (obtained from UCS tests) with adding different percentages of lime obtained on the basis of unconfined compressive strength of soil-fly ash mixes and the curves between UCS value and curing period (Fig. 5) reveal the influence of lime on UCS value of soil-fly ash mix. The addition of lime increases the UCS of the mix, but the increase is less.

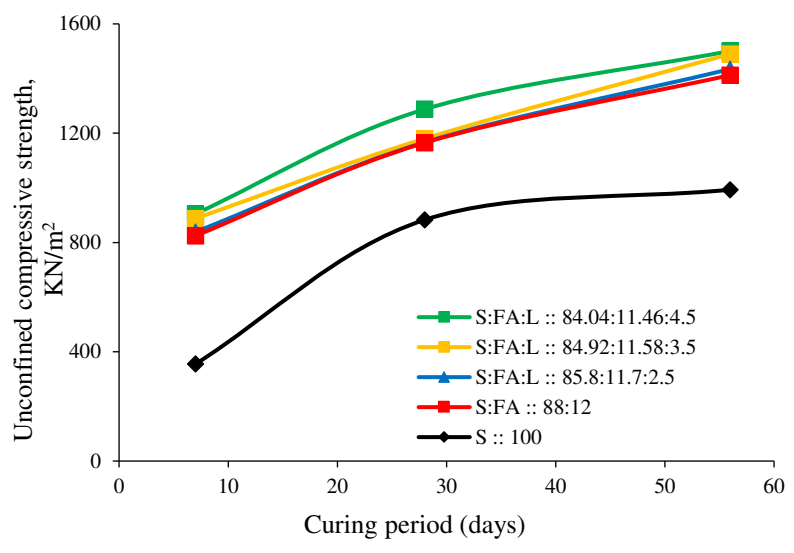


Fig. 5. UCS of soil, soil-fly ash mix, and soil-fly ash-lime mixes with curing period

The UCS value is more in the case of 84.04% soil + 11.46% fly ash + 4.5% lime, hence, this mix may be chosen as the optimum stabilized mix. The increase in strength is mainly because of the reduced rate of reaction among lime and soil-fly ash mix, since most of the pozzolanic reaction occurred with fly ash. A little increase in the UCS value of soil + fly ash mix on adding lime may be attributed to the presence of new compounds like calcite, as observed in the X-ray diffraction pattern presented in Fig. 6.

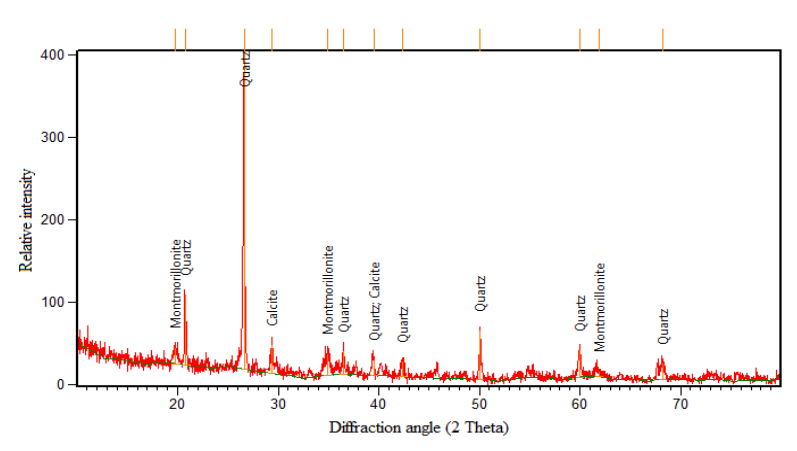


Fig. 6. XRD patterns of soil + fly ash + lime

Influence of addition of C&D waste and lime on UCS of soil

The optimum soil-C&D waste mix obtained based on the UCS test results was further stabilized by adding lime. The deviation of UCS value of soil-C&D waste mix with curing period corresponding to 0.49, 0.744, and 0.99 % lime contents is shown in Fig. 7, which indicates that 0.49 % lime content gives the maximum unconfined compressive strength value. Hence, 0.49 % lime content may be chosen as the optimum content for the stabilization of the soil-C&D waste mix. However, the addition of lime to the soil-C&D waste mix does not yield much increase in strength and lime may be added only if early strength is required. The little increase in strength is attributed to the reduced rate of reaction among lime and soil-C&D waste mix because the pozzolanic reaction already occurred with C&D waste. The addition of lime to the soil-C&D waste mix is a better option compared to soil-fly ash mix, which requires more lime content.

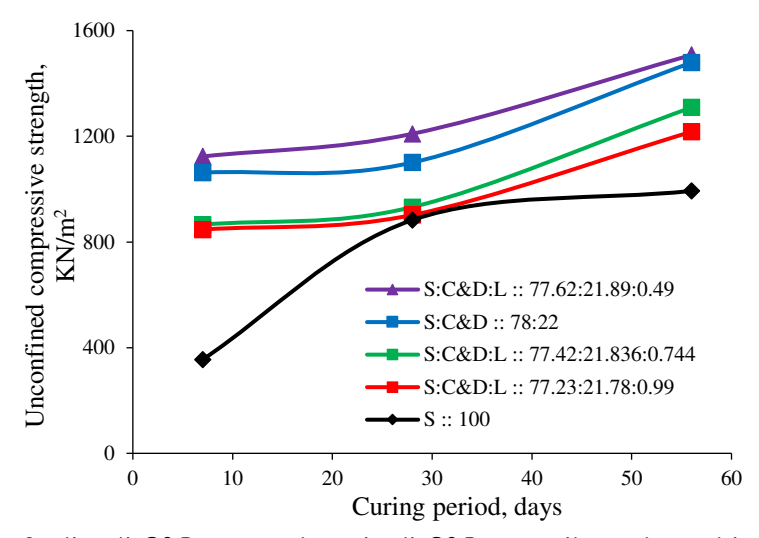


Fig. 7. UCS of soil, soil-C&D waste mix and soil-C&D waste-lime mixes with curing period

The X-ray diffraction pattern presented in Fig. 8 shows the presence of a small quantity of calcite, which causes less increase in unconfined compressive strength of soil + fly ash mixture on adding lime.

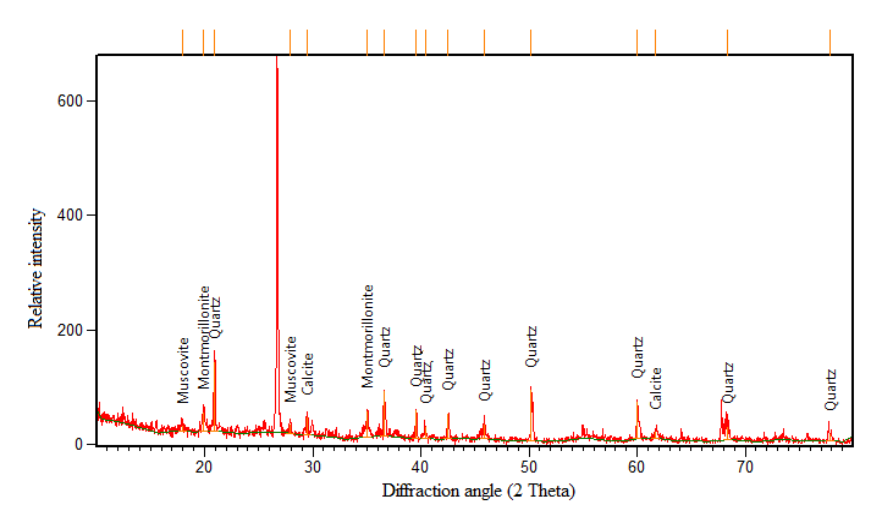


Fig. 8. XRD patterns of soil + C&D waste + lime

Influence of addition of fly ash and C&D waste on UCS of soil

The graph amongst UCS value and curing period presented in (Fig. 9) describes the influence of mixing of two waste materials fly ash and C&D waste. Adding both the materials fly ash and C&D waste together to the soil increases the unconfined compressive strength, which is more as compared to adding fly ash and C&D waste individually. The 7 days unconfined compressive strength is more for soil-C&D waste mix in comparison to soil-fly ash-C&D waste mix whereas 28 and 56 days UCS value is more for optimum soil-fly ash-C&D waste mix compared to soil-fly ash mix and soil-C&D waste mix and is mainly attributed to the higher pozzolanic reaction occurring among soil, fly ash and C&D waste. The UCS value of 65 % soil + 17 % fly ash + 18 % C&D waste is more compared to 64% soil + 18% fly ash + 18% C&D waste mix and 66% soil + 17% fly ash + 17 % C&D waste, and, therefore, 65 % soil + 17 % fly ash + 18 % C&D waste mix is finalized as an optimum mix to be used for soil stabilization. The stabilization of soil using both fly ash and C&D waste is an eco-friendly option because the dumping problem of both materials can be solved and the amount of fly ash (17 %) required in this mix is more than that of the amount of fly ash (12 %) required in soil stabilization using fly ash alone. Upon comparison of unconfined compressive strengths of optimum mixes of soilfly ash-lime, soil-C&D waste-lime, and soil-fly ash-C&D waste (Figs. 5,7,9), it may be observed that the strength achieved after 56 days curing period is nearly the same. The quantity of the admixtures used in the above combinations is 12 % fly ash + 4.5 % lime, 21.89 % C&D waste + 0.49 % lime, and 17 % fly ash + 18 % C&D waste respectively. This indicates that the optimum combination of soil-fly ash-C&D waste mix involves the utilization of 35 % of waste materials without the addition of lime (which is costly). Thus, the soil-fly ash-C&D waste mix is economical and helps in minimizing the adverse effects of the waste materials on the environment besides giving a solution to dumping problems of waste materials.

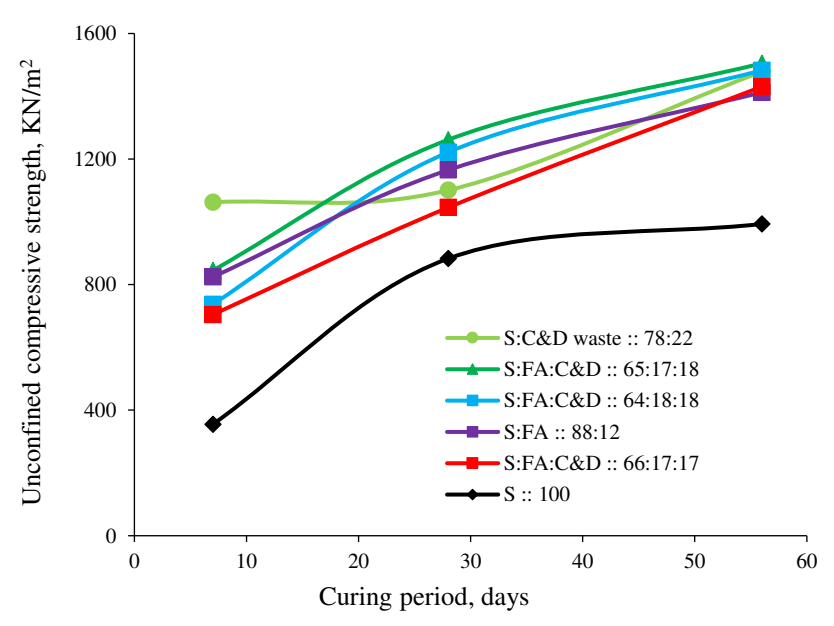


Fig. 9. Variation in UCS of soil and soil-fly ash-C&D waste mixes with curing period

The addition of waste materials such as fly ash and C&D waste to soil results in the formation of new compounds like mullite as observed in the X-ray diffraction pattern (Fig. 10), which increases the UCS value of soil.

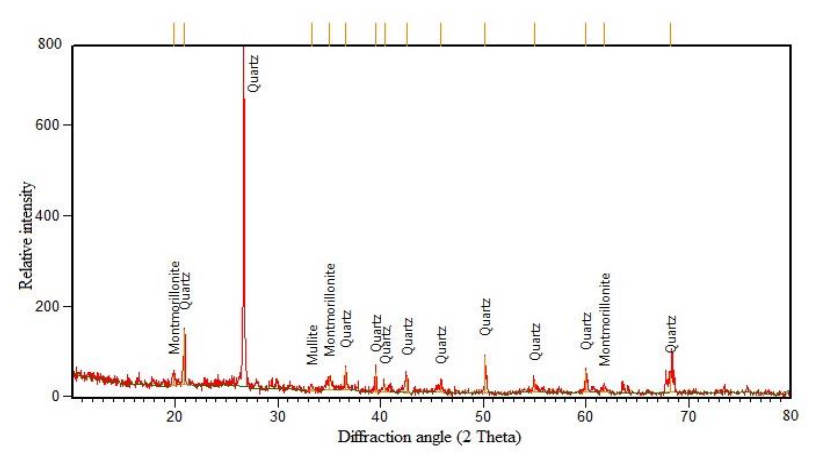


Fig. 10. XRD patterns of soil + fly ash + CDW

Influence of addition of fly ash, C&D waste and lime on UCS of soil

The lime was added to the optimum soil-fly ash-C&D waste mix in percentages of 0.99, 1.96, and 2.91 to explore its influence on UCS value. The curves between UCS value and curing period (Fig. 11) indicate that the unconfined compressive strength does not change appreciably up to 0.99 % lime content, but there is a reduction in strength for higher lime content (1.96 and 2.91 %). Thus, the addition of lime hardly shows any increase in strength with, however, 0.99 % lime content may be considered the optimum for the stabilization of soil-fly ash-C&D waste mix. The reduction in UCS value on the addition of lime occurs because of the presence of unreacted lime which creates a loose structure and causes sudden failure of the specimen as can be observed from the sudden drop in the unconfined compressive stress – axial strain curve shown in Fig. 12.

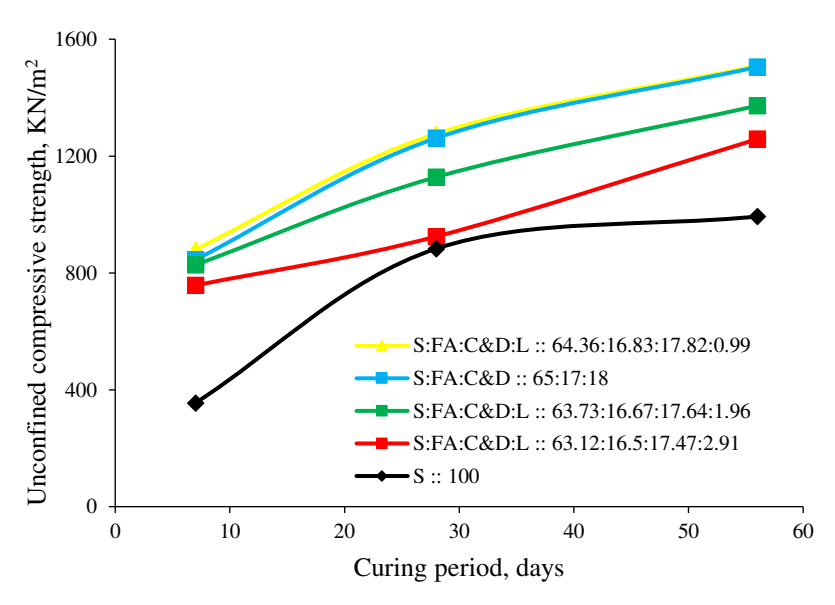


Fig. 11.-Variation in UCS of soil, soil-fly ash-C&D waste mix and soil-fly ash-C&D waste-lime mixes with curing period

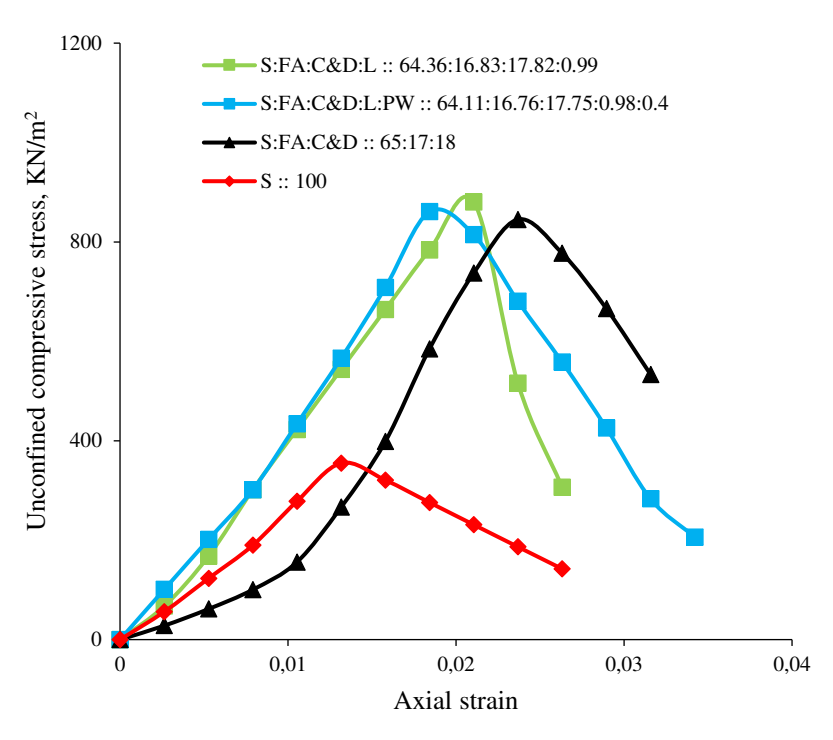


Fig. 12. Stress-strain curves of soil, soil-fly ash-C&D waste mix, soil-fly ash-C&D waste lime mix and soil-fly ash-C&D waste-lime-plastic waste mix

The lesser enhancement in UCS value can be accredited to the presence of minerals like calcite (Fig. 13) as observed from the X-ray diffraction pattern of soil + fly ash + C&D waste + lime.

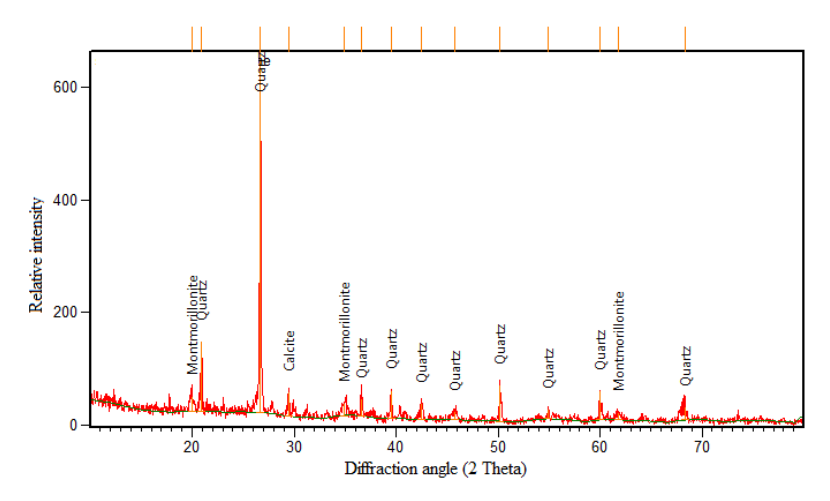


Fig. 13. X-Ray Diffraction patterns of soil + fly ash + C&D waste + lime

Influence of addition of fly ash, C&D waste, lime and plastic waste on UCS of soil

The effect of the addition of plastic waste to soil-fly ash-C&D waste-lime mix on UCS value and curing period is shown in Fig. 14. The addition of plastic waste (PW) decreases the UCS value of the mix. The rate of decrease is less in the case of the addition of 0.4 % plastic waste, followed by 0.6 and 0.2 % plastic waste contents. Hence, 0.4 % plastic waste content may be chosen as the optimum content for soil stabilization. The decrease in the UCS is due to the reduction in MDD, which may be due to a little loosening of the

mix with the addition of plastic waste. The curves of unconfined compressive strength versus the curing period for soil-fly ash-C&D waste-lime-plastic waste mixes reveal that there is a linear increase in strength with the curing period. Further, the addition of plastic waste changes the material behavior from brittle to ductile, as can be observed from the unconfined compressive stress—axial strain curves (Fig. 12). A similar trend indicating the change in stress-strain behavior from brittle to ductile upon the addition of fiber has been reported in [45].

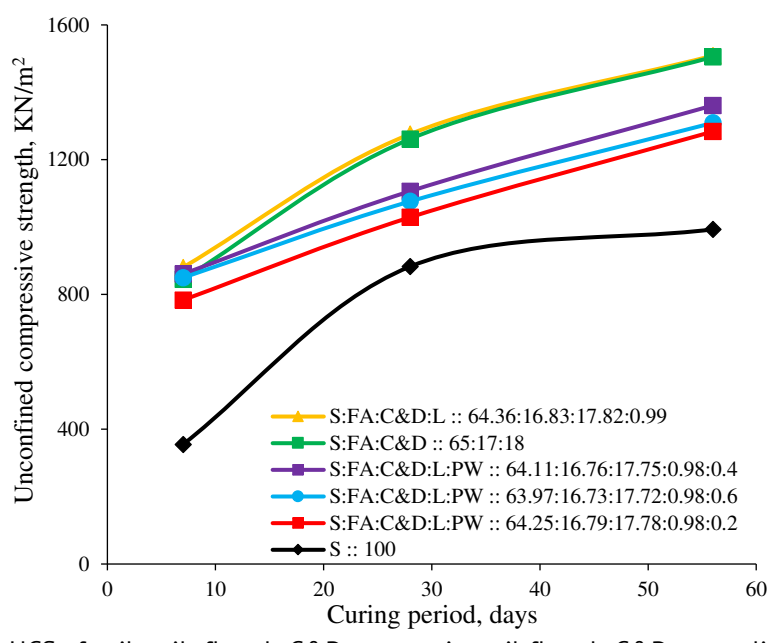


Fig. 14. Variation in UCS of soil, soil- fly ash-C&D waste mix, soil-fly ash-C&D waste-lime mix and soil-fly ash-C&D waste-lime-plastic waste mixes with curing period

Thus, based on the unconfined compressive strength values, it can be established that C&D waste is a better stabilizer in comparison to fly ash and lime when added individually to the soil. When two admixtures are added together to the soil, the best material combination is soil-fly ash-C&D waste followed by soil-C&D waste-lime and soil-fly ash-lime. The addition of lime to the soil-fly ash-C&D waste mix causes hardly any increment in UCS value. The addition of plastic waste to soil-fly ash-C&D waste-lime mix though reduces the unconfined compressive strength but deviates the composition of the mixture from brittle to ductile.

Split tensile strength

As per [60], the design of pavement is achieved on the basis of UCS and CBR values of the subgrade. Further, the tensile stresses are generated in the pavement due to variations in temperature and vehicle movement. In order to make the pavement free from tension cracks, the split tensile strength of sub-grade material should be known and should be included in the design of pavements as per [60]; this is the reason for including split tensile strength tests in present research work.

Influence of addition of lime, fly ash and C&D waste individually on STS of soil

The split tensile strength tests were performed on soil and various soil additives after a curing period of 7, 28, and 56 days. The influence of lime, fly ash, and C&D waste on the STS of soil at various curing periods is shown in Fig. 15. The curves reveal that STS increases with the curing period and the addition of different additives. The addition of lime increases STS value more due to the chemical reaction between the soil and lime particles, which is further followed by C&D waste and fly ash. The increase in strength on adding fly ash and C&D waste is due to the pozzolanic reaction between the particles of soil and admixtures. The split tensile strength increases with the curing period, irrespective of the type of additive and additive content. Based on the results, the strength of the soil-C&D waste mix is comparable with that of the soil-lime mix, and hence C&D waste is an effective stabilizing material.

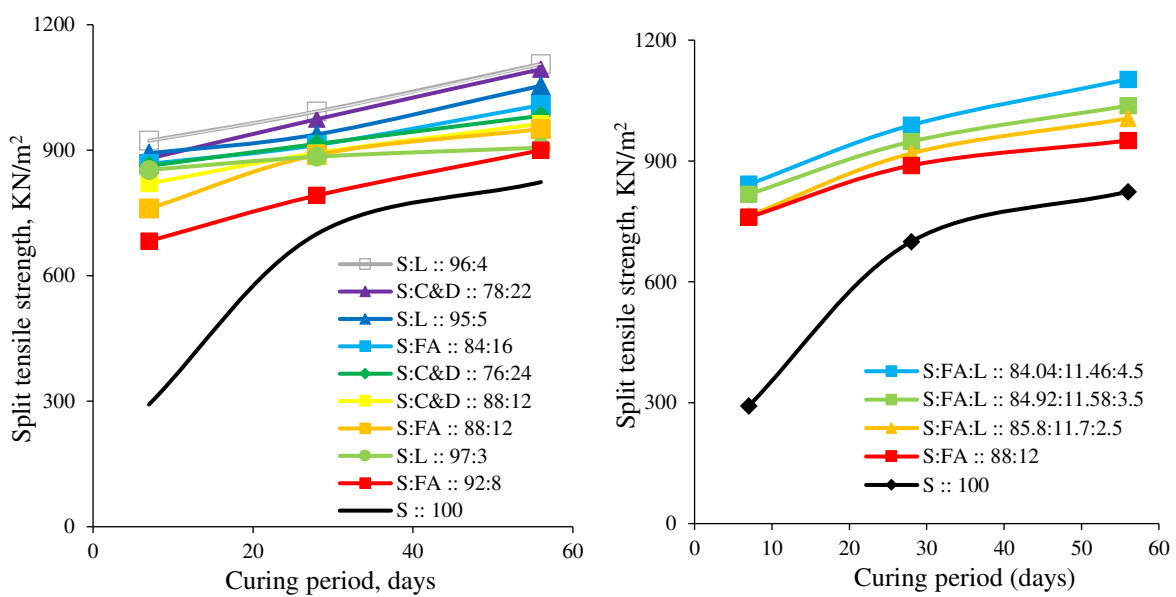


Fig. 15. Effect of addition of additives on STS of soil with curing period

Fig. 16. STS of soil, soil-fly ash mix and soil-fly ash-lime mixes with curing period

Influence of addition of fly ash and lime on STS of soil

Lime is added in percentages of 2.5, 3.5, and 4.5 %, respectively on the optimum soil-fly ash mix and STS tests were performed on these mixes. The influence of adding lime on the split tensile strength of the soil-fly ash mix is presented in Fig. 16. The split tensile strength of soil-fly ash-lime mix increases with an increase in lime content and curing period. This increase is attributed to the chemical reaction between lime and soil-fly ash particles. The split tensile strength is more on adding 4.5 % lime content, hence, 4.5 % lime content may be taken as the optimum value. Although the split tensile strength increases significantly, however, lime is a costly material.

Influence of addition of C&D waste and lime on STS of soil

The split tensile strength tests were conducted on optimum soil-C&D waste mix stabilized with 0.49%, 0.744%, and 0.99% lime contents. The split tensile strength results are plotted as split tensile strength (STS) versus the curing period (Fig. 17) showing the consequence of the addition of lime to the soil-C&D waste mix. Figure 17 reveals that there is hardly any enhancement in STS of soil-C&D waste mix with the addition of 0.49 % lime content, whereas higher lime content reduces the split tensile strength of the mix. The improvement in strength with the addition of lime is very limited, hence, it is better to avoid adding lime to the soil-C&D waste mix.

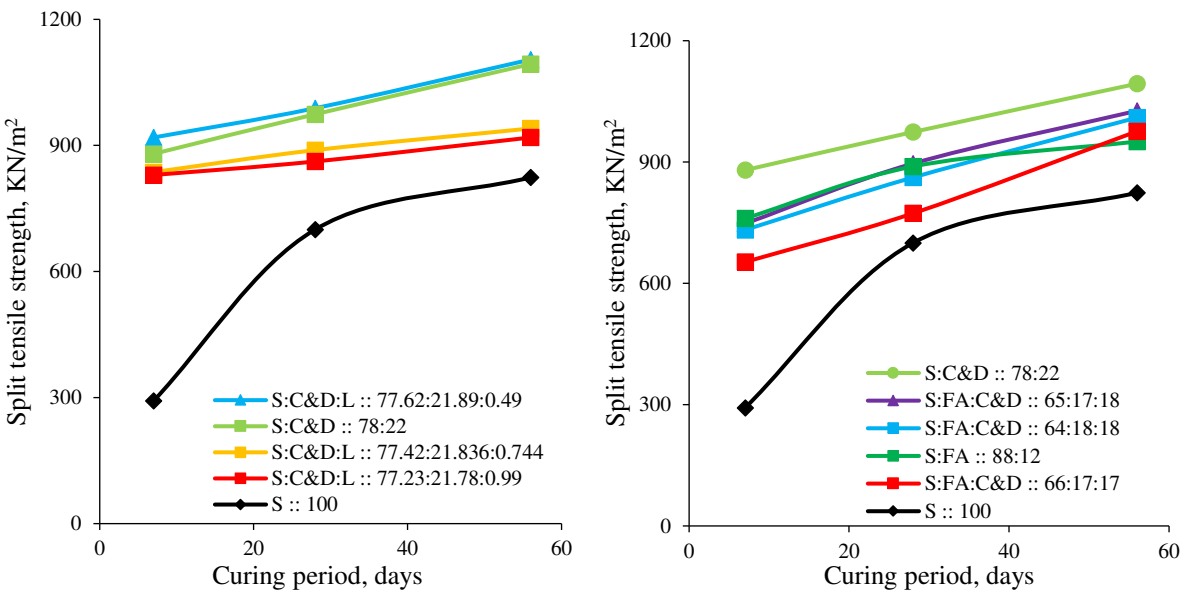


Fig. 17. STS of soil, soil-C&D waste mix and soil-C&D waste-lime mixes with curing period

Fig. 18. Variation in STS of soil and soil-fly ash-C&D waste mixes with curing period

Influence of addition of fly ash and C&D waste on STS of soil

The plot of the split tensile strength (STS) versus curing period (Fig. 18) shows the effect of the addition of two pozzolanic materials viz; fly ash and C&D waste to poor soil. The split tensile strength of the soil-fly ash-C&D waste mix is nearly the same as that of the soil-fly ash mix, but is less than that of the soil-C&D waste mix. The reduction in strength of soil-fly ash-C&D waste mixes compared to the soil-C&D waste mix is due to their less maximum dry density. The maximum split tensile strength is observed for 65% soil + 17% fly ash + 18% C&D waste mix compared to that of 64% soil + 18% fly ash + 18% C&D waste and 66% soil + 17% fly ash + 17% C&D waste mixes. There is no appreciable variation in split tensile strength of soil + fly ash mix on adding C&D waste, rather it is somewhat less for some combinations. However, more quantity of waste materials (34%-36% fly ash + C&D waste compared with 12% fly ash only) can be utilized, thus reducing detrimental effects on the environment.

Influence of addition of fly ash, C&D waste and lime on STS of soil

The effect of the addition of 0.99, 1.96, and 2.91 % lime content on the STS value of optimum soil-fly ash-C&D waste mix is shown in Fig. 19, which reveals that higher STS is observed for 0.99 % lime content and addition of more lime decreases the split tensile strength drastically which may be due to free the occurrence of unreacted lime. The increase in strength with the addition of lime is very, and it being a costly material should be used only when it is important from other design considerations.

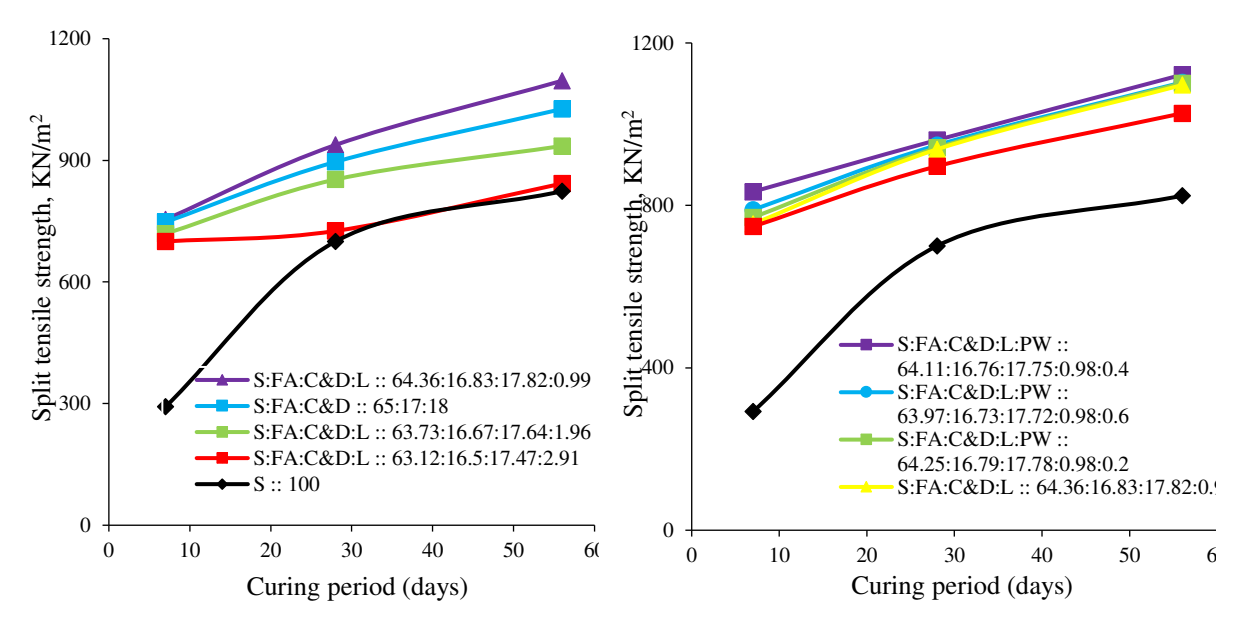


Fig. 19. Variation in STS of soil, soil-fly ash-C&D waste mix and soil-fly ash-C&D waste-lime mixes with curing period

Fig. 20. Variation in STS of soil, soil-fly ash-C&D waste mix, soil-fly ash-C&D waste-lime mix and soil-fly ash-C&D waste-lime-plastic waste mixes with curing period

Effect of addition of fly ash, C&D waste, lime and plastic waste on STS of soil

Plastic waste is added to the soil-fly ash-C&D waste-lime mix in percentages of 0.2, 0.4, and 0.6 to study its effect on split tensile strength of the mix. The STS versus curing period plot (Fig. 20) illustrates the effect of the addition of plastic waste to soil-fly ash-C&D waste mix. The slight increase in strength is pronounced by the addition of 0.4 % plastic waste content and is more as compared to 0.6 % plastic waste and 0.2 % plastic waste. Thus, 0.4 % plastic waste can be selected as the optimum content for the stabilization of soil-fly ash-C&D waste-lime mix. The reason for the enhancement in STS value may be due to increase in interfacial friction, which may be due to the effective contact area between plastic and the mixed material. Further, the reduction in the split tensile strength beyond 0.4 % plastic waste may be because plastic-to-plastic interaction dominates the plastic-to-particle interaction, making it the weakest failure plane to fail, which is in agreement with the results reported in [45].

It is observed on the basis of the above results that UCS value and STS value increase with curing time. The 360 days STS value is necessary for the design of pavement for high-intensity traffic. The correlation suggested between $q_{\rm t360days}$ and $q_{\rm t28days}$ [7], which is represented by the equation:

$$\frac{q_{t28days}}{q_{t360days}} = 0.60. \tag{1}$$

From the above equation, we can find out the 360 days split tensile strength of the mix, which can be used in the design of pavements. For the optimum soil-fly ash-C&D waste-lime-plastic waste mix, the 360 days split tensile strength is: $q_{t360days} = q_{t28days}/0.6 = 960.9 / 0.6 = 1601.5 \text{ KN/m}^2 = 1.6015 \text{ MPa}$, which is more than the required strength.

California bearing ratio

On the basis of optimum mixes obtained from UCS tests, the soaked CBR tests were piloted. The effect of the addition of various admixtures on the soaked CBR value of soil is shown in Fig. 21. The soaked CBR value of soil is 1.6% which with the addition of optimum content (12 %) of fly ash increases to 3.2 %. The soaked CBR value of 96 % soil + 4% lime is 12.7 % which is 8 times that of the CBR value of soil. The addition of 22 % C&D waste increases the soaked CBR value to 4.4% which is two and half times that of soil.

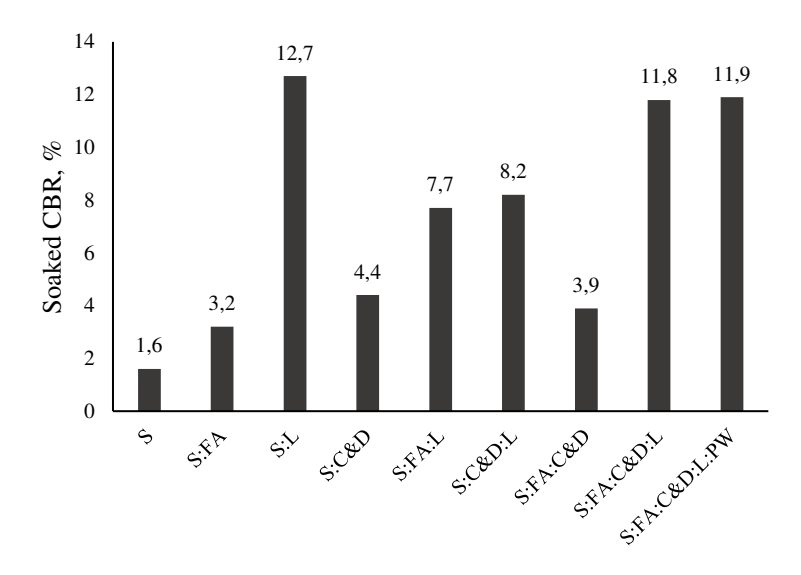


Fig. 21. Variation of soaked CBR values on addition of different admixtures

The soaked CBR value is 7.7 for 84.04 % soil + 11.46 % fly ash + 4.5 % lime, which can be used as a sub-grade material for pavement as per [60]. The soaked CBR value of 77.62 % soil + 21.89 % C&D waste + 0.49 % lime is 8.2 which is higher than the value of CBR obtained for the soil-fly ash-lime mix. The addition of fly ash and C&D waste together increases the soaked CBR value to 3.9 % which is very less compared to soil-fly ash-lime mix and soil-C&D waste-lime mix. The soaked CBR value of 64.36 % soil + 16.83 % fly ash + 17.82 % C&D waste + 0.99 % lime is 11.8 which is very close to that of 96 % soil + 4 % lime. The soaked CBR value of 64.11 % soil + 16.76 % fly ash + 17.75 % C&D waste + 0.98 % lime + 0.4 % plastic waste is 11.9, which is nearly the same as that of the soil-fly ash-C&D waste-lime mix. The above results reveal that the soil alone has a very low CBR value, and it requires stabilization using different additives. When stabilized by using two pozzolanic materials i.e. fly ash and C&D waste individually or in combination with each other, the CBR value increases, but the increase is not sufficient

to make it suitable for use as a sub-grade material in road pavement (CBR > 6 is generally required). The increase in CBR value is not appreciable due to the absence of a binder in the mixes, as reported in [45]. The CBR value increases appreciably when lime is added to soil + fly ash and soil + C&D waste mixes making it suitable as a sub-grade material. However, for soil + C&D waste mix, the lime content required is only 0.49 % which is much less compared to that required for 4.5 % for soil + fly ash mix. Also, the CBR value for soil + C&D waste mix is higher than that of soil + fly ash mix and a larger quantity of C&D waste (21.89% compared to 12 % fly ash) is used for stabilization. Also, the class F fly ash (used in this research work) may contain harmful trace elements such as Pb, Cd, Ni, etc. as shown in [34]. Thus, the use of class F fly ash alone may pollute the groundwater and cause adverse effects on the environment but when class F fly ash is used with lime, the release of metals is prevented as reported in [35] due to its alkaline nature (pH of lime = 12); thus, preventing detrimental effects to health and environment. The CBR value of the soil-fly ash-C&D waste-lime mix is very close to the soil-lime mix thus, based on the results soil-fly ash-C&D waste-lime mix is best to mix compared to the soil-lime mix because the amount of lime required in the soil-fly ash-C&D wastelime mix is less and also the waste materials such as fly ash and C&D waste which pose difficulty in their disposal can also be utilized in this mix. On adding plastic waste to soilfly ash-C&D waste-lime mix, there is a negligible effect of CBR value, but it can be used along with the mix because it improved the tensile strength of the composite and its disposal problem can also be solved.

Pavement design

The effect of the addition of admixtures on pavement design can be explained in terms of the pavement thickness required. The design of pavement is achieved by considering traffic of 10 million standard axles and as per [60]. The effect of stabilization of soil with various admixtures is observed on the thickness of the pavement. It was observed from Fig. 22 that pavement thickness decreases with stabilization. The decrease in pavement thickness is more in the case of soil stabilized with 4 % lime.

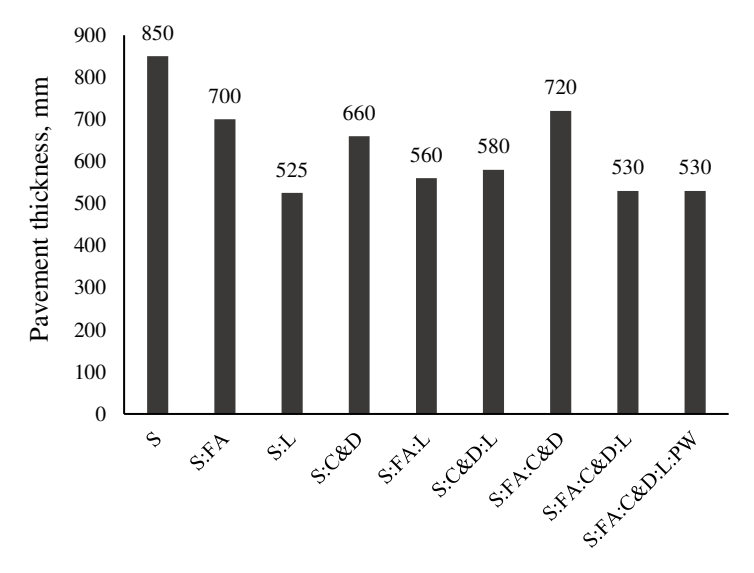


Fig. 22. Effect of addition of admixtures on pavement thickness

Similar pavement thickness can be observed for clay stabilized using fly ash, C&D waste & 0.99% lime content which is a cost-effective as well as eco-friendly mix since the disposal problem of fly ash and C&D waste can be solved. The effect of the addition of plastic waste on S+FA+C&D+L has a negligible effect on pavement thickness, but it increases the tension-carrying capacity of the sub-grade making it free from cracks. Thus, for sub-grade material, a combination of the soil-fly ash-C&D waste-lime-plastic waste mix can be effectively used.

Conclusions

Various tests were conducted in the laboratory to gain knowledge about the influence of the addition of fly ash, lime, C&D waste, and plastic waste on the clay and the following important conclusions were made:

- 1. A decrease in the value of maximum dry density is observed on the addition of various additives to the soil.
- 2. The unconfined compressive strength of the mix increases on adding various additives individually and in combination with each other, and it increases with curing period.
- 3. There is a little reduction in value of unconfined strength on adding plastic waste to soil mix.
- 4. With the curing period, the split tensile strength increases and also increases by adding different additives alone and in combination to each another.
- 5. The optimum mix is selected based on 7 days of unconfined compressive strength and split tensile strength of the mixes.
- 6. Considering the California bearing ratio, economy, and environment; the soil-fly ash-C&D waste-lime mix is selected as the optimum mix to be used as a sub-grade material. When the disposal of plastic is a problem, soil-fly ash-C&D waste-lime-plastic waste can be selected as sub-grade material.
- 7. When there is option of choosing fly ash or C&D waste, C&D waste can be selected as stabilizer for soil because it does not contain any harmful trace elements whereas fly ash contains harmful trace elements which are dangerous to the environment.
- 8. The use of fly ash alone may pollute the groundwater, whereas use of lime along with fly ash prevents the release of harmful metals from fly ash making it eco-friendly.

The results of the present study are applicable to improving the behaviour of poor clay soil ensuring the load-bearing capacity and quality of soil in preparation for road construction projects.

References

- 1. Bhardwaj A, Sharma RK. Effect of industrial wastes and lime on strength characteristics of clayey soil. *Journal of Engineering, Design and Technology.* 2020;18(6): 1749–1772.
- 2. Sharma A, Sharma RK. Sub-grade characteristics of soil stabilized with agricultural waste, constructional waste, and lime. *Bulletin of Engineering Geology and Environment*. 2021;80(3): 2473–2484.
- 3. Bhardwaj A, Sharma RK, Sharma A. Stabilization of clayey soil using waste foundry sand and molasses. In: Singh H, Singh Cheema PP, Garg P. (eds.) *Sustainable Development Through Engineering Innovations*. Singapore: Springer; 2021. p.641–649.
- 4. Bhardwaj A, Sharma RK. Designing thickness of subgrade for flexible pavements incorporating waste foundry sand, molasses, and lime. *Innovative Infrastructure Solution*. 2022;7(1): 1–18.

- 5. Prabakar J, Dendorkar N, Morchhale RK. Influence of fly ash on strength behavior of typical soils. *Construction and Building Material*. 2004;18(4): 263–267.
- 6. Kolias S, Kasselouri-Rigopoulou V, Karahalios A. Stabilisation of clayey soils with high calcium fly ash and cement. *Cement and Concrete Deposits*. 2005;27(2): 301–313.
- 7. Zentar R, Wang D, Abriak NE, Benzerzour M, Chen W. Utilization of siliceous—aluminous fly ash and cement for solidification of marine sediments. *Construction and Building Material*. 2012;35: 856–863.
- 8. Sezer A, Inan G, Yilmaz HR, Ramyar K. Utilization of a very high lime fly ash for improvement of Izmir clay. *Building and Environment*. 2006;41:150–155.
- 9. Zha F, Liu S, Du Y, Cui K. Behaviour of expansive soils stabilized with fly ash. *Natural Hazards*. 2008;47: 509–523. 10. Bell FG. Lime stabilization of clay minerals and soils. *Engineering Geology*. 1996;42(4): 223–237.
- 11. Rao SN, Rajasekaran G. Reaction products formed in lime-stabilized marine clays. *Journal of Geotechnical Engineering*. 1996; 122(5): 329–336.
- 12. Kavak A, Akyarli AA. Field application for lime stabilization. Environmental Geology. 2007;51: 987-997.
- 13. Dash SK, Hussain M. Lime stabilization of soils: reappraisal. *Journal of Materials in Civil Engineering*. 2012;24(6): 707–714.
- 14. Ghobadi MH, Abdilor Y, Babazadeh R. Stabilization of clay soils using lime and effect of ph variations on shear strength parameters. *Bulletin of Engineering Geology and Environment*. 2014;73: 611–619.
- 15. Nataatmadja A, Tan YL. Resilient response of recycled concrete road aggregates. *Journal of Transportation Engineering*. 2001;127(5): 451–453.
- 16. Fatta D, Papadopoulos A, Avramikos E, Sgourou E, Moustakas K, Kourmoussis F, Mentzis A, Loizidou M. Generation and management of construction and demolition waste in Greece—an existing challenge. *Resources Conservation and Recycling*. 2003;40(1): 81–91.
- 17. Poon CS, Chan D. Feasible use of recycled concrete aggregates and crushed clay brick as unbound road sub-base. *Construction and Building Material*. 2005;20(8): 578–585.
- 18. Leite FDC, Motta RDS, Vasconcelos KL, Bernucci L. Laboratory evaluation of recycled construction and demolition waste for pavements. *Construction and Building Material*. 2011;25(6): 2972–2979.
- 19. Jimenez JR, Ayuso J, Agrela F, Lopez M. Utilization of unbound recycled aggregates from selected CDW in unpaved rural roads. *Resources Conservation and Recycling*. 2012;58: 88–97.
- 20. Ransinchung RNGD, Kumar P, Sharma P. Stabilization of clayey soil with fines from waste crushed concrete cubes for construction of pavements. In: *Proceedings of international conference on engineering and information technology (ICEIT)*. Toronto: Canada; 2012. p.24–28.
- 21. Arulrajah A, Piratheepan J, Disfani MM, Bo MW. Resilient Moduli Response of recycled construction and demolition materials in pavement sub-base applications. *Journal of Materials in Civil Engineering*. 2013;25:1920–1928.
- 22. Arulrajah A, Disfani MM, Horpibulsuk S, Suksiripattanapong C, Prongmanee N. Physical properties and shear strength responses of recycled construction and demolition materials in unbound pavement base/sub-base applications. *Construction and Building Material*. 2014;58: 245–257.
- 23. Yadav JS, Saini A, Hussain S, Sharma V. Estimation of ultimate bearing capacity of circular footing resting on recycled construction and demolition waste overlaying on loose sand. *Journal of Building Pathology and Rehabilitation*. 2024;9(1): 25.
- 24. Saini A, Soni H, Yadav JS. Utilization of recycled construction and demolition waste to improve the bearing capacity of loose sand: an integrated experimental and numerical study. *Geomechanics and Geoengineering*. 2024;19(4): 444–461.
- 25. Soni H, Saini A, Yadav JS. Behaviour of Square Footing Over Recycled Concrete Aggregate Resting on Loose Sand: Integrated Experimental and Numerical Analyses. *International Journal of Geosynthetics and Ground Engineering*. 2022;8(5): 64.
- 26. Consoli NC, Montardo JP, Prietto PDM, Pasa GS. Engineering behavior of a sand reinforced with plastic waste. *Journal of Geotechnical and Geoenvironmental Engineering*. 2002;128(6): 462–472.
- 27. Kumar A, Walia BS, Mohan J. Compressive strength of fiber reinforced highly compressible clay. *Construction and Building Material*. 2006;20(10): 1063–1068.
- 28. Kalantari B, Huat BBK, Prasad A. Effect of polypropylene fibers on the California bearing ratio of air cured stabilized tropical peat soil. *American Journal of Engineering and Applied Sciences*. 2010; 3(1): 1–6.
- 29. Choudhary AK, Jha JN, Gill KS. A study on CBR behavior of waste plastic strip reinforced soil. *Emirates Journal of Engineering Research*. 2010;15(1): 51–57.

- 30. SivakumarBabu GL, Jaladurgam R. Strength and deformation characteristics of fly ash mixed with randomly distributed plastic waste. *Journal of Materials in Civil Engineering*. 2014;26(12): 04014093.
- 31. Ji-ru Z, Xing C. Stabilization of expansive soil by lime and fly ash. *Journal of Wuhan University of Technology-Mater*. 2002;17(4): 73–77.
- 32. Sharma NK, Swain SK, Sahoo UC. Stabilization of a clayey soil with fly ash and lime: a micro level investigation. *Geotechnical and Geological Engineering*. 2012;30: 1197–1205.
- 33. Sivapullaiah PV, Jha AK. Gypsum induced strength behaviour of fly ash-lime stabilized expansive soil. *Geotechnical and Geological Engineering*. 2014;32: 1261–1273.
- 34. Sharma SK, Kalra N. Effect of fly ash incorporation on soil properties and productivity of crops: A review. *Journal of Scientific and Industrial Research*. 2006;65: 383–390.
- 35. Jia Y, Maurice C, Ohlander B. Effect of the alkaline industrial residues fly ash, green liquor dregs, and lime mud on mine tailings oxidation when used as covering material. *Environmental Earth Sciences*. 2014;72: 319–334.
- 36. Sobhan K, Mashnad M. Tensile strength and toughness of soil—cement—fly-ash composite reinforced with recycled high-density polyethylene strips. *Journal of Materials in Civil Engineering*. 2002;14(2): 177–184.
- 37. Kumar A, Walia BS, Bajaj A. Influence of fly ash, lime, and polyester fibers on compaction and strength properties of expansive soil. *Journal of Materials in Civil Engineering*. 2007; 19(3): 242–248.
- 38. Twinkle, S, Sayida, MK. Effect of polypropylene fiber and lime admixture on engineering properties of expansive soil. In: *Proceedings Indian Geotecnical Confrence*. Kochi; 2011. p.393–396.
- 39. Al-Taie AJ, Al-Obaidi A, Alzuhairi M. Utilization of depolymerized recycled polyethylene terephthalate in improving poorly graded soil. *Transportation Infrastructure and Geotechnology*. 2020;7(2): 206–223.
- 40. de Araújo MT, Ferrazzo ST, Chaves HM, da Rocha CG, Consoli NC. Mechanical behavior, mineralogy, and microstructure of alkali-activated wastes-based binder for a clayey soil stabilization. *Construction and Building Materials*. 2023;362: 129757.
- 41. Şenol A. Effect of fly ash and polypropylene fibres content on the soft soils. *Bulletin of Engineering Geology and the Environment*. 2012;71(2): 379-387.
- 42. Muntohar AS, Widianti A, Hartono E, Diana W. Engineering properties of silty soil stabilized with lime and rice husk ash and reinforced with waste plastic fiber. *Journal of Materials in Civil Engineering*. 2013;25(9): 1260-1270.
- 43. Gumuser C, Senoi A. Effect of fly ash and different lengths of polypropylene fibers content on the soft soils. *International Journal of Civil Engineering*. 2014;12: 167–178.
- 44. Yadav JS, Tiwari SK. Behaviour of cement stabilized treated coir fibre-reinforced clay-pond ash mixtures. *Journal of Building Engineering*. 2016;8: 131–140.
- 45. Bharani S, Kumar GR, Ranjithkumar J, Boopathi G, Singaravelu G. Experimental study of regur soil stabilization by using Non-metallic waste bottles. *Materials Today: Proceedings*. 2022;52: 1598–1602.
- 46. Mahmood AA, Lin TY, Zhi JK. Sustainable Stabilization of Peat: A Literature Study. In: *Proceedings of the Canadian Society of Civil Engineering Annual Conference*. Singapore: Springer; 2021. p.13–24.
- 47. ASTM C977. Standard specification for quicklime and hydrated lime for soil stabilization. Annual book of ASTM Standards. Philadelphia: American Society for Testing and Materials; 1992.
- 48. ASTM D6913-04. Standard test methods for particle size distribution of soils. Annual book of ASTM Standards. Philadelphia: American Society for Testing and Materials; 2000.
- 49. ASTM D422-63. Standard test methods for hydrometer analysis of soils. Annual book of ASTM Standards, Philadelphia: American Society for Testing and Materials; 2000.
- 50. IS 1498. Method of tests for soil, Indian standard soil classification. New Delhi: Bureau of Indian Standards; 1970.
- 51. ASTM D 854-14. Standard test methods for specific gravity of soil solids by water pycnometer. Annual book of ASTM Standards. Philadelphia: American Society for Testing and Materials; 2000.
- 52. IS 2720. *Methods of tests for soil, part 17, Laboratory determination of permeability.* New Delhi; Bureau of Indian Standards; 1986.
- 53. IS 2720. Methods of tests for soil, part 40, Determination of free swell index of soil. Bureau of Indian Standards, New Delhi. 1977.
- 54. ASTM D698-07e1. Standard test methods for laboratory compaction characteristics of soil using standard effort. Annual book of ASTM Standards. Philadelphia: American Society for Testing and Materials; 2000.
- 55. ASTM D4318-10. Standard test methods for liquid limit, plastic limit, and plasticity index of soil. Pennsylvania, PA USA; American Society for Testing of Materials; 2000.
- 56. ASTM D2166-13. *Standard test methods for unconfined compressive strength test for soils. Annual book of ASTM Standards.* Philadelphia: American Society for Testing and Materials; 2000.

- 57. ASTM D3967-08. *Standard test method for splitting tensile strength of intact rock core specimens*. Pennsylvania, PA, USA: American Society for Testing of Materials; 2000.
- 58. ASTM D1883-05. Standard test methods for California bearing ratio test for soils. Annual book of ASTM Standards. Philadelphia: American Society for Testing and Materials; 2000.
- 59. IRC 37. Tentative guidelines for the design of flexible pavements. Indian road congress. New Delhi; 2018. 60. NF P 98–114-3. Roadway foundations methodology for laboratory study of materials treated with hydraulic binders Part 3: Soils treated with hydraulic binders possibly combined with lime. Association Française de Normalisation; 2001.

About Authors

Gaurav Juneja 🗓

Assistant Professor (Chandigarh Group of Colleges, Jhanjeri, Punjab, India)

Avinash Bhardwaj D Sc

Research Scholar (National Institute of Technology, Hamirpur, Himachal Pradesh, India)

Abhishek Sharma D Sc

Assistant Professor (Chandigarh University, Punjab, India)

Ravi Kumar Sharma Sc

Professor (National Institute of Technology Hamirpur, Hamirpur, India)

Submitted: August 7, 2023 Revised: September 20, 2023 Accepted: October 27, 2023

Research of hydrogen diffusion in a material with various types of traps

V.A. Polyanskiy, © E.A. Varshavchik ™, A.A. Chevrychkina, ©

Institute for Problems in Mechanical Engineering of the Russian Academy of Science, St. Petersburg, Russia

□ varshavchik.evgenii@gmail.com

ABSTRACT

In this paper a model of the process of hydrogen diffusion over the crystal structure in solids is presented. A defect-free and defective structure are considered. This study is relevant for the process of hydrogen embrittlement, which can lead to premature destruction of the material. A hypothesis about the creation of a surface layer upon pre-charging a sample with hydrogen is considered, which is necessary for further study of the hydrogen desorption process. The effect of the surface layer on the extraction curves is studied, and the simulated extraction curves are compared with the experimental ones. The results obtained make it possible to better understand the interaction of hydrogen atoms with the structure of a solid.

KEYWORDS

hydrogen diffusion • hydrogen charging • hydrogen traps • hydrogen desorption • diffusion equation

Acknowledgements. The research was carried out within the state assignment of Ministry of Science and Higher Education of the Russian Federation (FFNF-2024-0003 theme No. 124041100005-4).

Citation: Polyanskiy VA, Varshavchik EA, Chevrychkina AA. Research of hydrogen diffusion in a material with various types of traps. *Materials Physics and Mechanics*. 2024;52(3): 145–153. http://dx.doi.org/10.18149/MPM.5232024_13

Introduction

In the process of hydrogen sorption in the material, changes in the crystal structure in solids are possible. As a consequence, such effect can negatively affect the strength properties of the material. One of the most dangerous effects is hydrogen embrittlement of the material. This effect can lead to premature destruction of the material. To study the effects, the method of thermal desorption mass spectroscopy (TDS) is used [1-5]. The TDS method makes it possible to determine the binding energy of hydrogen in the crystal lattice in solids and crystal lattice defects [6,7]. This method is based on pre-charging the sample with hydrogen and further desorption of hydrogen from the sample when it is being heated. The flux of desorbed hydrogen is recorded by sensors, and extraction curves are plotted. The pre-charging of the sample with hydrogen and, as a consequence, hydrogen distribution over the sample is of great importance in obtaining the extraction curves. Under laboratory conditions, various methods of pre-charging a sample with hydrogen are used, such as: in gaseous hydrogen [8], in electrolyte solutions when a potential difference is applied [9-11] and in saline solutions [12,13].

When studying the process of hydrogen desorption, it is usually assumed that after charging the sample with hydrogen, the hydrogen concentration is uniformly distributed over the sample. Therefore, the distribution of hydrogen over the sample is often not studied in experimental papers, and sometimes the concentration after charging is not even measured [14–17]. However, it was experimentally observed that during laboratory saturation, hydrogen is not distributed uniformly [18,19], but instead forms a surface

layer, beyond which it almost does not penetrate [13,20]. This hypothesis is to be investigated.

The diffusion process is described by taking into account defects in the crystal lattice, which can affect the hydrogen diffusion process; these defects are called traps, [21–24]. The most popular traps model of hydrogen transport was proposed by Mac Nabb and Foster [25] and Oriani [26]. The models describe the capture of hydrogen in traps. The description of the process is based on Fick's first and second laws.

Oriani introduced a "phenomenological" diffusion coefficient, which in this paper will be called "effective diffusion coefficient" to considerate the effect of hydrogen trapping. Further on, on the assumption of local equilibrium between the concentration of hydrogen atoms in the crystal lattice of the sample and in the traps, Oriani derived an equation for describing the process of hydrogen diffusion with allowance for traps. Oriani's work investigated the effect of a single trap on the diffusion process. Fisher [14] generalized relations for several traps.

In the present paper to describe the diffusion process, we rely on the Oriani hypothesis of local equilibrium and calculate the effective diffusion coefficient for several traps following Fisher's equations. Fischer carried out simulations at a constant temperature of the sample in his work. In the present paper, the effect of thermal conductivity is taken into account when the sample is placed in a heated chamber.

The purpose of this article is to derive equations for the diffusion process taking into account traps, to show the effect of the presence of a boundary layer on extraction curves, and to argue for the hypothesis of the presence of a boundary layer.

Analytical description of the diffusion process in a defect-free structure

Consider a soled with a defect-free crystal lattice. Below is Fick's first law for the diffusion of hydrogen atoms in a defect-free lattice:

$$j = -D_L \operatorname{grad}(c_L), \tag{1}$$

where D_L is the diffusion coefficient of hydrogen in a defect-free lattice, c_L is the concentration of hydrogen atoms at a given point, j is the hydrogen flux.

According to Arrhenius's law, the diffusion coefficient \mathcal{D}_L can be represented as follows:

$$D_L = D_0 \exp\left(-\frac{U_L}{kT}\right),\tag{2}$$

where D_0 is the diffusion constant, U_L is the binding energy of hydrogen atoms with the crystal lattice, k is the Boltzmann coefficient, T is the absolute temperature.

For a homogeneous body structure, D_0 and U_L are constant for the whole body, therefore the diffusion coefficient D_L depends only on the temperature at the considered point of the body.

According to Fick's second law:

$$\Delta c = \frac{1}{D_L} \frac{\partial c}{\partial t}.$$
 (3)

Equation (3) establishes the relationship between the spatial and temporal changes in the concentration of hydrogen. Equation (3) is rewritten in the form of a difference scheme, then the finite element method with specified boundary conditions makes it possible to simulate the process of hydrogen diffusion. Further, according to Fick's first

law, it is possible to find the dependence of the hydrogen flux from the sample on time, that is, the extraction curves that are compared with the experimental ones.

Analytical description of the diffusion process in a defect structure

Almost any solid has defects at the molecular level, which can create obstacles for the diffusion of hydrogen atoms. These defects are called traps. The traps are divided into sorts that correspond to a certain binding energy with hydrogen atoms. Dislocation cores can serve as an example of a trap. For this sort of trap, hydrogen diffusion will proceed along the dislocation lines.

We consider m sorts of traps. Each sort of trap can be a new hydrogen diffusion channel with a corresponding diffusion coefficient. As a special case, the diffusion coefficient for some kind of traps can be zero. This means that hydrogen atoms do not move through traps of this sort. They can get out of the trap, move along the crystal lattice of the body and fall into the trap at another point in the body.

Since a new sort of traps can be represented as an additional diffusion channel, we rewrite Fick's first law (1) taking into account the influence of traps:

$$j = -D_L \operatorname{grad}(c_L) - \sum_{k=1}^{m} D_{Tk} \operatorname{grad}(c_{Tk}), \tag{4}$$

where j is the total diffusion flux of hydrogen atoms, D_{Tk} is the diffusion coefficient of hydrogen in traps of sort k, c_{Tk} is the concentration of hydrogen in a trap of sort k.

A closed system is considered. We introduce the following parameters: N_L is possible number of moles of hydrogen in the positions of defect-free crystal lattice of the body; N_{Tk} ($k=1,\ldots,m$) is the number of moles of positions of traps of sort k in the sample; y_L is the amount of hydrogen distributed in the lattice; y_{Tk} is the amount of hydrogen distributed in the trap of sort k.

Suppose that when a mole of hydrogen atoms is captured, the total energy of the system decreases by the value ΔE_k . Then the total Gibbs energy of the system can be written as:

$$G = G_0 + RT \left([y_L \ln y_L + (1 - y_L) \ln(1 - y_L)] N_L + \sum_{k=1}^m \left\{ [y_{Tk} \ln y_{Tk} + (1 - y_{Tk}) \ln(1 - y_{Tk})] N_{Tk} - \frac{\Delta E_k}{RT} y_{Tk} N_{Tk} \right\} \right),$$
 (5)

where R is the gas constant, T is the absolute temperature.

The parameter ΔE_k can be written as a difference between the binding energies of hydrogen in a crystal lattice and a trap of sort k:

$$\Delta E_k = U_k - U_L \,. \tag{6}$$

According to the law of conservation of mass in a closed system:

$$N_L y_L + \sum_{k=1}^{m} N_{Tk} y_{Tk} = \text{const.}$$
 (7)

The Oriani hypothesis about the local equilibrium between the concentration of hydrogen atoms in the crystal lattice of the body and in the traps corresponds to the minimum of function (5) with respect to the variables y_L and y_{Tk} , taking into account

relation (7). We will use the Lagrange multiplier method and find the minimum of function (8):

$$F = G + \lambda \left(N_L y_L + \sum_{k=1}^m N_{Tk} y_{Tk} - \text{const} \right), \tag{8}$$

where λ is the Lagrange multiplier.

The minimum of function (8) corresponds to the following system:

$$\begin{cases} \frac{\partial F}{\partial y_{L}} = RT[\ln y_{L} - \ln(1 - y_{L})]N_{L} + \lambda N_{L} = 0, \\ \frac{\partial F}{\partial y_{Tk}} = RT[\ln y_{Tk} - \ln(1 - y_{Tk})]N_{Tk} - \Delta E_{k}N_{Tk} + \lambda N_{Tk} = 0, \qquad (k = 1, ..., m). \end{cases}$$
(9)

System (9) can be reduced to the following expression:

$$\frac{y_L(1-y_{Tk})}{y_{Tk}(1-y_L)} = \exp\left(-\frac{\Delta E_k}{RT}\right) = K_k,\tag{10}$$

where K_k is the equilibrium constant.

We express y_{Tk} from Eq. (10):

$$y_{Tk} = \frac{y_L}{K_k + y_L(1 - K_k)}, \qquad (k = 1, ..., m).$$
 (11)

We introduce the variables V_{Tk} and V_L are volumes corresponding to one mole of hydrogen in traps of sort k and in the lattice, respectively.

Then the concentration of hydrogen in the lattice can be written as:

$$c_L = \frac{y_L}{V_L}. ag{12}$$

The concentration of hydrogen in traps of sort k, taking into account Eq. (11), can be represented as:

$$c_{Tk} = \frac{y_{Tk}}{V_{Tk}} = \frac{y_L}{V_{Tk}} \frac{1}{K_K + y_L(1 - K_k)}.$$
 (13)

Using Eq. (12), we get:
$$c_{Tk} = \frac{V_L}{V_{Tk}} \frac{1}{(K_k + V_L c_L (1 - K_k))} c_L. \tag{14}$$

Then the total concentration of hydrogen can be written:

$$c = c_L + \sum_{k=1}^{m} c_{Tk} = \frac{y_L}{V_L} + \sum_{k=1}^{m} \frac{y_L}{V_{Tk}} \frac{1}{K_K + y_L (1 - K_k)}$$

$$= \left(1 + \sum_{k=1}^{m} \frac{V_L}{V_{Tk}} \frac{1}{K_K + V_L c_L (1 - K_k)}\right) c_L.$$
(15)

The parameters $V_L, V_{Tk}, D_L, D_{Tk}, (k = 1, ..., m)$ are considered constant over the sample volume.

Let's return to Eq. (4) and write down the gradient:

$$j(x,t) = -\left(D_L \frac{dc_L}{dc}\Big|_{x,t} + \sum_{k=1}^m D_{Tk} \frac{dc_L}{dc}\Big|_{x,t} \frac{dc_{Tk}}{dc_L}\Big|_{x,t}\right) \operatorname{grad}(c) = -\widehat{D}\operatorname{grad}(c), \tag{16}$$

$$\widehat{D} = \left(D_L + \sum_{k=1}^m D_{Tk} \frac{dc_{Tk}}{dc_L} \Big|_{\mathbf{x},\mathbf{t}} \right) \frac{dc_L}{dc} \Big|_{\mathbf{x},\mathbf{t}}. \tag{17}$$

The parameter \widehat{D} will be called the effective diffusion coefficient. This parameter shows the effect of hydrogen diffusion along the crystal lattice and traps.

The derivatives on the right side of Eq. (17) are calculated for a given spatial position and a given time. The derivative $\frac{dc_L}{dc}$ follows from Eq. (15):

$$\frac{dc_L}{dc} = \left[1 + \sum_{k=1}^{m} \frac{V_L}{V_{Tk}} \frac{K_k}{(K_k + V_L c_L (1 - K_k))^2}\right]^{-1}.$$
(18)

The expression for the derivative $\frac{dc_{Tk}}{dc_L}$ follows from Eq. (14) as:

$$\frac{dc_{Tk}}{dc_L} = \frac{V_L}{V_{Tk}} \frac{K_k}{(K_k + V_L c_L (1 - K_k))^2}.$$
Then Fick's second law corresponds to Eq. (16) in the form:

$$\Delta c = \frac{1}{\widehat{D}} \frac{\partial c}{\partial t}.$$
 (20)

Thus, Eqs. (17) – (19) allow us to find the dependence $\widehat{D}(c_L)$. To find the dependence $\widehat{D}(c)$, it is necessary to solve the nonlinear Eq. (15) and express c_L in terms of c.

As a result, we obtain the dependence $\widehat{D}(c)$ and by representing Eq. (20) in the form of a difference scheme and writing the boundary conditions, we are able to simulate the process of hydrogen diffusion using finite element methods, taking into account different sorts of traps.

Experiment

To study the process of hydrogen diffusion, the following experiment was carried out. The sample was pre-charged with gaseous hydrogen and then placed in a preheated chamber. Then, using sensors, the flux of desorbed hydrogen from the sample surface was measured. Thus, we obtained experimental extraction curves showing the dependence of the desorbed hydrogen flux on time.

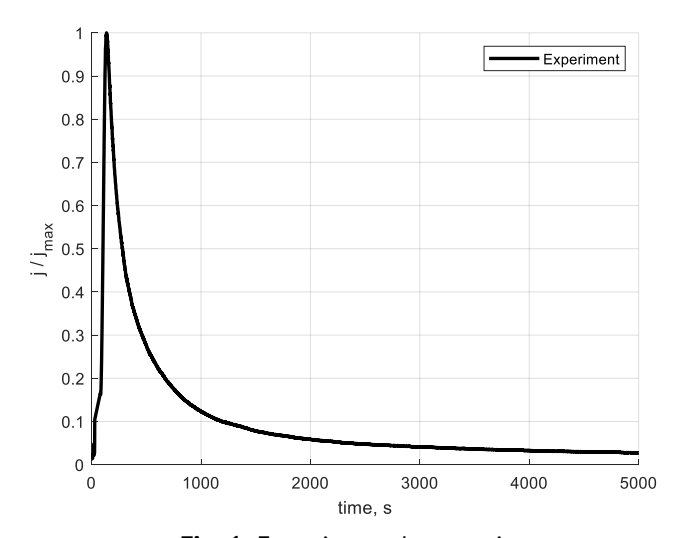


Fig. 1. Experimental extraction curve

Cylindrical billets made of BT16 titanium alloy are considered as samples. The radius of the samples under consideration is R = 11 mm, $0 \le r \le R$, and the height is 11 mm. It was experimentally found that after pre-charging the sample with hydrogen, the internal hydrogen content corresponds to 23 ppm. This content corresponds to a hydrogen concentration of 179.4 mol/m³. The temperature of the heated chamber, in which the sample was placed, was 750 °C. The experimental normalized extraction curve is shown in Fig. 1.

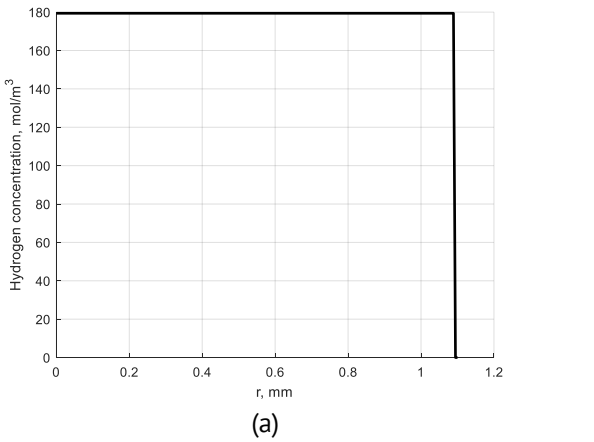
Modeling and discussion of the results

The modeling is qualitatively compared with the experimental extraction curves. The crystal lattice parameters are taken as follows: $D_0 = 3.1081 \cdot 10^{-9} \text{ m}^2/\text{s}$; $U_L = 0.1 \text{ eV}$; $k = 8.62 \cdot 10^{-5} \text{ eV/K}$; T = 750 °C = 1023 K; $V_L = 4.9 \cdot 10^{-6} \text{ m}^3/\text{mol}$.

Then, according to Eq. (2): $D_L = 10^{-9}$ m²/s. Consider a one trap with parameters: $V_{T1} = 6 \cdot 10^{-5}$ m³/mol; $\Delta E_1 = 25$ kJ/mol; $K_1 = 1.6 \cdot 10^{-5}$.

Below are the boundary conditions for modeling the process of hydrogen desorption: t = 0, c = 179.4 mol/m³, t > 0, r = R; c = 0.

Figure 2 shows the distribution of the initial hydrogen concentration along the radial coordinate of a cylindrical sample without taking into account (Fig. 2(a)) and taking into account (Fig. 2(b)) the surface layer of hydrogen.



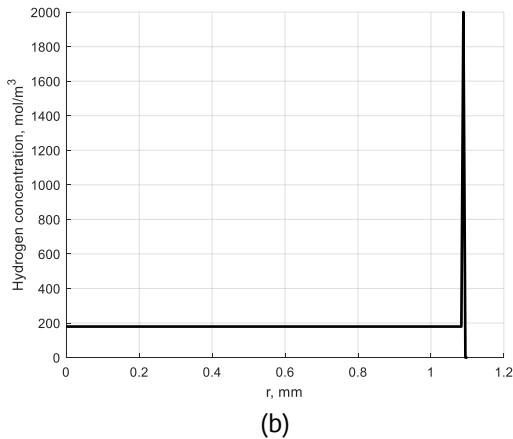


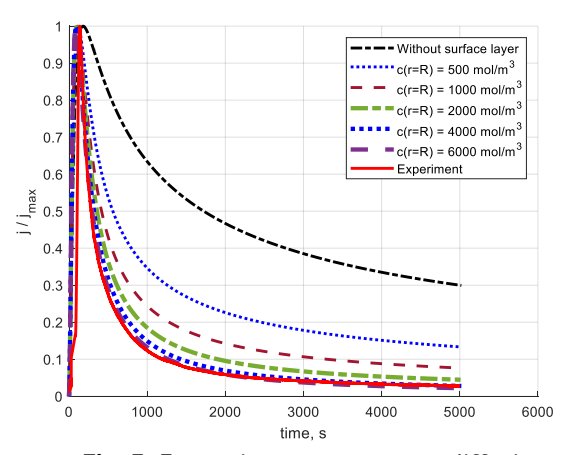
Fig.2. The form of the distribution of the initial hydrogen concentration without and taking into account the surface layer of hydrogen

First, we have investigated the process when the diffusion coefficient over a trap of the sort under consideration is zero: $D_{71} = 0$.

Figure 3 shows how the presence and size of the initial surface layer of hydrogen affects the qualitative behavior of the modeled extraction curve. According to Fig. 3, it can be concluded that an increase in the surface layer leads to a qualitative convergence of the modeled curve and the experimental curve.

Then we have studied the process when the diffusion coefficient for a trap of the sort under consideration is $D_{T1} = 10^{-13}$ m²/s. Figure 4 shows how the presence and size of the initial surface hydrogen layer affect the qualitative behavior of the modeled extraction curve in the case of a nonzero diffusion coefficient in the trap. According to

Fig. 4, it can be concluded that with a nonzero coefficient of hydrogen diffusion through the traps, an increase in the surface layer also leads to a qualitative convergence of the modeled curve and the experimental curve. Convergence occurs at a smaller surface layer than at a zero diffusion coefficient over the traps.



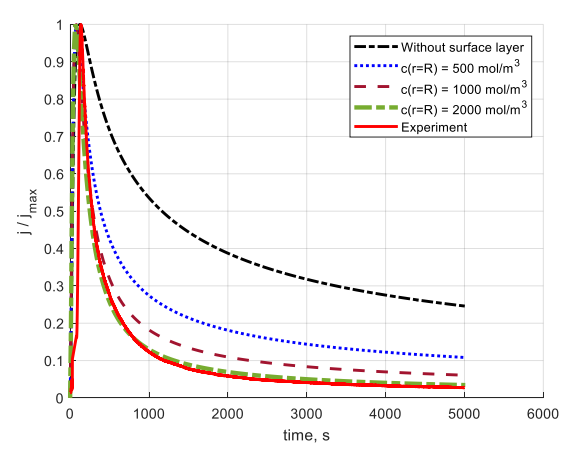


Fig. 3. Extraction curves at zero diffusion coefficient over traps

Fig.4. Extraction curves for a nonzero diffusion coefficient over traps

It can be concluded that the presence of a boundary layer changes the shape of the extraction curve and qualitatively brings it closer to the experimental one. Under the assumption of an initial uniform distribution of hydrogen, extraction curves were obtained, which, even at a qualitative level, did not agree with experiment. Including the nonzero coefficient of hydrogen diffusion through traps into consideration changes the shape of the extraction curve, but the presence of a boundary layer again brings the simulation closer to experiment.

Conclusions

In this paper, we considered the hypothesis of the presence of a surface layer when the sample is charged with gaseous hydrogen. A hydrogen diffusion model was presented for a defect-free body structure and for a body structure with traps. According to the described model, the diffusion process was modeled and the effect of the surface layer of hydrogen on the extraction curves was investigated. It was shown that the presence of a surface layer qualitatively changes the shape of the extraction curve and brings the simulated curves closer to the experimental ones. The diffusion coefficient over traps was investigated at zero and non-zero values. In both cases, the presence of a surface layer brought the simulation closer to experiment. This study is to be carried out for traps of other varieties and transfer from a qualitative description to a quantitative one.

References

- 1. Hurley C, Martin F, Marchetti L, Chêne J, Blanc C, Andrieu E. Numerical modeling of thermal desorption mass spectroscopy (TDS) for the study of hydrogen diffusion and trapping interactions in metals. *International Journal of Hydrogen Energy*. 2015;40(8): 3402–3414.
- 2. Yang X, Yu H, Song C, Li L. Hydrogen trapping behavior in vanadium microalloyed TRIP-assisted annealed martensitic steel. *Metals*. 2019;9(7): 741.

- 3. Depover T, Wan D, Wang D, Barnoush A, Verbeken K. The effect of hydrogen on the crack initiation site of TRIP-assisted steels during in-situ hydrogen plasma micro-tensile testing: Leading to an improved ductility? *Materials Characterization*. 2020;167: 110493.
- 4. Bellemare J, Laliberté-Riverin S, Ménard D, Brochu M, Sirois F. Subtleties behind hydrogen embrittlement of cadmium-plated 4340 steel revealed by thermal desorption spectroscopy and sustained-load tests. *Metallurgical and Materials Transactions A.* 2020;51: 3054–3065.
- 5. Fangnon E, Malitckii E, Yagodzinskyy Y, Vilaça P. Improved accuracy of thermal desorption spectroscopy by specimen cooling during measurement of hydrogen concentration in a high-strength steel. *Materials*. 2020;13(5): 1252.
- 6. Polyanskiy VA, Belyaev AK, Chevrychkina AA, Varshavchik EA, Yakovlev YuA. Impact of skin effect of hydrogen charging on the Choo-Lee plot for cylindrical samples. *International Journal of Hydrogen Energy*. 2021;46(9): 6979–6991.
- 7. Díaz A, Cuesta II, Martínez-Pañeda E, Alegre JM. Influence of charging conditions on simulated temperature-programmed desorption for hydrogen in metals. *International Journal of Hydrogen Energy*. 2020;45(43): 23704–23720.
- 8. Yamabe J, Awane T, Matsuoka S. Elucidating the hydrogen-entry-obstruction mechanism of a newly developed aluminum-based coating in high-pressure gaseous hydrogen. *International Journal of Hydrogen Energy*. 2015;40(32): 10329–10339.
- 9. Niu L, Cheng YF. Corrosion behavior of X-70 pipe steel in near-neutral pH solution. *Applied Surface Science*. 2007;253(21): 8626–8631.
- 10. Cheng YF. Fundamentals of hydrogen evolution reaction and its implications on near-neutral pH stress corrosion cracking of pipelines. *Electrochimica Acta*. 2007;52(7): 2661–2667.
- 11. Martinsson A, Sandstrom R. Hydrogen depth profile in phosphorus-doped, oxygen-free copper after cathodic charging. *Journal of Materials Science*. 2012;47(19): 6768–6776.
- 12. International Organization for Standardization. 16573-1:2020. Steel Measurement method for the evaluation of hydrogen embritlement resistance of high strength steels. 2020.
- 13. Alekseeva EL, Belyaev AK, Zegzhda AS, Polyanskiy AM, Polyanskiy VA, Frolova KP, Yakovlev YuA. Boundary layer influence on the distribution of hydrogen concentrations during hydrogen-induced cracking test of steels. *Diagnostics, Resource and Mechanics of Materials and Structures*. 2018;3: 43–57. (In Russian)
- 14. Fischer FD, Svoboda J, Kozeschnik E. Interstitial diffusion in systems with multiple sorts of traps. *Modelling and Simulation in Materials Science and Engineering*. 2013;21(2): 025008.
- 15. Kim Y, Kim Y, Kim D, Kim S, Nam W, Choe H. Effects of hydrogen diffusion on the mechanical properties of austenite 316L steel at ambient temperature. *Materials Transactions*. 2011;52(3): 507–513.
- 16. Winzer N, Rott O, Thiessen R, Thomas I, Mraczek K, Höche T, Wright L, Mrovec M. Hydrogen diffusion and trapping in Ti-modified advanced high strength steels. *Materials & Design*. 2016;92: 450–461.
- 17. Kyriakopoulou HP, Karmiris-Obratański P, Tazedakis AS, Daniolos NM, Dourdounis EC, Manolakos DE, Pantelis D. Investigation of hydrogen embrittlement susceptibility and fracture toughness drop after in situ hydrogen cathodic charging for an X65 pipeline steel. *Micromachines*. 2020;11(4): 430.
- 18. Wu TI, Wu JC. Effects of cathodic charging and subsequent solution treating parameters on the hydrogen redistribution and surface hardening of Ti-6Al-4V alloy. *Journal of Alloys and Compounds*. 2008;466(1-2):153–159. 19. Martinsson Å, Sandström R. Hydrogen depth profile in phosphorus-doped, oxygen-free copper after cathodic charging. *Journal of Materials Science*. 2012;47: 6768–6776.
- 20. Polyanskiy VA, Belyaev AK, Alekseeva EL, Polyanskiy AM, Tretyakov DA, Yakovlev YA. Phenomenon of skin effect in metals due to hydrogen absorption. *Continuum Mechanics and Thermodynamics*. 2019;31: 1961–1975.
- 21. Pressouyre GM. A classification of hydrogen traps in steel. *Metallurgical Transactions A*. 1979;10: 1571–1573.
- 22. Pressouyre GM. Hydrogen traps, repellers, and obstacles in steel; consequences on hydrogen diffusion, solubility, and embrittlement. *Metallurgical Transactions A*. 1983;14: 2189–2193.
- 23. Lecoester F, Chêne J, Noel D. Hydrogen embrittlement of the Ni-base Alloy 600 correlated with hydrogen transport by dislocations. *Materials Science and Engineering A.* 1999;262(1-2): 173–183.
- 24. Hirth JP. Effects of hydrogen on the properties of iron and steel. *Metallurgical Transactions A*. 1980;11: 861–890.
- 25. McNabb A, Foster PK. A new analysis of the diffusion of hydrogen in iron and ferrite. *Trans. of the Metallic Soc.* 1963;227: 618–627.
- 26. Oriani RA. The diffusion and trapping of hydrogen in steel. Acta Metallurgica. 1970;18(1): 147-157.

About Authors

Vladimir A. Polyanskiy (1) Sc

Doctor of Technical Sciences

Director of the Institute (Institute for Problems in Mechanical Engineering of the Russian Academy of Science, St. Petersburg, Russia)

Evgeniy A. Varshavchik Sc

Research Assistant (Institute for Problems in Mechanical Engineering of the Russian Academy of Science, St. Petersburg, Russia)

Anastasiia A. Chevrychkina 🗓 Sc

Candidate of Physico-Mathematical Sciences Senior Researcher (Institute for Problems in Mechanical Engineering of the Russian Academy of Science, St. Petersburg, Russia) Submitted: August 7, 2023 Revised: September 20, 2023 Accepted: October 27, 2023

Chromium plating of steel parts using the thermoemission field

N.A. Shaburova 🕒



South Ural State University (NRU), Chelyabinsk, Russia

[™] shaburovana@susu.ru

ABSTRACT

Experimentally, it was found that when a second metal component is added to the technological backfill during thermal diffusion chromium plating or when the inert separating additive of corundum is replaced by mineralssolid electrolytes, a current appears in the technological backfill directed to the saturable part. The appearance of an electric field is due to the emission of electrons (metal components of the filling) and oxygen anions (solid oxide electrolytes). It is determined that the emission flux makes a contribution to the saturation process that is commensurate with the diffusion flux formed according to Fick's laws. Experiments show an acceleration of diffusion processes and an increase in the depth of the diffusion layer of chromium by 2-2.5 times.

KEYWORDS

thermal diffusion chromium plating • thermal emission field • diffusion depth

Citation: Shaburova NA. Chroming plating of steel parts using the thermoemission field. *Materials Physics* and Mechanics. 2024;52(3): 154-160.

http://dx.doi.org/10.18149/MPM.5232024 14

Introduction

To protect the surface of parts of pipeline structures from external factors, to give them corrosion resistance, high hardness and wear resistance, the technology of thermal diffusion chromium plating has been used for many years [1-7]. This technology consists in heating parts in a sealed container with filling from a mixture of powders: chromium (ferrochromium), corundum and activators NH4Cl, NH4I at a temperature of 900 – 1000 °C. In the process of holding at the heating temperature, the formation of chromium halides occurs, their deposition on the surface of the part, decomposition and subsequent diffusion of atomic chromium into the metal of the part with the formation of a diffusion layer. The layer depth depends on the temperature, the duration of the process, and the carbon content in the steel [2,8–16].

Attempts to improve the traditional technology of thermal diffusion chromium plating consisted mainly in carrying out two or more component saturation with boron, vanadium and manganese, molybdenum [1,17-23]. In our work on joint chromium plating with tungsten and nickel, it was found that, in addition to increasing hardness, the introduction of the second component increases the depth of chromium diffusion on the metal surface. Thus, during thermal diffusion chromium plating of steel 35Kh2N3 at a temperature of 1000 °C for 24 hours without additional addition to the technological mixture, the depth of the diffusion layer was 30 µm [24], with joint saturation with nickel under the same conditions – 40 µm [25], with the introduction tungsten powder, the chromium diffusion depth was 55 µm [26]. From the point of view of only the concentration theory of diffusion, described by Fick's laws, it is impossible to explain the increase in the diffusion layer by 1.52 times at constant temperature-time parameters of 155 N.A. Shaburova

the process. At the same time, tungsten is known as an emissive electronics material used to make cathodes. The emission of electrons by tungsten occurs regardless of whether the tungsten sample is heated by passing current or by heat flows from another source. It has been suggested that the acceleration of chromium diffusion may be due to the electron flux emitted by the tungsten particles. Since iron and steel are always positive electrodes [27], it is obvious that, firstly, the resulting emission flux of negatively charged particles must be directed to the saturating part, and secondly, this flux must lead to the appearance of an electric current in the saturating mixture.

In developing the idea of the appearance of an emission current in a saturating mixture, it became necessary to determine the possibility of using not only metal components as emitter additives, but also oxides, which can play two roles - to be a separator for metal particles of the saturating element powder and to create an additional thermionic flow that promotes acceleration diffusion. It is known, for example, that solid electrolytes of the $ZrO_2 + 10 \% Y_2O_3$ type are most widely used in metallurgy. A distinctive feature of these substances is 100 % anionic conductivity O^{2-} . Taking into account this feature of solid electrolytes, the possibility of using oxide additives in chemical-thermal treatment is considered for the first time.

The purpose of this work is to determine the electrical characteristics of metal- and oxide-containing saturating mixtures and to establish their relationship with the depth of the emerging diffusion layer.

Methods

To measure the current arising in the technological backfill, an installation was designed (Fig. 1). The main element of the installation is a cell - a cylindrical corundum crucible with a diameter of 30 mm and a height of 80 mm. Two iron wire electrodes 1.4 mm in diameter were placed in the crucible. A sample of 35Kh2N3 steel 25 × 10 × 8 mm in size was welded to one electrode. The distance between the electrodes in the cell was maintained at 18 mm in all experiments. The technological mixture filled the volume with the cell by 80 % and was covered with asbestos cardboard. Further, a mixture of silicocalcium was covered with a layer of 6-8 mm, then, after a layer of asbestos, graphite powder, which was again covered with asbestos. To exclude a short circuit in the layer of corundum with graphite, the electrodes were insulated with corundum tubes. The electric circuit current was measured in cells with metal and oxide emitters added to saturating mixtures. The compositions of the investigated technological fillings are given in Table 1.

The electrical measuring cells were placed on a pallet, 2 pieces each, and placed in a Nabertherm 41/H chamber furnace. To measure the current that occurs during heating in the circuit \mid electrode 1 \rightarrow saturating mixture \rightarrow electrode 2 \mid , the electrode leads were connected to an APPA-207 digital multimeter. The furnace was heated up to 1050 °C. The furnace heating program was set in such a way that heating to 500 °C was carried out continuously, then every 50 °C a 10-minute exposure was made to measure the current in the circuit. The temperature in the furnace was controlled using a platinum exemplary thermocouple.

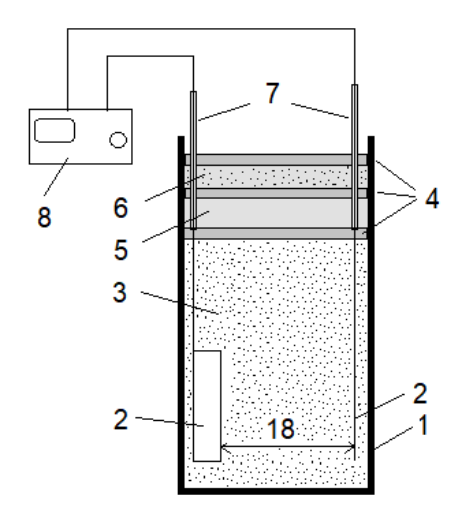


Fig. 1. Scheme of the measuring cell for studying the electric field formed during chemical-thermal treatment: 1 – cell body; 2 - electrodes; 3 - technological backfill; 4 - asbestos sheet; 5 – silicocalcium powder; 6 – graphite powder; 7 - insulating corundum tubes; 8 - digital multimeter

Table 1. Compositions of saturating mixtures

	Main saturating	Additive to the saturating		Corundum,	NH₄Cl,
No.	component mixture			(powder,	(powder,
of the mixture	Chromium, (powder, fraction 150 µm), wt. %	Type of additive	Mass. %	fraction 140 µm), wt. %	fraction 0.5 – 2.0 mm), wt. %
1	50	-	-	50	4
2	40	W (150 мкм)	10	50	4
3	40	Ni (150 мкм)	10	50	4
4	45	$CaWO_4$	15	40	4
5	45	MgO	15	40	4
6	45	MgO+2CaO·SiO ₂	5+10	40	4
7	45	WO ₃ +2CaO·SiO ₂	5+10	40	4
8	45	2CaO·SiO ₂	15	40	4
9	45	Y_2O_3	15	40	4

After complete cooling, the samples were removed from the saturating mixture, a fragment 10x8x8 mm in size was cut off from each sample to make transverse microsections. Then, the transverse sections of the samples were examined using a Jeol JSM 6460LV electron microscope equipped with an Oxford Instruments X-ray microanalysis (XMS) attachment. By point MRS analysis in the direction from the surface to the center of the section of the part, the composition of the diffusion layer was studied, and the depth of chromium diffusion was determined.

Results and Discussion

The results of measuring the magnitude of the thermionic current that occurs in the filling with two iron electrodes at 1000 °C between the cells with the addition of metal and oxide electron emitters in technological fillings are shown in Fig. 2. It can be seen that without the supply of additional electricity from the outside, electric fields appear in the cell, due to the composition of the technological mixture and temperature.

157 N.A. Shaburova

The magnitude of the emerging thermionic field for both metal and oxide additives varies greatly (Fig. 2). In contrast to all other systems under study, CaWO₄ emission begins at 500 °C and grows dynamically, reaching a maximum of 0.65 mA at 850 °C. For metal additives (W, Ni) and most oxide additives, a noticeable emission of charged particles begins at temperatures up to 800 °C. The strength of the resulting current when using metal additives is 0.14 and 0.21 mA, respectively, for Ni and W. MgO + 2CaO SiO₂ and 2CaO SiO₂ can be isolated from oxide additives, providing a thermionic current of 0.05 and 0.30 mA, respectively. In mixtures with other oxide additives, the current strength does not exceed 0.003 mA.

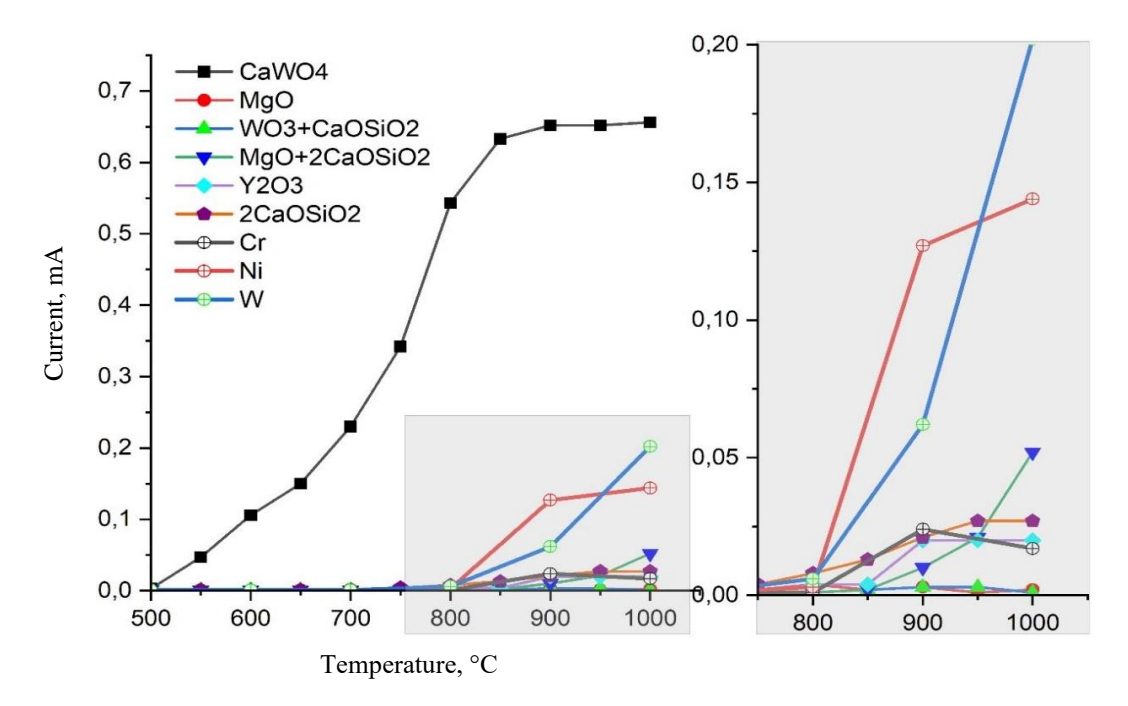


Fig. 2. Values of current strength in backfills

To establish the relationship between the magnitude of the emerging thermionic current and the depth of chromium diffusion, transverse sections of the electrode sample were studied.

The results of measuring the diffusion depth of chromium after 1 hour of exposure at 1000 °C from the strength of the emission current arising in the backfill are shown in Fig. 3. According to the data obtained, with an increase in the values of the emission current arising in the backfill, the depth of chromium diffusion also increases.

In the process of diffusion saturation of parts, refractory metals are a source of electrons. Oxides and their compounds are a source of oxygen anions. The mixed flow of electrons and oxygen anions is the field involved in the saturation of the surface of the parts with metal, which in atomic form moves to the surface of the workpieces. On the surface of the parts, the atoms of the diffusing substance move to the surface layer, which is described by Fick's 1st law [28,29]:

$$J_k = -D\frac{dc}{dx} = \frac{\Delta G_k}{S \cdot \Delta \tau},\tag{1}$$

where J_k is the amount of diffusing substance k that passes per unit of time through a section of a unit area located at a right angle to the direction of the diffusion flow, $\frac{kg}{m^2 \cdot sec}$;

 $\frac{dc}{dx}$ is the concentration gradient k; D is the diffusion coefficient (m²/sec); ΔG_k is an amount of substance, kg; $\Delta \tau$ is time, sec; S is square, m².

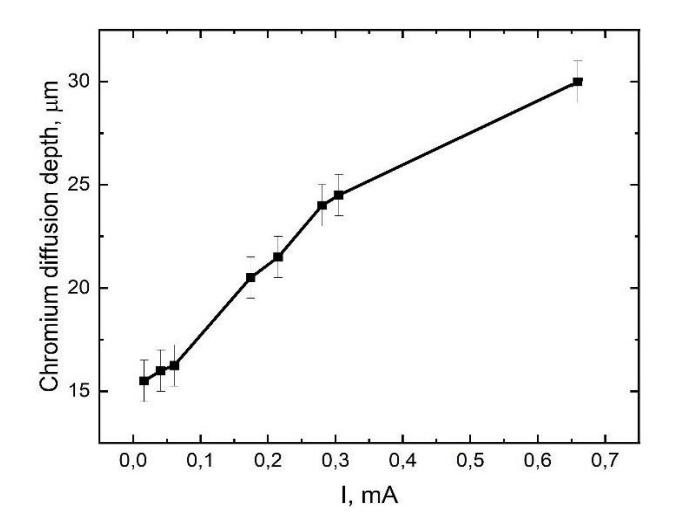


Fig. 3. Dependence of the chromium diffusion depth on the thermionic current

Since the minus sign in Fick's first law only indicates the direction of mass transfer, the amount of the transferred substance can be determined:

$$\Delta G_k = \left| -D \frac{dc}{dx} \right| \cdot S \cdot \Delta \tau. \tag{2}$$

The calculation of the diffusion coefficient D is presented in [30] and can be automated. Thus, all factors of Eq. (1) are definable and the amount of substance transferred by the concentration field is calculable.

It is more difficult to determine the participation of the emission field of oxygen anions created by the ceramic material of the technological mixture, and its share in the transfer of metal in the process of chemical-thermal treatment. As shown above, the strength of the resulting current is determined by the composition of the ceramic part of the backfill at a constant weight ratio (55–60 wt. % ceramics; 45–40 wt. % chromium). An analysis of the experimental results (Fig. 1) allows us to conclude that a solid powder mixture of metal and ceramic phases deposits a chromium layer on the sample surface in proportion to the passed electricity. What can be considered an application of Faraday's law for powdered electrolytes:

$$G_k = z \cdot Q,\tag{3}$$

where G_k is a mass of settled substance k, released on the electrode, kg; z is an electrochemical equivalent, kg/(A·h); Q is an amount of electricity passed ($Q = I \tau$); I is a direct current passing through the phase boundary, A; τ is the duration of the passage of current, hour. That is, from Eq. (3):

$$G_k = z \cdot I \cdot \tau. \tag{4}$$

The electrochemical equivalent z is the amount of substance that reacted as a result of the flow of a unit amount of electricity. The equation for calculating the electrochemical equivalent is as follows:

$$z = \frac{M}{n \cdot F},\tag{5}$$

159 N.A. Shaburova

where M is the molar mass of the reagent; n is the valency of the diffusing substance; F is the Faraday number or constant, $F = 96486 \approx 96500$ C/mol.

Using Eqs. (4) and (5) it is possible to determine the final equation for Faraday's law in powder electrolytes:

$$G_k = \frac{M}{n \cdot F} \cdot I \cdot \tau \tag{6}$$

Thus, taking into account the fact that in one technological process the diffusing element is transferred to the surface of samples (parts) in different fields, using Eqs. (2) and (6) we can write the general equation for the transfer of matter in the process of diffusion metallization:

$$\sum G_k = \left| -D \frac{dc}{dx} \cdot S \cdot \Delta \tau \right| + \frac{M}{n \cdot F} \cdot Q \cdot I \cdot \tau. \tag{7}$$

The resulting equation corresponds to the postulates of *K*. Wagner about the independence of the transfer of particles from the conditions [29] from the concentration and electric emission fields.

Conclusions

- 1. The formation of emission fields due to the release of electrons from metals and oxygen anions from amorphous solid electrolytes in technological fillings during thermal diffusion chromium plating has been proved;
- 2. A quantitative assessment of the participation of electric emission fields and concentration fields in saturation processes was carried out;
- 3. The possibility of accelerating the process of chromium diffusion during thermal diffusion saturation of steel parts by introducing additives-emitters of electrons or O²-anions into the saturating mixture has been proved;
- 4. It has been determined that the most promising and cost-effective emitter additives are oxide additives 2CaO·SiO₂, CaWO₄, which can partially or completely replace inert refractories in the filling.

References

- 1. Samuel RL, Lockington NA. Metal Treatment and Drop Forging. 1951.
- 2 Lyakhovich LS. Chemical-thermal treatment of metals and alloys. Moscow: Metallurgy; 1981. (In Russian)
- 3. Kitaev NI, Yakimovich YuV, Shigaev My, Pichkhidze SYa. Thermal diffusion chromium plating of structural carbon steel 20 by high frequency currents. *Voprosy Materialovedeniya*. 2021;106(2): 137–145. (In Russian)
- 4. Goyushov RG. Physical and mechanical properties of marine engine parts restored by diffusion chrome plating. *Universum*. 2023;10(115): 41–44.
- 5. Bobylyov EE, Storozhenko ID. Diffusion metallization of carbide cutting tools as a way to improve the surface treatment quality. *Journal of Physics: Conference Series*. 2019;1399(4): 044084.
- 6. Castle AR, Gabe DR. Chromium diffusion coatings. *International Materials Reviews*. 1999;44(2): 37 58.
- 7. Schwarz S, Rosiwa SM, Musayev Y, Singer RF. High temperature diffusion chromizing as a successful method for CVD-diamond coating of steel—Part II. *Diamond and Related Materials*. 2003;12(3–7): 701–706. 8. Zancheva L, Hillert M, Lange N, Seetharaman S, Staffansson LI. On the formation of carbide coatings by
- 8. Zancheva L, Hillert M, Lange N, Seetharaman S, Staffansson LI. On the formation of carbide coatings by chromizing carbon steels. *Metall. Trans. A.* 1978;9: 909.
- 9. Bogdanov SP, Khristiuk NA, Sychov MM. The structure of the chromium plating on steel fabricated using iodine transport. *Journal of Physics: Conference Series*. 2021;1967: 012039.
- 10. Zhang S, Zhang H, Zhang H, Zhao X, Li Y. Study on Diffusion Kinetics and Law of Chromium on the Surface of Low-Carbon Steel. *Coatings*. 2023;13(1): 98.

- 11. Zieliński M, Koniorczyk P, Surma Z. Studies on Influence of Chromium Layer on Inner Surface of Steel Tube on Heat Transfer. *Appl. Sci.* 2023;13: 5523.
- 12. Zhang SX, Li YG, Wang C, Zhao XP. Preparation of a Cr coating on low-carbon steel by electrodeposition in a NaCl-KClNaF-Cr2O3 molten salt. *Int. J. Electrochem. Sci.* 2019;14(1): 91–101.
- 13. Veselovsky A, Troyanovskaya I, Erofeev V. Predicting the Thickness of the Hardening Coating during Diffusion Metallization of Cast Iron. *Materials Research Proceedings*. 2022;21: 51–55.
- 14. Pastukhov A, Sharaya O, Timashov E, Bakharev D. Method of justification of machine parts hardening modes. *Engineering for Rural Development*. 2021;20: 74–79.
- 15. Wang B, Qiu F, Barber GC, Pan Y, Cui W, Wang R. Microstructure, wear behavior and surface hardening of austempered ductile iron. *Journal of Materials, Research and Technology*. 2020;9(5): 9838–9855
- 16. Veselovsky AA, Dema RR, Kalugina OB, Nefedyev SP. Determination of parts tolerances in friction knots of grey and nodular cast iron with thermal diffusion platings vanadium and chrom. *MATEC Web of Conferences*. 2017;129: 02043.
- 17. Lim SC, Lim CYH, Lee KS. The effects of machining conditions on the flank wear of TiN-coated high speed steel tool inserts. *Wear.* 1995;181/183(2): 901–912.
- 18. Sen S, Sen U, Bindal C. An approach to kinetic study of borided steels. Surface & Coating Technology. 2005;191(2-3): 274–285.
- 19. Aghaie-Khafri M, Mohamadpour Nazar Abady M. A Study of Chromo-Boronizing on DIN 1.2714 Steel by Duplex Surface Treatment. *JOM*. 2012;64(6): 694–701.
- 20. Meier GH, Cheng C. Diffusion chromizing of ferrous alloys. Surface and Coating Technology. 1989;39/40: 53-64.
- 21. Ennis PJ, Quadakkers WJ. High chromium martensitic steels-microstructure, properties and potential for further development. *VGB PowerTech.* 2001;81: 87–90.
- 22. Quadakkers WJ, Piron-Abellan J, Shemet V, Singheiser L. Metallic interconnectors for solid oxide fuel cells a review. *Mater. High Temp.* 2003;20(2): 115–127.
- 23. Singheiser L, Huczkowski P, Markus T, Quadakkers WJ. In: Richardson JA. (ed.) Shreir's Corrosion. Oxford: Elsevier; 2010.
- 24. Shaburova YUD, Shaburova NA, Pashkeev IYu. Investigation of the distribution of chromium in the diffusion layer during chromium plating of steel 35Kh2N3. *Bulletin of SUSU. Series Metallurgy*. 2022;22(1): 24–32. (In Russian)
- 25. Shaburova NA, Pashkeev IYu. Influence of the conditions of joint saturation of steel with chromium and nickel on the depth of the diffusion layer. *Ferrous metallurgy. Bulletin of Scientific, Technical and Economic Information*. 2022;78(6): 542–548.
- 26. Shaburova NA, Pashkeev IYu. Distribution of chromium and tungsten in the diffusion layer of steel 35Kh2N3 at joint thermal diffusion saturation. *Bulletin of SUSU. Series Metallurgy*. 2022;2:41–52. (In Russian)
- 27. Rogelberg IL, Beilin VM. Alloys for thermocouples. Moscow: Metallurgy; 1983. (In Russian)
- 28. Darken LS, Gurri RV. Physical chemistry of metals. New York: McGraw-Hill; 1953.
- 29. Chebotin VN. *Physical chemistry of a solid state*. Moscow: Chemistry; 1982. (In Russian)
- 30. Umansky YaS, Finkelstein BN, Blanter M. *Physical basis of metallurgy*. Moscow: Metallurgizdat; 1955. (In Russian)

About Author

Nataliya A. Shburova 🗓 Sc

Candidate of Technical Sciences Associate Professor (South Ural State University (NRU), Chelyabinsk, Russia)

МЕХАНИКА И ФИЗИКА МАТЕРИАЛОВ

52 (3) 2024

Учредители: Санкт-Петербургский политехнический университет Петра Великого, Институт проблем Машиноведения Российской академии наук Издание зарегистрировано федеральной службой по надзору в сфере связи, информационных технологий и массовых коммуникаций (РОСКОМНАДЗОР), свидетельство ПИ №ФС77-69287 от 06.04.2017 г.

Редакция журнала

Профессор, д.т.н., академик РАН, А.И. Рудской – главный редактор Профессор, д.ф.-м.н., член-корр. РАН, А.К. Беляев – главный научный редактор Профессор, д.ф.-м.н. И.А. Овидько (1961 - 2017) – основатель и почетный редактор Профессор, д.ф.-м.н. А.Л. Колесникова – ответственный редактор Профессор, д.ф.-м.н. А.С. Семенов – ответственный редактор Л.И. Гузилова – выпускающий редактор, корректор

> Телефон редакции +7(812)552 77 78, доб. 224

E-mail: mpmjournal@spbstu.ru Компьютерная верстка Л.И. Гузилова

Подписано в печать 31.07.2024 г. Формат 60х84/8. Печать цифровая

Усл. печ. л. <u>10.0</u>. Тираж 100. Заказ .

Experimental determination of physical, chemical and surface properties of biocompatible thermoplastic D.A. Erofeev, P.B. Pirozhnikov, I.A. Keresten, A.G. Titov	1-12
Influence of adhesive interaction on the sound speed in layered composites RR.V. Razakova, R.A. Turusov	13-21
Topology optimization algorithm for heterogeneous anisotropic materials and structu A.D. Novokshenov, D.V. Vershinin, I.I. Abdulin	res 22-32
Variants of physical equations in a curvilinear coordinate system and their comparison based on mixed FEM	33-43
R.Z. Kiseleva, N.A. Kirsanova, A.P. Nikolaev, Yu.V. Klochkov, V.N. Yushkin Synthesis and tensile behavior of Al7475-nano B ₄ C particles reinforced composites at elevated temperatures	44-57
G.L. Chandrasekhar, Y. Vijayakumar, M. Nagaral, A. Rajesh, K. Manjunath, R. Vara Prasad Kaviti,	V. Auradi
Unique properties of the Al-0.5Fe-0.3Cu alloy, obtained by casting into an electromagnetic crystallizer, after equal-channel angular pressing and cold draw A.E. Medvedev, O.O. Zhukova, V.U. Kazykhanov, A. F. Shaikhulova, M.M. Motkov, V.N. Timofeev, N.A. Enikeev, M.Yu. Murashkin	58-72 wing
Outstanding ductility of high-strength ultrafine-grained aluminium at cryogenic temperatures T.S. Orlova, D.I. Sadykov	73-79
The effect of high-temperature annealing on the properties of bulk β-Ga ₂ O ₃ obtained in different growth atmospheres V.A. Spiridonov, D.I. Panov, A.Yu. Ivanov, D.A. Bauman, A.E. Romanov	80-85
Influence of aluminum shell on the process of devitrification of amorphous titanium nanoparticles: molecular dynamics simulation G.M. Poletaev, Y.Y. Gafner, S.L. Gafner, I.V. Zorya, Y.V. Bebikhov, A.S. Semenov	86-95
Interaction of two circular holes in an infinite plate by body force method S. M. Badiger, D.S. Ramakrishna	96-107
The role of the hydrostatic pressure under dynamic fracture of rocks N.S. Selyutina, L.A. Igusheva, Y.V. Petrov	108-120
Laboratory study on use of lime and waste materials in improving geotechnical properties of clay G. Juneja, A. Bhardwaj, A. Sharma, R.K. Sharma	121-144
Research of hydrogen diffusion in a material with various types of traps V.A. Polyanskiy, E.A. Varshavchik, A.A. Chevrychkina	145-153
Chromium plating of steel parts using the thermoemission field	154-160



N.A. Shaburova